Advanced polymer compartments: From catalytic nanocompartments to organelle mimics for biomedical applications

Inauguraldissertation

zur

Erlangung der Würde eines Doktors der Philosophie

vorgelegt der

Philosophisch-Naturwissenschaftlichen Fakultät

der Universität Basel

von

Maria Korpidou

Basel, 2024

Genehmigt von der Philosophisch-Naturwissenschaftlichen Fakultät auf Antrag von

Prof. Dr. Cornelia G. Palivan
(Universität Basel)
Erstbetreuerin

Prof. Dr. Jörg Huwyler
(Universität Basel)
Zweitbetreuer

Prof. Dr. Sébastien Lecommandoux
(Université de Bordeaux)
External Expert

Basel, den 28.05.2024

Prof. Dr. Marcel Mayor
Dekan

Dedicated to my family, and my Alan

When you want something,

the entire universe conspires

in helping you achieve it.

- Paulo Coelho

Acknowledgements

First of all, I would like thank my late supervisor Prof. Wolfgang Meier for giving me the opportunity to pursue my PhD in his group under the European ITN 'BIOMOLMACS' project and the freedom to navigate my scientific ideas. I would especially like to thank my current supervisor Prof. Cornelia Palivan for supervising my work and her endless support throughout all the phases of this journey. I am grateful for the great workspace I was provided, the fruitful conversations and the opportunities I had to grow personally and professionally to who I am today.

I cordially thank Prof. Jörg Huwyler for being my second supervisor, his kindness and his support.

I thank very much Prof. Sébastien Lecommandoux, my external supervisor for reading and evaluating my thesis, and for the great BIOMOLMACS meetings and trainings we had.

A big thank you to Dr. Ionel Adrian Dinu for greatly supporting me throughout my PhD, his feedback to become better and for always believing in me. I would also like to thank Dr. Viviana Maffeis and Dr. Shabnam Tarvirdirpour for supporting my work, challenging me and broadening my perspectives. I deeply thank Dr. Cora-Ann Schönenberger not only for supporting me whenever I needed her, but most importantly for sharpening my critical thinking, pushing me to become a better scientist and her sense of humor. I would especially like to thank Dr. Myrto Kyropoulou for always being there for me, making me see the world with different eyes and the excellent, insightful conversations.

Lukas Heuberger with whom we started our PhDs together and proved to be an exceptional collaborator, listener and a dear friend. Dr. Michal Skowicki and Dr. Riccardo Wehr for the resources and the fun times in and out of the lab. Dr. Voichita Mihali for helping me with TEM measurements. Dr. Alessandro Angelini, Dr. Stefano Di Leone, Sven Kasper, Moritz Muthwill, John Coats, Christoph John, Dr. Daniel Messmer, Dr. Davy Daubian, Dr. Olivia Eggenberger Dr. Vittoria Chimisso, Dimitri Hürliman and Dr. Claire Meyer without whom this journey would not have been the same. And to current and former members of the Meier-Palivan group and friends, everyone contributed in their own way in these four unique years of my life.

A special thank you to the 'BIOMOLMACS' network, the supervisors, the researchers and everyone that got involved. It was an once in a life time experience, turning out better than I ever thought and providing me not only with valuable hard and soft skills, but also friends and great memories. Prof. Remzi Becer for his key role in this consortium, for our collaboration and his great advice. Prof. Jan Van Hest and Prof. Petra Schwille for their excellent hospitality, resources and generosity. Prof. Feringa for the resources and our collaborations. Ainoa Guinart for being an amazing collaborator and friend. Yusuf Qutbuddin for his lab support, fun and (life) lessons. Alexander Fusi and Clémence Schvartzman for the great times in and out of the lab. Jonas Becker for the great work and communication. Camilla Pegoraro for the unforgettable moments, laughs and discussions. And everyone else that made this journey insightful and enjoyable.

To Maya Greuter for the great administration support.

The European Union and the University of Basel for funding and financial support.

A much more than a thank you to my family, whose support, love and understanding had no limits. Especially to my mom, my rock, that has been through it all, supported me, listened to me, advised me and pushed out of my comfort zone. I am grateful for everything. Σας ευχαριστώ για όλα!

Last but not least, I want to thank my Alan for believing in my strength, for being there at my highest and my lowest and for loving me as I am. ‘If there is something I can gain from this, it’d be the knowledge that you gave me when I thought I’d heard it all’ – There was a time, Guns ‘n’ Roses.

Table of Contents

Summary

Polymersomes, vesicles enclosing an aqueous cavity and self-assembled by block copolymers are a powerful platform for creating various nano- and micro-devices, finding applications in therapeutic delivery and diagnostic systems, local and on-demand consumption or production of molecules by encapsulated enzymes and mimics of natural compartments. Highlighting the versatility of the block copolymers, this work presents how we can combine amphiphilic block copolymers with molecules and biomolecules to create advanced polymer nanocompartments for: 1. controlled drug delivery, 2. local inversion of a drug metabolite to its active form, 3. simultaneous generation of therapeutically relevant compounds for promoting drug synergism and 4. emulating naturally-occurring organelles in a bottom-up, photoreceptor mimic.

First, we engineered polymersomes for delivering drugs in a highly spatiotemporally controlled manner. A hydrophobic synthetic molecular rotary motor, activated by irradiation with low-power visible light was incorporated in the membrane of polymersomes. We then evaluated the rotation of the motor and its impact on the morphology and concentration of the nanocompartments. As a result of the architectural changes, we investigated the cargo release profile from the inner cavities. Release was achieved even with low quantities of the photoresponsive unit, while we observed an on/off release behavior over sequential irradiation cycles. The photoresponsive system was tested in a lung carcinoma cell line for its ability to efficiently deliver the drug pemetrexed intracellularly. With the cell viability decreasing ‘on demand’ upon light irradiation, our nanosystem is an important stepping stone in the next generation of smart delivery systems.

We continued with the formation of polymersome-based catalytic nanocompartments designed for counteracting metabolism. The nanocompartments were equipped with the pore forming peptide, melittin to allow for diffusion of substrates and products to and from the enzyme-filled cavities. The enzyme kinetics of β-glucuronidase, the enzyme selected for cleaving the glucuronide moiety from metabolites were investigated in simple and complex mediums, revealing the influence of encapsulation and the protection from environmental impact. Our nanocompartments were readily internalized by hepatocellular carcinoma cells producing hymecromone, a rapidly metabolized drug in the body. These catalytic nanocompartments proved to be a promising strategy in the efforts of increasing the half-lives and residence time of therapeutic molecules.

Enriching the characteristics and expanding their potential applications in the field of drug synergism, we developed glycooligomer-decorated catalytic nanocompartments co-loaded

with two distinct enzymes. The design is based on the fine-tuning of their co-encapsulation in a single compartment in order for parallel enzymatic reactions to occur, while the glycooligomer tethers on their outer membrane served the purpose of targeting mannose-binding receptors. As a proof of concept, we showed that our nanosystem was preferentially internalized and escaped the endosomes in hepatocellular carcinoma cells with a high expression profile of such receptors, in comparison to adenocarcinoma cells expressing lower levels. Meanwhile, the encapsulated enzymes β-glucuronidase and glucose oxidase catalyzed in parallel the production of the therapeutically relevant compounds hymecromone and H_2O_2, respectively. Their simultaneous, intracellular generation by specifically uptaken catalytic nanocompartments led to an increased death of liver cancer cells, in contrast to epithelial carcinoma derived ones, where such behavior was not observed. This nanomedicinal system proposes a novel approach in the field of combinatorial, targeted cancer therapy, supporting and broadening the recent clinical trends.

Finally, we shifted our endeavors towards bottom-up synthetic biology, where polymersome-based artificial organelles were used to compartmentalize and create artificial photoreceptors for studying intra- and intercellular communication and signal transduction regulation. The artificial organelles presented a variety of functionalities (chemo- & photoresponsiveness, catalysis) emerging from the optimized combination of the selected molecules (i.e. calcium sensitive dye, melittin, synthetic molecular motor, β-galactosidase, β-galactosidase substrate) with the amphiphilic block copolymers. The artificial organelles were an integral part of generating artificial cells able to respond to chemical (calcium, substrate) and light signals, leading to an intracellular communication pathway. By strategic segregation of the artificial organelles in separate synthetic cells, we developed an intercellular communication model among different cell populations and mimicked the signal transduction regulation seen in natural photoreceptive synapses. This work represents a breakthrough in synthetic close-to-nature protocells and aims to provide a deeper understanding of processes governing cell communication and signal transduction.

List of Figures

List of Tables

Abbreviations

OEG	Oligo ethylene glycol
4-MU	4-Methylumbelliferone (or hymecromone)
4-MUG	4-Methylumbelliferyl-β-D-glucuronide
ASNase	L-asparaginase
BCA	Bicinchoninic acid
BMA	Butyl methacrylate
CAC	Critical aggregation concentration
CAPsome	Carbohydrate-*b*-poly(propylene glycol) derived vesicles
cGMP	Cyclic guanosine monophosphate
CLSM	Confocal Laser Scanning Microscopy
CNC	Catalytic nanocompartment
ConA	Concanavalin A
COVID-19	Coronavirus disease 2019
Cryo-TEM	Cryogenic-TEM
CuAAC	Copper-Catalyzed Azide-Alkyne Cycloaddition
DBCO	Dibenzocyclooctyne
DCF	2’,7’-dichlorofluorescein
DC-SIGN	Dendritic Cell-Specific Intercellular adhesion molecule-3-Grabbing Non-integrin
DLS	Dynamic Light Scattering
DMEM	Dulbecco's Modified Eagle Medium
DPPC	1,2-dipalmitoyl-sn-glycero-3-phosphocholine
FBS	Fetal bovine serum
FCCS	Fluorescence cross-correlation spectroscopy
FCS	Fluorescence Correlation Spectroscopy

FDA	Food and Drug Administration
FDG	Fluorescein-di-β-D-galactopyranoside
FITC	Fluorescein isothiocyanate
GFP	Green fluorescent protein
GOx	Glucose oxidase
GUS	β-glucuronidase
GUV	Giant unilamellar vesicle
H2DCFDA	2’,7’-dichlorodihydrofluorescein diacetate
H_2O_2	Hydrogen peroxide
HBS	HEPES-buffered saline
HCC	Hepatocellular carcinoma
HRP	Horseradish peroxidase
IA	Inner aqueous
MBL	Mannose-binding lectin
MBR	Mannose-binding receptors
MEM	Minimum essential medium
Methods	Techniques/ Reactions
MR	Mannose Receptor 1
MRI	Magnetic resonance imaging
MTS	3-(4,5-dimethylthiazol-2-yl)-5-(3-carboxymethoxyphenyl)-2-(4-sulfophenyl)-2H-tetrazolium
Mw	Molecular weight
NgR	Nogo-66 receptor
NTA	Nanoparticle Tracking Analysis
OA	Outer aqueous
P(TMC-DTC)	Poly(trimethylene carbonate-co-dithiolane trimethylene carbonate)

PBD	Polybutadiene
PBS	Phosphate buffered saline
PC	Polycarbonate
PCL	Polycaprolactone
PDEA	Poly(2-(diethylamino)ethyl methacrylate
PDI	Polydispersity index
PDLLA	Poly-d,l-lactic acid
PDMS	Poly(dimethylsiloxane)
PDPA	Poly(diisopropylaminoethyl methacrylate)
PEG	Polyethylene glycol
PEI	Poly(ether imide)
PEM	Pemetrexed
PEMA	2-(piperidin-1-yl)ethyl methacrylate
PEO	Poly(ethylene oxide)
PGG	Poly(L-γ-glutamyl-glutamine)
PHPMA	Poly(2-hydroxypropyl methacrylate)
PIAT	Polyisocyanoalanine(2-thiophene-3-yl-ethyl)amide
PiB	Polyisobutylene
PICsomes	Polyion complex vesicle
PLA	Polylactic acid
PMOXA	Poly(2-methyl-2-oxazoline)
PMPC	Poly(2-methacryloyloxyethyl phosphorylcholine)
PNIPAM	Poly(N-isopropylacrylamide)
PO	Polymer organic
POPC	1-palmitoyl-2-oleoyl-sn-glycero-3-phosphocholine
PPG	Poly(propylene glycol)
PS	Polystyrene

PVA	Polyvinyl alcohol
ROS	Reactive oxygen species
RT	Room temperature
SAXS	Small-angle X-ray diffraction
SEC	Size Exclusion Chromatography
SLS	Static Light Scattering
SPIONs	Superparamagnetic iron oxide nanoparticles
SPR	Surface plasmon resonance
ssDNA	Single-stranded DNA
TEM	Transmission Electron Microscopy
WGA	Wheat Germ Agglutinin
βGal	β-galactosidase

1. Introduction

This chapter introduces the principles underlying the formation of polymersomes, self-assembled vesicles from block copolymers in aqueous solution. The parameters governing the self-assembly of amphiphilic block copolymers and the methods used are presented. Next, the preparation of advanced, functional polymersomes is highlighted: how synthetic and biological molecules can be combined with polymersomes for obtaining systems with improved properties and functionality. Then, recent advances of nanometer-sized polymersomes developed for biomedical applications are presented with focus on therapeutics delivery systems and catalytic nanocompartments. Finally, the reader is introduced to mimics of natural nanometer- and micrometer-sized compartments, i.e. artificial organelles and cells which are engineered for studying and understanding complex cellular processes.

This chapter contains adapted with permission under CC BY 4.0 parts from the review Heuberger, L., ***Korpidou, M.****, Eggenberger, O.M., Kyropoulou, M., Palivan, C.G., 2022. Current Perspectives on Synthetic Compartments for Biomedical Applications. International Journal of Molecular Sciences, 23(10), 5718*

1.1 Compartmentalization: nature's way of regulating cellular processes

1.1.1 Compartmentalization in nature

In nature, compartmentalization is a governing characteristic that affects many aspects of the cellular life. Cells are the most prominent example of compartments where a thin phospholipid membrane form the individual cells and serve as the interface with their external environment and neighboring cells (**Figure 1.1**).[1] Further sub-compartmentalization, i.e. organelles provide a higher level of complexity and support distinct biological processes, such as molecule transportation, signal transduction and inter- and intracellular communication. Although the phospholipid membranes are the structural basis, their enrichment with biomolecules, e.g. proteins provide them with distinct functionalities and the ability to support a hierarchical way of responses. Therefore, compartmentalization as a fundamental, biological principle is important for the spatiotemporal separation of molecules and reactions and results in numerous studies concerning the exploration, mimicking or exploitation of biological functions.

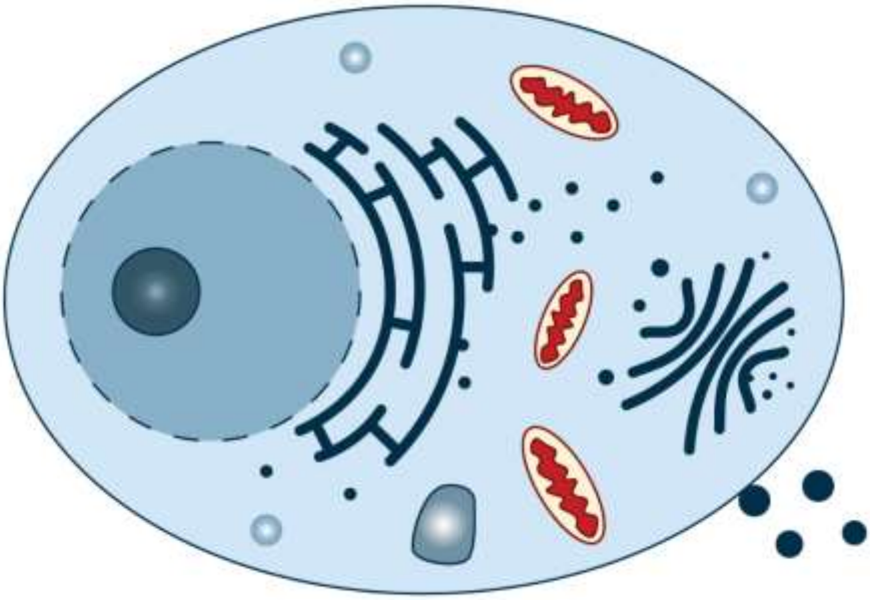

Figure 1.1. *Schematic representation of a eukaryotic cell and its compartmentalization.*

1.1.2 Mimicking naturally-occurring compartments

The generation of synthetic compartments has been established in the past decades as a way of mimicking biological compartments for purposes ranging from study models to biomedical applications.[2] In these biomimetic approaches, lipids, synthetic lipids and block copolymers have been utilized in the creation of the compartments.[3,4] Micrometer-sized vesicles have been the backbone of engineering artificial cells, while the nanometer-sized counterparts have been explored in bottom-up synthetic biology as artificial organelles, as well as in nanomedicine for the development of smart drug delivery systems or diagnostics.[5,6] Compartments, such as liposomes, lipid-derived spheres, or polymersomes offer the advantages of cargo loading in the vesicles' lumen and/or membrane and membrane decoration highlighting their potential for multifunctionality.

Although liposomes have the benefits of intrinsic biocompatibility and biodegradability, they often lack in mechanical properties and amenability for chemical modifications, limiting their applications.[7] In this regard, the polymer-based synthetic analogues have several advantages and represent a promising alternative. They are characterized by higher stability and robustness, as well as chemical versatility. Despite the thicker membranes of polymersomes, when appropriately selected, their flexibility allows for the incorporation of functional molecules and biomolecules, providing them with advanced functionalities including stimuli responsiveness and permeability.[8,9] Owed to their chemical versatility, biomolecules, such as proteins, peptides, sugars and nucleic acids can be conjugated on the synthetic membranes, expanding their applications and functions.[10] Additionally, the advancements in polymer chemistry have yielded a variety of copolymers that possess biocompatibility and/or biodegradability comparable to the natural counterparts. These characteristics place synthetic copolymers in a great position of choice for building advanced compartments for biomedical applications.

1.2 Amphiphilic block copolymers: formation of vesicles

1.2.1 Structure and synthesis of amphiphilic block copolymers

Amphiphilic block copolymers are renowned for their hydrophilic and hydrophobic characteristics. They can consist of two (AB) or more (ABA/ABC/ABABAB…) distinct blocks, where one is hydrophilic (A, C) and the other hydrophobic (B).[11,12] To date, there are many different strategies for synthesizing amphiphilic block copolymers with the desired numbers and types of monomers. These include controlled radical polymerization [e.g. atom transfer radical polymerization (ATRP), reversible addition-fragmentation chain transfer (RAFT)], anionic living polymerization, ring-opening polymerizations (ROPs) and their combinations. In particular, living polymerizations are preferred for acquiring distinct block copolymers, owed to the precision and control over the molar-mass and end-groups they offer. By carefully selecting the hydrophobic and hydrophilic blocks, a library of copolymers is generated that can provide desired properties to the formed structures.

1.2.2 Block copolymers and membrane formation

The types of membranes formed by block copolymers are defined by the different types of block copolymers used. In principle, the block copolymers are arranged in forms where the hydrophilic blocks are oriented to the aqueous environments, while the hydrophobic are hidden in the core of the membrane (**Figure 1.2A**). An example of polymer membranes closely resembling the lipid bilayers found in nature are the membranes formed by diblock copolymers (AB), where A is directed to the aqueous solutions, while B blocks face each other to create the hydrophobic part. Monolayer or bilayer structures are also formed by ABA copolymers, where a U turn configuration is required for forming the latter structure (**Figure 1.2A**).[13] When the hydrophilic blocks are different to each other (e.g. A, C) and carefully designed, this can result in asymmetric membranes or domains within the vesicles' membranes.[14] Domains can be created when the hydrophilic blocks are immiscible, while asymmetric membranes are driven by the different lengths of the two blocks: the shorter block is oriented towards the interior of the vesicle and the longer block towards the exterior.[15] Especially when aiming for bio-hybrid compartments, the lengths of the blocks, as well as the glass-transition temperature T_g need to be taken into great account.[16] The block lengths mainly dictate the thickness of the vesicles' membrane, which varies between 5 nm and 30 nm.[17] When the thickness is comparable to biological ones, the insertion of biomolecules, e.g. membrane proteins is favored and a specific orientation of insertion can be achieved in the case of asymmetry. T_g is equally important when engineering bio-hybrid vesicles as it determines the flexibility of the membrane in a range of temperatures and therefore, affects the insertion of biomolecules. Taking these into consideration, the characteristics of the building blocks directly influence the properties (mechanical stability, permeability, biomolecule insertion ability) of the resulting vesicles, the platforms of the bio-hybrid compartments. For example, vesicles formed by PEG-PHPMA block copolymers have been reported to possess intrinsic permeability, while vesicles made from PDMS-PMOXA are typically impermeable.[18]

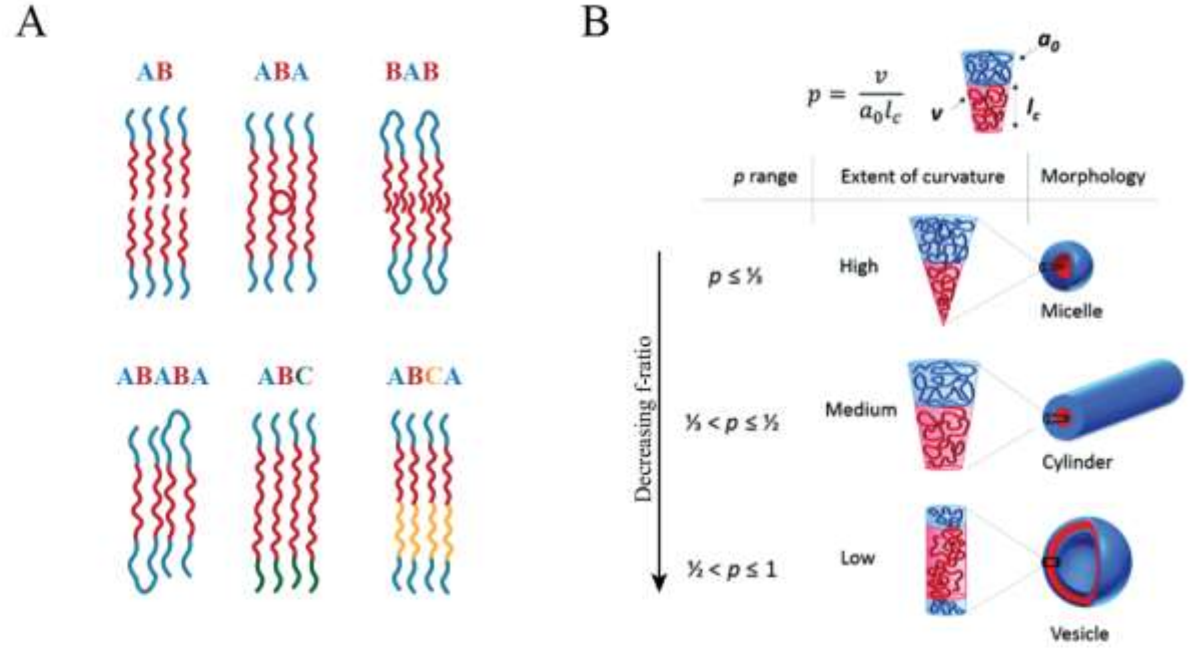

Figure 1.2. *Membrane architectures and self-assembled structures formed by amphiphilic block copolymers. (A) Schematic representation of the membrane architectures, which is a direct result of the copolymer's structure. (B) Self-assembled structures formed by amphiphilic block copolymers. The resulting structures is influenced by the copolymer's f-ratio. Adapted with permission from reference*[19] *under CC BY 3.0.*

1.2.3 Parameters of block copolymers self-assembly

The self-assembly of amphiphilic block copolymers in aqueous solutions results in supramolecular architectures (micelles, polymersomes, worms) and is driven by noncovalent interactions.[20] The packing parameter p, defined as $p=v/\alpha_O l_c$, where v the volume and l_c the length of the hydrophobic block and α_O the contact area of the head group, describes the influence of the design of the copolymers on the resulting assemblies (**Figure 1.2B**).[19,21] Prediction of the supramolecular assemblies can be performed depending on the p value. For example, for $1/2 \leq p \leq 1$, vesicles are formed. However, spherical and cylindrical micelles are created when $p \leq 1/3$ and $1/3 \leq p \leq 1/2$, respectively. The curvature of the structures' membrane is greatly determined by the f-ratio, i.e. the ratio of the hydrophilic block's molecular weight (Mw) to the total block copolymer Mw and characterizes the tendency for a particular structure.[22] For example, when the f-ratio is in the range of 35 ± 10%, vesicles are the favored supramolecular assembly, even if the copolymers have a rather high polydispersity index (PDI).[23] The formation of spherical micelles is defined by a higher membrane curvature, meaning higher f-ratios. It is important to note that the greater stability of the block copolymer assemblies compared to the lipidic analogues is illustrated by critical aggregation concentration (CAC). CAC is the required concentration of amphiphiles to start forming colloidal systems and is 10’000-fold lower for block copolymers in comparison to lipids.[24] Although the composition, Mw and dispersity of the block copolymers influence the self-assembly, secondary factors, such as temperature, ionic strength, pH and formation technique also have a large impact.[25]

1.2.4 Vesicle formation techniques

The self-assembly of block copolymers in nanometer- and micrometer-sized vesicles is supported by various techniques (**Figure 1.3**)[26] and extended information and comparison are provided in other sources.[6,20,27] In the solvent switch method, the block copolymer is dissolved in a water-miscible organic solvent, followed by the dropwise addition of an aqueous buffer to slowly replace the organic phase.[28] On the contrary, the cosolvent method is based on the dropwise addition of a copolymer solution to an aqueous buffer phase, which induces the self-assembly process of copolymers. The main drawback of these approaches is the residual presence of organic solvent in the final solution, which is undesirable for biologically relevant applications. The film rehydration method (**Figure 1.3A**) follows a more biocompatible manner, as the organic solution of the copolymer is completely dried, forming a film. The thin copolymer film is subsequently rehydrated with an aqueous solution, inducing the self-assembly process. This is a well-suited technique for loading the vesicles’ cavities with sensitive molecules, such as enzymes and inserting membrane proteins, during the rehydration step. However, as the resulting vesicle populations are heterogeneous in size, they can be extruded through a membrane with defined size of pores in order to obtain nanometer-sized polymersomes with narrower size distribution.

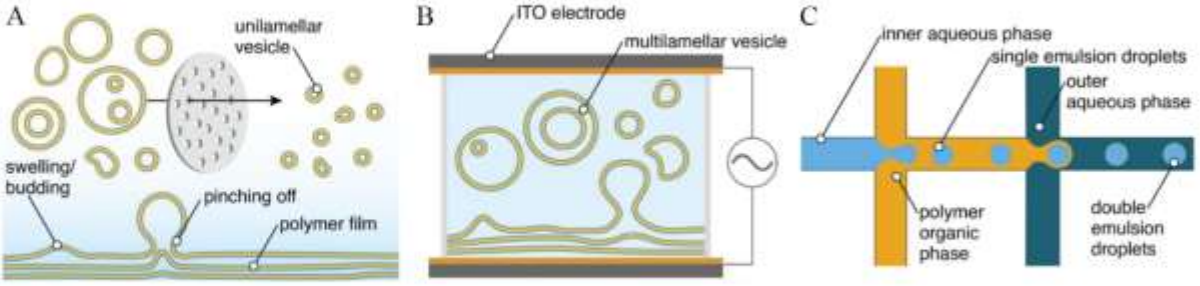

Figure 1.3. *Schematic representation of selected production methods of synthetic compartments. (A) film rehydration and subsequent extrusion of block copolymers. (B) electroformation. (C) double*

emulsion formation with a microfluidic setup. Adapted with permission from reference[26] under CC BY 4.0.

Micrometer-sized (or giant) unilamellar vesicles (GUVs) can be generated by the above-mentioned methods, including electroformation (**Figure 1.3B**).[26] The electroformation technique is based on the spontaneous swelling of a dried block copolymer film that has been deposited on two electrodes of indium tin oxide (ITO)-coated glass or platinum and the consequent formation of GUVs in the presence of an aqueous solution is stimulated by an electric field.[29] Microfluidic technology (**Figure 1.3C**), based on microdevice channel sizes and junction design represents a step forward and has been used for high-throughput GUV formation with a narrow size distribution.[30,31] Polymer-stabilized water–oil–water (w/o/w) double emulsions are used to form GUVs with the support of different microfluidic designs. Subsequent evaporation of the volatile organic solvent leads to the formation of highly monodisperse GUVs with a polymer membrane. This technique has been utilized in the encapsulation of biomolecules within the cavities with high encapsulation efficiencies (99%), as well as membrane insertion of biopores and membrane proteins.[32]

1.2.5 Preparation of advanced polymersomes

1.2.5.1 Surface functionalization

Under the scope of utilizing polymersomes for biomedical applications, their external surfaces can be functionalized to attach different molecules with the aims of targeting specific cells, biolocations or organs.[33–35] The desired molecules can be attached covalently (e.g. azide-alkyne cycloaddition, maleimide and thiol-ene, amine coupling)[35–39] or by molecular recognition.[40] For example, the functionalization of PMOXA-*b*-PDMS polymersomes with 4-formylbenzoate facilitated the attachment of hydrazone(HyNic)-functionalized antibodies for biotin.[39] Proteins can also be covalently attached on the surface of polymersomes. Prominent examples include horseradish peroxidase (HRP) on the surface of PS-*b*-PIAT-based vesicles[41] and transferrin on PEG-*b*-P(TMC-DCT)-based ones (**Figure 1.4A**).[42] As antibodies and proteins are large in size, they can be replaced by targeting and cell penetrating peptides to target polymersomes to specific cells or organelles, and increase their tumor penetration.[33,43–46] Nucleic acids, such as DNA or RNA single strands can also be used to decorate the surface of polymersomes and can be exploited in targeting applications.[47,48] Sugars, e.g. galactose can also functionalize the surface of nanomedicinal systems for targeting purposes, as well as increasing the uptake.[49] In this case, receptors recognizing a specific type of sugar can be targeted, leading to cell-specific internalization of the vesicles.

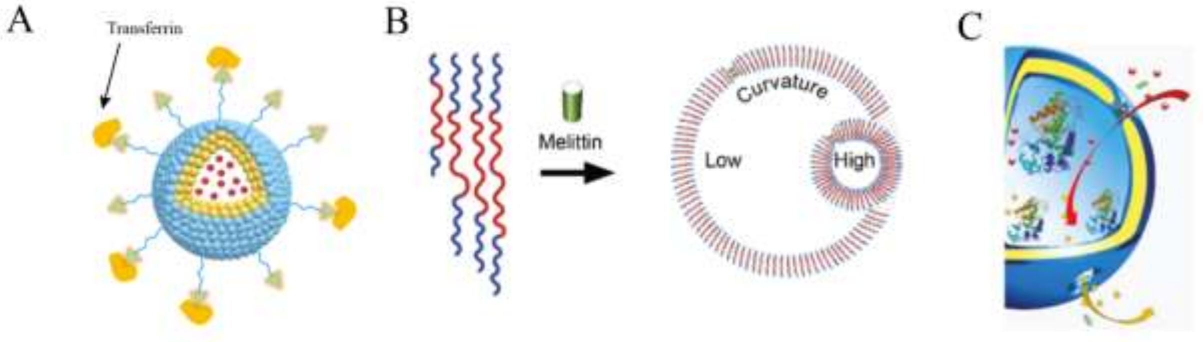

Figure 1.4. *Tailoring polymeromes for acquiring different functionalities. (A) Polymersomes loaded with doxorubicin and surface decorated with transferrin for targeted drug delivery. Adapted with permission from reference.*[42] *(B) Pore formation by melittin inserted in self-assembled PMOXA-b-PDMS-b-PMOXA copolymers. The insertion is influenced by the route of insertion, the copolymer characteristics and membrane properties. Adapted with permission from reference.*[50] *(C) Catalytic nanocompartments encapsulating HRP developed for consumption of cytotoxic* H_2O_2*. Adapted with permission from reference*[51] *under CC BY 4.0.*

A second option for attaching the desired molecules at the surface of compartments is to use molecular recognition as the driving force. Among the most effective pairs of molecules involved in molecular recognition are biotin–streptavidin proteins and nucleic acid hybridization.[40,52] A highly specific conjugation method was mediated by oligonucleotide sequences such as single-stranded DNA (ssDNA).[40,53] In detail, azide-exposing PMOXA-*b*-PDMS polymersomes enabled coupling of dibenzocyclooctyne (DBCO)-derivatized ssDNA or its complementary oligonucleotide.[54] Because of the specificity of complementary base pairing, DNA can be used as a means to direct the self-organization of polymersomes into more complex structures.

1.2.5.2 Membrane functionalization

Biomolecules with a hydrophobic domain have the potential of being inserted into the polymer membrane, enriching the compartments with new functionalities, like stimuli-responsiveness. The insertion can take place either during the self-assembly, or in preformed vesicles, although the latter appears to be governed by the concentration of the biomolecule and the hydrophobic forces.[55,56] Although ionophores have been entrapped into the membrane of polymersomes to achieve ion-selective membrane permeability,[55] larger entities, like proteins and membrane proteins have also been inserted, possessing a critical role in the functionality of the resulted bio-hybrids.[57,58]

Reconstitution of membrane proteins in polymer membranes have offered the advantage of permeabilizing otherwise impermeable polymersomes.[18,57,59] Remarkably, such proteins have been successfully reconstituted, even though the thickness of the polymer membranes is bigger than this of a cellular, suggesting a conformational adaptation between the polymer and the protein.[8] However, there are specific parameters that govern the successful insertion: high flexibility of the block copolymers to achieve membrane fluidity, higher PDIs that allow the polymer chains to adapt to the protein dimensions and a hydrophobic mismatch between the membrane thickness and the size of the protein in a 3.5 - 5 times range. Outer membrane protein F (OmpF) is a typical example.[55] Owed to its Mw cut-off (≤ 600 Da), this porin enables the flow-through of small molecules, while restricting larger, encapsulated biomolecules to escape the cavities. The list of other reconstituted proteins includes α-hemolysin,[60] bacteriorhodopsin[61] and aquaporinZ,[62] each providing unparalleled properties to the respective polymersomes.

Amphiphilic peptides have also been investigated for their spontaneous insertion in polymer membranes with subsequent organization into pores, leading to membrane permeabilization.[50] Melittin, the main component of bee venom is a 26-amino acid peptide that changes its conformation to an α-helical bent rod when entrapped in membranes.[63,64] Inserted peptides can then accumulate together to form pores and each pore can consist of 3 to 19 melittin monomers, resulting in an inner pore diameter in the range 1-6 nm.[65] Because of its antimicrobial properties,[66] its insertion in lipids membranes has been extensively investigated,[67,68] inspiring the evaluation of its insertion into polymer membranes. It was recently reported that the insertion of melittin in PMOXA-*b*-PDMS-*b*-PMOXA vesicles is strongly depended on: the route of insertion, the inherent copolymer characteristics and the membrane properties and curvature (**Figure 1.4B**).[50] Melittin was also successfully utilized for its membrane permeabilization abilities in PDMS-*b*-PMOXA enzyme-bearing polymersomes to accommodate a molecular through-flow of substrates and products, greatly expanding its use in biomedical applications.[69]

1.2.5.3 Encapsulation within the cavity

When the objective is the encapsulation of hydrophilic molecules, polymersomes are an appealing platform compared to liposomes for reasons rooting in their higher stability and reduced leakage. A widely investigated and developed field for their application is the delivery of drugs or imaging agents.[26] For their loading in the lumen of the vesicles, the hydrophilic molecules are added to the aqueous solution during the polymersome formation. Prominent examples of imaging agents that have been encapsulated include quantum dots,[70] triplet–triplet annihilation-based molecular photon upconversion (TTA-UC) chromophores[71] and fluorescent dyes.[72] Meanwhile, hydrophilic drugs, e.g. doxorubicin and pemetrexed have been efficiently loaded in the aqueous cavities of polymersomes.[73,74] In these cases, apart from the above-mentioned advantages, carefully engineered polymersomes can provide the means of the hydrophilic molecules to cross the cell membranes and be efficiently delivered to the target site, while reducing any molecule-associated side effects. These nanomedicinal systems are often built by stimuli-responsive polymers (e.g. PNIPAM which is temperature-responsive) in order to release the drugs at the desired biolocation.[75]

Particularly in the case of sensitive and catalytic molecules, such as nucleic acids and enzymes, their encapsulation in the aqueous cavity of polymersomes offers the extra advantage of protection from external factors and thus prolongation of their activity. For example, nucleic acids (e.g. plasmids, DNA, RNA) loaded in polymer vesicles were protected from nuclease degradation, making the system a great candidate for gene delivery applications.[76,77] On the other hand, enzymes can be loaded in polymer vesicles for two main purposes in biomedical applications. In the first approach, the biomolecules are delivered at the desired biolocation and are subsequently released from the cavities.[78,79] The rationale of this approach is mostly inspired by the enzyme replacement therapy, where the delivery of the enzyme aims to replace its missing or defective natural analogue.[80]

The second strategy includes the generation of catalytic nanocompartments (CNCs) with the aim being the retention of the enzymes in the confined space for producing or degrading compounds of interest (**Figure 1.4C**).[81] When CNCs are internalized by cells, they can act as artificial organelles performing enzyme-specific reactions.[51] Importantly, the efficiency of these nanocompartments is governed by the permeability of the polymer membrane for establishing a molecular through-flow to and from the enzyme-rich cavities. Polymersomes with inherent permeability, e.g. assembled from PS-PIAT[41] or PGG[82] allow for the diffusion of small molecules, in contrast to impermeable polymersomes (e.g. made from PDMS-PMOXA) for which membrane pores or channels are crucial.[51] Having established a molecular through-flow, the segregation of the enzymes in the confined space of polymersomes has shown to have an impact on the enzyme kinetics.[57,83] In the confined space, the collision frequency between the reagents is higher, leading to a lower Michaelis-Menten constant (K_m) compared to non-encapsulated enzymes. Moreover, the maximal enzyme velocity (V_{max}) and the turnover rate (k_{cat}) are also decreased, attributed to the slower influx and efflux of substrates and products inside the nanocompartments. Expanding the complexity and functionalities of these bio-hybrid nanocompartments, more than one enzymes can be utilized to work in tandem for therapeutic applications.[83–85] The enzymes can be either confined in separate compartments or in the same, participating in a cascade reaction. While segregation of enzymes in different vesicles for parallel reactions has been investigated,[83,85] their encapsulation in the same compartment has yet to be explored. A list of biomolecules that have been encapsulated or incorporated in polymersomes for biomedical applications can be found in **Table 1.1**.

Table 1.1. *Biomolecules for the development of advanced nanocompartments for biomedical applications. Adapted with permission from reference*[26] *under CC BY 4.0.*

Biomolecule	**Polymer**	**Location in Assembly**
Catalase	PEG-*b*-PPG-*b*-PEG[86]	Encapsulated within the cavity
Cytochrome bo$_3$ ubiquinol oxidase	PBD–PEO:POPC hybrid,[87] PDMS-g-PEO and PDMS-g-PEO/PC hybrid[88]	Incorporated within the membrane
Dopa decarboxylase	PDMS-*b*-PMOXA[89]	Encapsulated within the cavity
Glucose oxidase (GOx)	PDMS-*b*-PMOXA,[69] PEG-*b*-P(CPTKMA-*co*-PEMA)[90]	Encapsulated within the cavity
Horseradish peroxidase (HRP)	PMOXA-*b*-PDMS-*b*-PMOXA,[51] carbohydrate-*b*-PPG[82]	Encapsulated within the cavity
Inducible nitric oxide synthase	PMOXA-*b*-PDMS-*b*-PMOXA[85]	Encapsulated within the cavity
Laccase	PDMS-*b*-PMOXA[91]	Encapsulated within the cavity
Lactoperoxidase	PDMS-*b*-PMOXA[69]	Encapsulated within the cavity
L-asparaginase	PMPC-*b*-PDPA and PEO-*b*-PBO,[92] PEG-*b*-PHPMA[93]	Encapsulated within the cavity
Lipase	PMOXA-*b*-PDMS-*b*-PMOXA[94]	Encapsulated within the cavity
Luciferase	PDMS-*b*-PMOXA[95]	Encapsulated within the cavity
Melittin	PDMS-*b*-PMOXA[69]	Incorporated within the membrane
Outer membrane protein F from E. coli (OmpF)	PMOXA-*b*-PDMS-*b*-PMOXA[51,96]	Incorporated within the membrane
Penicillin acylase	PMOXA-*b*-PDMS-*b*-PMOXA[96]	Encapsulated within the cavity
β-galactosidase	carbohydrate-*b*-PPG[82]	Encapsulated within the cavity
Soluble guanylyl cyclase	PMOXA-*b*-PDMS-*b*-PMOXA[85]	Encapsulated within the cavity
Trypsin	PMPC-*b*-PDPA[97]	Encapsulated within the cavity
Tyrosinase	PDMS-*b*-PMOXA[98]	Encapsulated within the cavity
Urate oxidase	PMOXA-*b*-PDMS-*b*-PMOXA[83]	Encapsulated within the cavity

1.3 Polymersomes designed for biomedical applications

Ever since their conception in 1994,[5] polymersomes with diverse physicochemical properties and cargo have been developed for a plethora of biomedical applications. This section aims to provide the reader with an overview of such applications, including some noteworthy examples that intent to highlight their diverseness.

1.3.1 Delivery systems

Polymersomes are appealing candidates when it comes to designing therapeutic delivery systems for reasons elaborated above. Polymer nanosystems have been developed to date for imaging, theranostic and therapeutic purposes.[26] For example, prepared for cellular imaging, quantum dots were encapsulated in PDMS-*b*-PMOXA polymersomes.[70] Compared to the respective liposome counterparts, they exhibited higher stability, as they did not release the cargo in the cytoplasm. Taking advantage of both the hydrophobic membrane and the hydrophilic lumen, PiB-*b*-PEG polymersomes were equipped with a fluorescent probe in their membranes and a second in the aqueous cavities (**Figure 1.5A**).[72] These polymersomes, prepared for dual fluorescent imaging remained intact and active 96 h postinjection in zebrafish embryos and were not excreted, degraded or cause any animal death. Going a step further, a theranostic system can be established, offering diagnosis and treatment simultaneously.[37] A prominent example includes PEI-*b*-PDLLA polymersomes developed for neuronal restoration treatment trackable by magnetic resonance imaging (MRI).[99] Superparamagnetic iron oxide nanoparticles (SPIONs) and the siRNA targeting the Nogo-66 receptor (NgR) gene were encapsulated in these nanocompartments and when tested on an acute ischemic stroke rat model, they promoted a better recovery than the control group.

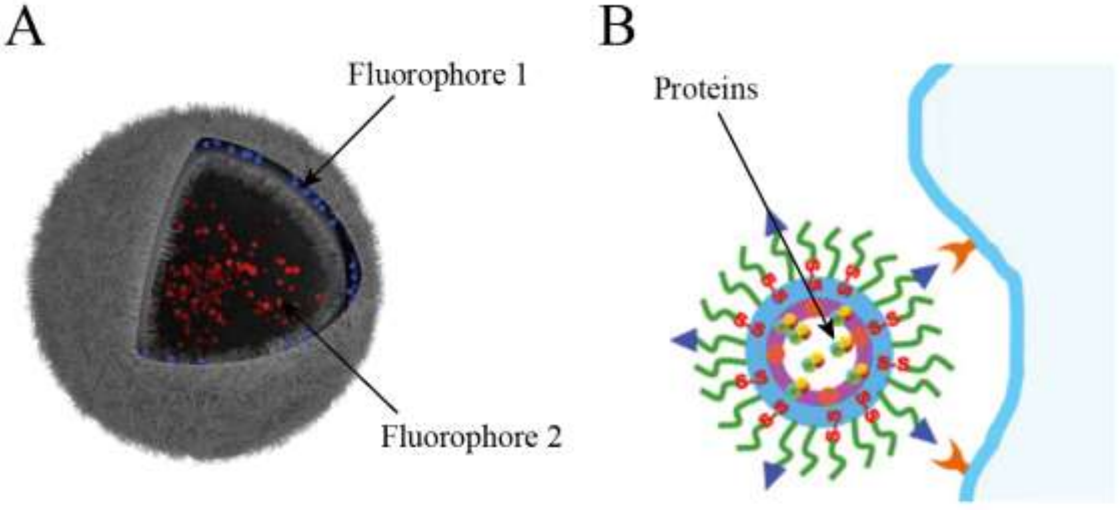

Figure 1.5. *Representative examples of polymersome-based delivery systems. (A) Dual fluorescence of polymersomes for optical imaging. Adapted with permission from reference.*[72] *(B) Galactose-decorated reduction-sensitive polymersomes for active loading and intracellular delivery of proteins. Adapted with permission from reference.*[49]

In regards to therapeutic delivery systems, there are numerous examples of nanosystems developed either for small molecule delivery or biologics (e.g. enzymes).[5,78,79,100] Profiting from the different segments of polymersomes, drug nanocarriers made of a mixture of PEG-*b*-PLA or PEG-*b*-PCL with PEG-*b*-PBD were able to simultaneously carry the anticancer drugs paclitaxel (in the hydrophobic membrane) and doxorubicin (in the aqueous lumen), leading to growth arrest and shrinkage of rapidly growing tumors in nude mice.[101] On the other hand, polymer vesicles can be engineered for delivery of larger biologic molecules, such as proteins. Chimeric polymersomes made of precisely mixing the block copolymers PEG-*b*-PCL-*b*-PDEA, Gal-PEG-*b*-PCL and PEG-SS-PCL were loaded with either bovine serum albumin, ovalbumin, or cytochrome c (**Figure 1.5B**).[49] Attributed to their response in a reductive environment, proteins were released from the polymersomes in the presence of dithiothreitol. Particularly in the case of cytochrome c, its targeted intracellular delivery and release in HepG2 hepatocellular carcinoma cells resulted in a cell viability of about 31.5%, indicating the therapeutic potential of this nanosystem. It is noteworthy that when it comes to efficient intracellular and targeted drug delivery, numerous stimuli-responsive polymersomes have been presented.[102] Among the stimuli, pH,[103] redox,[104] enzymes,[105] glucose,[106] CO_2,[107] temperature,[108] light,[109] ultrasound[110] and electromagnetic field[111] triggers are the predominant choices.

1.3.2 Catalytic nanocompartments

Catalytic nanocompartments have been investigated for their application in nanomedicine in areas including detoxification, enzyme replacement therapy or enzyme prodrug therapy.[26,112,113] For example, HRP-loaded PMOXA-*b*-PDMS-*b*-PMOXA CNCs were developed as antioxidants, consuming cytotoxic H_2O_2 *in vitro* and *in vivo* (**Figure 1.6A**).[51] The use of HRP was expanded in a cascade reaction system for the treatment of gout and oxidative stress.[83] CNCs were prepared encapsulating either HRP or uricase and tested on kidney-derived HEK293T cells for their ability to detoxify uric acid, while preventing accumulation of H_2O_2. Similarly, a cascade reaction *in situ* inside epithelial cells of adenocarcinoma and myoblasts served for the production of cyclic guanosine monophosphate (cGMP), a second messenger molecule involved in a number of pathologies.[85] Inducible nitric oxide synthase and soluble guanylyl cyclase were encapsulated in separate nanocompartments, and the production of cGMP was monitored by measuring the cytoplasmic calcium levels. The highest response was recorded when both of the nanocompartments were present, highlighting their potential to influence cell physiology.

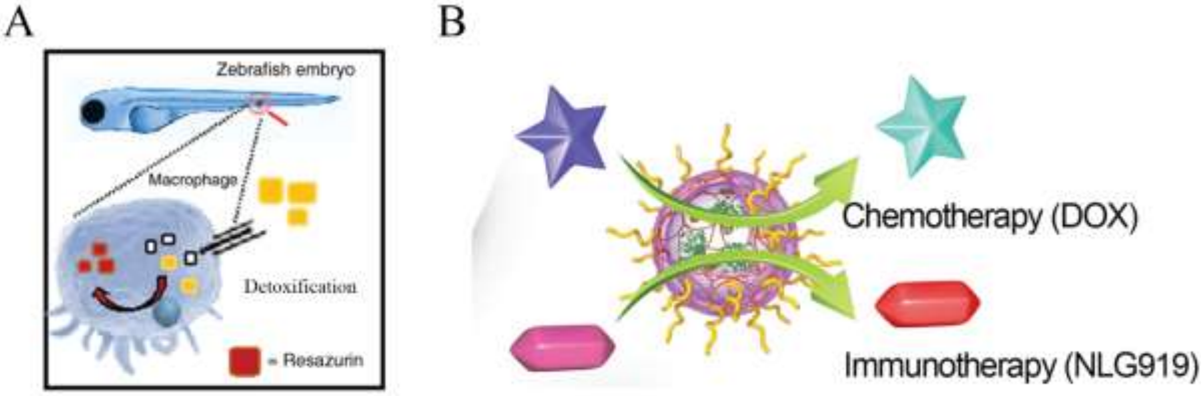

Figure 1.6. *Representative examples of polymersome-based catalytic nanocompartments. (A) Detoxifying HRP-encapsulating catalytic nanocompartments, acting as artificial organelles in a zebrafish embryo. Adapted with permission from reference*[51] *under* CC BY 4.0. *(B) Catalytic nanocompartments developed for enhanced enzyme prodrug chemo-immunotherapy. Adapted with permission from reference.*[114]

When the objective is the specific and local production of drugs, catalytic nanocompartments with a number of encapsulated enzymes have been designed.[112] For example, carbohydrate-*b*-PPG nanocompartments with intrinsically permeable membranes and encapsulated β-galactosidase (βGal) were able to produce doxorubicin from 5-*N*-(β-Dgalactopyranosiylbenzyloxy-carbonyl)-doxorubicin in the selected cell lines and in tumor-bearing mice.[82] Adjusting to the recent trends of combinatorial therapeutic strategies, βGal-loaded PEG-*b*-P(PEMA-*co*-BMA) polymersomes were able to activate DoxGal and 1-cyclohexyl-2-(5H-imidazo[5,1-a]isoindol-5-yl)ethanol, highlighting the improved therapeutic outcome from the simultaneous production of doxorubicin and NLG919 (**Figure 1.6B**).[114] Although cancer therapy possesses a predominant place in the applications of CNCs, others, such as production of antibiotics have also benefited from their development.[26] An exemplary case is the generation of PMOXA-*b*-PDMS-*b*-PMOXA polymersomes equipped with penicillin acylase and permeabilized with OmpF.[96] These CNCs locally produced and released antibiotics and effectively inhibited bacterial growth, expanding the areas of CNCs application.

1.4 Mimics of natural compartments: artificial cells and organelles

Apart from their use in nanomedicinal systems, synthetic compartments have been an integral part of bottom-up synthetic biology, offering simplified views on cellular processes.[26,32,115,116] Synthetic cells and organelles have reduced complexity relative to native cells and support our better understanding of complex metabolic processes. Insights into the fundamental elements that control cellular behavior and function can be developed and greater knowledge of diseases and treatment approaches can be acquired. The bottom-up strategy also offers the unique opportunity to combine artificial and biological components to create hybrid biological systems augmenting certain aspects of living systems. GUVs serve as excellent models for cells because of their size similarity and unilamellar membrane structure. Specifically, in the case of polymer GUVs, the complexity of natural cell membranes in composition and architecture can be achieved.[117] For example, for the generation of membrane domains, DPPC was mixed with mPEG-*b*-PCL (**Figure 1.7A**).[118] The generated hybrid GUVs were characterized by DPPC-rich and block copolymer-rich phase-separated domains, indirectly influencing the mechanical and permeability properties of the membrane. Moreover, natural membranes are constantly being remodeled in a dynamic process, enabling the adaptation of cells to their current environment.[119] Such a procedure was demonstrated in asymmetric PBD-*b*-PEO/POPC membranes, where the trans-bilayer migration of amphiphilic molecules lasted around 7.5 h, comparable to lipid vesicles.[30]

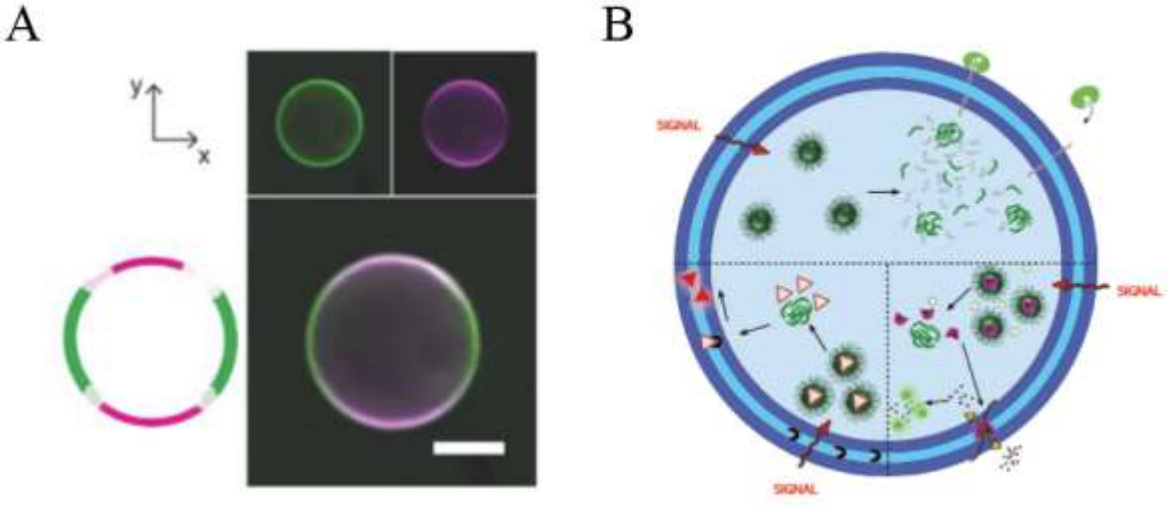

Figure 1.7. *Representative examples of cell mimics to study cellular aspects. (A) Hybrid GUVs with phase-separated domains stained via fluorescein isothiocyanate (FITC, green) and Liss Rhod PE (red). Adapted with permission from reference*[118] *under CC BY 4.0. (B) Schematic representation of a subcompartmentalized artificial cell containing reduction sensitive artificial organelles for triggered enzymatic activity and ion channel recruitment. Adapted with permission from reference.*[120]

Most cellular systems are compartmentalized across several length scales and sub-compartments, i.e., organelles are essential to spatially separate processes within cells.[121] Using multicompartmental vesicles, supramolecular assemblies with hierarchical organization, increased complexity, and subcompartments can be created. For example, PS-*b*-PIAT catalytic nanocompartments were loaded in PBD-*b*-PEO artificial cells performing a three-enzyme cascade reaction.[122] Such an artificial system aimed to investigate how cellular reactions or interactions take place and understand how the complexity of eukaryotic cells is established. Multicompartmental GUVs formed by the encapsulation of responsive nanoparticles loaded with biomolecules inside GUVs is another exemplary study (**Figure 1.7B**).[120] The nanoparticles were loaded with either enzyme substrates or biopores and disassembled in the presence of dithiothreitol, thus releasing the nanoparticles' cargo. The release of the substrates triggered their catalysis by coencapsulated enzymes, while the release of the ion channels (gramicidin) allowed them to integrate into the vesicle membrane, inducing controlled permeabilization. Using this approach, a multicompartment cellular system was created that was able to change membrane permeability upon external signals, a process naturally occurring in neurons. It is therefore highlighted that synthetic vesicles, accompanied by their characteristics, advantages and functionalities are strong candidates not only for direct biomedical applications, but also for the development of natural mimics investigating the fundamentals of life, cellular processes and diseases.

2. Aim of the Thesis

The aim of this thesis is the development of polymersome-based nanocompartments as the means towards advanced drug delivery and production systems, as well as integrated organelle mimics by implementing the above-mentioned strategies. The below-presented nanosystems are composed of PDMS-PMOXA diblock copolymers, while the encapsulated, inserted and functionalized synthetic and biological molecules are carefully selected depending on the target application. In their larger conception, these nanocompartments compose a versatile platform envisioned to be utilized and modified for novel biomedical applications.

To engineer a novel, stimuli-responsive, drug delivery nanosystem, we generated polymersome-based, drug-loaded nanocarriers bearing a synthetic, light-activated molecular motor (Chapter 3). To overcome one of the major drawbacks of photoresponsive systems, we employed synthetic molecular motors entrapped in the hydrophobic membrane, able to be activated by low-power visible light. We investigated the morphological changes of the polymersomes as a function of the inserted, activated molecular motor and evaluated the cargo release profile over sequential cycles of light irradiation. We further monitored the cytotoxicity and efficiency of our photoresponsive nanosystem to deliver the FDA-approved drug pemetrexed in a lung carcinoma cell line, highlighting the advantages, novelty and potential it represents in the field of smart drug delivery.

Aiming to propose an innovative way to counteract drug metabolism, we developed enzyme-loaded catalytic nanocompartments able to invert a glucuronidated drug metabolite towards its active form (Chapter 4). Motivated by the adverse effects of rapid glucuronidation of drugs, we proposed an unparalleled platform of local reactivation of drug glucuronides. Catalytic nanocompartments encapsulating β-glucuronidase, the enzyme responsible for cleaving the glucuronide moiety were permeabilized with the pore-forming peptide melittin and evaluated for their activity. Michaelis-Menten kinetic analysis was performed to provide a deeper understanding of the mechanism of action of the encapsulated enzyme in solution and in cell culture medium. Our catalytic nanocompartments were further tested for their uptake, cytotoxicity and activity in a hepatocellular carcinoma cell line owing to the relevance and applicability for their envisioned biomedical application.

To offer a novel approach in the field of drug synergism and related areas, we engineered advanced glycooligomer-decorated, dual enzyme-loaded catalytic nanocompartments for targeted, parallel enzymatic reactions (Chapter 5). To achieve synergism, the encapsulated enzymes, β-glucuronidase and glucose oxidase were carefully selected for the design of parallel reactions aiming to: 1. produce an active drug from a prodrug form, while 2. inducing cell starvation and generating cytotoxic H_2O_2 by glucose consumption. The catalytic activity of the nanocompartments was enabled by melittin induced pores allowing for molecular throughflow. Aiming for targeting the mannose-binding receptors, glycooligomer tethers consisting of eight pendant mannose units were used for decorating their outer membranes. Their enzymatic activity was investigated in cell culture medium, rich in glucose and the glucuronide form of hymecromone. As a proof of concept, we co-cultured of two cell lines with different mannose-binding receptor expression profiles and evaluated our nanosystem for their cell-specific targeting potential and enhanced internalization. To provide evidence of its applicability and activity, we assessed the levels of cell viability when both hymecromone and H_2O_2 were produced by our catalytic nanocompartments, paving the way for new strategies not only in combinatorial cancer therapy, but also in enzyme-based therapies.

To expand and enrich the field of bottom-up synthetic biology, polymersome-based artificial organelles with varying functionalities were integrated in artificial cells towards the formation of photoreceptor mimics (Chapter 6). Chemo-, photoresponsive and catalytic artificial organelles were encapsulated in micrometer-sized artificial cells, creating advanced compartmentalized systems. Their fine-tuned response to calcium input was evaluated by encapsulating a calcium sensitive dye, while their response to visible light irradiation by the release of cargo regulated by the activation of a synthetic molecular motor. Catalytic artificial organelles were based on melittin-permeabilized polymersomes loaded with β-galactosidase, able to catalyze the conversion of fluorescein-di-β-D-galactopyranoside to fluorescein. Increasing the level of complexity towards establishing intra- and intercellular communication in photoreceptor mimics, photoresponsive and catalytic artificial organelles were encapsulated in the same or different artificial cells. Similar to nature, we investigated the effect of calcium on modulating the signaling propagation in our artificial synapse, contributing to our knowledge of cellular communication, broadening the spectrum of potential applications and inspiring the development of a wider range of organelle and cell mimics.

3. Synthetic Molecular Motor-bearing Polymersomes for Intracellular Drug Delivery

This chapter describes the design of a polymer-based delivery system for intracellular drug release on demand. A PDMS-b-PMOXA diblock copolymer combined with a hydrophobic synthetic molecular rotary motor create a responsive self-assembled system with high spatiotemporal control and tunable release profiles. The delivery of a fluorescent dye with high efficiencies (up to 75%) and with an on demand on/ off responsive behavior over sequential cycles was triggered by the selective activation with low-power visible light (λ = 430 nm, 6.9 mW) of the successfully incorporated motor. Our stimuli-responsive system was further tested under relevant physiological conditions using the lung cancer cell line A549 and the encapsulation of pemetrexed, a Food and Drug Administration (FDA)-approved drug. As shown by the similar levels of cell viability compared to the free given drug, our platform successfully delivered pemetrexed, highlighting its potential to deliver functional drugs on request with high efficiency. Our system is an important step for the application of synthetic molecular machines in the next generation of smart delivery systems, aiming to enrich and broaden the field, as well as provide solutions to current hurdles of nanomedicine.

This study is published as Guinart, A., **Korpidou, M.***, Doellerer, D., Pacella, G., Stuart, M.C.A., Dinu, I.A., Portale, G., Palivan, C.G. and Feringa, B. L., 2023. Synthetic molecular motor activates drug delivery from polymersomes. PNAS, 120(27), e2301279120. * these authors contributed equally. Adapted with permission* under CC BY 4.0

3.1 Introduction

Drug delivery systems are one of the most established fields of nanomedicine.[123–128] These engineered at a molecular level nanocarriers allow the transportation of toxic compounds, change the uptake route of drugs and maximize their efficiencies by decreasing their dosages and increasing their bioavailability.[129–131] Since the FDA approval of the first nanotherapeutic,[132,133] the field of drug delivery rapidly has evolved and is now recognized as a prominent field of science.[134–136] Originated from their biocompatibility and cost-effectiveness, lipid-based nanosystems were the first developed drug nanocarriers.[137–139] However, hurdles associated with low stability, high polydispersity and limited potential for surface modification have been overcome by polymer-based nanosystems.[137–139] Such systems show higher stability, tunability, robustness and modular chemistry, allowing the field to address unmet medical needs.[6,135,140–142]

Stimuli-responsive delivery systems have emerged in recent years as a promising approach to better control the administration of drugs.[124,143–145] Upon the receiving of external stimulus (e.g. pH,[146] temperature,[147] magnetic[148] or electrical[149] field, ultrasound[150]), a physical or chemical transformation of the system triggers the precise delivery of the medicine.[151] In relation to these stimuli, light can be better focused and regulated, allowing for higher temporal and spatial control together with a deep penetration and a low toxicity in the human body (provided that visible or infrared wavelengths are used).[152] Photoswitches are molecules that undergo conformational changes upon irradiation and therefore, have been widely utilized in light-actuated drug delivery.[153] However, light-responsive delivery systems have yet to make it into clinical trials due to several limitations.[154] These include poor control over drug release,[155] need of high concentrations of potentially toxic photoresponsive units[156–158] and use of ultraviolet light.[159] Most of the photoswitches are activated by UV light, which suffers from limited penetration and high ionizing toxicity within the body.[160]

Light-driven synthetic molecular motors have emerged from chiroptical molecular switches and offer a more controlled motion.[161] These molecules fulfill three basic requirements of a motorized machine: a complete 360° unidirectional rotation, repetitive motion, and energy consumption.[161,162] The first molecules reported to undergo photochemically powered unidirectional rotation across a double bond were overcrowded alkene motors.[163] In recent years, the field has rapidly evolved, making it possible to adapt the molecular design to a broad range of applications, including actuators, mechanically dynamic responsive materials, surfaces, and artificial muscles.[164–167]

In this study, our exemplary approach is to incorporate a light-driven molecular motor into a $PDMS_{25}$-*b*-$PMOXA_{10}$ diblock copolymer delivery system and showcase the potential therapeutic use of this first-of-its-kind system (**Figure 3.1**). Owing to the continuous rotation of molecular motors, we envision to obtain a higher degree of control and enhanced delivery efficiencies. As opposed to switches, we expect that by generating effective mechanical work to progressively drive the multicomponent system out of equilibrium. A more efficient system with lower quantities of the responsive unit is anticipated to reduce the cost and toxicity of the delivery system without compromising its responsive behavior. Its practice in medical setups (e.g. by clinical lasers) is hence facilitated by the use of a single wavelength of visible light. Here, visible-light responsive polymersomes were designed based on a rotary molecular motor. We report their physicochemical characterization, along with the cargo release under irradiation when loaded with a fluorescent dye. Furthermore, we explore the potential of our approach for therapeutic applications. Specifically, we evaluate the delivery and cellular effects of our system in a lung carcinoma-derived model when encapsulating the hydrophilic drug pemetrexed (PEM) in our polymersomes. Although PEM was used as a proof of concept, potential encapsulation and subsequent release of other therapeutically relevant molecules will highlight not only its applicability and importance, but also novelty.

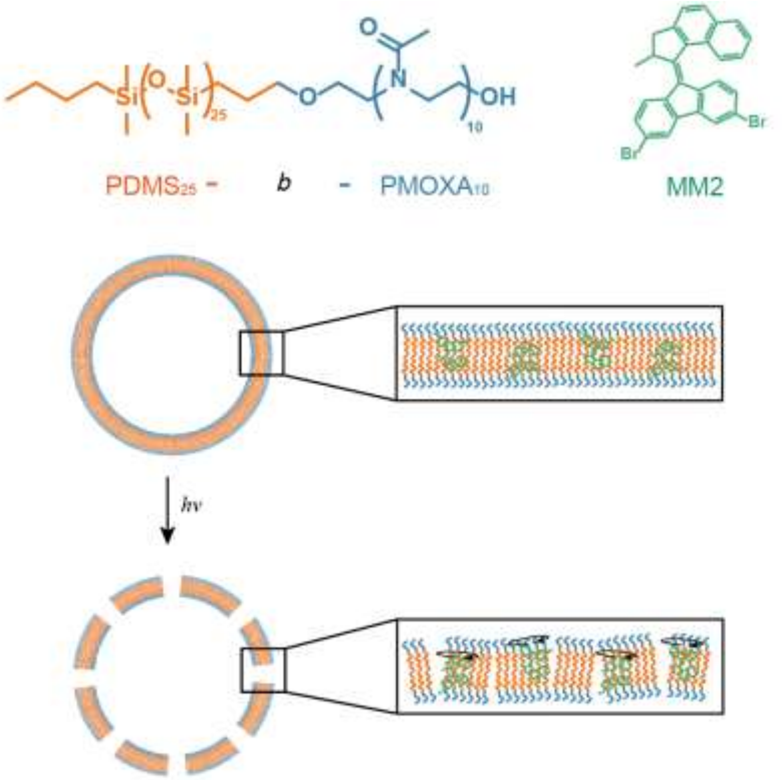

Figure 3.1. *Chemical structure of the $PDMS_{25}$-b-$PMOXA_{10}$ diblock copolymer and molecular motor MM2 (Top). Schematic representation of the vesicular system and magnification region of the*

multicomponent motor-block copolymer assembly in the bilayer of the delivery system (Bottom). (MM2 not to scale).

3.2 Results and Discussion

3.2.1 Formation and Characterization of Synthetic Molecular Motor-bearing Polymersomes – Morphological Changes Under Light Irradiation

For the formation of synthetic molecular motor-bearing polymersomes, we chose the amphiphilic diblock copolymer poly(dimethylsiloxane)$_{25}$-*block*-poly(2-methyl-2-oxazoline)$_{10}$ (PDMS$_{25}$-*b*-PMOXA$_{10}$). This polymer has already shown to be promising for several biological applications due to its low toxicity, stability, and protective effect on enzymes against protease degradation.[168,169] For achieving precise control of the opening of the polymersomes, we envisioned to incorporate a synthetic, light-responsive, dibromomolecular motor (MM2) into the hydrophobic domain of the block copolymer membrane (**Figure 3.1**). A self-assembly of the motor-bearing polymersomes was achieved by the film hydration method to obtain vesicles of ~150 nm diameter and a ~9 nm bilayer membrane thickness, as indicated by cryogenic transmission electron microscopy (cryo-TEM, **Figure 3.2A**, **B**, see **Figure 10.1**, **Table 10.1** in *Appendix*).

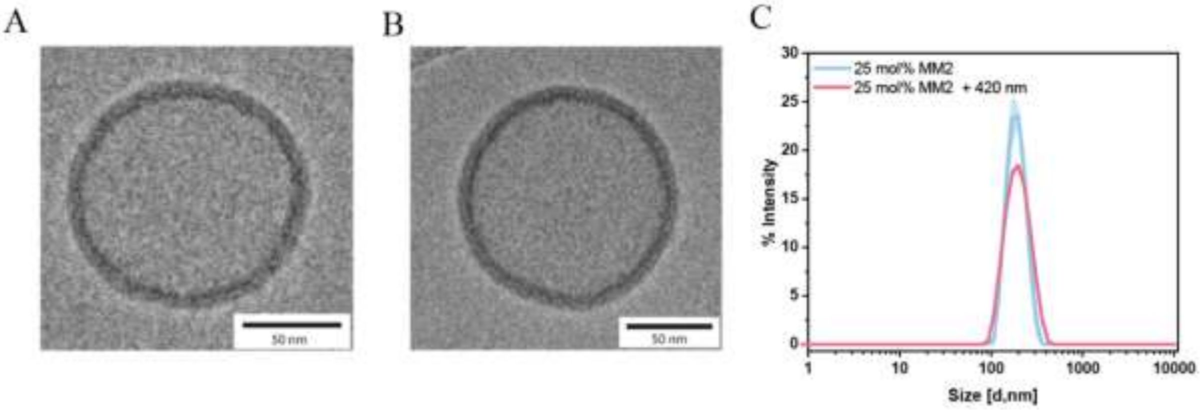

Figure 3.2. *Morphological characterization of polymersomes. (A) cryoTEM image of empty PDMS$_{25}$-b-PMOXA$_{10}$ polymersome. (B) cryoTEM image of PDMS$_{25}$-b-PMOXA$_{10}$ polymersome containing 25 mol% MM2 (Ps_MM2). (C) Size distribution of Ps_MM2 measured by DLS.*

Dynamic light scattering (DLS) was used to verify the presence of vesicles and to obtain information about their hydrodynamic diameter (D_h, **Figure 3.2C**). Static light scattering (SLS) revealed the radius of gyration (R_g) and the DLS profile the hydrodynamic radius (R_h).

The R_g/R_h or shape parameter ρ was around 1, which corresponds to spheres (see **Figure 10.2** in *Appendix*).[170] By measuring their z-potential, a slight increase in their net charge was observed with increasing molecular ratios of MM2, indicating its incorporation (see **Table 10.2** in *Appendix*).[171] Their colloidal stability was also confirmed, as no aggregation was observed during the characterization process. The insertion of MM2 did not affect the size of the polymersomes significantly, and was successful in all molecular ratios studied (0.5 to 50 mol%, see **Figure 10.3A-H** in *Appendix*) with a mean encapsulation efficiency (%) of 74.57 ± 18, assessed by UV spectroscopy after purification of the samples by size exclusion chromatography (SEC) (see **Table 10.3** in *Appendix*). The saturation content of MM2 was found to be 25 mol% (see **Figure 10.3I** in *Appendix*). As the maximum absorbance of MM2 is located at 400 nm and is directly proportional to MM2 content, the plateau phase can be detected, if the absorbance is followed at this value.[172] The structural and functional stability of $PDMS_{25}$-*b*-$PMOXA_{10}$ polymersome systems has been deeply studied in physiological conditions for up to 6 months.[98] As combination of the system with MM2 had not been done before, and we carried out stability studies accordingly. Samples were found to be structurally stable for over a week (see **Figure 10.4A** in *Appendix*) and up to 6 months when stored at 4 °C in the dark (see **Figure 10.4B** in *Appendix*).

Small-angle X-ray diffraction (SAXS) was used to further evaluate the incorporation of MM2 inside the polymer bilayer (**Figure 3.3A**, **B**). Intensity oscillations in the q-range 0.2 to 2 nm^{-1} are related to the thickness and the electron density profile of the polymersome membrane (**Figure 3.3A**). The position of the oscillations does not shift upon motor incorporation, suggesting that the membrane thickness does not change between the empty (EPs) and the MM2-bearing polymersome (Ps_MM2). Remarkably, the amplitude of the oscillation changes, indicating change of the difference between the electron density of the inner and the outer part of the bilayer membrane (**Figure 3.3A**). The SAXS profiles were fitted using a model for a spherical polymersome with a bilayer membrane with Gaussian electron density profiles.[173] Since the size of the polymersome is outside of the measured q-range, it was kept fixed to 200 nm in agreement with the transmission electron microscopy (TEM) observations. In agreement with the molecular structure, the PDMS layer shows a lower scattering length density with respect to water, while the PMOXA layers have higher scattering length density (**Figure 3.3B**).[174] As expected, the PMOXA layers are substantially swollen by water, showing a scattering length density sensibly lower than the expected bulk value. The distance between the centres of the PMOXA outer layers is calculated to be 9 nm, in close agreement with the wall thickness observed by TEM. The system with MM2 shows a clear increase of the electron density of the inner membrane layer, confirming the successful incorporation of the motor in the hydrophobic PDMS layer.

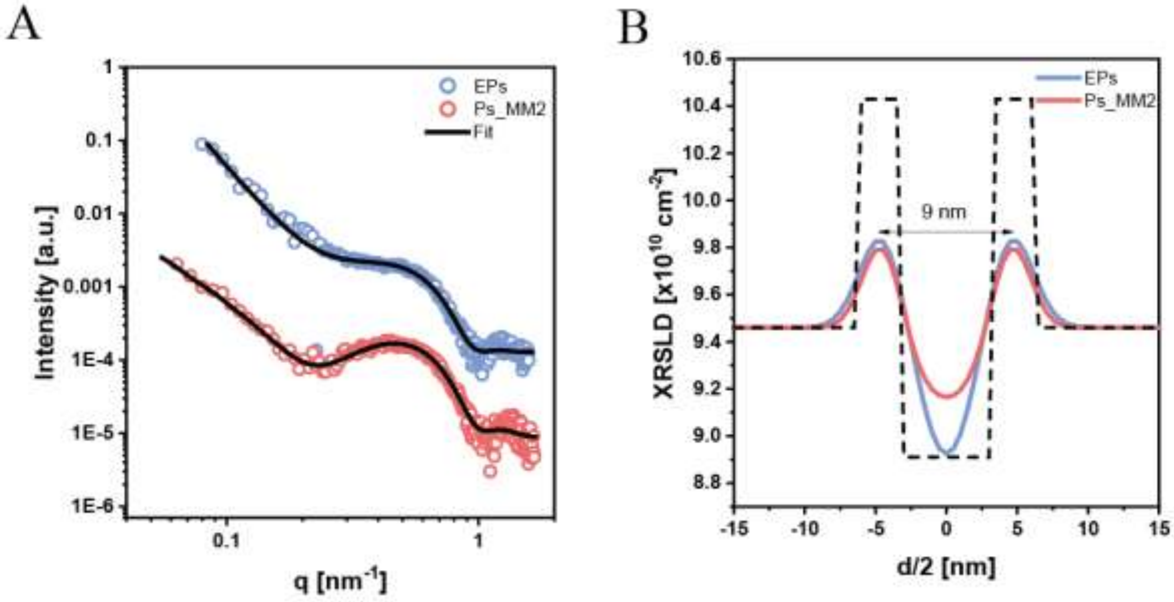

Figure 3.3. *SAXS measurements and insertion of MM2. (A) SAXS intensity profiles for EPs and Ps_MM2 systems, along with the fitted curves. (A) Extracted X-ray scattering density profiles. The dashed line represents the expected values for the bulk PMOXA and PDMS layers. The 0 value is placed in the center of the inner polymersome layer.*

The absorption spectra of the MM2-bearing polymersomes change under irradiation with visible light (**Figure 3.4A**). A characteristic exponential decay (200 to 250 nm) indicates the presence of polymersomes and the spectral change of the MM2 absorption peak (λ_{max} = 405 nm) corresponds to the successful photochemical E-Z isomerization and thus the rotation of the molecular motor inside the polymersomes. In short, overcrowded alkene molecular motors are able to undergo unidirectional rotation across the central double bond when irradiated with light. The 360° rotation cycle is possible as the molecule undergoes four sequential steps in an overall unidirectional manner.[162] The process is characterized by two photochemical E-Z isomerizations each followed by a thermal helix inversion step that brings the system back to the initial state, resulting in continuous motion as long as there is a photon supply.

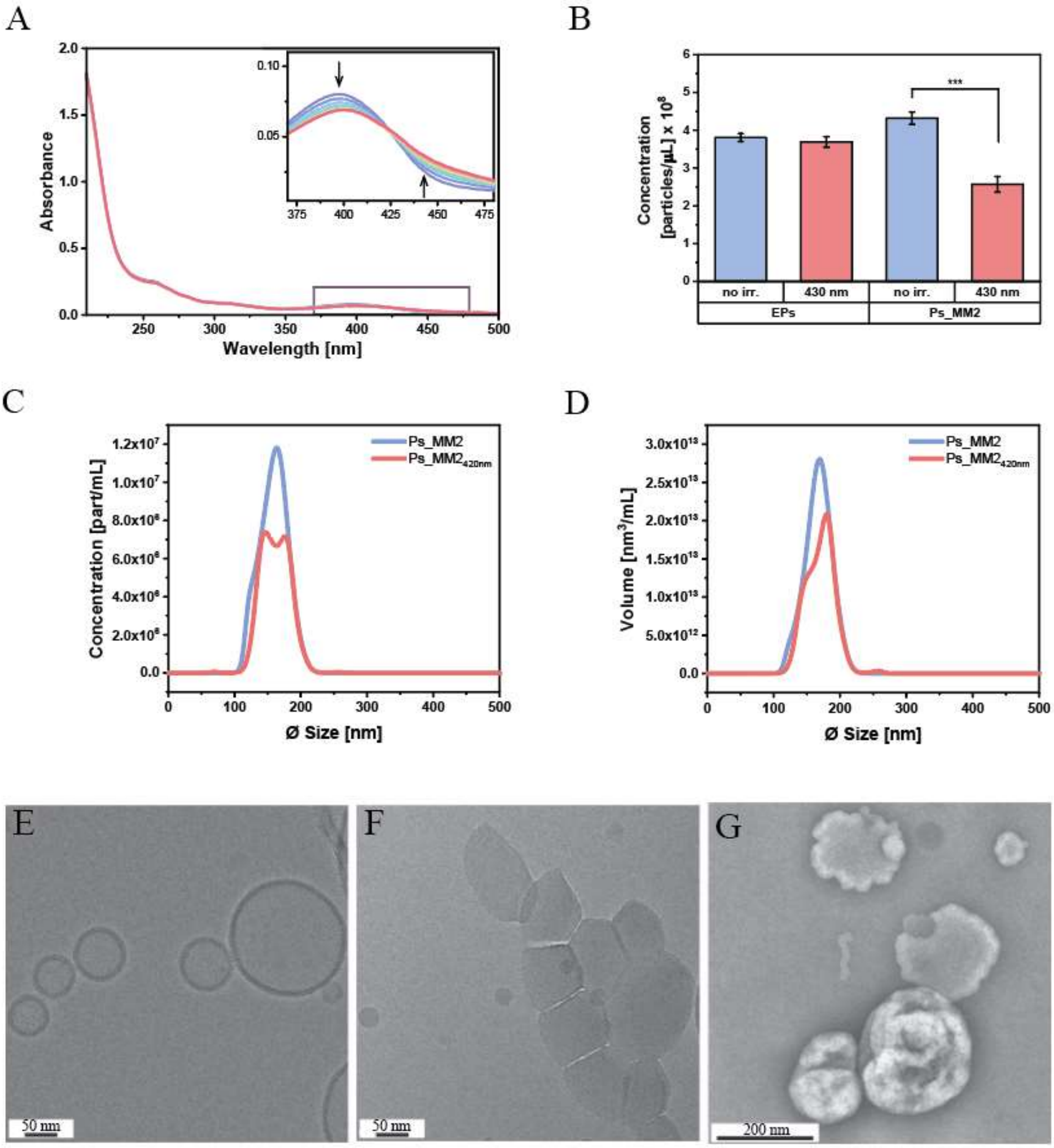

Figure 3.4. *Morphological changes of polymersomes upon MM2 insertion and activation. (A) Visible light (30 s, λ = 420 nm, 6.9 mW) irradiation of aqueous solution of polymersome with 10 mol% MM2. Inset showing the MM2 absorption peak changes due to light irradiation and the isosbestic point, as indication of selective E-Z isomerization across the double bond. (B) NTA concentration size distribution of non/irradiated vesicles. (C) Change in the concentration of EPs and Ps_MM2 after irradiation distribution analyzed by NTA. (D) NTA volume size distribution of non/irradiated vesicles. (E) cryoTEM image before irradiation. (F) cryoTEM image after irradiation. (G) TEM image after irradiation showing two bursted (Top) and two entire polymersomes (Bottom). B-G samples containing MM2 at a concentration of 25 mol%. All irradiations were performed under the same irradiation conditions (1 min, λ = 420 nm, 6.9 mW). ***indicates statistically significant data ($P \leq 0.001$).*

The influence of visible light irradiation on the morphology of polymersomes was also evaluated. DLS measurements on control or MM2-bearing vesicles irradiated for 1 min with

420 nm light did not show a significant change in their D_h (**Figure 3.2A**). However, in the case of polymersomes containing 25 mol% of MM2, measurements on the sample concentration using nanoparticle tracking analysis (NTA) did show a significant decrease in the amount of vesicles present, indicating a disruption of particles (**Figure 3.4B**, **C**). We also observed a change in the homogeneity of size distribution by means of volume denoting a population alteration after sample irradiation (**Figure 3.4D**). Changes in the PDI and correlation function intercept of irradiated vesicles were not significant (see **Table 10.3** in *Appendix*). To further study the effect of irradiation on the shape and structure of the vesicles we analyzed them using TEM and cryo-TEM. Micrographs before irradiation showed the usual shape of spherical polymersomes (**Figure 3.4E**). After irradiating for 1 min with visible light (λ = 420 nm, 6.9 mW), an obvious change was observed in all samples containing MM2, where a clear bursting of the vesicles can be noticed loss of the three-dimensional structure (**Figure 3.4F**). The wrinkled oval-shaped appearance is representative of a three-dimensional nature after negative staining, indicating a hollow sphere structure which disappears after irradiation (**Figure 3.4G**). These results are a visible indication of the ability of MM2 to open polymer vesicles using exclusively light energy as fuel.

3.2.2 On/Off Release Profile of Calcein

Following the confirmation of morphological changes of our polymersomes under irradiation, we next investigated the release profile and how it could be controlled on-demand using light. For this reason, calcein was employed as a fluorescent probe as its release is often used in vesicular systems due to its self-quenching fluorescence behavior.[175] Polymersomes loaded with a calcein concentration above the self-quenching value exhibit nonfluorescent values. Only when release occurs from the vesicles, the concentration drops, mixing with the calcein-free environment, and fluorescence starts to increase (**Figure 3.5A**). By measuring the fluorescence intensity before and after sequential irradiations and comparing it to complete release (by disrupting the systems by adding 1% EtOH under sonication for 15 min), the release percentage can be determined over time. All polymersomes (with/without MM2) were loaded with 20 mM calcein solution in phosphate buffered saline (PBS) with an average encapsulation efficiency of 67 ± 2%, still in the self-quenched regime (see **Figure 10.5** in *Appendix*). Samples were subjected to the same irradiation setup; an initial fluorescence measurement was taken before any light exposure. All polymersome solutions were then irradiated for 1 min with visible light (λ = 420 nm, 6.9 mW) and another measurement was performed. Subsequently, polymersome solutions were kept in the dark for 30 min to evaluate release kinetics and a final measurement was taken before irradiating again. This process was repeated during three irradiation cycles (**Figure 3.5B**).

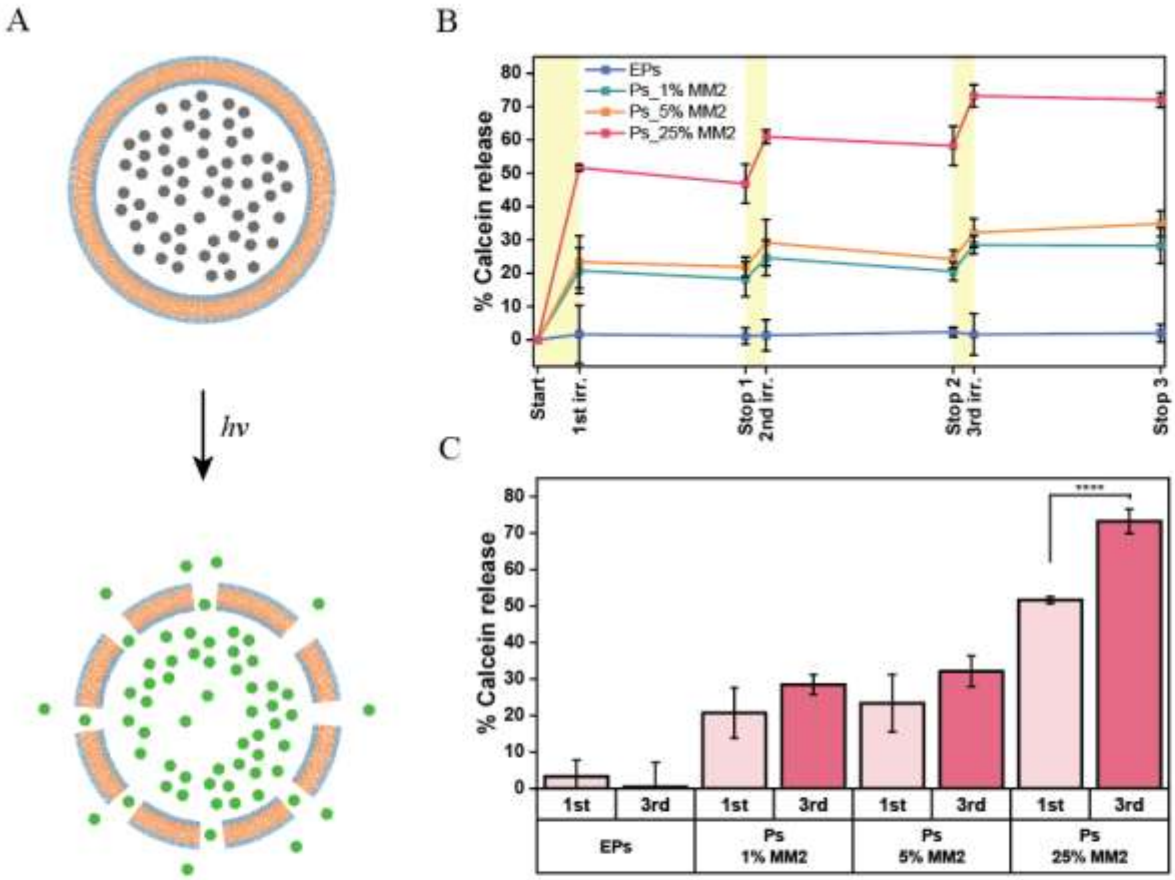

Figure 3.5. *Calcein release studies upon light irradiation. (A) Self-quenching behavior of calcein dye and induced light-release from polymersome vesicles. (B) Percentage of calcein release during sequential irradiations over different concentrations of MM2. Yellow bars indicate the period when samples are under irradiation conditions. Data points show the mean ± SD of three independent experiments. (C) Percentage of calcein release after the first irradiation (light) and the third (dark) for each of the different conditions. **** indicates statistical significance with P <0.0001.*

Calcein-loaded polymersomes without MM2, the light-responsive unit, did not show a significant release at any time point during the sequential irradiations, as expected (**Figure 3.5B**). For calcein-loaded polymersomes containing 1, 5 and 25 mol% of MM2 the first irradiation event triggered the largest release content, up to 21, 24, and 52%, respectively. Subsequent irradiations were able to increase the release by ~18% each. Most interestingly, release was completely suppressed when stopping the light input, showing that no vesicles were bursting without irradiation. A small decrease in the release can be attributed to bleaching of the released dye when keeping the samples in the dark for 30 min after irradiation. Release was increased by 37%, 29%, and 42% with 1, 5, and 25 mol% of MM2, respectively, between the first and third cycle (**Figure 3.5C**). Total release after three irradiations was found to be highly effective for 25 mol% MM2 samples (around 75%). Notably, even with low concentration of the molecular motor, such as 1 mol% MM2, a significant release of around 30% was observed. A sustained release over time was also achieved by constant irradiation of polymersomes with 25 mol% of MM2 (see **Figure10.6** in *Appendix*) demonstrating a control on the release behavior by manipulating the irradiation conditions. These results establish not only a competent release for small guest molecules encapsulated in the vesicles with very small amounts of light-responsive motor, but also a precise temporal control on the release behavior being able to switch the system on and off on demand.

3.2.3 Pemetrexed Delivery in Cells

The potential of MM2-bearing polymersomes to function as a drug delivery system was investigated in cells. PEM is a drug approved for the treatment of pleural mesothelioma and nonsmall cell lung cancer.[176] However, due to its high hydrophilicity and polarity, strategies to increase its permeability and bioavailability have been developed.[177–179] In our model approach for a light-controlled delivery system, PEM was encapsulated in the aqueous cavity of polymersomes equipped with the synthetic molecular motor (Ps_MM2_PEM). The drug encapsulation efficiency was calculated at 43 ± 7% based on SEC (see **Figure 10.7** in *Appendix*). Subsequently, we explored the effects of irradiation on cells with or without drug treatment. Adenocarcinomic human alveolar basal epithelial cells (A549) were incubated with PEM (5 μM) or the respective amount of PBS and were irradiated at 430 nm for 1 min. In the conducted experiment it was shown that the irradiation by itself had no effect on cell viability (**Figure 3.6A**) As expected, exposure of nonirradiated A459 cells to PEM reduced cell viability to about 60% ($P < 0.00001$).

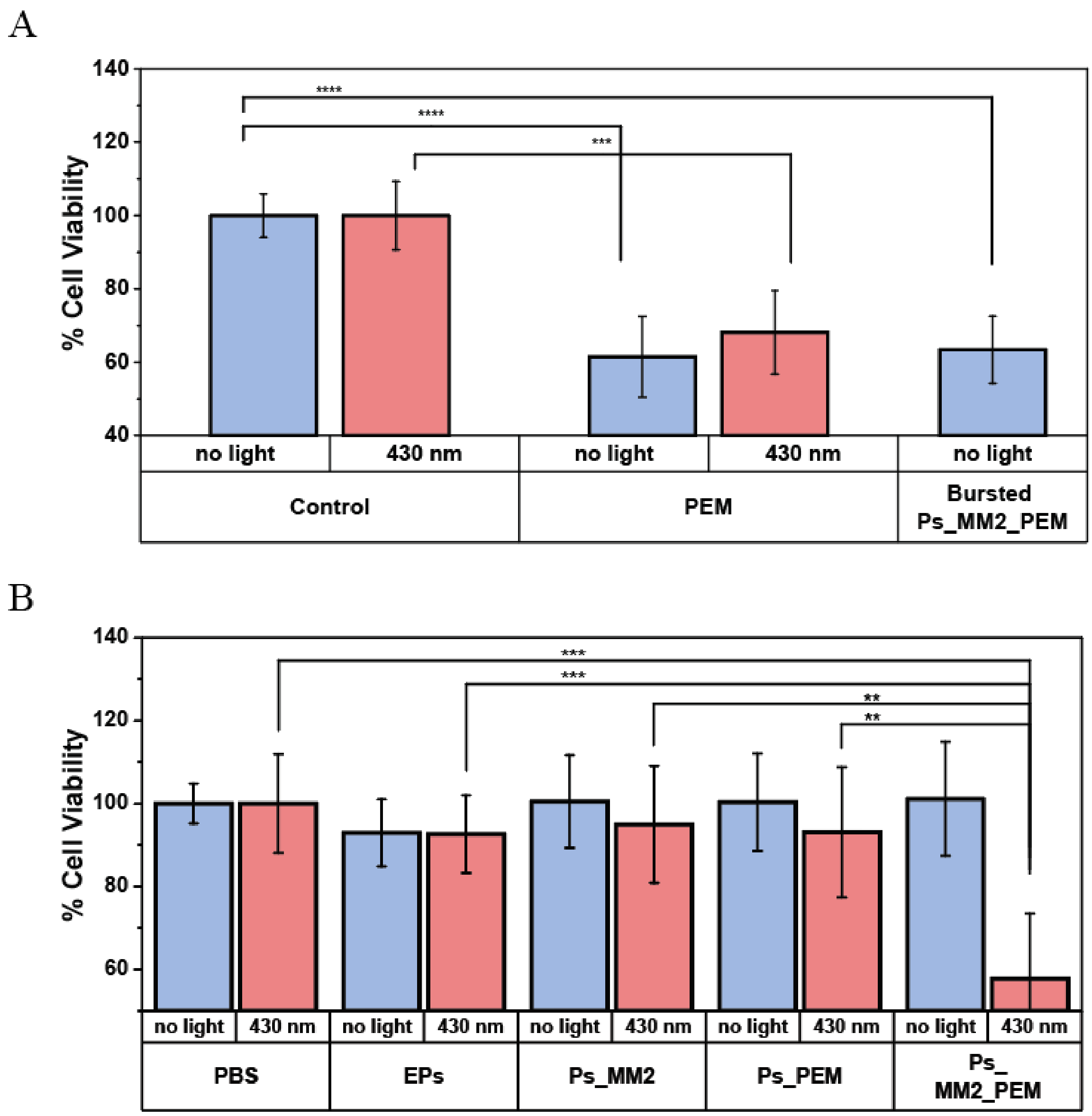

Figure 3.6. *Cell viability studies upon light irradiation and drug delivery. (A) Cell viability as percentage of irradiated (λ = 430 nm, 1 min) and nonirradiated A549 cells incubated with only PBS (control), 5 µM PEM and supernatant of irradiated Ps_MM2_PEM (5 µM PEM). (B) Cell viability as percentage of irradiated (λ = 430 nm, 1 min) and nonirradiated A549 cells incubated with only PBS (control), EPs, Ps_MM2, Ps_PEM and Ps_MM2_PEM. Graph shows mean ± SD of three independent experiments. Statistically significant data (****, ***, ** equivalent to a P ≤ 0.0001, ≤ 0.001 and ≤ 0.01, respectively).*

However, no further reduction was observed when PEM-treated cells were irradiated, even after 24 h of incubation (P = 0.00042) (**Figure 3.6A**). To evaluate the drug release from Ps_MM2_PEMs and its efficacy, Ps_MM2_PEMs that were irradiated at 430 nm for 1 min were centrifuged to remove ruptured membranes, and the supernatant was used for the incubation with cells. Based on the encapsulation efficiency and the calcein release studies, we calculated the final PEM concentration to match the free-drug-treated cells at 5 µM.

Consistent with this observation, the viability of cells treated with Ps_MM2_PEM supernatant was also reduced to 60% ($P < 0.000001$) (**Figure 3.6A**).

After establishing the effects of irradiation and PEM on cell viability, we incubated A549 cells with intact polymersomes for 24 h. Polymersomes with PDMS and PMOXA domains have been previously shown to be internalized by cells and preserve their integrity for up to 48 h.[169,180] The following day, extracellular polymersomes were removed by washing and cells irradiated at 430 nm for at least 1 min. After a subsequent 24 h incubation, the cell viability was assessed (**Figure 3.6B**). Compared to irradiated cells lacking polymersomes, cells containing Ps_MM2_PEM showed a decrease in cell viability to 60% in response to irradiation, as was observed for cells treated with free PEM ($P = 0.00029$). In the case of cells incubated with EPs, Ps_MM2, and Ps_PEM, cell viability was not significantly decreased, irrespective of irradiation. Taken together, these findings indicate that neither the polymer (EPs) nor the synthetic molecular motor entrapped in the hydrophobic domain of the polymer membrane (Ps_MM2) are cytotoxic at the concentrations used for polymersome assembly.[169] The structural integrity of polymersomes within cells is evidenced by the lack of decrease in cell viability in the case of PSs_PEM and PSs_MM2_PEM nonirradiated. More importantly, cytotoxicity of Ps_MM2_PEM is dependent on irradiation, inducing a conformational change of membrane-embedded synthetic molecular motors, which in turn causes the membrane to disrupt and release PEM. Based on previous studies and the mechanism of action of PEM, we consider that the polymersomes internalized by cells preserve their integrity in the cytoplasm where they release their hydrophilic cargo upon irradiation.[180,181] These experiments with A549 carcinoma cell line and the molecular motor-based vesicles Ps_MM2_PEM show that the presence of molecular motor and light irradiation are necessary to promote drug release and raise the potential of such systems to be investigated in larger context .

3.3 Conclusions

For the first time, we demonstrate the use of synthetic molecular motors in a stimuli-responsive polymer-based drug delivery system. In our model, the unidirectionality and continuous rotation of the molecular motor provides a high spatiotemporal resolution and control on the release profile. The release of calcein was precisely turned on and off by our system during sequential irradiations using light as the only stimulus. An efficient release from the polymeric vesicles was observed after the irradiation cycles (>75% with 25 mol% of MM2) using low-power visible light ($\lambda = 420$ nm, 6.9 mW). Remarkably, the fluorescent probe was also released when using minimal concentrations of photo-responsive units (30% release with

1 mol% of MM2). Furthermore, our system was tested under relevant physiological conditions and successfully functioned as a drug delivery system of the chemotherapeutic agent pemetrexed in a A549 lung carcinoma cell line. Similar levels of cell viability were observed compared to free-given drugs showing the potential of our system to deliver functional drugs on demand with the same efficiency and lower toxicity. We also proved that neither the polymer vesicles, the irradiation setup or the molecular motor content used in our experiments induced any kind of cytotoxicity to the living cells. Summarizing, molecular motors-containing polymersomes were able to release drugs on-demand using low-power visible light together with the low toxicity. We envision that our exemplary system will facilitate in broadening the next applications of stimuli-responsive compartments in the development of smart delivery systems. Given the modularity of our nanocompartments, various fields of nanomedicine could benefit from such a design. Our responsive, pemetrexed-loaded nanocompartments could be employed in a more efficient treatment of mesothelioma and non-small-cell lung cancer. In addition, by strategically choosing the encapsulated therapeutic molecules, the respective cancer types could be targeted or expand the potential of our nanosystem to an on-demand release of antimicrobial agents. Finally, with the use of synthetic molecular motors responding to different wavelengths, greater selectivity and tissue penetration could be achieved.

4. Catalytic Nanocompartments for *in situ* Inversion of Glucuronidated Drugs

In this chapter, we study the formation of a nanocompartment-based system for inverting drug glucuronidation using hymecromone as a model therapeutic. Glucuronidation is the main metabolic process responsible for the rapid elimination of drugs from the body and short half-life circulation times. Herein, we propose synthetic catalytic nanocompartments (CNCs) cleaving the glucuronide moiety from the metabolized form of the drug hymecromone and converting it to the active drug. The catalytic nanocompartments shield β-glucuronidase in their inner cavity, where it catalyzes the conversion of the hydrophilic hymecromone–glucuronide conjugate to hymecromone. The diffusion of the substrates and products is facilitated by the pore-forming peptide, melittin in the synthetic membrane of CNCs. Our CNCs are readily taken up by HepG2 cells, where they produce the drug in situ over 24 hours. Our nanosystem, which locally reverts a drug metabolite into its active form is expected to introduce a new perspective in the field of metabolism and a new approach in the design of therapeutics that aim at prolonging the residence time of a drug.

This study is published as ***Korpidou, M.****, Maffeis, V., Dinu, I.A., Schoenenberger, C.A., Meier, W.P. and Palivan, C.G., 2022. Inverting glucuronidation of hymecromone in situ by catalytic nanocompartments. Journal of Materials Chemistry B, 10(20), pp.3916-3926 and adapted with permission under CC BY 3.0*

4.1 Introduction

Living organisms use metabolism for the biotransformation of endogenous and exogenous substances, such as drugs. The hydrophilic derivatives that are created during the metabolic processes are rapidly excreted and eliminated from the body.[182] Drugs with shorter half-life often tend to act quickly with their effects wearing off rapidly. As a result, more frequent administrations or higher doses are needed which can lead to abuse of these compounds and even addiction.[183,184] Therefore, altering the pharmacodynamic and pharmacokinetic parameters of rapidly metabolized drugs is the focus of intense research. One state-of-the-art approach involves drug delivery systems that offer a more controlled and/or targeted drug delivery.[185–187] Although these systems were shown to enhance the biodistribution, pharmacokinetics, stability and solubility of the active compounds, limitations concerning low drug loading capacity, toxicity and environmental concerns remain.[188,189]

These limitations can be overcome by developing enzyme-loaded nanocompartments able to convert prodrugs into drugs, in order to achieve a spatiotemporally controlled drug production.[82,90,96,112] These biosynthetic nanocompartments protect the encapsulated enzymes from their surroundings, leading to prolonged activity and less immunogenicity.[81,113,190] Polymer-based compartments offer several advantages over liposomes,[6,168] such as enhanced mechanical and colloidal stability,[191] tuneable permeability[192] and stimuli responsiveness, when appropriately selected.[193,194] In order to improve their properties, e.g. toxicity or stability against degradation, enzyme biopharmaceuticals have been encapsulated in different types of nanocompartments.[195] Encapsulation of L-asparaginase (ASNase) in polyion complex vesicles (PICsomes)[196] or in permeable, asymmetric polymersomes[92] are indicative examples. When systemically injected into mice, ASNase PICsomes exhibited sustained conversion of L-asparagine in the blood stream due to their prolonged blood circulation compared with free ASNase.[196] In contrast to this study, in which the enzyme itself was the therapeutic, encapsulation of β-galactosidase in carbohydrate-*b*-poly(propylene glycol) derived vesicles (CAPsomes) afforded the conversion of a co-administered prodrug into an active compound, while protecting the enzyme from degradation.[82] Advances in nanocompartments designed for enzyme replacement therapy,[196–198] cancer treatment[82,90] and other *in vitro and/or in vivo* applications[89,96,199] have increased the interest and research in the field. Inverting metabolic inactivation of a drug *in situ* is a novel concept that has yet to be explored.

Hymecromone or 4-methylumbelliferone (4-MU) is an inhibitor of hyaluronan synthesis and primarily used as a drug in bile therapy.[200] Recently, its effectiveness in treating cancer,[201] type 1 diabetes[202] and COVID-19[203] is being explored. Glucuronidation of hymecromone to 4-methylumbelliferyl glucuronide (4-MUG) rapidly takes place in the liver.[204] As a result, its poor pharmacokinetics and quick elimination from the body (oral bioavailability < 3%, t½ = 28 min) may rise the daily administered hymecromone dose up to 2400 mg and was thus selected as our model drug.[201,205,206]

In this study, we developed catalytic nanocompartments (CNCs) based on polymersomes rendered permeable by melittin biopores that confine β-glucuronidase (GUS) in their cavity. The design of these catalytic nanocompartments is based on the catalysis of a pro-drug or metabolite from its glucuronide form to the active compound *in vitro* and in cells (**Figure 4.1**). Our choice of encapsulating bacterial GUS was endorsed by its ability to cleave the glucuronide moiety from a variety of molecules under a broad range of conditions (pH 5.5-7.8 and temperatures up to 60 °C).[207–209], while exploring the production of model, active 4-MU from the glucuronide conjugate 4-MUG which is the main 4-MU metabolite found in the body.[210]

Known for their stealth properties, non-toxicity, and biocompatibility, poly(dimethylsiloxane)-*block*-poly(2-methyl-2-oxazoline) (PDMS-*b*-PMOXA) amphiphilic block copolymers were used for the self-assembly of our polymersomes.[168,211] Meanwhile, a porous membrane was critical to our CNC design, facilitating the diffusion of substrates and products to and from the nanocompartments' GUS-containing cavities.[69,83,95] Hence, we generated polymersomes by self-assembly of $PDMS_{25}$-*b*-$PMOXA_{10}$, a diblock copolymer where its short block lengths aid the insertion of melittin, leading to membrane permeabilization.[69,95,212] Here, we report the physicochemical characterization of CNCs and their enzymatic efficiency in phosphate buffered solution (PBS) and cell culture medium. Exploring their potential for therapeutic applications, we examined cellular toxicity, uptake into cells and their intracellular activity in HepG2 cells, considering the glucuronidation of hymecromone mainly occurs in the liver.[204] Our CNCs are unique in representing a prototype for the locally confined transformation of a prodrug/metabolite to an active compound, providing the example for building such systems for a variety of purposes and making them a stepping stone toward a whole new field of biomedical applications.

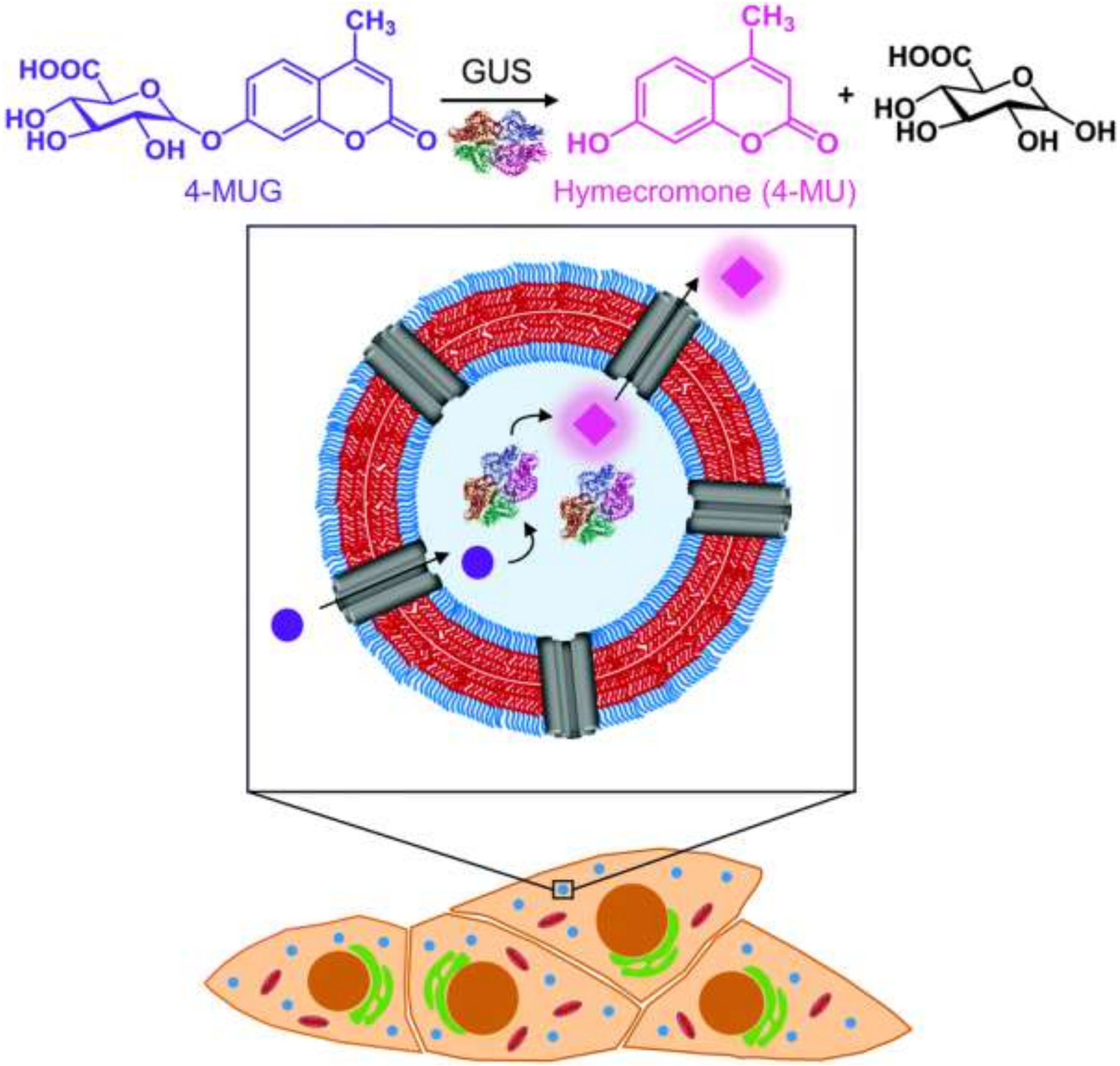

Figure 4.1. *Schematic representation of the catalytic nanocompartment containing GUS and its enzymatic activity. Melittin pores in the PDMS$_{25}$-b-PMOXA$_{10}$ membrane provide a pathway to from the compartment interior where β-glucuronidase (GUS) catalyses the production of hymecromone (4-MU) from its glucuronide conjugate (4-MUG) within cells that have taken up CNCs.*

4.2 Results and Discussion

4.2.1 Formation and Characterization of CNCs

The choice of the diblock copolymer $PDMS_{25}$-*b*-$PMOXA_{10}$ to generate CNCs was endorsed by its short block lengths, resulting in the self-assembly of polymersomes whose thin membrane is conducive to the insertion of pore-forming membrane proteins.[50,89] In addition, polymersomes assembled from block copolymers based on PDMS and PMOXA are predisposed for biomedical applications as they have been shown to be non-toxic and biocompatible.[95,168] In the body, these block copolymers are non-degradable and excreted mainly via feces.[213] The film rehydration method was selected to form our nanocompartments as organic solvents that can adversely affect enzymes and peptides were avoided.[57,95] To obtain membrane-permeabilized CNCs encapsulating bacterial β-glucuronidase (GUS-melCNCs), a thin $PDMS_{25}$-*b*-$PMOXA_{10}$ film was rehydrated with a mixture of enzyme and pore-forming melittin in phosphate buffered saline (PBS). Polymersomes containing GUS but lacking melittin pores (GUS-CNCs) and polymersomes permeabilized with melittin but lacking enzymes (melPSs) were prepared as controls. All CNCs were incubated with proteinase K prior to their SEC purification in order to remove non-encapsulated enzyme and melittin where applicable.[96]

The morphology of our polymersomes was characterized by a combination of light scattering (LS), transmission electron microscopy (TEM) and nanoparticle tracking analysis (NTA).[95] Dynamic light scattering (DLS) measurements indicated an average diameter of 136 ± 37 nm for GUS-melCNCs and 137 ± 37 nm for GUS-CNCs (**Figure 4.2A, D**). Revealed by the DLS profile, the hydrodynamic radius (R_h) and obtained by static light scattering (SLS), the radius of gyration (R_g) (see **Figure 10.8** in *Appendix*) are presented in **Table 4.1**. Typical for the morphology of hollow spheres, the R_g/R_h ratio or shape parameter ρ was around 1 (**Table 4.1**).[95,214] The vesicular nature of the polymersomes was further corroborated by TEM (**Figure 4.2B, E**). Polymersome concentration was assessed by NTA measurements which also confirmed the narrow size distribution of CNCs (**Figure 4.2C, F**). Comparison of GUS-melCNCs with non-permeabilized GUS-CNCs by light scattering techniques, NTA and TEM indicated that melittin-induced membrane permeability had no effect on morphology or dispersity of the nanocompartments. Similarly, as shown by us and others, the morphology of polymersomes harbouring other enzymes was barely affected by enzyme encapsulation.[89,95,215]

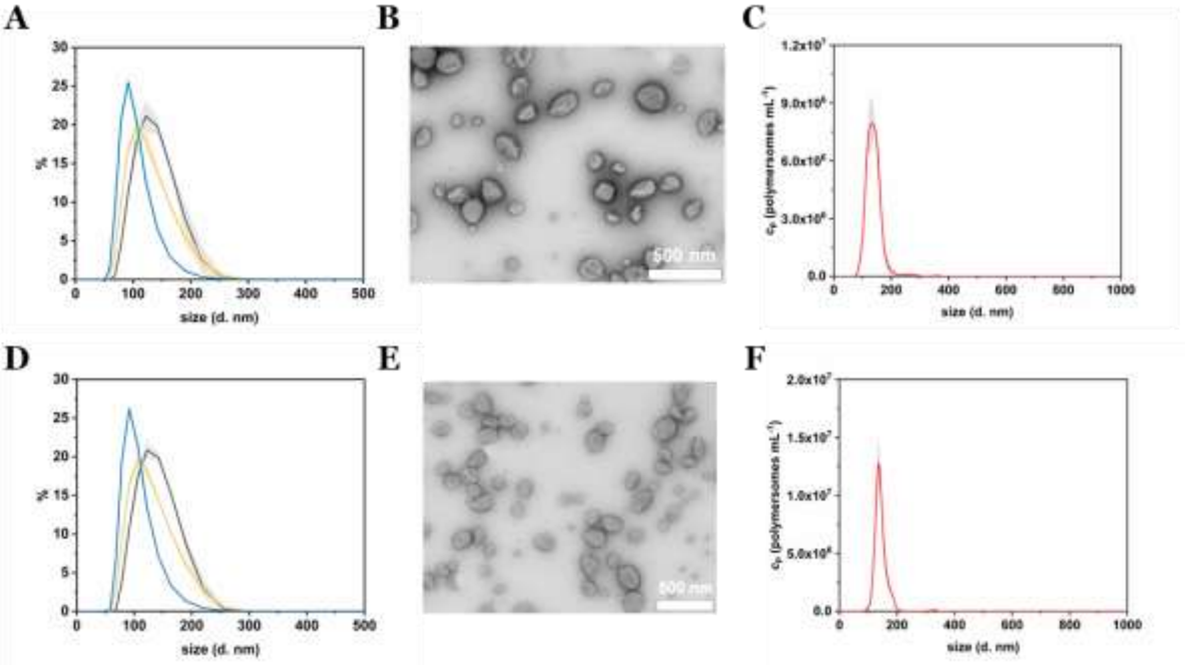

Figure 4.2. *Characterization of CNCs. Size distribution of (A) GUS-melCNCs and (D) GUS-CNCs measured by DLS (black: intensity, yellow: volume, blue: number; curves represent mean ± s.d. of 3 replications). TEM micrograph of (B) GUS-melCNCs and (E) GUS-CNCs showing the deflated structure typical for hollow spheres and the variation in their size. Scale bar: 500 nm. Determination of size and respective concentration of (C) GUS-melCNCs and (F) GUS-CNCs by NTA (curves represent mean ± s.d. of 3 replications).*

Table 4.1 *Characterization of GUS-melCNCs and GUS-CNCs.*

	Radius of gyration (R_g) (nm)	**Hydrodynamic radius (R_h) (nm)**	**ρ (R_g/ R_h)**	**Concentration (polymersomes mL^{-1})**
GUS-melCNCs	69 ± 6	68 ± 7	1.01 ± 0.3	(3.5 ± 0.3) × 10^{12}
GUS-CNCs	62 ± 6	66 ± 2	0.95 ± 0.1	(3.3 ± 0.1) × 10^{12}

The autocorrelation curves of standalone Atto488-labeled GUS and CNCs encapsulating Atto488-enzyme were compared to free dye (**Figure 4.3A, B**). A shift of the diffusion time (τ_D) calculated from the FCS autocorrelation curve of Atto488-GUS to increased values indicated the successful labelling of the enzyme (τ_D of free dye compared to τ_D of Atto488-GUS, see **Table 10.4** in *Appendix*), τ_D of Atto488-GUS being directly correlated to its size. A further increase of the diffusion time was observed for Atto488-GUS-melCNCs, indicating the successful encapsulation of the enzyme (τ_D of Atto488-GUS-CNCs compared to τ_D of Atto488-GUS, see **Table 10.4** in *Appendix*). By using Stockes-Einstein equation, the respective sizes of the nanocompartments were calculated derived from the FCS diffusion times. Their values agreed with the sizes obtained by LS and NTA, indicating that there was no tendency of CNCs aggregation (see **Table 10.4** in *Appendix*).

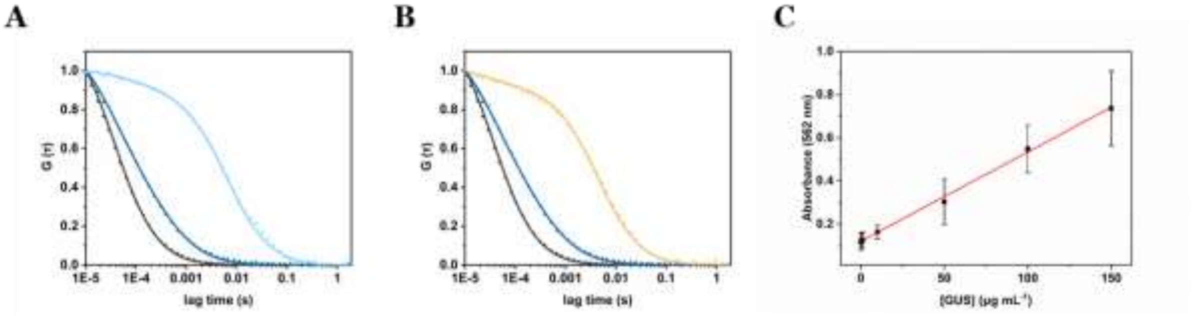

Figure 4.3. *Encapsulation of GUS in CNCs. Normalized FCS autocorrelation curves (solid lines) of (A) GUS-melCNCs and (B) GUS-CNCs for free Atto488 dye (black), Atto488-GUS (blue) and Atto488-GUS-melCNCs (cyan). Symbols represent raw data and solid lines represent fitted curves. (C) GUS calibration curve for the BCA protein assay (R^2 = 0.99).*

The overall catalytic activity of CNCs largely depends on the amount of enzyme encapsulated.[83,89,95,96] Therefore, we evaluated the encapsulation of GUS by FCS. Based on the molecular brightness of the free fluorophore, Atto488-GUS and Atto488-GUS-melCNCs, we calculated that the enzyme was labelled on average with 1 dye molecule, and 2 molecules of GUS were encapsulated per CNC. To estimate the number of melittin pores per GUS-melCNC, corresponding polymersomes were prepared that lack GUS but are melittin-permeabilized (melPSs). The total GUS-melCNC concentration (**Figure 4.3C**) and the total amount of melittin present in the melPSs solution was calculated and correlated with the average number of melittin monomers constituting each pore (12), resulting in approximately 200 pores per GUS-melCNC.[65] According to our previous study on melittin pores in PMOXA-*b*-PDMS-*b*-PMOXA membranes, we expect a pore diameter of at least 1 nm.[50] Our data regarding size and distribution of GUS containing CNCs, enzyme encapsulation and melittin pore formation are in good agreement with other studies addressing nanocompartments self-assembled by film rehydration of PDMS-PMOXA block copolymers.[50,69,95,216,217]

4.2.2 Catalytic Conversion of 4-MUG to Hymecromone

The enzymatic activity of free and encapsulated GUS in solution was evaluated by monitoring the conversion of 4-MUG (5 µM) to hymecromone (4-MU) at 445 nm under different conditions (**Figure 4.4**).[218] First, we compared GUS activity of free versus encapsulated enzyme in PBS (**Figure 4.4A**). Upon addition of 4-MUG to free enzyme (**Figure 4.4A**, blue squares), fluorescence associated with the catalytic conversion to hymecromone rapidly increased and reached a plateau after about 10 min. In contrast, hymecromone production by GUS-melCNCs (**Figure 4.4A**, cyan circles) constantly increased up to 80 min, and then appeared to plateau. A corresponding behavior was reported for other CNCs and is attributable to the diffusion time of substrate and product through the (melittin) pores of CNCs.[83] Consistent with this notion, when GUS-CNCs without pores were incubated with 4-MUG, fluorescence at 445 nm remained minimal over time (**Figure 4.4A**, yellow rhombi). This highlights the importance of melittin pores as in their absence, the polymer membrane does not allow for the passive diffusion of 4-MUG towards the confined enzymes.

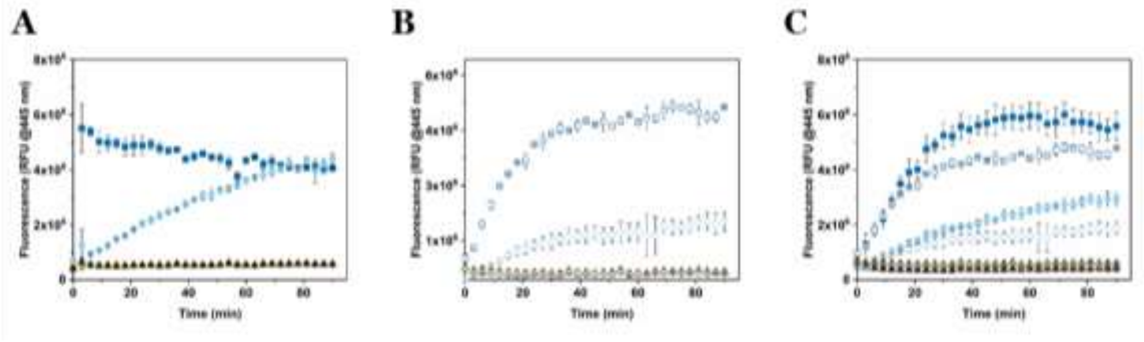

Figure 4.4. Enzymatic efficiency of CNCs at 37 °C. (A) 4-MUG (5 µM) conversion to 4-MU in PBS, (B) in cell culture medium supplemented with 10% fetal bovine serum (FBS), and (C) in PBS (filled symbols) and cell culture medium (empty symbols), each supplemented with 10% FBS. Squares represent free GUS (24 U mL^{-1}), circles: GUS-melCNCs, rhombi: GUS-CNCs triangles: corresponding reaction mix without enzyme. Measurements represent triplicates, symbols might overlap.

Furthermore, the absence of fluorescence confirms that the incubation of GUS-CNCs with proteinase K prior to their purification successfully eliminated unencapsulated enzymes. Similarly, 4-MUG by itself showed no increase in fluorescence in PBS (**Figure 4.4A**, black triangles) or cell culture medium with 10% fetal bovine serum (FBS; **Figure 4.4B**, white triangles) which suggests that in the absence of the enzyme, the hydrolysis of the ether bond and therefore production of 4-MU, does not occur. This is in accordance with clinical data showing that only a small percentage of hymecromone glucuronidation is reversible by the β-glucuronidase present in the bacteria of the small intestine.[219] The stability of the CNCs and their enzymatic activity were assessed with samples stored in PBS at 4 °C for 2 months (**Figure 4.5**). All our GUS-melCNCs retained their size and virtually full enzymatic activity.

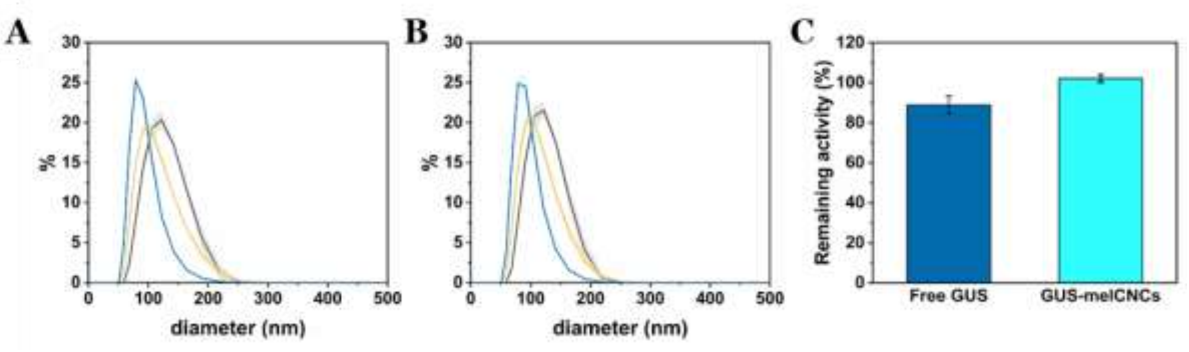

Figure 4.5. *Stability of CNCs stored at 4 °C for 2 months. Size distribution of (A) GUS-melCNCs and (B) GUS-CNCs, measured by DLS, after storage for 2 months at 4 °C. (black: intensity, yellow: volume, and blue: number). (C) Remaining percentages of activity of free (blue) and encapsulated (cyan) GUS upon storage at 4 °C for 2 months. Measurements represent the mean ± s.d.*

We chose to assess the activity of free and encapsulated GUS in culture medium containing 10% FB, in order to more closely mimic the environmental conditions of living systems (**Figure 4.4B**).[220] Upon addition of 4-MUG to free GUS (**Figure 4.4B**, white squares), fluorescence slowly increased over the first 30 min and then reached a plateau. This suggests that molecular crowding related to the presence of 10% FBS decreased the efficiency of hymecromone production. In the case of GUS-melCNCs (**Figure 4.4B**, white circles), the time course of hymecromone production was similar to that in PBS (**Figure 4.4A**, cyan circles), suggesting that the confined enzyme was barely affected by protein-rich serum. The amount of hymecromone produced was estimated based on a 4-MU reference curve (see **Figure 10.9** in *Appendix*). In PBS, approximately 4.5 µM hymecromone were produced by the free enzyme and 3 µM by GUS-melCNCs. In complete cell culture medium, free enzyme was able to produce approximately 4.3 µM of hymecromone, while GUS-melCNCs produced 2.2 µM. The lower levels of hymecromone production by confined GUS are likely to be caused by the restriction of diffusion by the compartment membrane. Furthermore, we investigated the possibility that the drug was entrapped within the polymer membrane (**Figure 4.6**). Based on a calibration curve using different concentrations of hymecromone, we calculated that only 4% of the drug produced remains associated with the nanocompartment.

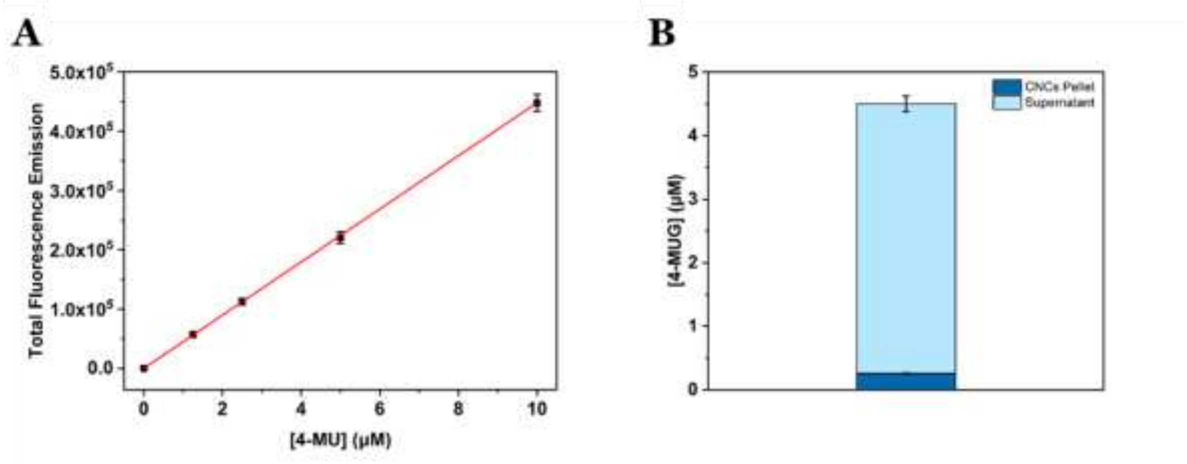

Figure 4.6. *Hymecromone production and release. (A) Calibration curve using 4-MU standards in PBS (R^2 = 0.99), (B) Concentration of 4-MU found in GUS-melCNCs (blue) and in the supernatant (cyan) after incubation of GUS-melCNCs with 5 µM 4-MU for 1 h.*

To explore whether the FBS in the cell culture medium accounted for the difference in hymecromone production between free and encapsulated GUS (**Figure 4.4B**), we compared its production in PBS containing 10% FBS (**Figure 4.4C**, filled symbols) to culture medium with 10% FBS (**Figure 4.4C**, empty symbols). Indeed, the difference in hymecromone production between free and encapsulated enzyme was similar for PBS and culture medium. In fact, the FBS interfered with the kinetics of hymecromone production for the free enzyme but not for GUS-melCNCs. Because the GUS inside CNCs is protected by the membrane and only small molecules can diffuse through the pores, molecular crowding brought about by FBS mainly affected the activity of the free enzyme. Notably, in the highly complex environment of living cells, we expect other small molecules to affect the intracellular production of hymecromone by GUS-melCNCs.

4.2.3 Kinetic Analysis of Catalytic Nanocompartments

The kinetic analysis of both free and encapsulated GUS (GUS-melCNCs) was assessed first in PBS, and then in complete cell culture medium (**Table 4.2**).[220] The kinetic analysis of the reaction was modelled in a first approximation with the Michaelis-Menten kinetics since the substrate (4-MUG) was added in excess (from 100 to 4000-fold molar excess of [4-MUG] over [GUS]) (**Figure 4.7**).[221] CNCs without melittin pores (GUS-CNCs) were not amenable to kinetic analysis since they did not exhibit any drug producing activity (**Figure 4.4**, yellow rhombi).

Table 4.2. *Comparison of Kinetic Parameters for free and encapsulated GUS.*

	Free GUS (PBS)	**GUS-melCNCs (PBS)**	**Free GUS (MEM)**	**GUS-melCNCs (MEM)**
K_M (μM)	$1.2 \pm 0.4 \times 10^3$	$3.8 \pm 1.4 \times 10^2$	$1.9 \pm 0.2 \times 10^2$	$3.4 \pm 1 \times 10^2$
V_{max} (μmoles s^{-1})	$7 \pm 1.7 \times 10$	$4.2 \pm 1 \times 10$	$4.2 \pm 0.4 \times 10$	$3.3 \pm 0.2 \times 10$
k_{cat} (1 s^{-1})	$2.7 \pm 0.6 \times 10^2$	$1.6 \pm 0.4 \times 10^2$	$1.6 \pm 0.2 \times 10^2$	$1.3 \pm 0.1 \times 10^2$

The kinetic parameters of encapsulated enzymes in polymersomes are influenced in several ways: the velocity of the reaction is decreased and the affinity for the substrate is increased.[83,222] Accordingly, in PBS, K_M and V_{max} of GUS-melCNCs decreased 3 and 1.5 times, respectively, compared to free enzyme (**Table 4.2**). Lower K_M values of GUS-melCNCs reflect a higher affinity for the substrate[83,215,223] which is attributable to the increased probability of an interaction between enzyme and substrate within the confined reaction space.[83,215,223] The turnover parameter, k_{cat}, is decreased 1.5-fold for GUS-melCNCs. As k_{cat} indicates the maximum number of 4-MUG molecules that are converted to hymecromone per enzyme per second, any reduction in GUS-melCNCs versus free GUS is associated with limited diffusion of 4-MUG and 4-MU by the polymer membrane.[83]

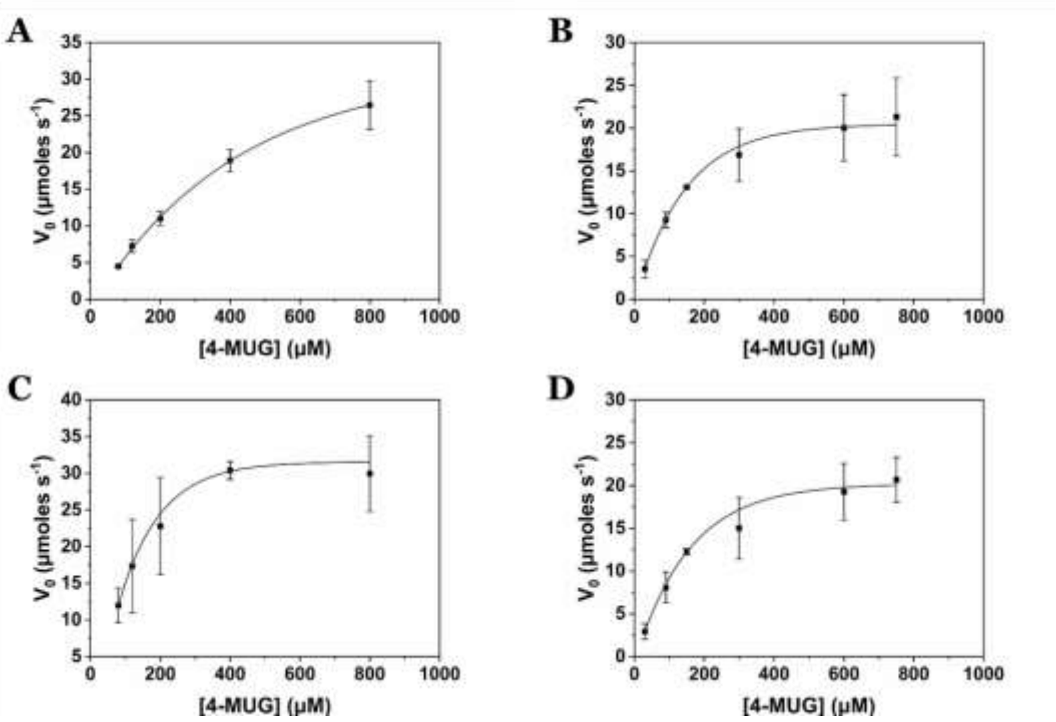

Figure 4.7. *Michaelis-Menten kinetics of free and encapsulated GUS. (A) free GUS in PBS. (B) GUS-melCNCs in PBS. (C) free GUS in MEM and (D) GUS-melCNCs in MEM. ($R^2 = 0.99$).*

Comparison of the kinetic parameters of free GUS in PBS and MEM revealed a decrease in V_{max}, K_{M} and k_{cat} in MEM, which could be expected considering the complexity of cell culture medium.[224,225] It is conceivable that proteins, vitamins and nutrients present in cell culture media might interact with the substrate and/or enzyme, thereby decreasing the efficiency of catalysis. In contrast, the kinetic parameters of the encapsulated GUS in PBS and MEM are comparable. These results taken together suggest that the catalytic efficiency of our GUS-melCNCs is predominantly governed by the influx and efflux of the substrate and product molecules. Based on the enzymatic activity of GUS-melCNCs in cell culture medium we next assessed their activity and efficiency of producing hymecromone in living cells.

4.2.4 Hymecromone production in cells

The glucuronidation of hymecromone in the body occurs mainly in the liver. Being liver-derived, we chose the HepG2 cancer cell line for studying the effects of GUS CNCs in vitro.[226] Our choice was further endorsed by recent findings showing an association of hymecromone with anticancer properties.[227,228] Confocal laser scanning microscopy (CLSM) of HepG2 cells incubated with Atto647-encapsulating polymersomes (Atto647-PSs) at 1.25 mg mL^{-1} for 24 h revealed the presence of Atto647-PSs throughout the cytoplasm (**Figure 4.8A1-2**, see **Figure 10.10A-C** in Appendix). No fluorescence was shown by control cells that had not been treated with Atto647-PSs (**Figure 4.8B**, see **Figure 10.10D-F** in Appendix). We addressed the cytotoxicity of CNCs and free enzyme by carrying out MTS proliferation assays with HepG2 cells (**Figure 4.8C**).[229] None of the nanocompartments nor the free enzyme had a negative impact on the cell viability. Although melittin is a bee venom, when inserted as pores in the

CNC membrane at the concentrations indicated, it apparently had no adverse effect on cell proliferation.

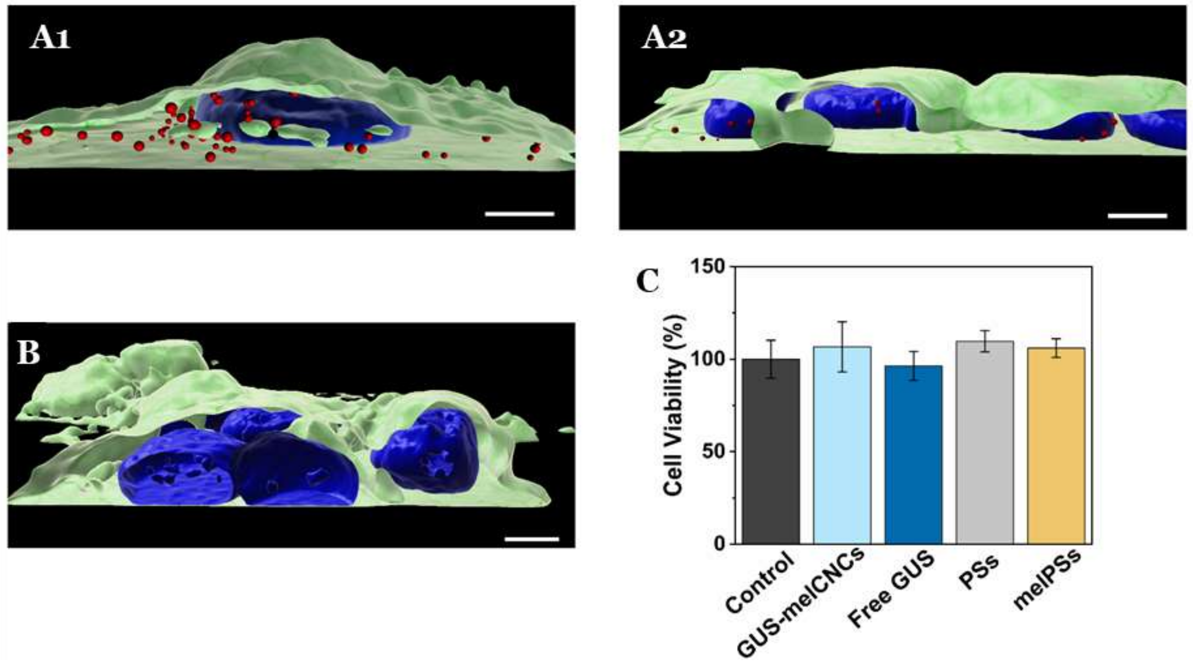

Figure 4.8. *Uptake of Atto647-PSs by HepG2 cells. 3D reconstructions of multiple confocal sections of HepG2 cells incubated with Atto647-PSs (1.25 mg mL^{-1}) for 24 h (A1, A2, red spheres). (B) HepG2 cells incubated with the respective amount of PBS. Nuclei (blue) were stained with Hoechst 33342 fluorescent dye, cellular membranes (green) with Atto555-WGA fluorescent dye. Scale bar: 5 µm. (C) Cell viability as percentage of HepG2 cells incubated with only PBS (control, black), GUS-melCNCs (cyan), free GUS (blue), PSs (grey) and melPSs (yellow). Graph shows mean ± s.d. of three independent experiments.*

The ability of CNCs to produce hymecromone in living cells was explored by incubating HepG2 cells with either GUS-melCNCs, GUS-CNCs, free GUS or the respective amount of PBS for 24 h. Subsequently, fresh culture medium containing 400 µM 4-MUG was added as at this concentration, hymecromone was shown to inhibit hyaluronan synthesis in cancer cell lines, and cultures were returned to the 37 °C incubator.[230–233] The change in fluorescence was recorded at 0, 2, 4, 8, 12 and 24 h (**Figure 4.9A, C**). After 24 h, cells that had taken up GUS-melCNCs, showed a fluorescence signal that corresponds to approximately 12 µM of hymecromone (**Figure 4.9B**). In fact, this amount might be an underestimation as some of the hymecromone produced in situ will be metabolized to 4-MUG in cells. Furthermore, although there is a possibility of intracellular components blocking individual melittin pores, considering their transient formation and their number per CNC, a potential blockage would only be a minor drawback. No increase in fluorescence was observed when untreated cells were incubated with 4-MUG (**Figure 4.9A**, black triangles), an indication that HepG2 cells by themselves are not able to produce such levels of hymecromone. However, we cannot exclude that small amounts of 4-MUG are converted to 4-MU by endogenous GUS (**Figure 4.9A, C**, black triangles).[204] In addition, 4-MUG was not converted to 4-MU in cells that were treated with non-permeabilized GUS-CNCs (**Figure 4.9A**, yellow rhombi) or with polymersomes lacking GUS (**Figure 4.9C**).

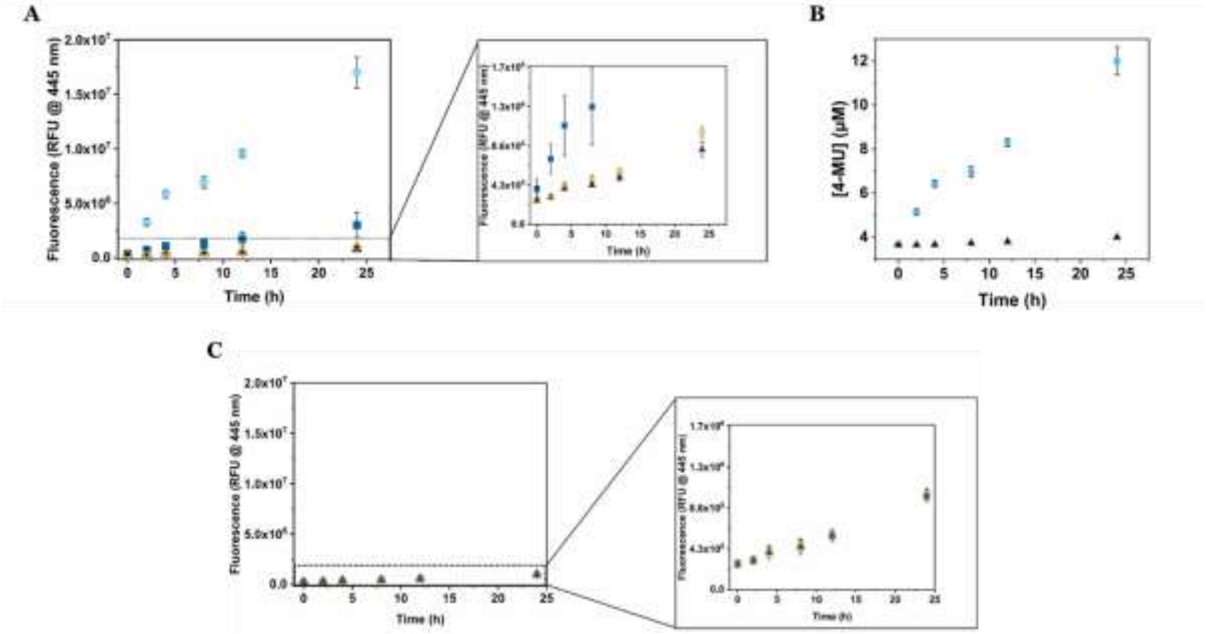

Figure 4.9. Intracellular production of hymecromone. (A) HepG2 cells were incubated for 24 h with CNCs for uptake, washed to remove extracellular CNCs, then exposed to a single dose of 400 µM 4-MUG, after which the increase in fluorescence was recorded at 0, 2, 4, 8, 12 and 24 h. GUS-melCNCs (cyan circles), free GUS (blue squares), GUS-CNCs (yellow rhombi), PBS (black triangles). (B) Concentration of hymecromone produced by GUS-melCNCs (cyan circles) or PBS (black triangles) treated HepG2 cells over time. Relative fluorescence units from (A) were converted to 4-MU concentrations according to the calibration curve shown in Figure 10.9B. (C) Increase in fluorescence in HepG2 cells incubated for 24 h with PBS (black triangles), PSs (grey squares), melPSs (yellow circles) and 400 µM 4-MUG. *Graphs shows mean ± s.d. of three independent experiments.*

In patients with Sly syndrome, free β-glucuronidase applied in clinical treatment was shown to be quickly degraded and to elicit an immune response.[234,235] One of the advantages of polymersomes is that they provide a protective shell for the encapsulated enzyme and thereby prolong its activity.[81,113] Consistent with this notion, the increase in fluorescence was significantly higher in cells incubated with GUS-melCNCs compared to those incubated with free GUS (**Figure 4.9A**, **B**, blue squares), confirming that our nanocompartments shield GUS from proteolysis and degradation inside cells.

Our PDMS-*b*-PMOXA based CNCs are prone to accumulation in the liver where they encounter high levels of metabolized hymecromone.[213,236,237] Undoubtedly, differences in pharmaco-kinetics will have to be taken into account in order to optimize GUS-melCNC efficiency *in vivo*. Beforehand, however, further studies are necessary to elucidate the bio-distribution of our PDMS-*b*-PMOXA-based nanocompartments.

4.3 Conclusions

In this chapter, we demonstrate the formation of catalytic nanocompartments containing enzymes able to produce a drug from its glucuronide conjugate and the potential of the platform in future applications. Our optimized design, i.e. the use of biocompatible and short block length copolymer, the permeabilization of the nanocompartments' membrane in combination with the mild enzyme encapsulation conditions permitted the efficient loading of GUS in melittin-permeabilized polymersomes, leading to the formation of our catalytic nanocompartments. GUS-melCNCs successfully converted hymecromone-glucuronide into hymecromone over the course of 90 min, both in PBS (60% conversion) and in cell culture medium containing 10% FBS (44% conversion). Highlighting their robustness, catalytic nanocompartments retained their size and virtually full enzymatic activity upon storage at 4 °C. Attributed to its confinement in CNCs, Michaelis-Menten kinetic analysis of GUS-melCNCs revealed decreased K_m, V_{max} and k_{cat} values compared to free enzyme.

Naturally occurring during the drug's metabolism, glucuronidation of hymecromone mainly occurs in the liver. In liver-derived HepG2 cells, our uptaken catalytic nanocompartments had no adverse effect on the cell viability and were able to produce hymecromone over 24 h by inverting glucuronidation. The locally confined catalysis of the model hymecromone-glucuronide to hymecromone inside cells led to 17-fold higher levels of the drug compared to hymecromone-glucuronide converted by endogenous glucuronidase. Pioneering the way, our CNCs render the first report of an intracellular conversion of a metabolite into an active drug. In the particular case of hymecromone, this could imply a potential increase of its half-life greater than 28 min. Such a novel example opens new approaches for extending the lifetime of drugs by counteracting metabolism. Although hymecromone was presented as an example of proof-of-concept, most of the small therapeutic molecules used in clinical treatment undergo glucuronidation, which highlights the unique opportunity our system offers to impose a change on their pharmacokinetics. By further controlling the biolocation of our nanocompartments, the conversion to the active drug could take greater dimensions in nanomedicine and inspire the broader use of catalytic nanocompartments in a wider range of therapeutic areas, such as prodrug therapy.

5. Bioorthogonal, Parallel Reactions for Drug Synergy: Glycooligomer-functionalized Catalytic Nanocompartments Co-loaded with Enzymes Promote Cell Internalization and Death

A major shortcoming associated with the application of enzymes in enzyme therapy and drug synergism originates from the lack of site-specific, multifunctional nanomedicine. Here, we introduce multifunctional catalytic nanocompartments with improved cellular uptake by targeting specific cell receptors. Made of a mixture of PDMS-b-PMOXA diblock copolymers, these nanocompartments are decorated with a glycooligomer and co-encapsulate two enzymes, providing the multifunctionality by in situ parallel reactions. B-glucuronidase serves for local reactivation of the drug hymecromone, while glucose oxidase induces cell starvation through glucose depletion and generation of the cytotoxic H_2O_2*. The insertion of melittin, a pore-forming peptide facilitates the diffusion of substrates and products through the membranes of the dual enzyme-loaded nanocompartments. Owned to decoration with glycooligomer tethers comprising eight mannose-containing repeating units, these catalytic nanocompartments specifically interact with mannose-binding lectins overexpressed on the surface of hepatocellular carcinoma (HepG2) cells. Increased internalization of the catalytic nanocompartments results in a substantial decrease in HepG2 cell viability after 24 hours, attributed to simultaneous production of hymecromone and* H_2O_2*. Such parallel enzymatic reactions taking place in nanocompartments pave the way to achieve efficient combinatorial cancer therapy by enabling localized drug production along with reactive oxygen species (ROS) elevation, and potentially inspire novel enzyme and drug combinations for a wider range of therapeutic purposes.*

This study is published as ***Korpidou, M.****, Becker, J., Tarvirdipour, S., Dinu, I.A., Becer, C.R. and Palivan, C.G., 2024. Glycooligomer-Functionalized Catalytic Nanocompartments Co-Loaded with Enzymes Support Parallel Reactions and Promote Cell Internalization. Biomacromolecules. Adapted with permission* under CC BY 4.0

5.1 Introduction

Enzyme-based treatments emerge as an innovative therapeutic strategy for a number of pathologies, spanning from metabolic and ocular disorders to cancer.[78,80] One of the main strategies used in the development of enzyme-based therapeutics include their loading inside so-called catalytic nanocompartments (CNCs), where the enzymes perform *in situ* their activity.[78,79] The approach of CNCs has the advantages to protect the encapsulated enzymes from proteolytic attack,[51] localize them in specific bio-regions to promote their efficacy,[238] and under specific conditions to increase their activity by confinement.[83] Of particular interest are polymer-based nanocompartments due to their advantages in comparison to lipid-based,[239] including enhanced mechanical and colloidal stability and versatile chemistry supporting fine tuning of properties, external functionalization for targeting or immobilization on different surfaces.[140,238,240] Catalytic nanocompartments encapsulating single enzymes have been successfully developed for conversion of prodrugs into their active therapeutic form,[112,114,169,241] detoxification of harmful reactive oxygen species[83] or as artificial organelles.[51,113] However, the recent trends in treating complex pathological conditions, including cancer, are shifting from conventional monotherapeutic approaches towards combinatorial strategies that simultaneously address multiple facets of the disease.[242,243] To this end, single enzyme-containing catalytic nanocompartments able to exhibit a dual functionality were introduced.[90,114,244,245]

A complementary strategy to extend the multifunctionality of CNCs is to co-encapsulate different enzymes capable to simultaneously produce distinct therapeutic molecules. While enzymes have been co-encapsulated inside CNCs, they were only participating in cascade reactions.[84,246] Despite the advantage of simultaneously producing distinct therapeutic molecules, the co-encapsulation of different types of enzymes in CNCs for parallel reactions has not yet been explored. Another drawback of nanosystems is related to the non-specific or insufficient cell uptake.[247] Incorporation of targeting moieties on the surface of nanocarriers for site-specific delivery and optimal therapeutic response has been largely developed for enzyme delivery carriers[248] and reported only for a few single-enzyme CNCs acting as advanced artificial organelles.[249,250] While expected to have significant advantages in terms of efficacy, combinatorial response and improved up-take, integration of multifunctionality and targeting in one nanocarrier has yet to be thoroughly investigated due to the complexity of accommodating both the biofunctionality and spatial localization.

We propose to cover this gap by introducing dual enzyme-loaded polymer nanocompartments for catalysis of parallel reactions and which have improved cellular uptake due to decoration with specific targeting molecules. We selected to encapsulate inside polymersomes two enzymes with high potential in combinatorial cancer therapy: β-glucuronidase (GUS), which produces the drug hymecromone (or 4-MU) from its glucuronide conjugate (4-MUG) and glucose oxidase (GOx), which generates cytotoxic H_2O_2 (**Figure 5.1**). GUS is an important enzyme in prodrug therapy, cancer prognosis and hepatoprotection.[251,252] Meanwhile, GOx is among the enzymes under intense investigation for its therapeutic potential, because it induces cancer cell starvation by consuming the glucose that is abundantly present in the tumor microenvironment, while simultaneously generating cytotoxic H_2O_2.[253,254] Notably, intracellular reactive oxygen species, in particular hydrogen peroxide (H_2O_2) have been widely exploited in the development of nanomedicine-based cancer therapies due to their role in activating apoptosis, necroptosis, inducing DNA damage and impairing the resistance against several drugs.[255–257] However, we recognize that different combinations of a variety of enzymes would expand only the functionality, but also the applications of the respective nanosystems. As nanocompartments, we self-assembled polymersomes from a mixture of unfunctionalized and azide-functionalized poly(dimethylsiloxane)$_{25}$-*b*-poly(2-methyl-2-oxazoline)$_{10}$ (PDMS$_{25}$-*b*-PMOXA$_{10}$) diblock copolymers which have been reported to allow the encapsulation of biomolecules in their inner cavity and support attachment of targeting moieties.[89,169,211] The copolymers consisting of hydrophobic PDMS and hydrophilic PMOXA blocks are known for their biocompatibility, non-toxicity and stealth properties that are required for biomedical applications.[100,168,211,258] In order to allow both enzymes to act *in situ* inside the nanocompartments, a molecular flow through the polymersomes' membrane is essential. To permeabilize the membrane of the nanocompartments, which is otherwise impermeable,[259] we selected to insert melittin, a peptide shown to form pores in the membranes of PDMS-*b*-PMOXA or PMOXA-*b*-PDMS-*b*-PMOXA polymersomes.[50,169]

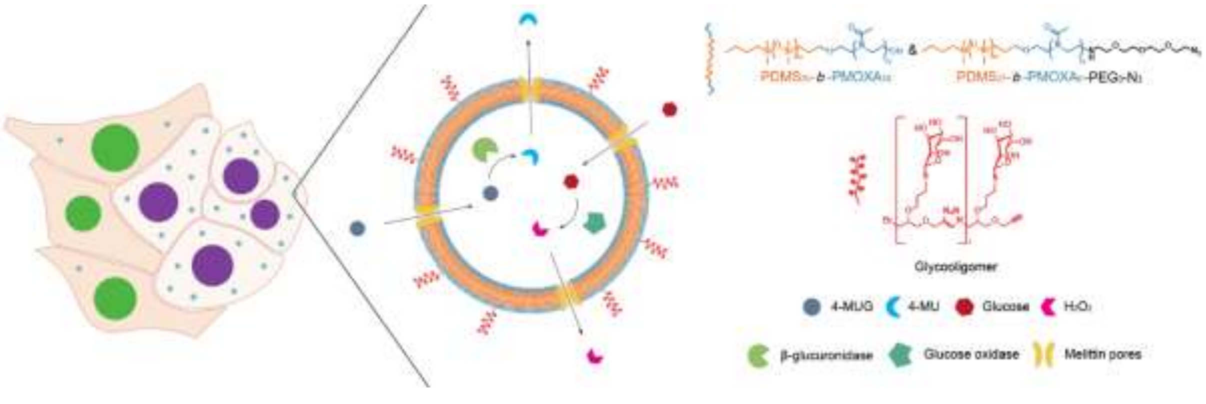

Figure 5.1. *Schematic representation of the glycooligomer-functionalized catalytic nanocompartments (GUS-GOx-CNCs-Gly) and their enzymatic activity in cells. Β-glucuronidase (GUS) and glucose oxidase (GOx) are co-encapsulated in PDMS-b-PMOXA-based nanocompartments decorated with glycooligomer tethers for targeting liver cancer cells. The melittin pores inserted into the polymer membrane facilitate the diffusion of substrates (4-MUG, glucose) and products (4-MU, H_2O_2) of the enzymes.*

To favor efficient cellular uptake of the resulting CNCs, specific targeting molecules were attached at the azide-groups exposed on their external interface to the environment. As a proof of concept of the versatility of our platform, we aim the active targeting of mannose-binding receptors (MBRs), which belong to the group of carbohydrate-binding proteins (a.k.a. lectins) that are highly expressed on the surface of cancer cells, providing selective carbohydrate recognition and subsequent endocytosis.[260–264] As a result, glycooligomers and glycopolymers, renowned for their excellent lectin-binding ability are ideal candidates for cell-targeting nanomedicinal systems in cancer therapy.[265–271] Associated with the invasiveness of liver cancer cells and the progression of hepatocellular carcinoma (HCC), the sixth most common cancer and the fourth leading cause of cancer-related death worldwide, MBRs have become the focal point in novel therapeutic approaches.[272,273] Notably, mannose-containing glycooligomers and glycopolymers have demonstrated their effectiveness in targeting MBRs, enhancing the therapeutic efficacy of nanosystems.[267,268,274] For this reason, we selected glycooligomer tethers consisting of eight pendant mannose units to be attached at the surface of CNCs via Copper-Catalyzed Azide-Alkyne Cycloaddition (CuAAC).[268,275] As a proof of concept for cell targeting, we chose two cell lines, each possessing different MBRs expression profiles; liver-derived HepG2 cells with high expression levels and cervix-derived HeLa cells expressing lower levels of such proteins.[268,272,276–278] We explored the synergistic effect of the *in situ* produced hymecromone and H_2O_2 on the cell viability. Dual enzyme-loaded catalytic nanocompartments for multifunctional response to pathologic conditions and with an improved internalization by efficient targeting open new avenues in combinatorial treatment of complex pathologic conditions. In a larger context, the concept of functionalized, dual-enzyme loaded nanocompartments has the potential to revolutionize the current approaches and state-of-the-art in a number of other applications and enzyme-based therapeutics.

5.2 Results and Discussion

5.2.1 Formation and Characterization of glycooligomer-decorated polymersomes

In order to generate polymersomes with functional groups exposed for the attachment of targeting moieties, we used a mixture of amphiphilic diblock copolymers, $PDMS_{25}$-*b*-$PMOXA_{10}$ and $PDMS_{22}$-*b*-$PMOXA_8$-OEG_3-N_3 (in a 1:1 molar ratio).[89,169] The azide-functionalized diblock copolymer served for covalent attachment of glycooligomer tethers. First, polymersomes (hereinafter referred to nanocompartments without encapsulated enzymes) were formed by film rehydration using phosphate buffered saline (PBS) solution. The supramolecular assemblies were then decorated with a glycooligomer, specifically designed to interact selectively with mannose-binding lectins.[271,279] To decorate the polymersomes with glycooligomer tethers, we used the CuAAC reaction between the alkyne end of glycooligomers and the azide moieties present on the outer membrane of polymersomes and were purified by size exclusion chromatography (SEC). Considering the potential biomedical applications of our catalytic nanocompartments, we performed colorimetric copper detection assays to evaluate the level of residual copper. The amount of free copper remaining after purification was well below physiological thresholds and therefore, not expected to be toxic (see **Figure10.11** in *Appendix*).[280]

Their morphological characterization was performed using a combination of dynamic and static light scattering (DLS/SLS), nanoparticle tracking analysis (NTA) and transmission electron microscopy (TEM, **Figure 5.2A-F**). An average diameter of 122 ± 40 nm for the non-functionalized polymersomes and 135 ± 54 nm for the glycosylated ones was obtained by DLS (**Figure 5.2A**). The slight increase in the apparent diameter of functionalized polymersomes was also observed by NTA and it can be attributed to the presence of glycooligomer tethers on their surface (**Figure 5.2B**; see **Table 10.5** in *Appendix*), as previously reported for other targeting molecules attached to polymersomes.[250]

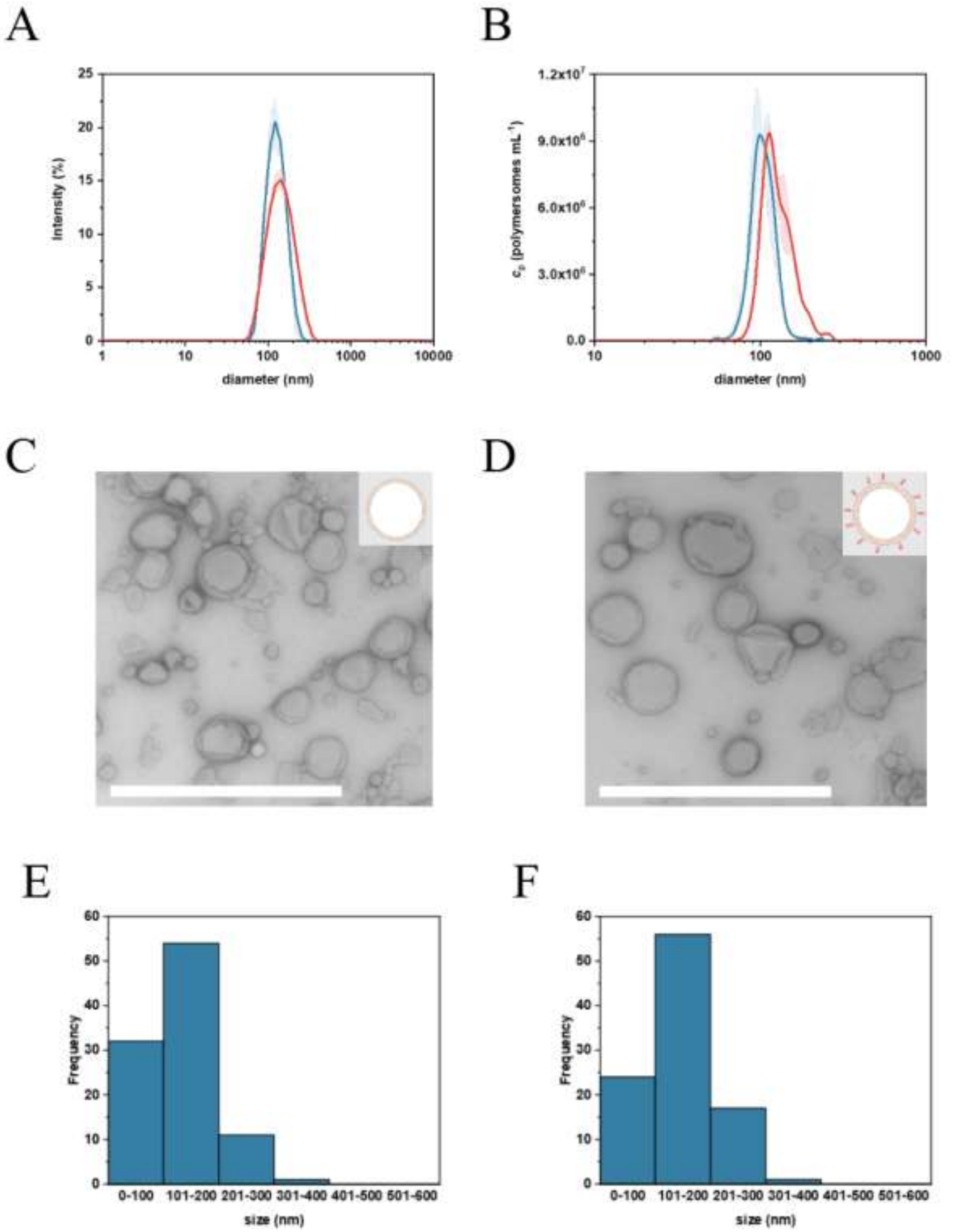

Figure 5.2. *Development of glycooligomer-decorated polymersomes. (A) DLS intensity size distribution of non-functionalized (blue) and glycooligomer-functionalized polymersomes (red); (curves represent mean ± s.d. of three independent measurements). (B) NTA concentration size distribution of non-functionalized (blue) and glycooligomer-functionalized polymersomes (red); (curves represent mean ± s.d. of three independent measurements). TEM micrographs of (C) non-functionalized and (D) glycooligomer-functionalized polymersomes. Scale bar: 1000 nm. Histogram showing the size distribution (diameter) of (E) non-fnctionalized polymersomes and (F) glycooligomer-functionalized polymersomes. The data were obtained by measuring the diameter of 100 nanocompartments for each set in TEM micrographs.*

The radius of gyration (R_g) values of 66 ± 4 nm and 79 ± 13 nm, respectively, were obtained by SLS (see **Table 10.5** and **Figure 10.12** in *Appendix*). The ratio of R_g to the hydrodynamic radius (R_h, obtained by the DLS profile, see **Figure 10.12** in *Appendix*) (ρ factor) of around 1 for both non- and glycooligomer-functionalized polymersomes indicated the typical vesicular structure and preservation of polymersome morphology after attachment of the targeting molecules (see **Table 10.5** in *Appendix*). The size distribution, polymersome morphology and lack of aggregation for both non- and glycooligomer-functionalized polymersomes were further corroborated by TEM micrographs (**Figure 5.2C-F**). The integrity of non- and glycooligomer-functionalized polymersomes was additionally evaluated after the encapsulation of the fluorescent Atto647 dye in their cavities during the self-assembly process. Diameters of 137 ± 39 nm for the glycooligomer-functionalized and 128 ± 40 nm for non-functionalized Atto647-loaded polymersomes indicated that the encapsulation of the dye neither affected the size nor the morphology of the polymersomes (see **Table 10.5** in *Appendix*).

The pore-forming peptide, melittin, was added to the rehydration buffer in order to permeabilize the membrane of the resulting polymersomes and to allow the essential molecular through-flow. To assess its insertion into the polymersomes' membrane, a series of fluorescence correlation spectroscopy (FCS) measurements were performed on non- and glycooligomer functionalized polymersomes permeabilized with various concentrations of Cy5-labeled melittin (25, 50 or 75 µM). The diffusion times corresponding to polymersomes confirmed the association of melittin with the polymersomes' membrane (see **Table 10.6** in *Appendix*). By correlating the molecular brightness values of free Cy5-melittin and Cy5-melittin polymersomes, we estimated the average number of pores per polymersome, which ranged from 133 to 242. The concentration of melittin was chosen at 50 µM for further studies, as the number of inserted pores did not significantly change between 50 µM and 75 µM of initial melittin concentration. The comparable number of melittin pores between non-functionalized (242 ± 28 pores/polymersome) and glycoligomer-functionalized (220 ± 16 pores/polymersome) polymersomes indicates that surface functionalization with glycooligomers neither affected the accessibility of the melittin pores nor induced aggregation.

The covalent attachment of glycooligomer tethers was followed by clustering experiments using Concanavalin A labeled with fluorescein isothiocyanate (FITC-ConA) for detection under a fluorescence microscope.[281,282] Confocal laser scanning microscopy (CLSM) analysis revealed that only glycooligomer-functionalized polymersomes, loaded with Atto647 fluorescent dye, formed clusters with FITC-labeled ConA (**Figure 5.3**). This was evidenced by a calculated Pearson's colocalization coefficient of 0.778 ± 0.071 for the two dyes present in the system. In contrast, non-functionalized polymersomes exhibited no cluster formation, as indicated by the low Pearson's coefficient of 0.012 ± 0.009, emphasizing the importance of functionalization in the process of clustering. As determined by glycooligomer absorbance at 250 nm (absorbance peak of glycooligomer), approximately 30% (equivalent to 0.23 mM) of the initial amount of glycooligomer was successfully conjugated onto the polymersomes (see **Figure 10.13** in *Appendix*). By correlating the amount of glycooligomer with the maximum polymersome concentration, we estimated an average number of 125 ± 5 glycooligomers per polymersome.

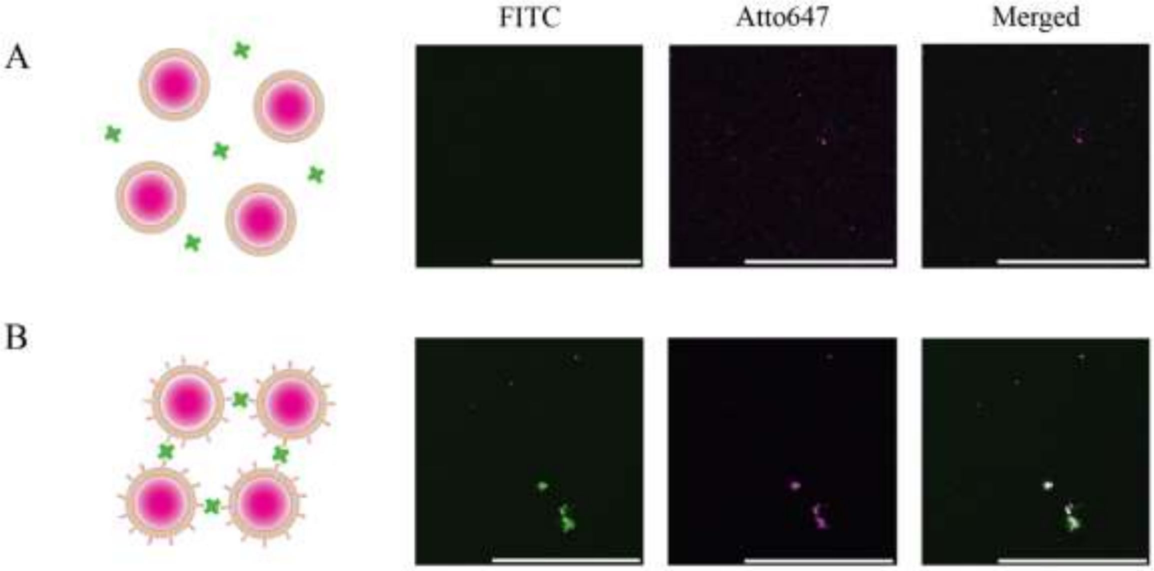

Figure 5.3. *ConA-glycooligomer cluster studies. CLSM micrographs of (A) non-functionalized and (B) glycooligomer-functionalized Atto647-loaded polymersomes upon incubation with FITC-ConA. Scale bar: 20 µm.*

To further explore the functional glycosylation of polymersomes and evaluate their binding properties with carbohydrate-binding proteins (lectins), we used surface plasmon resonance (SPR) (**Figure 5.4**). Human lectins such as Mannose-binding lectin (MBL), Mannose Receptor 1 (MR, CD206), Dectin-1 (CD369) and Dendritic Cell-Specific Intercellular adhesion molecule-3-Grabbing Non-integrin (DC-SIGN, CD209), known for their role in the innate immune response and various cancers were selected as binding ligands to study the interaction with our glycooligomer.[262,283–285] The acquired binding curves are a clear indication of the glycooligomer ability to specifically interact with MBL, as evident from the very sharp increase in signal intensity upon sample injection (**Figure 5.4A**). This was followed by a plateau, suggesting saturation of the chip-bound lectins, and a subsequent signal decrease upon buffer injection due to carbohydrates disassociating from the lectins. Glycooligomer-functionalized polymersomes also showed a strong binding to MBL. However, the curve shapes during the association phase were less distinct due to the higher molecular weight of the glycooligomer-functionalized polymersomes (**Figure 5.4B**). These findings underpinned by the calculated association constants (K_A, see **Table 10.7** in *Appendix*), revealed an approximately 4.5-fold stronger binding of the free glycooligomer compared to glycooligomer-decorated polymersomes. Interestingly, this trend was also observed for DC-SIGN (see **Table 10.7** in *Appendix*). However, in the case of MR, the functionalized polymersomes showed faster binding kinetics compared to the free ligand, with a difference in K_A of about 3.2-fold. Steric hindrance posed by the larger polymersomes appeared to predominantly affect the slower binding kinetics observed for MBL and DC-SIGN. Both the free glycooligomer and the glycooligomer-functionalized polymersomes bound to Dectin-1, a lectin known to recognize β-glucans, indicating a certain level of off-target interaction with mannose moieties.[286] Non-functionalized polymersomes showed weak, non-specific binding to MBL, Dectin-1, MR and DC-SIGN with significantly lower response levels (**Figure 5.4C**).

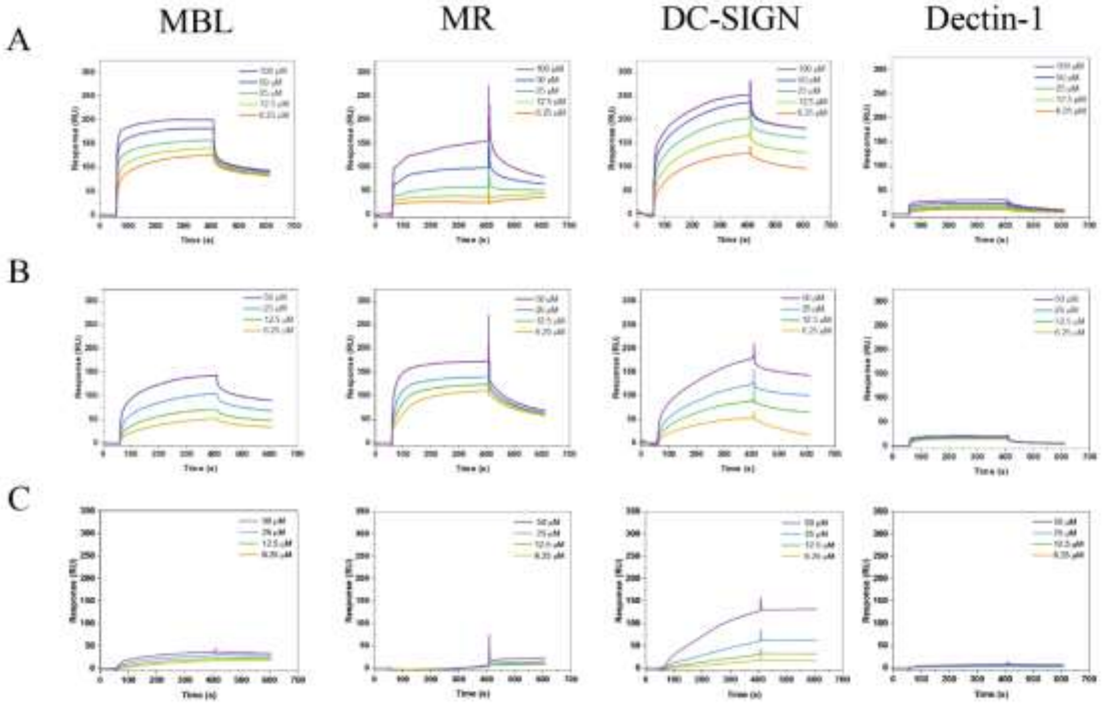

Figure 5.4. *Glycooligomer binding to various lectins. Surface Plasmon Resonance (SPR) binding curves of (A) glycooligomer, (B) glycooligomer-decorated polymersomes and (C) non-functionalized polymersomes using MBL, MR, DC-SIGN as strong mannose-binding C-type lectins, and Dectin-1 as a non-mannose-binding control lectin.*

5.2.2 Formation and Characterization of glycooligomer-decorated CNCs

Our catalytic nanocompartments were produced by rehydrating the polymer film in the presence of a mixture of β-glucuronidase (GUS, 0.5 mg mL^{-1}), glucose oxidase (GOx, 0.5 mg mL^{-1}) and melittin (50 μM) in PBS solution (**Figure 5.5A**). These conditions of encapsulation were chosen based on the similar catalytic activity of the enzymes. The resulting CNCs (GUS-GOx-CNCs) were incubated with proteinase K for deactivation of non-encapsulated enzymes, purified and functionalized with the glycooligomer (GUS-GOx-CNCs-Gly), in similar condition to polymersomes. The size analysis of GUS-GOx-CNCs-Gly revealed diameters of 152 ± 54 nm (by DLS; **Figure 5.5B**) and 137 ± 38 nm (by NTA; **Figure 5.5C**). The co-encapsulation of enzymes and simultaneous insertion of melittin did not affect the self-assembly process and their size distribution. With a calculated ρ factor of around 1, the morphology of CNCs remained vesicular as of the empty polymersomes (see **Figure 10.14** in *Appendix*). TEM micrographs indicated a vesicular, collapsed architecture of the CNCs, typical of PDMS-*b*-PMOXA polymersomes (**Figure 5.5D**).[95,169] The size distribution of GUS-GOx-CNCs-Gly was also confirmed by measuring their diameter in TEM micrographs (**Figure 5.5E**). These results taken together indicate that the encapsulation of two enzymes and insertion of melittin had no effect on the self-assembly, size distribution and morphology of our CNCs.

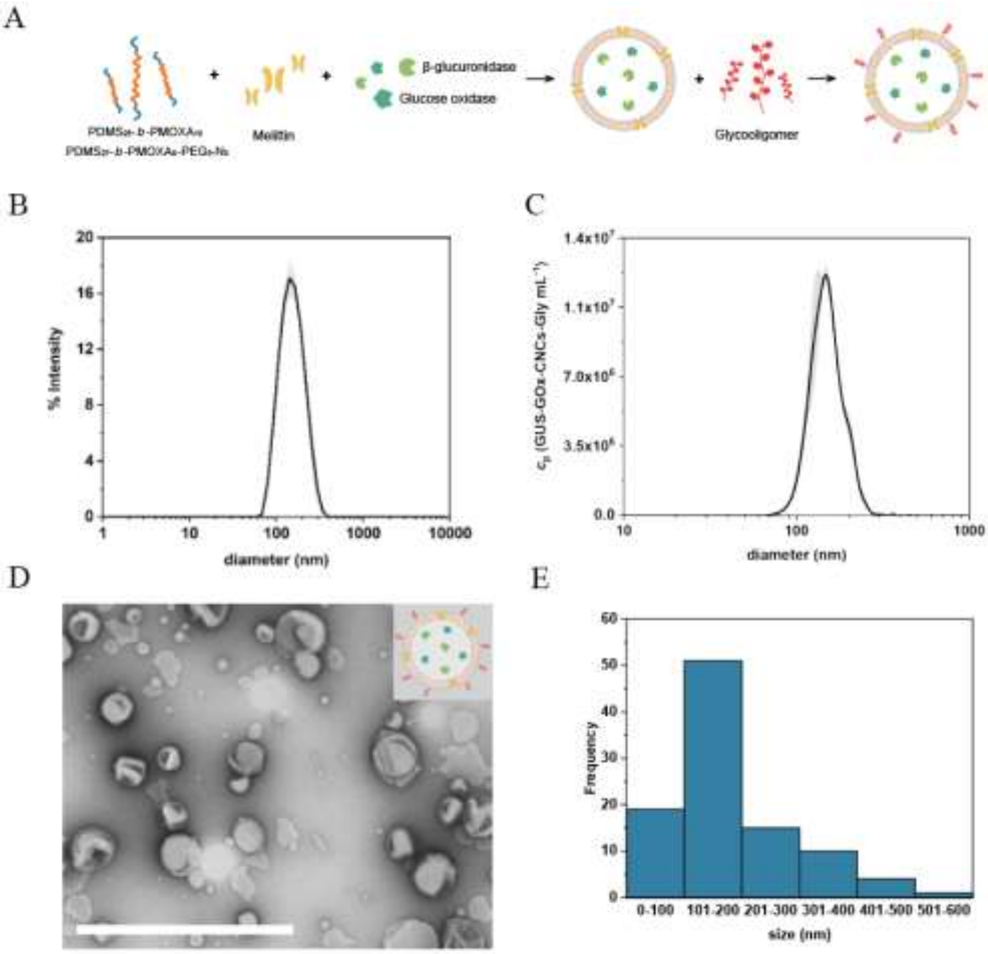

Figure 5.5. *Development of GUS-GOx-CNCs-Gly. (A) Schematic representation illustrating the formation of GUS-GOx-CNCs-Gly. (B) DLS intensity size distribution (curves represent mean ± s.d. of three measurements). (C) NTA concentration and size distribution (curves represent mean ± s.d. of three measurements). (D) TEM micrograph of GUS-GOx-CNCs-Gly. Scale bar: 1000 nm. (E) Histogram showing the size distribution (diameter) of GUS-GOx-CNCs-Gly. The data were obtained by measuring the diameter of 100 nanocompartments for each set in TEM micrographs.*

The encapsulation of both enzymes in CNCs was evaluated by fluorescence correlation and cross-correlation spectroscopy (FCS/FCCS, **Figure 5.6A**). GUS was labeled with Atto488 (τ_D free Atto488 29 ± 4 µs, τ_D GUS-Atto488 250 ± 92 µs, 1.7 ± 0.1 dyes/enzyme, **Figure 5.6B**), and GOx was labeled with Atto633 (τ_D free Atto633 57 ± 6 µs, τ_D GOx-Atto488 424 ± 32 µs, 1.5 ± 0.1 dyes/enzyme, **Figure 5.6B**). The FCS autocorrelation curves indicated the successful encapsulation of GUS (4 ± 2 molecules) and GOx (7 ± 4 molecules) within the CNCs based on the significant change in diffusion time (τ_D GUS-GOx-CNCs-Gly 6900 ± 3940 µs). FCCS can be utilized to study the association between two different fluorophores when their signals correlate.[287] Therefore, we used FCCS analysis to investigate the co-encapsulation of the two enzymes in the cavities of CNCs, as GUS and GOx were fluorescently labeled with different fluorophores. The increased cross-correlation (**Figure 5.6A**; blue curve) of GUS and GOx when they were encapsulated in CNCs in comparison to the free enzymes (**Figure 5.6A**; black curve) indicated their co-encapsulation in the CNCs' cavities. Correlating the number of both encapsulated enzymes to the concentration of CNCs measured by NTA, we calculated an enzyme encapsulation efficiency of 16% ± 8% for GUS and 11% ± 6% for GOx. We also used the Bicinchoninic acid (BCA) assay for quantification of total amount of protein in our CNCs (**Figure 5.6C**). A total 24% ± 7% of the initial amount of enzyme (both GUS and GOx) was obtained, which is in line with the calculated sum of the encapsulation efficiency. Applying the Stokes–Einstein equation together with the FCS diffusion times, a calculated CNCs size of 144 ± 64 nm in diameter was obtained, which is in agreement with the values obtained from DLS, SLS, NTA and TEM measurements.

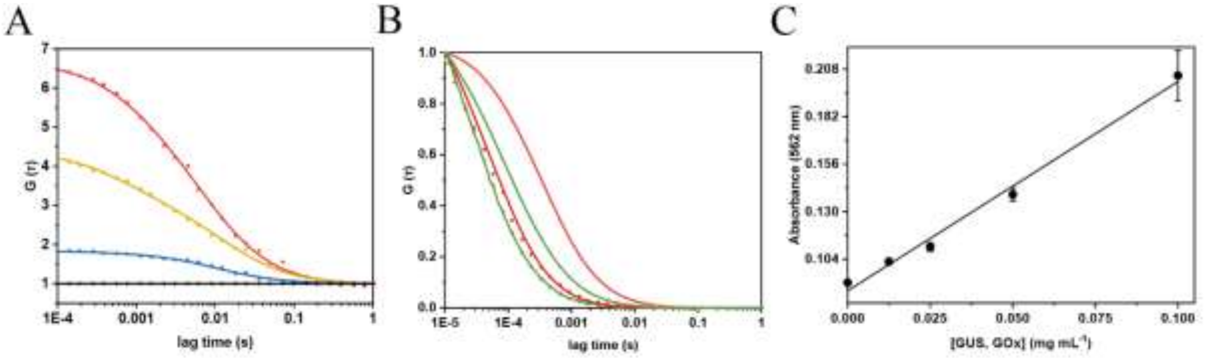

Figure 5.6. *Encapsulation of GUS and GOx in CNCs. (A) FCS curves of GUS-GOx-CNCs-Gly (yellow: channel for Atto488-GUS, red: channel for Atto633-GOx) and FCCS curves of GUS-GOx-CNCs-Gly (blue) and free Atto488-GUS/Atto633-GOx (black). (B) FCS curves for free Atto488 (green, full symbols), free Atto633 (red, full symbols), GUS-Atto488 (green, empty symbols) and GOx-Atto633 (red, empty symbols). Symbols: raw data, Lines: fitted curves. (C) GUS, GOx calibration curve for the BCA protein assay (R^2 = 0.99).*

5.2.3 Parallel production of hymecromone and H_2O_2 by CNCs

As a proof of concept, our CNCs were designed to facilitate parallel production of hymecromone and H_2O_2. When provided with its glucuronide conjugate, GUS produces the drug hymecromone, whilst GOx consumes the existing glucose in the medium and produces H_2O_2 (**Figure 5.7**). Free and encapsulated enzymes were assessed for their enzymatic activity in a PBS solution comprising 50% Dulbecco's Modified Eagle Medium (DMEM) Phenol Red free with 10% Fetal Bovine Serum (FBS). This formulation was selected to mimic the cell culture environment, as it is essential for evaluating the therapeutic potential of our CNCs. First, we monitored the activity of GUS by tracking the conversion of hymecromone glucuronide (4-MUG) into hymecromone (λ_{em} 445 nm) over 60 min (**Figure 5.7A**). Upon the addition of 4-MUG (10 μM) to free GUS, the fluorescence levels corresponding to hymecromone rapidly reached a plateau within 20 min (**Figure 5.7A**, black). GUS-GOx-CNCs and GUS-GOx-CNCs-Gly gradually reached a plateau at around 45 min (**Figure 5.7A**, yellow and red). Comparing the slopes of the linear part of the reaction, which describe the rate of 4-MU production, we observed a decrease in their value for encapsulated GUS (0.78 ± 0.11 for GUS-GOx-CNCs and 0.71 ± 0.09 for GUS-GOx-CNCs-Gly), compared to free enzyme (4.37 ± 0.10). This behavior is characteristic of pore-permeabilized enzyme-encapsulating nanocompartments, where the diffusion of substrates and products to and from the cavities might affect the velocity of the reaction.[83,169] As expected, non-permeabilized CNCs (cGUS-GOx-CNCs) demonstrated a minimal hymecromone fluorescence level over time because the polymersome membrane did not allow the diffusion of substrate into the cavity (**Figure 5.7A**, green). No increase in fluorescence was observed for 4-MUG alone (**Figure 5.7A**, blue), revealing that in the absence of GUS, hydrolysis of the ether bond and production of 4-MU does not occur. According to the 4-MU calibration curve, free GUS generated 7.4 ± 0.4 μM, while GUS-GOx-CNCs produced 2.8 ± 0.2 μM and GUS-GOx-CNCs-Gly 2.4 ± 0.2 μM of hymecromone (see **Figure 10.15A** in *Appendix*; **Figure 5.7B**). These differences in hymecromone production between free and encapsulated GUS are attributed to the molecular crowding caused by FBS and the diffusion of substrates and products through the CNCs' membrane.[169] In PBS containing 10 μM 4-MUG and 12.5 mM glucose, the fluorescence signal rapidly increased for free GUS, reaching a plateau in 10 min (**Figure 5.7C**). On the contrary, the fluorescence signal continued to increase over 35 min for GUS-GOx-CNCs and GUS-GOx-CNCs-Gly, revealing that FBS affects the kinetics of the free enzyme, but not those of the confined one (**Figure 5.7C**).[15] To investigate whether the co-encapsulation of GUS with GOx had an influence on the GUS reaction kinetics, we confined the enzymes into the cavities of separate nanocompartments produced in similar conditions (GUS-CNCs and GOx-CNCs, **Figure 5.7D**). As evident by the similarity between the increase in fluorescence of GUS-GOx-CNCs and GUS-CNCs, as well as the slopes of the reactions (0.69 ± 0.03 for GUS-CNCs), the enzymatic activity of GUS was not affected by its co-encapsulation with GOx, thus these reactions are bioorthogonal. This represents a crucial requirement when dual-enzyme CNCs are developed to not compromise the *in situ* reactions.

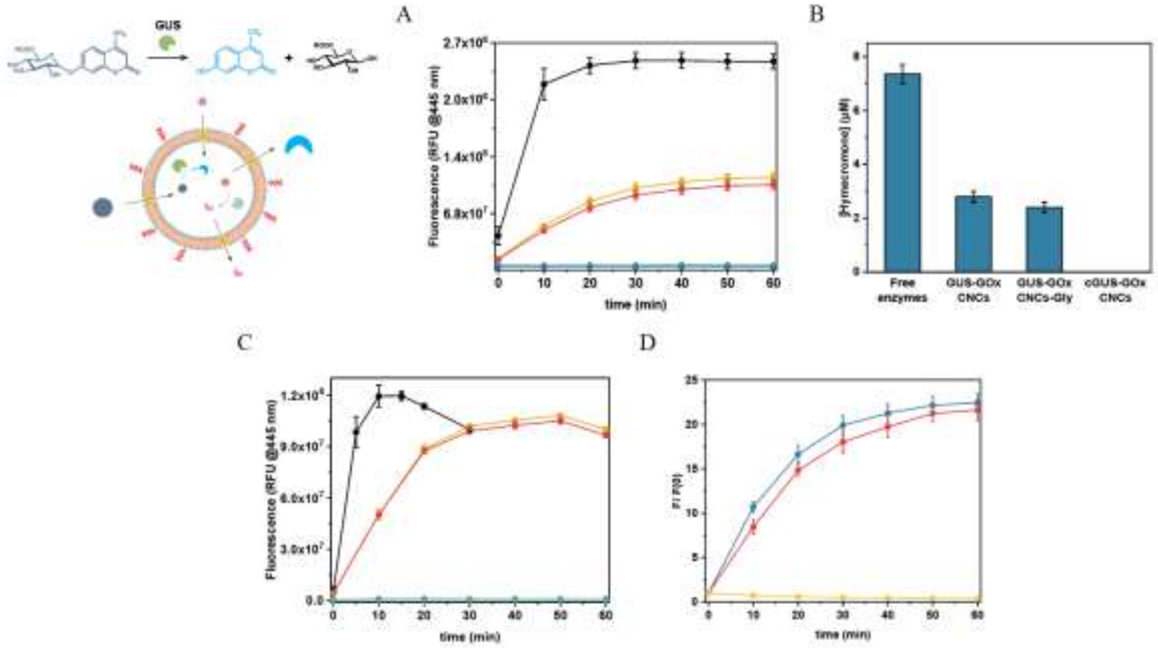

Figure 5.7. *Enzymatic efficiency of GUS. (A) 4-MUG (10 µM) conversion to 4-MU in PBS containing 50% DMEM Phenol Red free with 10% FBS at 37 °C, black: free enzymes, yellow: GUS-GOx-CNCs, red: GUS-GOx-CNCs-Gly, green: non-permeabilized CNCs, blue: reaction mixture without enzymes. Mean ± s.d. of 3 experiments. (B) Amount of hymecromone produced after 60 min. Mean ± s.d. of 3 experiments. (C) Enzymatic efficiency of CNCs in PBS at 37 °C, 4-MUG (10 µM) conversion to 4-MU, black: free enzymes, yellow: GUS-GOx-CNCs, red: GUS-GOx-CNCs-Gly, green: non-permeabilized CNCs, blue: reaction mix without enzymes. (D) 4-MUG (10 µM) conversion to 4-MU in PBS containing 50% DMEM Phenol Red free with 10% FBS, blue: GUS-GOx-CNCs, red: GUS-CNCs, yellow: reaction mix without enzymes. Mean ± s.d. of 3 repetitions.*

In parallel, the available glucose (12.5 mM) was consumed by the second enzyme, GOx, resulting in the production of H_2O_2. To accurately monitor and quantify the generated H_2O_2, we employed the Amplex™ Red (AR) assay, which in the presence of horseradish peroxidase (HRP) stoichiometrically reacts with H_2O_2 (**Figure 5.8**). HRP and AR were added to the solution of CNCs and AR reacted with the H_2O_2 released from the CNCs producing fluorescent resorufin (λ_{em} 590 nm). For free GOx in solution, the resorufin fluorescence signal increased approximately 470 times, equivalent to 6.0 ± 1.3 mM of H_2O_2 according to the resorufin reference curve (**Figure 5.8A**, **B**; see **Figure 10.15B** in *Appendix*). For GUS-GOx-CNCs and GUS-GOx-CNCs-Gly, the fluorescence increased by 400 and 330 times, respectively, corresponding to 5.2 ± 2.1 mM H_2O_2 for GUS-GOx-CNCs and 4.7 ± 1.1 mM H_2O_2 for GUS-GOx-CNCs-Gly. Comparable amounts of H_2O_2 were produced by free GOx, GUS-GOx-CNCs, and GUS-GOx-CNCs-Gly due to the high excess of glucose within the system. On the contrary, minimum fluorescence signal was detected for non-permeabilized CNCs and AR alone, associated with the autooxidation of AR.

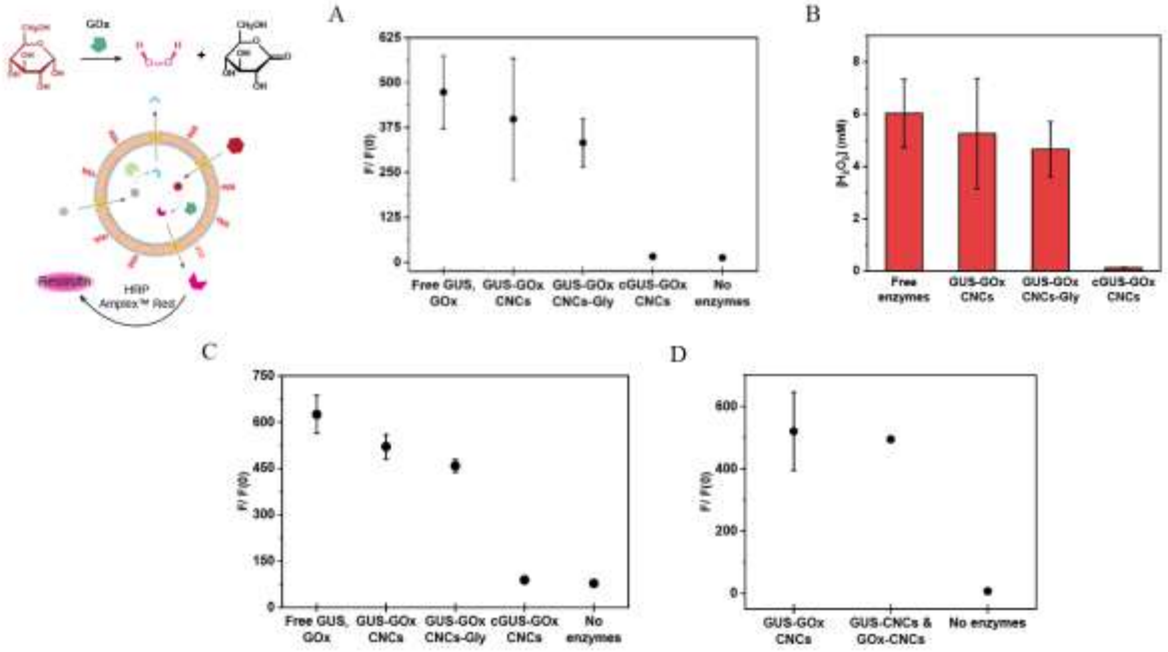

Figure 5.8. *Enzymatic efficiency of GOx. (A) Conversion of Amplex™ Red (10 μM) into resorufin after 2 h in PBS containing 50% DMEM Phenol Red free with 10% FBS at 37 °C. Mean ± s.d. of 3 experiments. (B) Amount of H_2O_2 produced after 2 h. Mean ± s.d. of 3 experiments. (C) Enzymatic efficiency of CNCs in PBS at 37 °C. (C) Amplex™ Red (10 μM) conversion to resorufin. (D) Amplex™ Red (10 μM) conversion to resorufin after 2 h by GUS-GOx-CNCs and GOx-CNCs. Mean ± s.d. of 3 repetitions. Error bars might be smaller than the symbol.*

The impact of FBS on the kinetics of GOx was also evaluated. When the reactions were conducted in PBS containing 10 μM 4-MUG and 12.5 mM glucose, free GOx showed a 625-fold increase in resorufin fluorescence, whereas GUS-GOx-CNCs and GUS-GOx-CNCs-Gly showed increases of 520 and 458 times, respectively. This difference indicates the crowding effect of the protein-rich FBS (**Figure 5.8C**). Co-encapsulation with GUS did not affect the reaction kinetics of GOx, as indicated by the similar changes in resorufin fluorescence between co-encapsulated and separately encapsulated enzymes (**Figure 5.8D**). Importantly, the enzyme reactions kinetics (**Figure 5.7A**, **Figure5.8A**) and the catalytic efficiencies (**Figure 5.7B**, **Figure 5.8B**) of both GUS and GOx were similar in GUS-GOx-CNCs-Gly and GUS-GOx-CNCs. Therefore, the presence of glycooligomers on the outer membrane did not restrict the diffusion of substrates and products to and from the CNCs' cavities. Our CNCs were stored for up to 2 months at 4 °C in PBS. Remarkably, they preserved their size as measured by DLS and retained their GUS and GOx activity, which is an important aspect in nanosystems developed for therapeutic applications (**Figure 5.9**).

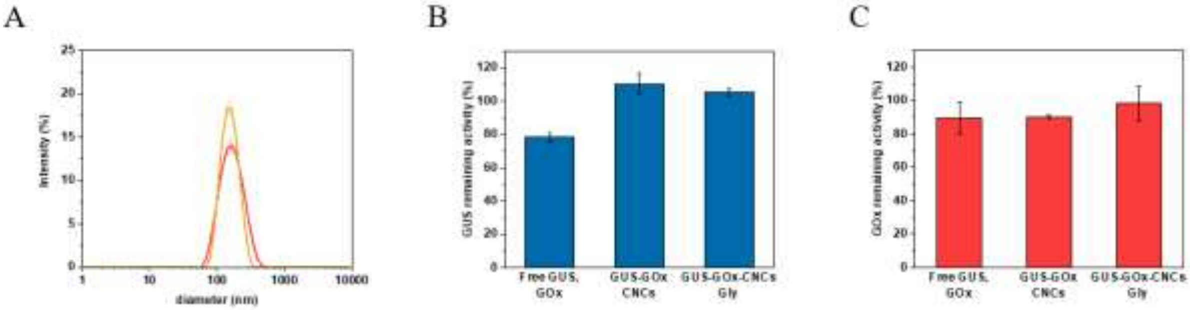

Figure 5.9. *Stability of CNCs stored at 4 °C for 2 months. (A) Size distribution of GUS-GOx-CNCs (yellow) and GUS-GOx-CNCs-Gly (red) measured by DLS, after storage for 2 months at 4 °C. Remaining percentages of activity of (B) GUS and (C) GOx upon storage at 4 °C for 2 months. Measurements represent the mean ± s.d.*

5.2.4 Cell targeting, uptake and endosomal escape of glycooligomer-decorated nanocompartments

Liver cells are known to express a high level of mannose receptors, facilitating receptor-assisted endocytosis and internalization of the mannose-containing molecules.[288] To assess the targeting efficiency and uptake potential of glycooligomer-functionalized polymersomes, we used two distinct cell lines: HepG2 (a liver-derived cancer cell line overexpressing mannose-binding lectins) and HeLa cells (a cervix-derived cancer cell line with low expression of mannose-binding lectins) (**Figure 5.10**; see **Figure 10.16** in *Appendix*).[268,275–278] First, we studied the ability of conjugated glycooligomer to promote polymersome uptake in HepG2 cells. Cells were incubated for 24 h with either glycooligomer-functionalized or non-functionalized Atto647-containing polymersomes and were imaged using CLSM. Analysis of CLSM micrographs in HepG2 cells showed a considerable increase in the uptake of glycooligomer-functionalized polymersomes compared to non-functionalized ones (**Figure 5.10A**, **B**). Quantification of the fluorescence intensity revealed a 4-fold increase (P-value < 0.01) for glycosylated polymersomes.

To further explore the specificity in cell uptake of glycooligomer-decorated polymersomes, HepG2 and HeLa S3 H2B-GFP cells were co-cultured and subsequently incubated with Atto647-loaded polymersomes for 24 h (**Figure 5.10C-D**). Analysis of CLSM micrographs revealed that glycooligomer-functionalized polymersomes were predominantly found in HepG2 cells. Upon quantifying the fluorescence intensity corresponding to Atto647, we obtained that glycosylated polymersomes were 3 times (P-value < 0.05) more abundant in HepG2 cells in comparison to HeLa cells. These findings underline the key role of glycooligomer functionalization in enabling specific cell uptake, particularly demonstrating the enhanced uptake of our catalytic nanocompartments in liver cells expressing high levels of mannose-binding lectins.

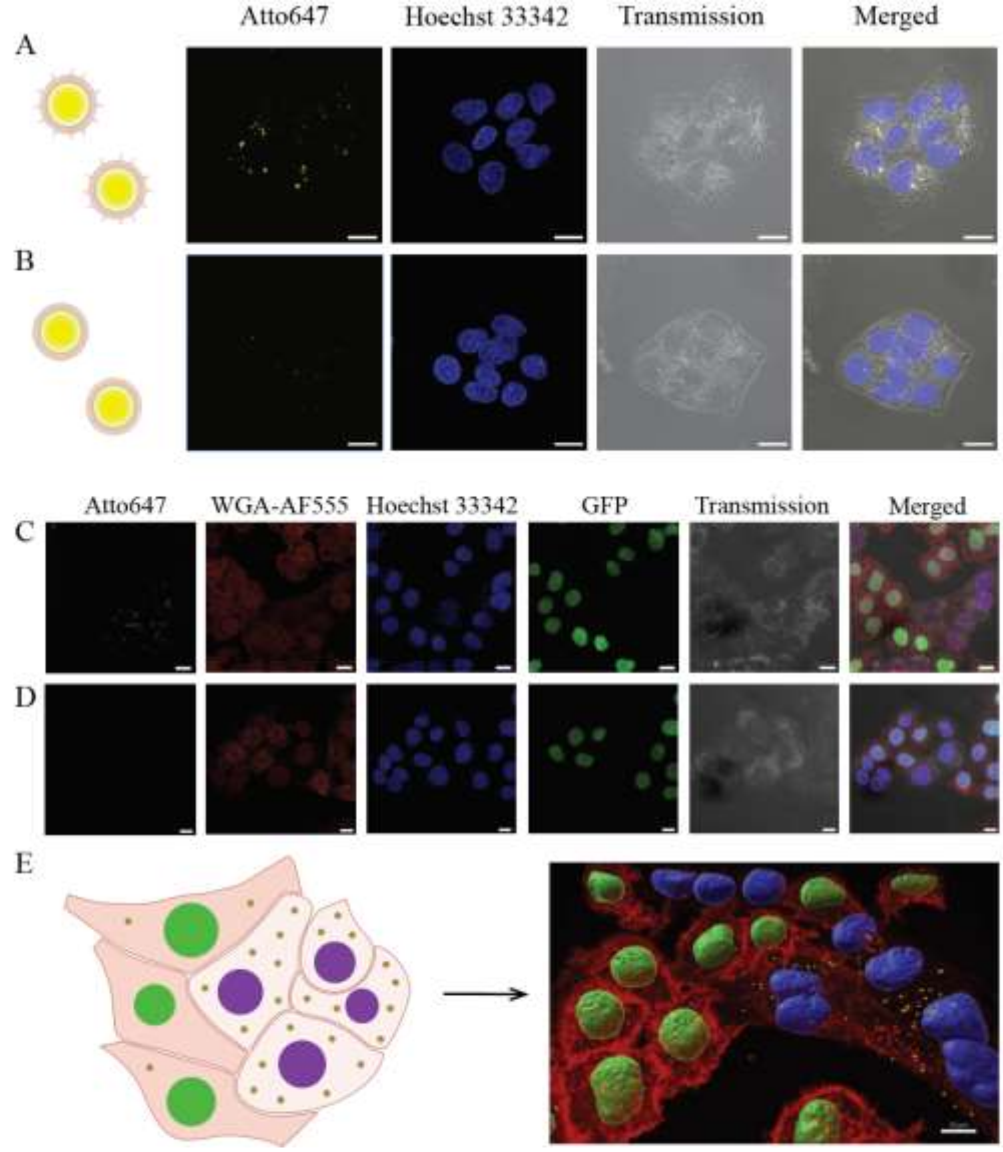

Figure 5.10. *Uptake of Atto647-encapsulating polymersomes. Superimposed CLSM micrographs of multiple confocal sections. (A) HepG2 cells incubated with glycooligomer-functionalized polymersomes. (B) HepG2 cells incubated with non-functionalized polymersomes. (C) HepG2 and HeLa S3 H2B-GFP cells incubated with glycooligomer-functionalized polymersomes. (D) HepG2 and HeLa S3 H2B-GFP cells incubated with non-functionalized polymersomes. (E) Schematic and 3D reconstructions of multiple confocal sections of HepG2 and HeLa S3 H2B-GFP cocultured cells incubated with glycooligomer-functionalized polymersomes. Yellow: polymersomes, Atto647, Red: Cell membranes, Atto555-WGA, Blue: nuclei, Hoechst 33342, Green: HeLa S3 H2B-GFP nuclei, GFP. Scale bar: 10 µm.*

To evaluate whether our polymersomes successfully escape the endosomes after cell uptake, we performed endosomal escape assays by co-incubating HepG2 cells with a mixture of non-or glycooligomer-functionalized polymersomes and free calcein for 4 h. CLSM imaging indicated that glycooligomer-functionalized polymersomes had escaped the endosomes and were localized within the cytoplasm of cells, as indicated by the dispersed green cytosolic fluorescence (**Figure 5.11**). The higher endosomal escape observed with glycooligomer-functionalized polymersomes compared to non-functionalized ones correlates with their higher uptake level (**Figure 5.10**). These results are in agreement with previous studies demonstrating that the endosomal escape of nanoparticles in HepG2 cells occurs over a period of 3-14 h.[289–292]

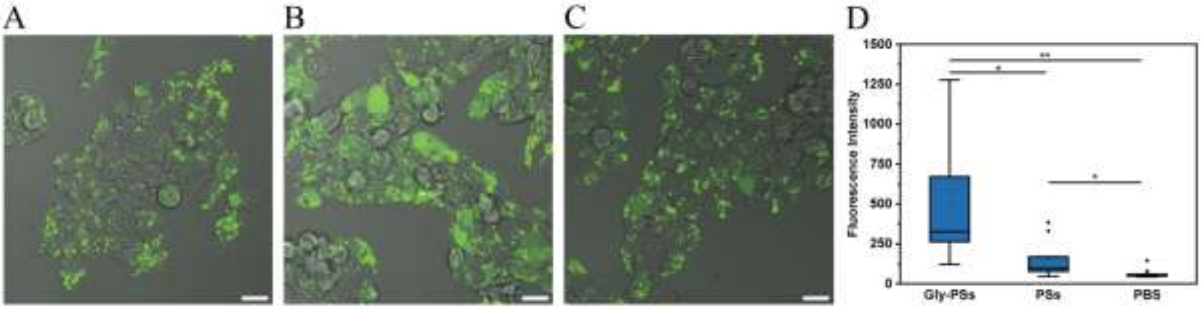

Figure 5.11. *Endosomal escape of polymersomes in HepG2 cells. (A) PBS-incubated cells, (B) glycooligomer-functionalized polymersomes-incubated cells, (C) non-functionalized polymersomes-incubated cells for 4 h with calcein (250 µM). (D) Fluorescence intensity of calcein as measured in the cytoplasm of HepG2 cells by CLSM micrographs (Gly-PSs: glycooligomer-functionalized polymersomes, PSs: non-functionalized polymersomes). Green: calcein. Scale bar: 20 µm.*

5.2.5 Catalytic nanocompartments in cells – bioorthogonal reactions and synergistic effect of hymecromone and H_2O_2

We evaluated the multifunctionality of the glycooligomer-functionalized catalytic nanocompartments in cells as an essential step to assess their potential (**Figure 5.12**). We first examined hymecromone production in HepG2 and HeLa S3 H2B-GFP cells after incubation with GUS-GOx-CNCs-Gly, GUS-GOx-CNCs, non- permeabilized CNCs, free GUS and GOx or an equivalent volume of PBS for 24 h. After cell washing for removal of non-uptaken CNCs or enzymes, fresh medium containing 4-MUG (500 µM) was added, and the increase in hymecromone fluorescence signal was monitored for 24 h (**Figure 5.12A**, **B**). At this concentration, hymecromone has shown inhibitory effect on hyaluronan synthesis and induced cell death.[231,232] In HepG2 cells, exposure to GUS-GOx-CNCs-Gly resulted in a progressive increase of the fluorescence signal, corresponding to 190 ± 23 µM of hymecromone at 24 h (see **Figure 10.17** in *Appendix*). In contrast, no fluorescence increase was observed in cells incubated with PBS, free GUS, GUS-GOx-CNCs and non-permeabilized

CNCs. Proteins are large, hydrophilic molecules that cannot pass directly through the cell membrane and are degraded by extracellular proteases.[293–295] Therefore, only when encapsulated inside catalytic nanocompartments, GUS is effectively shielded, thus prolonging the activity and facilitating the cellular uptake (**Figure 5.12A**). Notably, GUS-GOx-CNCs and GUS-GOx-CNCs-Gly in solution demonstrated a similar enzymatic activity (**Figure 5.7**), indicating the intracellular production of hymecromone specifically by the cells that have taken up the catalytic nanocompartments. However, in HeLa S3 H2B-GFP cells characterized by a lower expression of mannose-binding lectins, GUS-GOx-CNCs-Gly produced only 8 ± 2 μM of hymecromone, indicating a significantly lower uptake of the CNCs (**Figure 5.12B**; see **Figure 10.17** in *Appendix*). When free GUS, GUS-GOx-CNCs and cGUS-GOx-CNCs was added to HeLa S3 H2B-GFP cells, no increase in fluorescence corresponding to hymecromone production was observed. Similarly as in solution, drug production does not occur in the case of non-permeabilized CNCs (**Figure 5.12A**).[169]

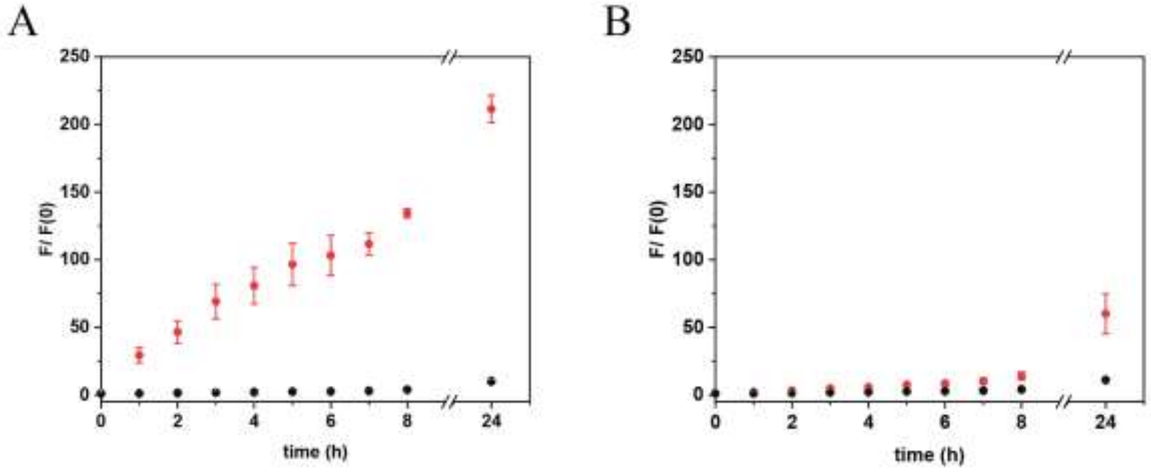

Figure 5.12. *Intracellular production of hymecromone. (A) HepG2 and (B) HeLa S3 H2B-GFP cells after incubation with GUS-GOx-CNCs (yellow), GUS-GOx-CNCs-Gly (red), cGUS-GOx-CNCs (green), free GUS&GOx mixture (blue) or PBS (black) for 24 h. Cells were washed and exposed to a single dose of 500 μM 4-MUG. Fluorescence was recorded for 24 h. Graph shows mean ± s.d. of three experiments.*

We then detected the intracellularly produced H_2O_2 in HepG2 and HeLa S3 H2B-GFP cells using a cell-permeable 2',7'-dichlorodihydrofluorescein diacetate (H2DCFDA) probe. This non-fluorescent probe, upon cleavage by intracellular esterases and ROS oxidation, is converted to fluorescent 2',7'-dichlorofluorescein (DCF) (**Figure 5.13**). Total fluorescence analysis of HepG2 cells incubated with GUS-GOx-CNCs-Gly exhibited significantly higher DCF fluorescence intensity compared to cells incubated with GUS-GOx-CNCs (1-fold, P-value < 0.05), thus indicating higher intracellular ROS levels (**Figure 5.13A**, **B**). These increased levels correlate with the enhanced cellular uptake and endosomal escape of glycooligomer-functionalized CNCs in HepG2 cells. Cells incubated with GUS-GOx-CNCs-Gly also showed significantly higher DCF fluorescence intensity compared to non-permeabilized CNCs (cGUS-GOx-CNCs, 2-fold, P-value < 0.01) and free GUS & GOx (3-fold, P-value < 0.001), respectively, highlighting the importance of our permeabilized, glycooligomer-functionalized CNCs for intracellular uptake and activity. Moreover, GUS-GOx-CNCs-Gly induced significantly higher intracellular DCF fluorescence intensity compared to empty polymersomes (EPs, 3-fold, P-value < 0.001) and PBS (3-fold, P-value < 0.001), respectively. The DCF fluorescence intensity detected in untreated HepG2 cells is associated with their intrinsic ROS levels.[296] These findings further underline the efficacy of our GUS-GOx-CNCs-Gly in inducing high intracellular ROS levels. In contrast, total DCF fluorescence analysis in HeLa S3 H2B-GFP cells did not reveal significant differences in intracellular ROS levels when incubated with CNCs or free enzymes (**Figure 5.14A**, **B**). Similar to hymecromone production, free GOx and CNCs are not efficiently uptaken by HeLa S3 H2B-GFP cells, with non-permeabilized CNCs bearing the extra constraint of an impermeable membrane.

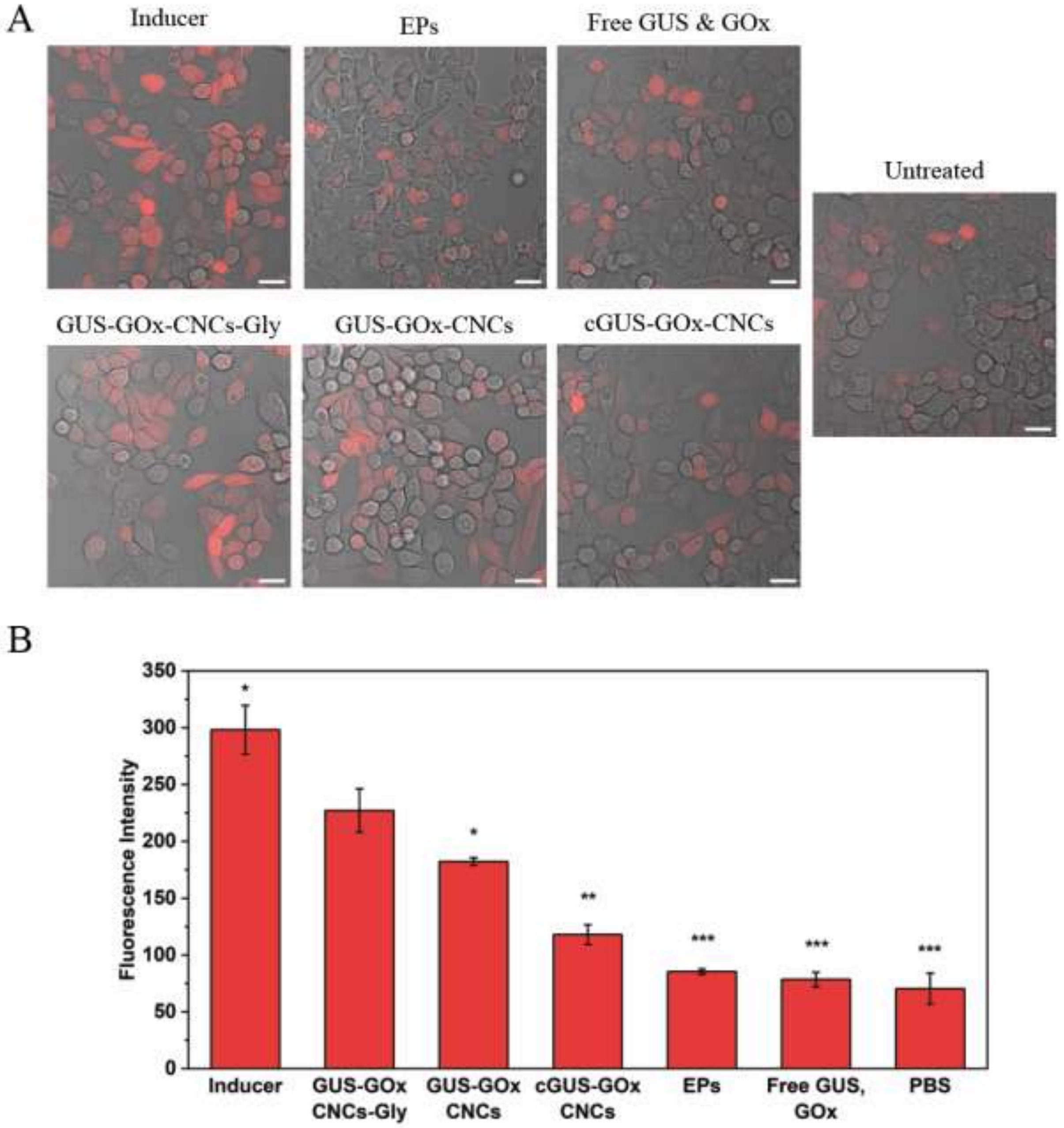

Figure 5.13. *Intracellular ROS levels in HepG2 cells. (A) CLSM micrographs of 2',7'-dichlorodihydrofluorescein diacetate incubated cells. Red: ROS species, DCF. Scale bar: 20 µm. (B) Total fluorescence intensity of DCF as analyzed by CLSM micrographs. Asterisks: statistical significance between GUS-GOx-CNCs-Gly and the corresponding column. Graph shows mean ± s.d. of three micrographs.*

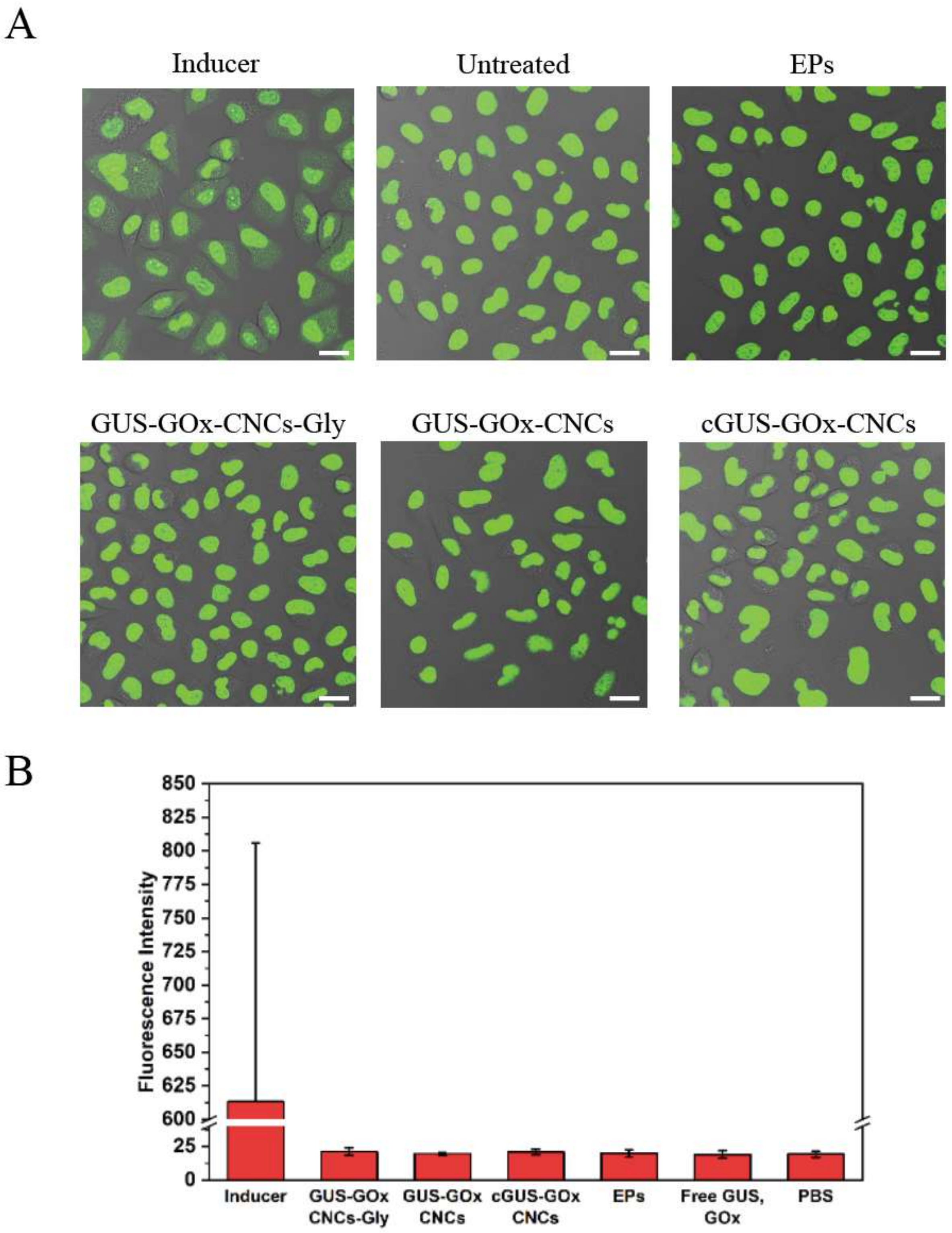

Figure 5.14. *Intracellular ROS levels in HeLa S3 H2B-GFP cells (A) CLSM micrographs of 2',7'-dichlorodihydrofluorescein diacetate incubated cells. Green in cytoplasm: ROS species, DCF. Scale bar: 20 µm. (B) Total fluorescence intensity of DCF as analyzed by CLSM micrographs. Graph shows mean ± s.d. of three micrographs.*

The synergistic potential of hymecromone in combination with sorafenib has been well investigated, revealing effects such as decreasing cell proliferation and motility, and inducing apoptosis and capillary formation in tumors.[297] However, the synergy of hymecromone with H_2O_2 has not yet been explored. To investigate how the simultaneous production of intracellular hymecromone and H_2O_2 by our CNCs influences cell viability, MTS cell proliferation assays were performed (**Figure 5.15**). First, the incubation effects of the CNCs, empty polymersomes, glycooligomer and enzymes on cell viability after 24 h were examined (**Figure 5.15A**, **B**). GUS-GOx-CNCs, empty polymersomes, glycooligomer and free GUS or GOx were not cytotoxic as displayed by the lack of negative impact on the viability of HepG2 and HeLa S3 H2B-GFP cells. Subsequently, we investigated the synergistic effect of hymecromone and H_2O_2 production on cell viability. To note, glucose was constant in our experiments, as it is a necessary component of the cell culture medium and supports the mimicking of the glucose-rich tumor microenvironment.[298] To investigate the potential synergy, we controlled the providing of 4-MUG. No significant decrease in cell viability was observed for the cells incubated with GUS-GOx-CNCs and non-permeabilized CNCs regardless of 4-MUG addition, indicating limited cellular uptake, lack of intracellular hymecromone production and significantly lower ROS levels (**Figure 5.10**; **Figure 5.12-5.14**, **Figure 5.15C**). Similarly, cells incubated with free GUS and GOx presented no decreased viability, associated with low intracellular ROS and hymecromone amounts (**Figure 5.15C**). The highest decrease (85% ± 15%) was observed in HepG2 cells incubated with GUS-GOx-CNCs-Gly and 4-MUG. Importantly, cells incubated with GUS-GOx-CNCs-Gly but without 4-MUG addition, showed 37% ± 21% reduction in cell viability which is attributed to the intracellularly produced H_2O_2. It is noteworthy that cells incubated with 190 μM hymecromone, experienced only 27% ± 3% decrease in viability, which is in accordance to previous studies investigating the antitumoral effects of hymecromone (see **Figure 10.18** in *Appendix*).[231,299] In combination, these results highlight two main aspects of our glycooligomer-functionalized nanosystem: the crucial role of the glycooligomer unit in enhancing cellular uptake in HepG2 cells and the subsequent synergistic effect of the bioorthogonally generated hymecromone and H_2O_2 on cell viability. On the contrary, HeLa S3 H2B-GFP cells exhibited no significant decrease in viability when incubated with differently loaded nanocompartments or free enzymes, regardless of 4-MUG addition (**Figure 5.15D**). The low cytotoxicity in HeLa S3 H2B-GFP is in agreement with the cell uptake assays and intracellular hymecromone and H_2O_2 production in this cell line. These results further underline the importance of the glycooligomer unit in the efficient, cell-specific uptake and the resulting cytotoxic effects of our catalytic nanocompartments.

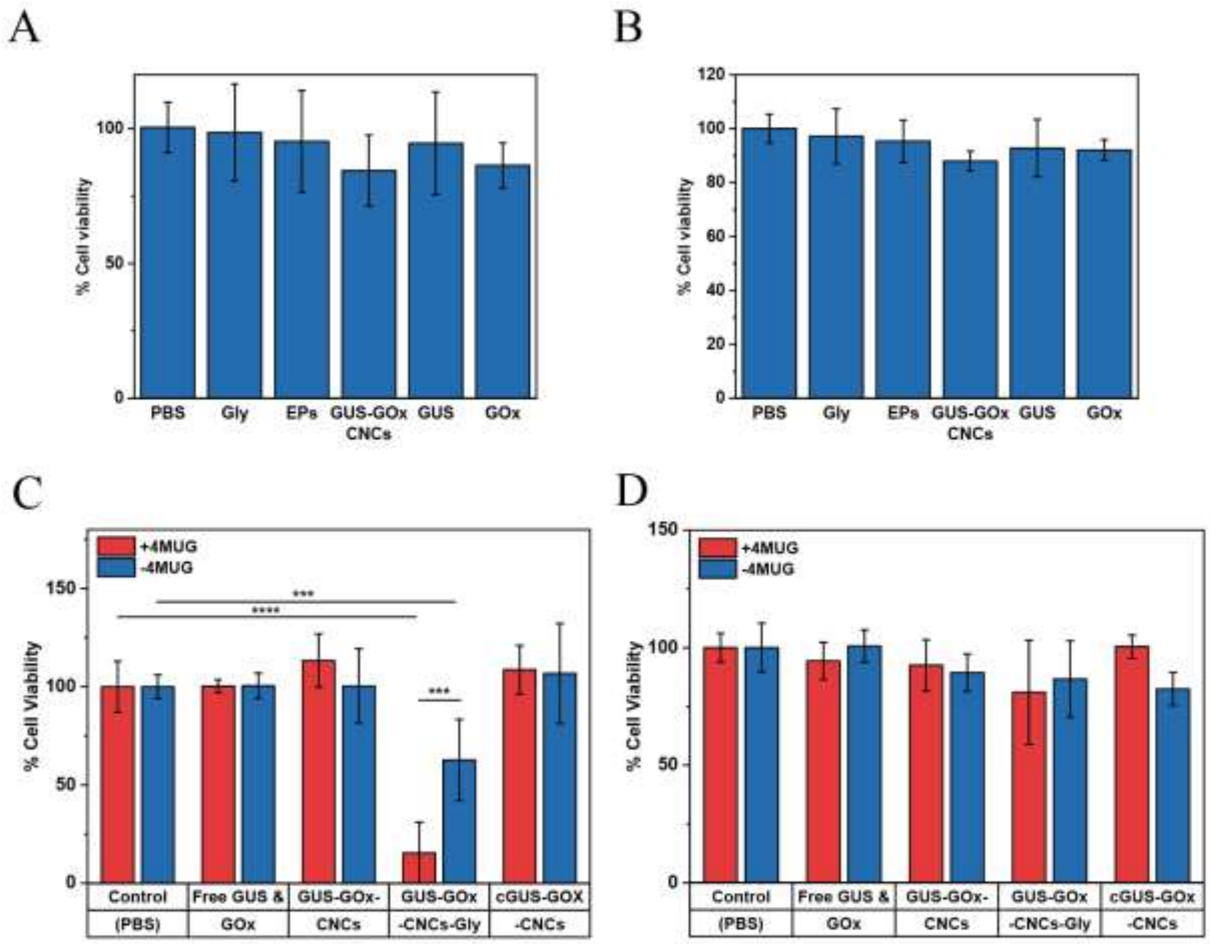

Figure 5.15. Cell viability of HepG2 and HeLa S3 H2B-GFP cells. Cell viability as percentage of (A) HepG2 and (B) HeLa S3 H2B-GFP cells incubated with only PBS (control), glycooligomer, empty polymersomes, GUS-GOx-CNCs, GUS or GOx. Graph shows mean ± s.d. of six repetitions. Cell viability as percentage of (C) HepG2 and (D) HeLa S3 H2B-GFP cells. Graph shows mean ± s.d. of 3 experiments.

5.3 Conclusions

Our study introduces a novel concept of multifunctional catalytic nanocompartments to produce a synergistic effect with controlled localization at the target site. The exemplary catalytic nanocompartments efficiently catalyze two independent reactions in parallel through co-encapsulation of two enzymes, β-glucuronidase and glucose oxidase, which simultaneously produce the cytotoxic drug hymecromone from its glucuronide conjugate and H_2O_2 through glucose consumption, respectively. The selective cell internalization in HepG2 is driven by the glycooligomer functionalization of the compartments, serving the interaction with the overexpressed mannose-binding receptors. The synergistic effect of hymecromone and H_2O_2 resulted in a significant reduction of HepG2 cell viability. Together, targeted and multifunctional compartments combining bioorthogonal reactions – such as drug production and cell starvation – provide optimal response. The promise of our nanosystem lies in its potential to refine enzyme-based therapeutic approaches, offering more effective outcomes through the convergence of parallel production of desired compounds. For example, in a clinical setting, an elicited synergistic effect by the simultaneous production of hymecromone and H_2O_2 could further support the inhibition of e.g. pancreatic or ovarian cancer growth, where hymecromone has exhibited its anticancer properties. This study sets the stage for further exploration and development of such nanosystems, contributing to the ongoing demand for innovative therapeutic strategies. This means that by carefully selecting the produced drug that is paired with H_2O_2, a synergistic effect suitable for combating other types of malignancies could be achieved. In our example, we focused on combinatorial cancer therapy, but the versatility and potential modifiability of this platform further inspires and supports the use of such nanocompartments in other therapies and applications. For instance, the parallel generation of a traceable and a therapeutic compound could introduce our nanocompartments in the field of theranostics, while the choice of other types of glycooligomers could target them in new biolocations.

6. Artificial Organelles for Mimicking Inter- and Intra-Cell Communication in a Photoreceptor Mimic

Exploring inter- and intracellular signaling pathways in synthetic biology, this study presents the example of integrating of Ca^{2+}-sensitive, photoresponsive and catalytic artificial organelles (AOs) within giant unilamellar vesicles (GUVs) to build photoreceptor mimics. With the strategic optimization, generation and spatial separation of the artificial organelles, we demonstrate inter- and intracellular communication across different artificial cells (ACs), mimicking natural photoreceptors. We further highlight the sensitivity modulation of our system by the addition of extracellular messengers, closely emulating one of the characteristic functions of photoreceptive synapses. Our findings broaden the understanding of cell-cell communication mechanisms, providing a new perspective on the intricacies of intracellular signaling. This breakthrough offers potential applications in developing advanced synthetic biology tools and studying abstracted cellular signaling pathways, significantly contributing to our knowledge of cellular communication and signaling dynamics. Meanwhile, the versatility of the platform enables the vision of their use in a broader spectrum of models and applications.

This study is submitted: Heuberger, L.,* ***Korpidou, M.****, *et.al. * these authors contributed equally. Parts of this chapter also appear in the PhD thesis of Lukas Heuberger (University of Basel)*

6.1 Introduction

Inter- and intracellular signaling pathways belong to the core of how cells receive, transmit and process signals from their environment.[300,301] Depending on the nature of the signal, a number of organelles are involved with a variety of characteristics and functionalities. Organelles often have a key role not only in internal signal transduction and subsequent cell reaction, but also in exchange of information between cell populations for a coordinated behavior. The bottom-up design of synthetic (sub-compartmentalized) cellular models provides the means to study and understand the complex underlying principles of inter- and intracellular communication networks.[240,302,303] While artificial cells mimicking cellular processes such as protein production, or DNA- and self-replication,[304,305] have been engineered, models for intra- and even more intercellular communication and signal transduction are still sparse.[94,120,240,306–308] One of the reasons for this shortcoming includes the complexity of building hierarchically compartmentalized ACs, i.e. artificial organelles loaded in ACs together with the limited permeability of artificial membranes and the absence of suitable communication channels.

Most of the artificial cells that have been engineered to date encapsulate a variety of biomolecules in their inner cavity.[309,310] GUVs (1-100 µm in diameter) can be used as mimics of natural cells both in size and membrane structure and are often assembled from lipids, peptides or amphiphilic block copolymers.[26,309] Although such systems contribute to a better understanding of simple cellular processes, more complex ones cannot be mimicked due to the absence of cell-mimetic organization and structures, i.e. organelles. Therefore, encapsulation of AOs with distinct functionalities in ACs results in models that more closely mimic natural processes. Particularly in communication and signaling, signaling molecules must be able to transmit information between AOs and/or between ACs and their diffusion can be facilitated by permeabilized boundaries, i.e. membrane pores,[311–313] membrane proteins,[314–316] or pore-forming peptides.[50,317,318]

Here, we follow a bottom-up strategy for developing an AO-compartmentalized photoreceptive model and explore its competence to execute complex inter- and intracellular signaling cascades in response to multiple external stimuli (**Figure 6.1**). This exemplary model aims to serve as a proof of concept and blueprint of engineering polymer-based, subcompartmentalized ACs for a variety of applications and natural-processes mimics. First, we present the detailed design, formation and optimization of AOs and thoroughly investigate their activity in solution. In particular, chemo- and photoresponsive AOs are capable of sensing Ca^{2+} ions and release signaling molecules upon a light cue, respectively. In nature, light is the activator of photoreceptors, while Ca^{2+} in the outer segment controls photoreceptor light adaptation and at the synaptic terminal is an important modulator of downstream signaling.[319] Next, we proceed with increasing the level of complexity of our intracellular signaling model by utilizing photoresponsive AOs to activate a signaling cascade, beginning with the release of a substrate from their cavity and its subsequent processing by catalytic AOs. Such a response exemplifies rod and cone cells below the pigment epithelium of the eye, where a series of signal transduction reactions upon light exposure are performed.[320] Although artificial, lipid-based nanovesicles embedded with photoreceptors were previously reported to show specific color sensitivity, they were not further exploited in the context of an artificial communication and signaling model.[321] Our artificial cells and organelles are based on an amphiphilic diblock copolymer, poly(dimethylsiloxane)-*block*-poly(2-methyl-2-oxazoline) (PDMS-*b*-PMOXA), which is known to assemble highly stable nano- and micrometer-sized vesicles that are able to encapsulate a variety of molecules in their aqueous cavity.[26,168,322] Due to the fluidity of PDMS-*b*-PMOXA membranes, the incorporation of native and artificial membrane constituents is facilitated, resulting in increased functionality, permeability and stimulant sensitivity of the vesicles.[69,95,169,259] Artificial organelles of defined size (0.1-1 µm) that mimic naturally occurring organelles were created through film rehydration and subsequently extruded,[26] while ACs with a high-throughput microfluidic setup.[32,318,323–326]

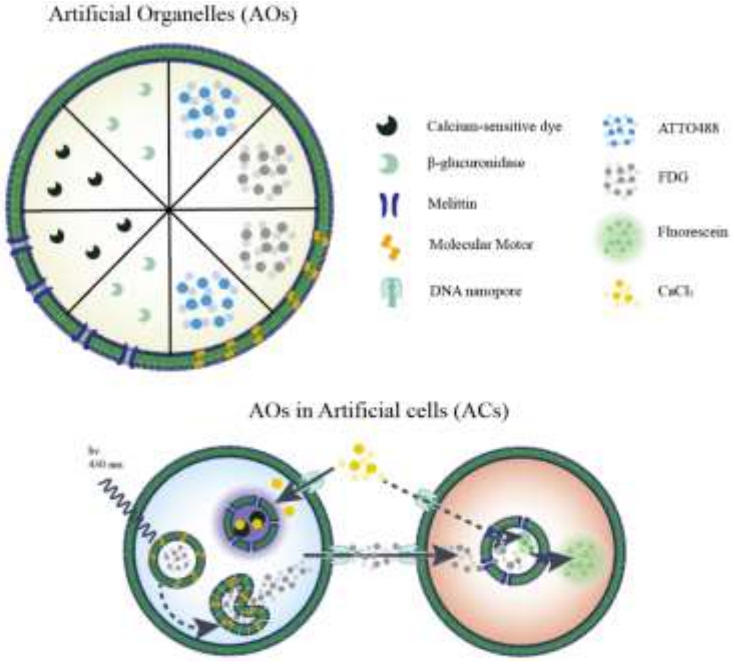

Figure 6.1. *Schematic of the design of artificial organelles for inter- and intra-cellular communication, integrated in photoreceptive mimics.*

Finally, we present our engineered AO-encapsulating photoreceptors and artificial retinal synapse.[327] We established a cell-cell communication pathway by spatially separating substrate-releasing and catalytic AOs across distinct cells. By incorporating both photoresponsive and calcium-responsive AOs within a single AC, our model demonstrates dual sensitivity to Ca^{2+} and light. Importantly, an imitation of the outer segment of native photoreceptive cells was achieved, by modulating the downstream signaling response with varying environmental calcium levels.[319] Based on the modifiability and versatility of our proposed platform, AOs and ACs with a variety of functionalities, and their combinations will enable the generation of a number of different models and support the expansion of the field of bottom-up, synthetic biology.

6.2 Results and Discussion

6.2.1 Formation, characterization and integration of AOs in ACs

For determining and optimizing AO encapsulation for creating hierarchical ACs (see **Figure 10.19** in *Appendix*), models of nanometer-sized AOs encapsulating the fluorescent dye Atto488 (AO_A488) were created by drying a thin layer of $PDMS_{25}$-*b*-$PMOXA_{10}$ copolymer and rehydrating overnight with an aqueous solution containing the fluorescent dye. Subsequent extrusion reduced the diameter of the resulting AOs to approximately 182 ± 59 nm as determined by dynamic light scattering (DLS) and 192 ± 39 nm by nanoparticle tracking analysis (NTA) (**Figure 6.2A**, **B**). The radius of gyration (R_g, 104 ± 3 nm) was calculated by SLS and the hydrodynamic radius (R_h, 100 ± 5 nm) using the DLS profile (**Figure 6.2C**). The shape parameter ρ (R_g/R_h) was determined to be approximately 1, which is typical for the morphology of hollow spheres.[169,212] To create AO_A488-bearing ACs, AO_A488 were added to the IA phase in various dilutions (1:10 – 1:1000, see **Figure 10.20**, **Table 10.8** in *Appendix*). Even at the highest AO concentration, AO_A488 were distributed evenly, retained their structural integrity and were not found to interact with the membrane, as analyzed by 3D AC reconstructions (see **Figure 10.21** in *Appendix*).

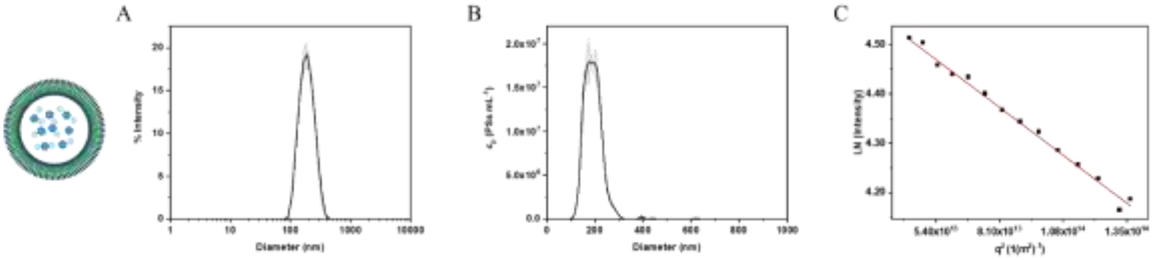

Figure 6.2. *Characterization of AO_A488. (A) Size distribution of AO_A488 measured by DLS. (B) Determination of the size and respective concentration of AO_A488 by NTA. (C) SLS data of AO_A488 and linear fit to the Guinier equation.*

Further investigations on the motion of AO_A488 in solution and in ACs were performed using fluorescence correlation spectroscopy (FCS) (**Figure 6.3A**, **B**). Comparison of the diffusion times (τ_D) of AO_A488 before and after encapsulation confirmed that neither the buffer composition nor the confinement affected AO diffusion and no AO aggregation was observed inside ACs (**Figure 6.3A**). The increasing correlation *G(τ)* was a consequence of the number of AO_A488 in the cavity of ACs and inversely proportional to their concentration (**Figure 6.3B**). FCS measurements in the extravesicular environment of the ACs showed no diffusion times corresponding to AO_A488, indicating the high stability of the ACs, as no AOs were released from the GUVs.

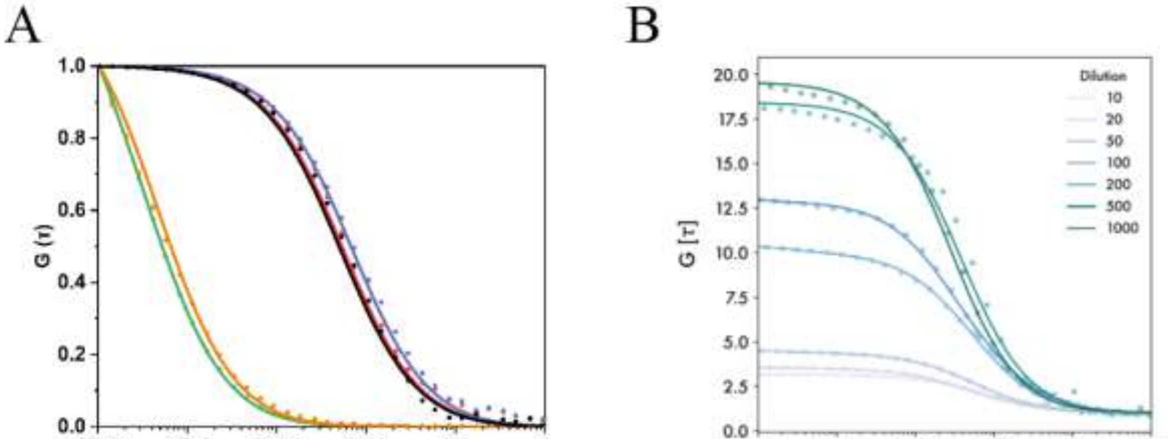

Figure 6.3. *Encapsulation of AO_Atto488 in protocells.Normalized FCS autocorrelation curves of free Atto488 (green, τ_D = 37 ± 3 µs), AO_Atto488 in PBS (red, τ_D = 5558 ± 1558 µs), AO_Atto488 in IA (black, τ_D = 5158 ± 1056 µs), AO_Atto488 in GUV's cavity (blue, τ_D = 4573 ± 1918 µs) and in extravesicular environment (orange, τ_D = 47 ± 10 µs). (B) FCS autocorrelation curves for AO_A488 encapsulated in the cavity of artificial cells at different concentrations. Symbols represent raw data and solid lines represent fitted curves.*

6.2.2 AOs and response to chemical signals

Calcium is an important second messenger in cells and, intracellularly, it is mostly stored in small vesicles, such as lysosomes.[328–330] In photoreceptive cells, calcium ions (Ca^{2+}) have multiple roles spreading from detection, transduction and synaptic transfer of light stimuli to control of the gain in the outer segment of the photoreceptor.[319] AOs were generated with Ca^{2+} detection ability by encapsulating CalciumGreen™-5N (CaGreen), whose fluorescence increases upon binding to Ca^{2+}, and permeabilized with the pore-forming peptide melittin (AO_mel_CaGreen).[50,169] By DLS measurements, their diameter was calculated at 170 ± 42 nm and by NTA at 157 ± 29 nm (**Figure 6.4A**, **B**). By SLS measurements, the R_g was calculated at 91 ± 3 nm and the R_h at 88 ± 3 nm ($\rho = 1$, **Figure 6.4C**). The number of melittin pores was estimated to be 43 ± 1 per AO by FCS measurements on AOs prepared with Cy5-labeled melittin (**Figure 6.5A**). The diameter of non-permeabilized control AOs (AO_CaGreen) was calculated at 169 ± 49 nm by DLS and 157 ± 30 nm by NTA (**Figure 6.4D**, **E**). The R_g was found at 91 ± 3 nm and the at R_h 89 ± 9 nm ($\rho = 1$, **Figure 6.4F**). AO_mel_CaGreen and AO_CaGreen were first analyzed in bulk for their permeability to Ca^{2+} ions and subsequent sensing of Ca^{2+} by CaGreen using FCS. With increasing $CaCl_2$ concentration, the fluorescence intensity of AO_mel_CaGreen (τ_D = 4663 ± 173 µs, **Figure 6.5B**) increased 2-4-fold, indicating the diffusion of Ca^{2+} through the melittin pores (**Figure 6.5C**). The minimal detectable Ca^{2+} concentration of 10 µM was in the range of naturally occurring Ca^{2+} concentrations in lysosomes.[331] By analyzing the AO_mel_CaGreen with FCS, diffusion times of a second component corresponding to free CaGreen (τ_D = 33 ± 1 µs) were not detected, confirming that the dye was too big to diffuse through the melittin pores (1192.2 Da, **Figure 6.5B**).[332]

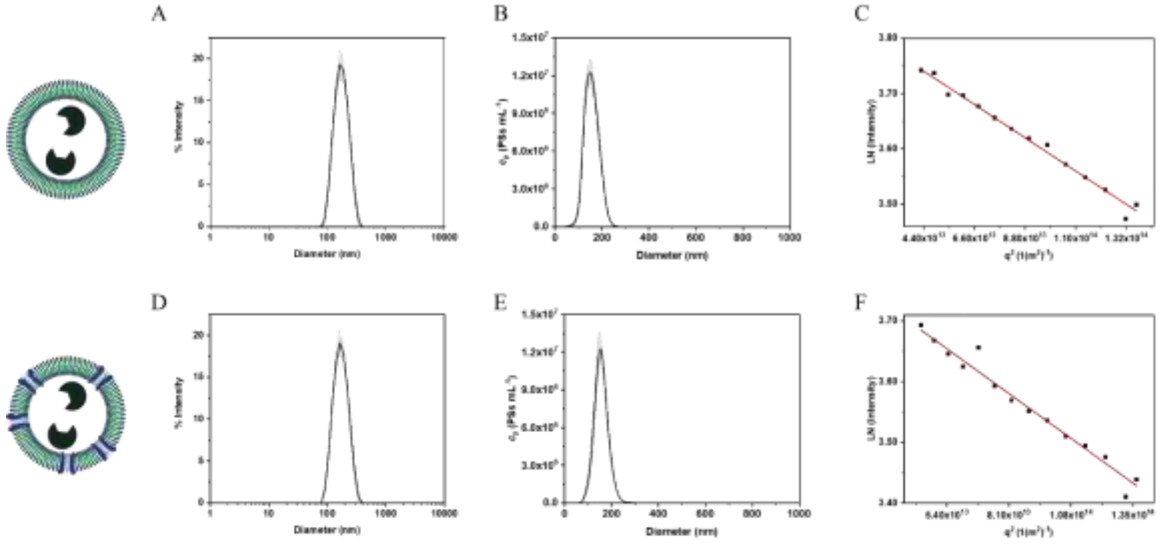

Figure 6.4. *Characterization of AO_CaGreen and AO_mel_CaGreen. Size distribution of (A) AO_CaGreen and (D) AO_mel_CaGreen measured by DLS. Determination of the size and respective concentration of (B) AO_CaGreen and (E) AO_mel_CaGreen by NTA. SLS data of (C) AO_CaGreen and (F) AO_mel_CaGreen and linear fit to the Guinier equation.*

We then proceeded with creating our first signaling cell mimic by encapsulating approximately ~ 10^3 AO_mel_CaGreen per protocell, emulating the role of lysosomes as a major regulator of Ca^{2+} as a primary messenger signal. Ionomycin facilitated the transport of Ca^{2+} across the AC membrane (see **Figure 10.22A** in *Appendix*) and melittin across the AO membrane, leading to a 2.5-fold increase in CaGreen fluorescence of AOs when 1 mM $CaCl_2$ was added in the extravesicular environment (see **Figure 10.22B** in *Appendix*). Although lacking melittin pores, a slight increase in fluorescence of AO_CaGreen in ACs was observed, but significantly less than of AO_mel_CaGreen. This can be attributed to the fact that the membranes of artificial cells and organelles were made from the same $PDMS_{25}$-*b*-$PMOXA_{10}$ copolymer and ionomycin is rendered hydrophobic when complexed with Ca^{2+} ions. Therefore, upon contact, it would be possible that membrane fractions or ionomycin-Ca^{2+} complexes were transferred between AOs and ACs.

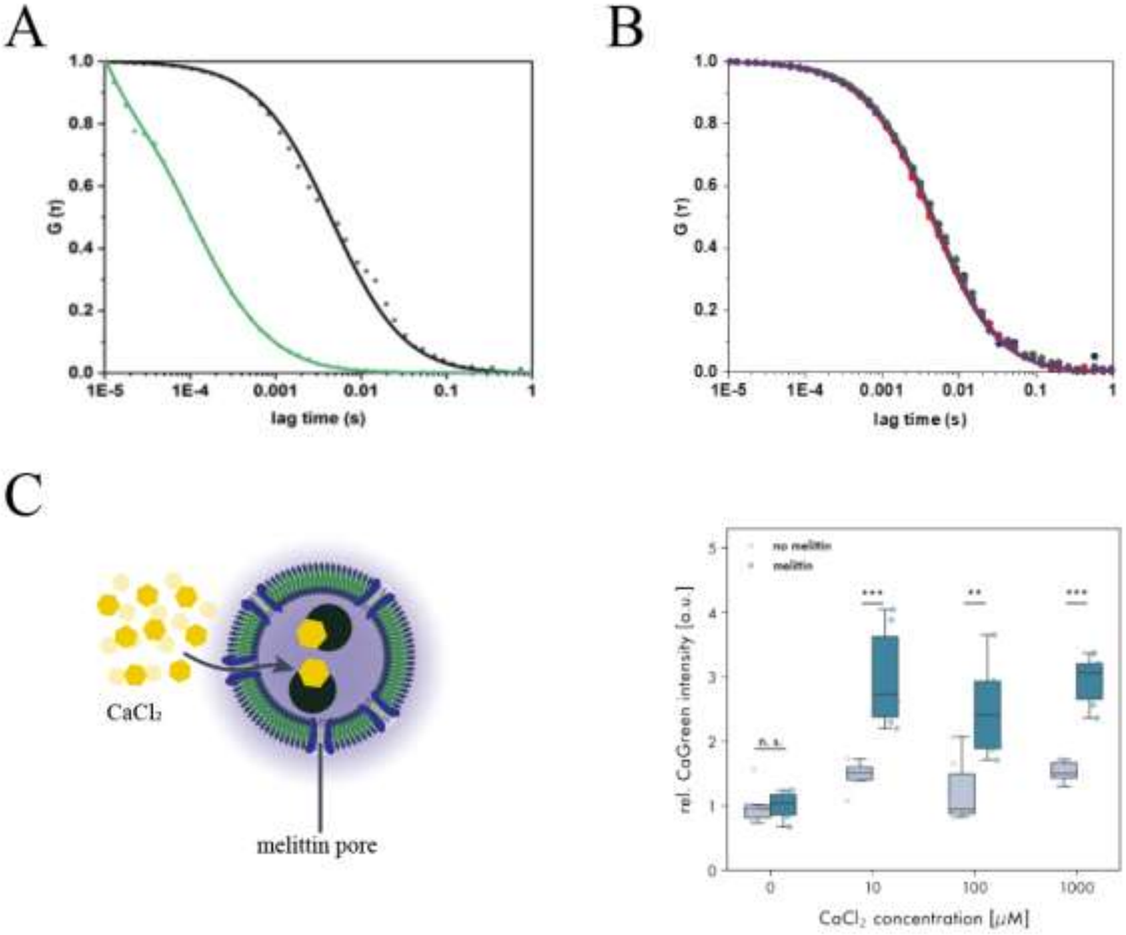

Figure 6.5. *Response to calcium signals by AOs. Normalized FCS autocorrelation curves of (A) free Cy5-melittin (green, τ_D = 500 µs) and AO_Cy5-melittin (10 µM initial melittin concentration, black, τ_D = 4500 µs) and (B) AO_mel_CaGreen with 0 (blue, τ_D = 4365 µs), 10 (green, τ_D = 4785 µs), 100 (red, τ_D = 4725 µs) and 1000 µM $CaCl_2$ (purple, τ_D = 4777 µs). Symbols: raw data, Lines: fitted curves. Due to similar τ_D, lines and symbols overlap. (C) Normalized CaGreen fluorescence inside AOs measured by FCS upon addition of 0-1000 µM $CaCl_2$ (n=6). (n>5 per condition) Significance levels: $p > 0.05$ (n.s.), $p < 0.05$ (*), $p < 0.005$ (**), and $p < 0.0005$ (***).*

6.2.3 AOs and response to light cues

Achieving controlled release of encapsulated compounds from AOs is a key aspect in the development of artificial cell communication. Thus, we first optimized the formation of light-responsive AOs, using Atto488 encapsulated in AOs with a synthetic dibromo molecular motor (MM) incorporated in the hydrophobic part of their membrane (AO_MM_A488).[259] Their diameter was measured at 191 ± 67 nm by DLS and 173 ± 36 nm by NTA (**Figure 6.6A**, **B**). The R_g was found at 103 ± 15 nm and the R_h at 101 ± 16 nm (ρ = 1, **Figure 6.6C**).

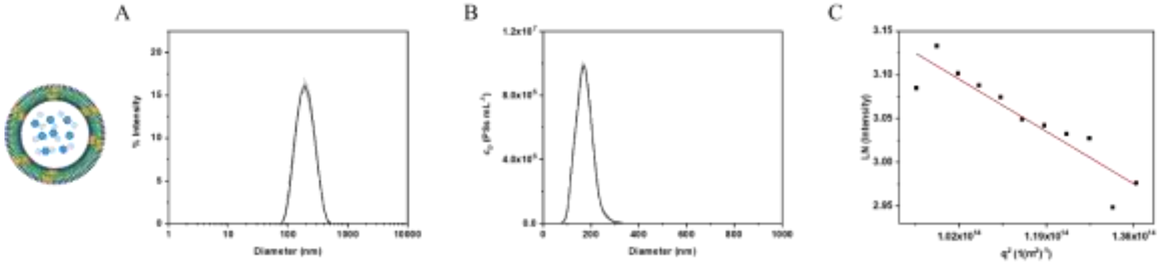

Figure 6.6. *Characterization of AO_MM_A488. (A) Size distribution of AO_MM_A488 measured by DLS. (B) Determination of the size and respective concentration of AO_MM_A488 by NTA. (C) SLS data of AO_MM_A488 and linear fit to the Guinier equation.*

Next, we established and optimized light-mediated cargo release from AO_MM_A488. The MM is able to rotate when irradiated with light at 430 nm.[259] It has recently been shown that light-induced MM rotation leads to membrane rupture and a release of cargo from the AO cavity.[259] The successful insertion of MM into our AOs was demonstrated by UV/Vis spectroscopy of empty AO_MM (see **Figure 10.23A**, **B** in *Appendix*). The spectral changes observed for the MM peak (λ_{max} = 405 nm) confirmed the successful photochemical E-Z isomerization and thus the rotation of the MM within the AOs (see **Figure 10.23C**, **D** in *Appendix*). The quantum yield of photoisomerization was reduced by half for integrated MM compared to free MM, while the rotation speed of the integrated MM increased 1.4-fold due to the shielding effect of the hydrophobic AO membrane domain (see **Figure 10.24**, **Table 10.9** in *Appendix*).[333] The release of cargo was evaluated by the release of Atto488 from AOs_MM_A488 in response to irradiation (λ = 430 nm) for up to 20 min. A ~ 15-fold increase in fluorescence intensity was observed after 10 minutes of irradiation for free AO_MM_488 (**Figure 6.7**). AOs without MM (AO_A488) were stable regardless of the irradiation conditions and did not release their cargo.[259] A similar release profile by AO_MM_A488 in ACs was observed after ~ 10 min of light exposure (see **Figure 10.25** in *Appendix*). However, the relative fluorescence increase was lower compared to free AO_MM_488, due to the lower relative concentration of AOs (~ 6.7 ± 1.2 x 10^9 AO AC^{-1}).

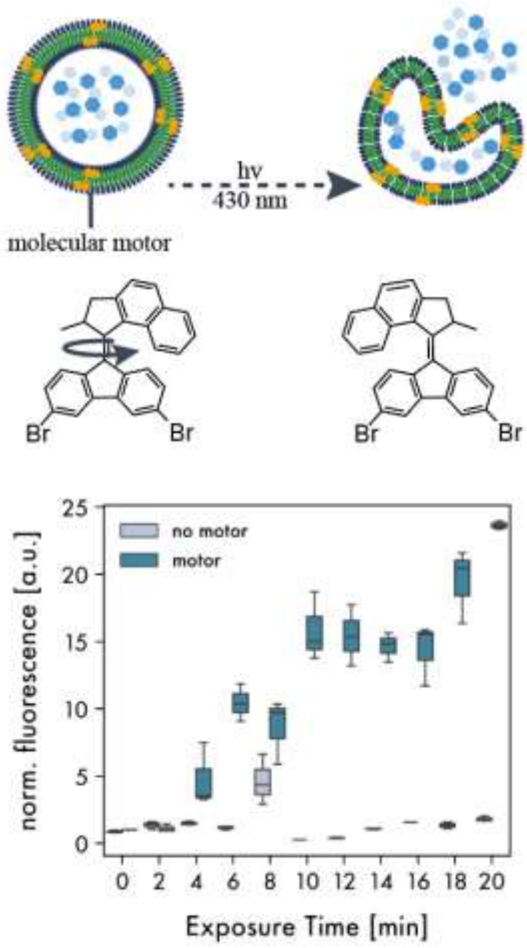

Figure 6.7. *Response to light triggers and cargo release by AOs. Schematic representation of stimuli responsive AOs containing molecular motors in their membranes. Upon illumination with light (hv) at 430 nm, the molecular motors rotate, thereby destabilizing the polymer membrane and releasing the cargo from the AO lumen. Release of ATTO488 dye from the AO lumen upon exposure at 430 nm. Fluorescence measured from fluorescence micrographs (n=3 samples per condition).*

6.2.4 Intra- and inter-cellular signaling pathway mimics facilitated by AOs

Light signal in photoreceptive cells results in a complex network of signaling cascades.[334] In order to closely mimic a light-triggered two-compartment intracellular signaling pathway, precisely designed artificial organelles (AO_MM_FDG, AO_mel_βGal) were engineered. Upon light activation, the released, non-fluorescent substrate fluorescein-di-β-D-galactopyranoside (FDG) generated downstream signaling when converted to fluorescein by β-galactosidase (βGal) within melittin-permeabilized artificial organelles (AO_mel_βGal). The physicochemical characterization of these AOs revealed diameters of 180 ± 56 nm by DLS for AO_MM_FDG, while for AO_FDG, 192 ± 66 nm (**Figure 6.8A**, **D**). By NTA, their diameters were measured at 177 ± 37 nm and 190 ± 38 nm, respectively (**Figure 6.8B**, **D**). By

SLS, the R_g of AO_MM_FDG was found 101 ± 13 nm and the R_h 99 ± 11 nm (ρ = 1, **Figure 6.8C**), while for AO_FDG, the R_g was 107 ± 11 nm and the R_h 100 ± 5 nm (ρ = 1.1, **Figure 6.8F**).

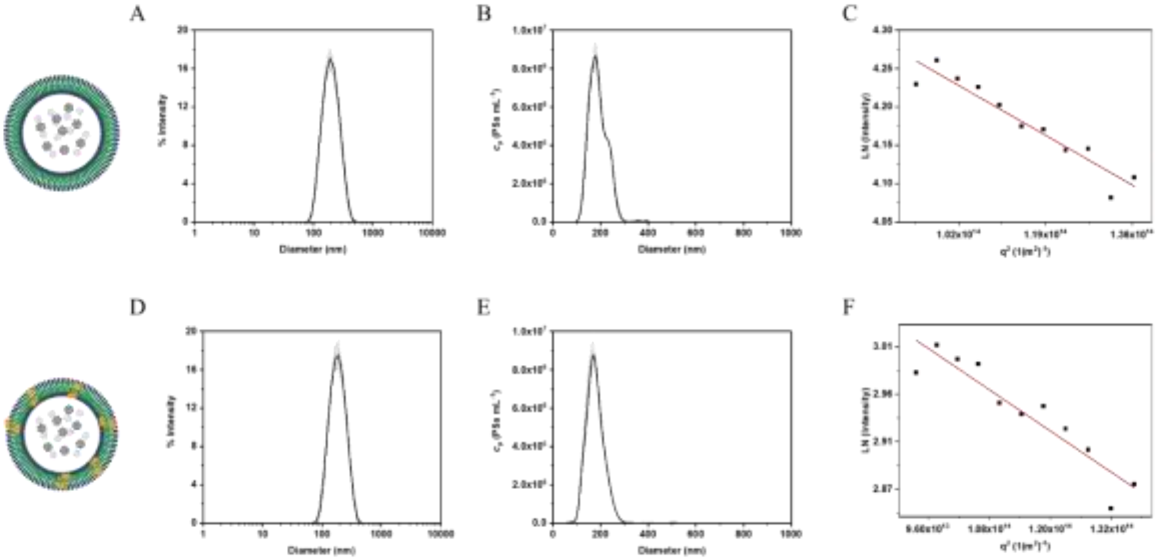

Figure 6.8. *Characterization of AO_FDG and AO_MM_FDG. Size distribution of (A) AO_FDG and (D) AO_MM_FDG measured by DLS. Determination of the size and respective concentration of (B) AO_FDG and (E) AO_MM_FDG by NTA. SLS data of (C) AO_FDG and (F) AO_MM_FDG and linear fit to the Guinier equation.*

For the catalytic AOs, the diameter of AO_mel_βGal was calculated at 179 ± 66 nm by DLS and 177 ± 40 nm by NTA, while for AO_βGal at 143 ± 38 nm and 142 ± 26 nm, respectively (**Figure 6.9A-D**). The R_g of AO_mel_βGal was found 105 ± 3 nm and the R_h 100 ± 5 nm (ρ = 1, **Figure 6.9E**). Meanwhile, the R_g of AO_βGal was found 109 ± 3 nm and the R_h 95 ± 8 nm (ρ = 1.1, **Figure 6.9F**). The number of melittin pores per AO_mel_βGal were 177 ± 37, as calculated by FCS on Cy5-melittin-incorporating AOs (see **Figure 10.26A** in *Appendix*). The encapsulation efficiency of βGal within the AOs' cavities was estimated at 31% ± 17% by the Bicinchoninic acid assay (BCA), which is used for the determination of protein content in a sample (see **Figure 10.26B** in *Appendix*).

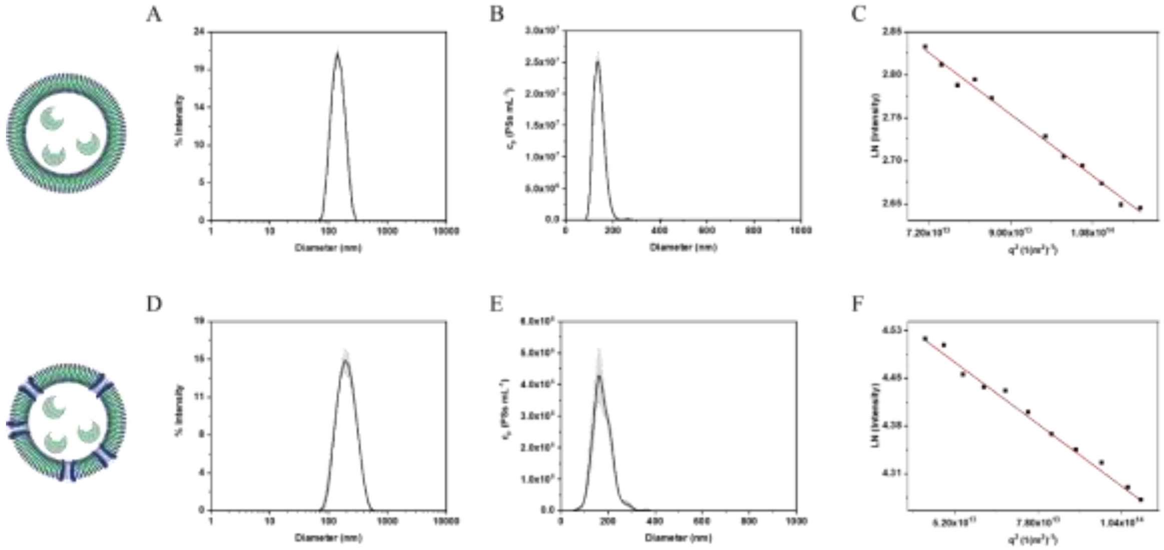

Figure 6.9. *Characterization of AO_βGal and AO_mel_βGal. Size distribution of (A) AO_βGal and (D) AO_mel_βGal measured by DLS. Determination of the size and respective concentration of (B) AO_βGal and (E) AO_mel_βGal by NTA. SLS data of (C) AO_βGal and (F) AO_mel_βGal and linear fit to the Guinier equation.*

In a first bulk experiment comparing the conversion of FDG released by AO_MM_FDG to fluorescein by βGal upon 10-minute irradiation, we observed a slower reaction in βGal encapsulated within artificial organelles (AO_mel_βGal, constant increase over 60 min) compared to its free counterpart (rapid increase within 10 min, **Figure 6.10A**). This difference is attributable to the substrate needing to diffuse through pores into the AO cavity to reach the βGal.[169] As expected, light-mediated disruption of the AO_MM_FDG is the defining point in the production of fluorescein. When the system was not irradiated, FDG was not released in the surrounding environment, making it inaccessible to βGal for catalysis (**Figure 6.10A**). The release of FDG from AO_MM_FDG is also a restricting factor in the overall enzymatic efficiency of the system. When compared to free given FDG, the increase in fluorescence corresponding to fluorescein was similar to FDG released from AO_MM_FDG, but the overall relative fluorescence increase was lower (**Figure 6.10A**, **B**). Control AOs without melittin pores (AO_βGal) and without MM (AO_FDG) showed no catalytic activity owed to the lack of diffusion and release, respectively (**Figure 6.10B**, **C**). These results taken together underscore the critical role of the stimulus-responsive molecular motor in artificial organelles when developing a signaling and communication pathway mimic.

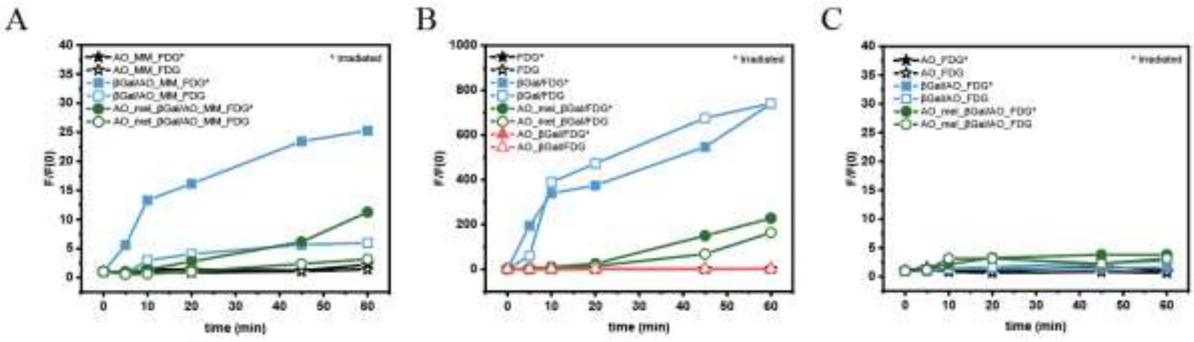

Figure 6.10. Conversion of FDG (25 nM) to fluorescein by βGal (10 U mL^{-1}). (A) Conversion of (A) AO_MM_FDG, (B) free FDG and (C) AO_FDG to fluorescein by βGal. Stars: Absence of catalyst. Filled symbols: FDG, AO_FDG and AO_MM_FDG irradiated for 10 min, 430 nm, RT, PBS, 1 h. Empty symbols: FDG, AO_FDG and AO_MM_FDG not irradiated.

Integrating AO_mel_βGal and AO_MM_FDG in photoreceptive protocells, the emulation of an intracellular, inter-organelle signaling cascade was achieved (see **Figure 10.27A** in *Appendix*). Similar to bulk, AO_MM_FDG released FDG upon illumination, which in turn diffused into AO_mel_βGal. βGal hydrolyzed FDG to fluorescein, resulting in significant increase in fluorescence. No significant fluorescence increase was observed for AO_βGal or AO_FDG (see **Figure 10.27B** in *Appendix*), regardless of illumination. Increasing the complexity of our system, we explored the efficiency seen in nature and in particular, how cells manage multiple signaling pathways. For this purpose, light- and calcium-responsive AOs were combined within a single AC (see **Figure 10.27C** in *Appendix*). The calcium sensitive dye Rhod-5N was used to generate the calcium-sensitive AOs (AO_mel_R5N) to reduce fluorescence spectra overlap of fluorescein and CaGreen. Their diameter was measured at 184 ± 65 nm by DLS, while by NTA at 175 ± 34 nm (**Figure 6.11**), in agreement with the AOs of this study. SLS analysis could not be conducted due to the compatibility of Rhod-5N with the technique.

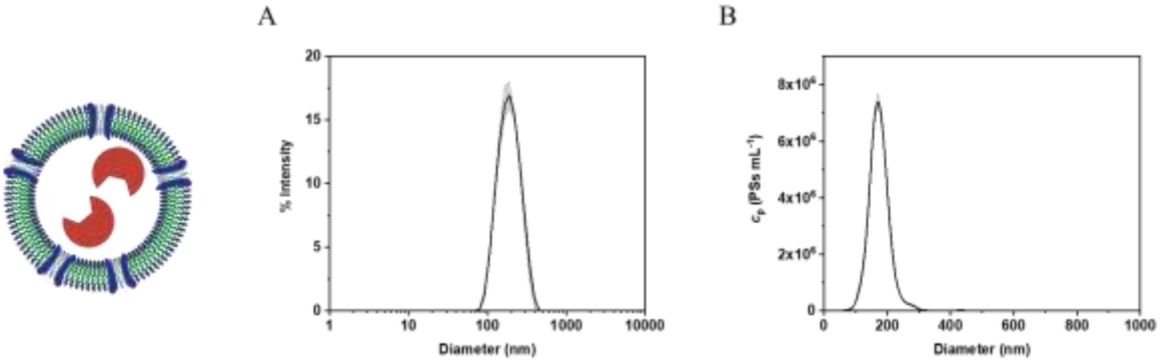

Figure 6.11. *Characterization of AO_mel_R5N. (A) Size distribution measured by DLS. (B) Determination of the size and respective concentration by NTA.*

Rhod-5N and AO_mel_R5N were first investigated for their calcium sensing ability in bulk (**Figure 6.12**). It was observed that the fluorescence corresponding to Rhod-5N was increasing with increasing concentrations of $CaCl_2$ (0 – 1000 μM). Exposure to 1 mM $CaCl_2$ exhibited the highest Rhod-5N fluorescence increase, both for the free dye and AOs, and it was selected for the rest of the study. Next, DNA nanopores (cutoff ~ 50 kDa),[312] replaced ionomycin on the AC bilayer membrane, aiming to expand the range of molecules able to pass, and ACs were coloaded with AO_mel_R5N and light-sensitive AO_MM_FDG. When both 1 mM extravesicular $CaCl_2$ and illumination were present, Rhod-5N fluorescence of AO_mel_R5N exhibited a significant decrease (see **Figure 10.27C** in *Appendix*). In contrast, in the absence of illumination, AO_mel_Rhod-5N fluorescence increased significantly. This is attributed to an increased background fluorescence caused by the released FDG of AO_MM_FDG, modulating the $CaCl_2$-response (see **Figure 10.28** in *Appendix*).

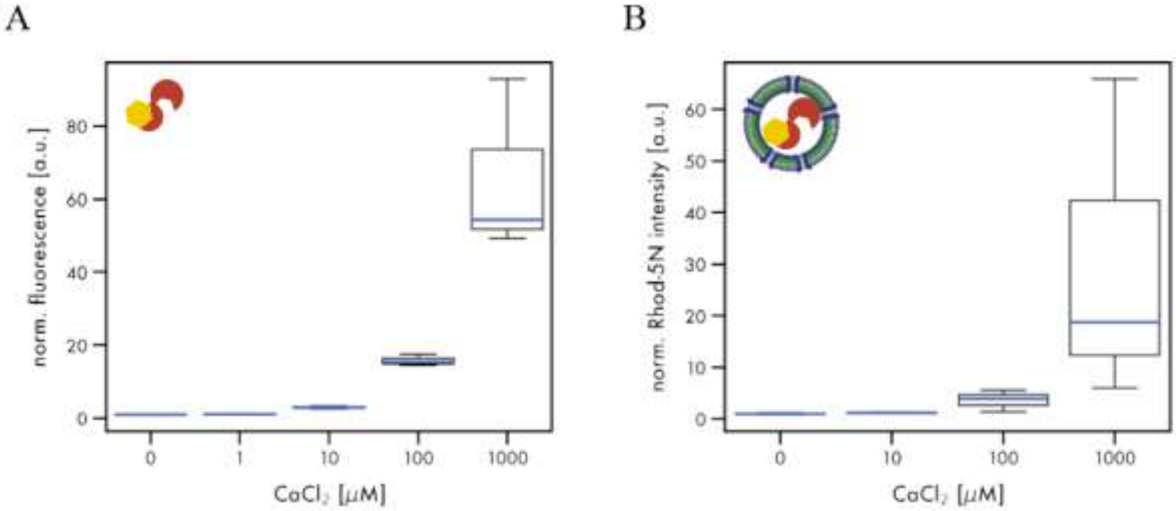

Figure 6.12. *$CaCl_2$ sensitivity of Rhod-5N. Fluorescence changes of (A) free Rhod-5N and (B) AO_mel_R5N in response to increasing $CaCl_2$ concentrations for 1 h.*

We then proceeded with seggregating the AOs in two distinct ACs, emulating a signaling network of a synapse (see **Figure 10.29** in *Appendix*). Sender ACs were equipped with AO_MM_FDG, while receiver ACs with AO_mel_βGal and CF633-Dextran (70 kDa) for distinction (see **Figure 10.29A** in *Appendix*). Intracellular communication facilitated by AOs was established only upon illumination, where released FDG from AO_MM_FDG entered receiver ACs and was catalyzed to fluorescein by encapsulated βGal of AO_mel_βGal (see **Figure 10.29B, C** in *Appendix*). Going a step further and inspired by native rod and cone photoreceptors,[319,335] we introduced Ca^{2+}-responsiveness to the system by adding AO_mel_R5N in the sender ACs (see **Figure 10.30** in *Appendix*). First, we examined the influence of Ca^{2+} on the fluorescence of fluorescein and the activity of βGal (**Figure 6.13**). It was found that with increasing concentrations of $CaCl_2$, the fluorescence of fluorescein was not significantly affected (**Figure 6.13A**). However, the activity of free (**Figure 6.13B**) and encapsulated βGal (**Figure 6.13C**) was decreased in the presence of 1 mM $CaCl_2$ and free FDG. Without $CaCl_2$, the reaction by free βGal took place rapidly and a plateau was observed after 2 h. On the contrary, $CaCl_2$ decelerated the reaction which reached a significantly lower plateau with a 3-fold signal reduction after 3 h. The calculated slopes of the reactions, corresponding to the rate of fluorescein production, revealed the a ~ 5-fold decrease of hydrolysis rate of βGal (**Figure 6.13D**), which is in agreement with the reported effect of calcium and heavy metals on βGal activity.[336–338] Finally, the influence of $CaCl_2$ on the activity of βGal was also demonstrated in the receiver ACs, where a fluorescein signal decrease of approximately 10% was observed (see **Figure 10.30** in *Appendix*). Meanwhile, the changes in Rhod-5N fluorescence of AO_mel_R5N in sender ACs followed the previously observed profile (see **Figure 10.31** in *Appendix*). These results highlight the directional communication between distinct sub-compartmentalized artificial cells with the opportunity for sensitivity modulation.

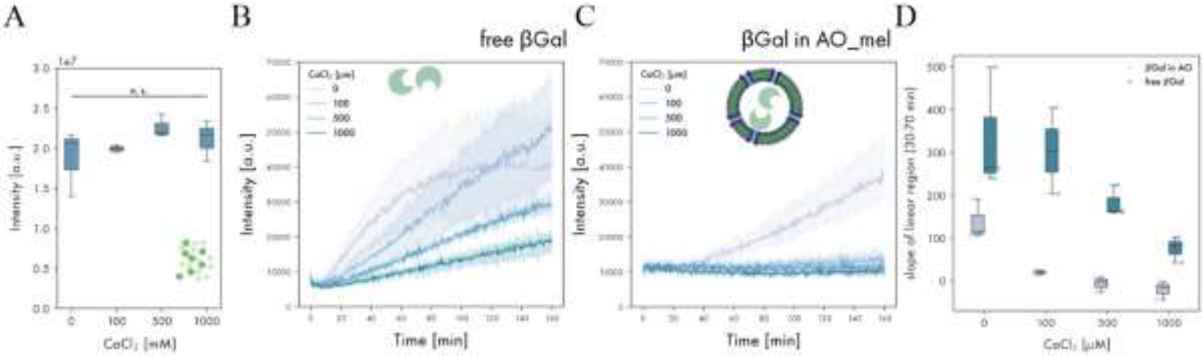

Figure 6.13. *Influence of $CaCl_2$ on Fluorescein Fluorescence and FDG hydrolysis by βGal. Fluorescence of fluorescein with and without 1 mM $CaCl_2$ added. (B, C). Fluorescence increase during hydrolysis of FDG to fluorescein by free βGal (B) or AO_mel_βGal (C) in the presence of different $CaCl_2$ concentrations. (D) Slopes determined for the linear regions of (B) and (C) (between 30 and 70 min).*

6.3 Conclusions

In summary, we engineered artificial organelles and utilized them in bottom-up compartmentalized artificial cells and networks with our example focusing on photo- and chemoresponsive properties. The exemplary artificial organelles were designed, optimized and characterized for their physicochemical properties and multiple functionalities to ensure optimal conditions for AC generation. The compartmentalization of ACs was achieved by the encapsulation of AOs in a controlled manner, allowing for a fine tuning of organelle encapsulation. Functionalization of the artificial membranes through the addition of light-responsive molecular motors, ionophores, or pores facilitated spatiotemporal control over their response and generated a multi-stimuli responsive network by combining functionalities responsive to different external cues. The generated calcium-sensitive protocells utilized the ionophore ionomycin in the cells' membrane and the pore-forming peptide melittin in AOs, while photoresponsive cells were equipped with molecular motor-bearing AOs, that underwent structural changes upon light exposure, thereby releasing the AOs content. The encapsulation of substrate-releasing photoresponsive AOs and enzyme-based catalytic AOs in a single or distinct ACs led to the engineering of inter- and intracellular signaling mimics upon light illumination. The creation of a dual-responsive system with light adaptation features was achieved by adding Ca^{2+}-responsive AOs to the sender cells. With external administration of $CaCl_2$ and light activation, the signal transduction in the receiver cells could be modulated, similarly to natural rod or cone cells. Our prototype has a solid base for safely introducing more components, such as other proteins, stimuli or natural cells to bring it even closer to photoreceptors and photoreceptive synapses. This would not only expand our knowledge on these systems, but also become the platform on which these types of biomaterials are being established in regenerative engineering. Therefore, owing to the modularity of the presented system, the strategy outlined in this work can be utilized in combination with a wide range of artificial organelles and cell mimics possessing various functions, aiming to address a larger scope of applications and fields. For example, the choice of light and calcium as stimuli in the presented work is not restrictive or exhaustive. With the appropriate fine modulations and optimizations, our platform has the potential to support the generation of other element-responsive mimics, e.g. temperature, to create artificial thermoreceptors.

7. Conclusions & Outlook

In this thesis, we engineered different synthetic polymersome-based nanocompartments with hosted synthetic and biological molecules in order to obtain nanosystems with advanced functionalities for biomedical applications. Their adaptability and wide range of utilization was emphasized by generating nanocompartments for counteracting drug metabolism, cancer therapy and as synthetic cell-integrated organelle mimics. The strategies followed for producing these novel nanocompartments can be summarized in: 1. choice of block copolymers that self-assemble easily into polymersomes, while their propertied allow the incorporation of small molecules and proteins in the membrane, 2. functionalization of their outer surface with appropriately selected moieties, 3. selection of stimuli-responsive units, substrates, therapeutic compounds and enzymes with desired activity and 4. co-encapsulation of different enzymes in a single nanocompartment. PDMS-*b*-PMOXA copolymers with short block lengths were chosen for building the synthetic compartments owed to their efficient self-assembly into polymersomes in a wide range of conditions, and allowing functional incorporation of the selected components and biomolecules.

We generated a light-responsive drug delivery system using low-power visible light for activation. By incorporating synthetic rotary molecular motors into the polymer membrane and encapsulating the hydrophilic, FDA-approved drug pemetrexed, our nanosystem exhibited high spatiotemporal control and tunable release profiles in a range of quantities of the light-responsive unit, following sequential irradiation cycles. The responsive nanocarriers efficiently delivered the drug intracellularly and on demand, reducing the cell viability of cancer cells, highlighting its advantages over the free-drug approach. These results represent an unpresented approach in the field of smart drug delivery and pave the way for further advancements. For example, using a library of molecular motors with different activation wavelengths, drugs and testing conditions we can appreciate its applicability, achieve a higher level of control and therapeutic outcome.

Expanding our endeavors, we developed bio-hybrid catalytic nanocompartments for inverting the glucuronidation of a therapeutic compound *in situ*. B-glucuronidase was encapsulated in the aqueous cavity of the nanocompartments, producing the active drug of hymecromone from its glucuronide conjugate. Analysis of the enzymatic kinetics revealed the influence of encapsulation and the importance of membrane permeabilization. This design further highlighted the protective aspect of our nanocompartments, prolonging and enabling the catalytic activity of the enzymes in complex environments and in the cytosol. Our work proposed a new way of counteracting metabolism by locally reverting the glucuronidation of drugs, aiming to extend their half-lives and activity. Varying the selected glucuronides and biological testing conditions, e.g. *in vivo* assessments, further insights and possible applications can be gained.

By a similar catalytic nanocompartment layout, we engineered dual enzyme-loaded nanocompartments decorated with glycooligomers, proposing an innovative strategy in the field of drug synergism. Originating from their surface functionalization with glycooligomer tethers, our nanocompartments showed enhanced, cell-specific internalization and endosomal escape in cells with a high expression profile of mannose-binding receptors. With the careful selection of β-glucuronidase and glucose oxidase as the co-encapsulated enzymes in the cavities, we achieved parallel, bioorthogonal reactions for the simultaneous production of two therapeutically relevant compounds: hymecromone and H_2O_2. We showed that the intracellular, simultaneous catalytic activity of the nanocompartments in function with the targeting ability promoted a cell-specific decreased viability. This is the first time that co-encapsulated enzymes performed parallel enzymatic reactions, achieving a synergistic effect. These results inspire further investigation of our system and its application. For example, we can evaluate a library of glycooligomers with diverse targeting profiles, as well as a combination of enzymes working in parallel. Furthermore, different therapeutic molecules with a variety of potencies can be tested for their production by our system and move our investigating conditions towards *in vivo* evaluation.

Artificial organelles and cells were constructed to form photoreceptor mimics, aiming to expand our knowledge of cellular communication, and signal regulation and transduction. The polymersome-based artificial organelles were equipped with responsive or catalytic molecules, enabling them to react to environmental changes and perform enzymatic reactions with spatiotemporal control. Apart from establishing an intracellular communication model with chemo- and photoresponsiveness, we also mimicked a photoreceptive synapse by strategically segregating artificial organelles in separate cells. We were able to demonstrate the signal transduction between the populations of artificial cells, as well as its regulation by external factors, i.e. calcium. This study offered significant advancements in the field of bottom-up synthetic biology and contributed to better understand naturally-occurring processes. To enhance the complexity of our system, we can generate artificial organelles responding to different stimuli, e.g. temperature or pH and perform various catalytic reactions as a result of the selected enzymes. We can also increase the level of segregation to separate artificial cells, aiming to bring it even closer to the natural analogues and tissue architecture.

In conclusion, the exemplary systems of this thesis corroborated our vision of creating a platform of nanocompartments that its versatility and modifiability has the potential of expanding the cutting-edge technologies for biomedical applications. We particularly chose to highlight how powerful this platform can be by utilizing it not only in enzyme-mediated drug production, but also in drug delivery and bottom-up synthetic biology, emphasizing the wide range of applications of our nanosystem.

8. Materials & Methods

8.1 Chapter 3

8.1.1 Materials

Sepharose® (4B, 45 to 165 µm beads diameter), penicillin, streptomycin, calcein, PEM and Whatman® Nucleopore™ Track-Etched membranes (100 nm) were purchased from Sigma-Aldrich. PBS and fetal bovine serum (FBS) were purchased from BioConcept. Dulbecco's Modified Eagle Medium (DMEM) with GlutaMAX™ was purchased from Gibco Life Sciences. CellTiter 96® AQueous One Solution Cell Proliferation Assay (MTS) was purchased from Invitrogen. Irradiation experiments with λmax = 430 nm were conducted using Lite-On LEDs (six LEDs, 3.5 cm from each other, device dimensions: (13 × 9 × 3.5) cm, Mouser Electronics, 3.4 V, 50 Hz, 0.5 Ampere (AMPS).

8.1.2 Polymersome preparation

Synthesis and characterization of amphiphilic diblock copolymer PDMS-*block*-poly(2-methyl-2-oxazoline) ($PDMS_{25}$-*b*-$PMOXA_{10}$) was described previously.[212]

Polymer vesicles were prepared by thin film hydration method followed by extrusion through polycarbonate pore membranes of desired size (100 nm) and purification by SEC. A $PDMS_{25}$-*b*-$PMOXA_{10}$ solution in EtOH (10 mg mL^{-1}) was mixed with a solution of molecular motors (1 mg mL^{-1}, 25 mol%) in EtOH or the absence of them. The mixed solutions were vortexed and sonicated to ensure the homogeneity of the samples before the solvent was completely removed by evaporation under rotation using a stream of N_2 and 1 h vacuum. The dry films were hydrated with 1 mL PBS buffer, Calcein (20 mM final concentration) or PEM (0.1 mM final concentration) and stirred overnight at 1,200 rpm to generate the polymersomes by self-assembly. The resulting turbid solutions were extruded 21 times using Avanti Mini Extruder (Avanti™) and the corresponding polycarbonate membrane (Avanti™) prewetted in PBS buffer. Purification was performed using Sepharose® 4B (45–165 µm beads diameter). The obtained samples were used within 48 h after purification. During the experimental procedure all setups were protected from light.

8.1.3 Characterization of polymersomes

Light scattering: The size of the vesicles after purification was determined using a Zetasizer Ultra (MAL1255805 serial number, Malvern Panalytical, UK). Samples were measured in PBS buffer, 37 °C, seven attenuations using a disposable ZEN1002 cuvette (Malvern Panalytical) positioned at 4.64 mm from the scattering detector fixed at angle 174.7°.

The shape parameter ρ (R_g/R_h) was obtained by combining dynamic and SLS measures done on a light scattering spectrometer (LS instruments), equipped with a He–Ne 21 mW laser (λ = 632.8 nm) at scattering angles from 30° to 135° at 25 °C. Guinier plots were used for obtaining the radius of gyration (R_g), while the hydrodynamic radius (R_h) was obtained from DLS.

Zeta-potential: Zeta-potential was measured using a Zetasizer Ultra (MAL1255805 serial number, Malvern Panalytical). Samples were diluted in water and added to a disposable folding capillary DTS1070 cuvette. The zeta-potential was recorded after each polyelectrolyte deposition (20 mV).

Nanoparticle Tracking Analysis (NTA): The concentration, volume, and surface area changes of the vesicles were determined using a NanoSight NS 300 instrument (NanoSight Ltd., 488 nm laser). Samples were measured in PBS buffer at room temperature.

UV–VIS absorption: Absorption spectra of the samples were recorded on an Agilent 8453 Ultra Violet - Visible (UV–VIS) Spectroscopy System (Agilent, USA) equipped with a TC1 temperature controller (Quantum Northwest) in a 1-mm quartz cuvette, PBS buffer and 37 °C.

Small-angle X-ray diffraction (SAXS): SAXS analysis was performed at the Multipurpose Instrument for Nanostructure Analysis beamline at the University of Groningen. The diffractometer was equipped with Cu rotating anode (λ = 1.5413 Å) using a sample-to-detector distance of 28.1 cm. The scattering patterns were collected using a Bruker Vantec 500 detector. The scattering angle scale was calibrated using the known position of diffraction rings from a silver behenate standard sample. The scattering intensity curves are reported as a function of the modules of the scattering vector $q = 4\pi/\lambda(\sin \theta)$, with 2θ being the scattering angle and λ the wavelength of the X-rays. The samples were placed in sealed glass capillaries and then measured under vacuum. Polymersomes samples were prepared in MilliQ with a 200 nm diameter size and a total concentration of 5 mg mL^{-1}. Samples containing MM2 were prepared with a concentration of 25 mol% of molecular motor.

Transmission electron microscopy (TEM): Polymersomes aliquots of 5 µL (0.1 mg mL^{-1}) were adsorbed to 400 mesh square copper grids. Excess liquid was blotted and grids were negatively stained with 2% uranyl acetate. All process was performed in the dark. Micrographs of nanostructures were recorded on a Philips CM100 transmission electron microscope at an accelerating voltage of 80 kV. Irradiations were performed right before preparation of the sample.

Cryo-TEM: Polymersomes samples of 2.5 µL (2 mM) were placed on a glow-discharged holy carbon-coated grid (Quantifoil 3.5/1, QUANTIFOIL Micro Tools GmbH). After blotting, the corresponding grid was rapidly frozen in liquid ethane (Vitrobot, FEI) and kept in liquid nitrogen until measurement. The grids were observed with a Gatan model 626 cryostage in a Tecnai T20 Field Electron and Ion Company (FEI) cryo-electron microscope operating at 200 keV. Cryo-TEM images were recorded under low-dose conditions on a slow-scan Charge-Coupled Device (CCD) camera. All processes were performed in the dark. For irradiated samples, the same procedure as described before was carried out in a quartz cuvette immediately before freezing.

8.1.4 Encapsulation/ Insertion efficiencies

Estimation of molecular motor incorporation efficiency: Estimation of molecular motor encapsulation was achieved by using an absorbance standard curve of known concentration values (from 0.1 to 100 µM) of molecular motor at 405 nm. Theoretical absorbance values were calculated for each of the samples as the maximum encapsulation efficiency. Experimental absorbance values were used to estimate the amount of encapsulation.

Estimation of calcein encapsulation efficiency: Estimation of dye encapsulation efficiency was done by taking the absorbance of a calcein 20 mM solution in the same sample conditions at 495 nm as the maximum value. Relative absorbance of the samples at the same wavelength was used to estimate the amount of encapsulated dye.

Estimation of drug encapsulation efficiency: Free drug was run through the SEC column used for the purification of polymersomes. Applying a 280 nm detector, the area under the curve of its peak was calculated employing the UNICORN software. Polymersomes containing the drug were extruded at 100 nm and purified by SEC. The amount of free drug was calculated taking the area under the curve of its peak and by subtracting it from the initial amount, the amount of encapsulated drug in the polymersomes was estimated.

8.1.5 Fluorescence release studies

Polymer vesicles containing calcein solution in PBS were used for fluorescence release studies. Fluorescent release studies were performed in a Spectrofluorometer FS5 (Edinburgh instruments) with excitation 495 nm and emission 515 nm in PBS buffer and room temperature. Fluorescence emission spectra of the calcein-loaded polymersomes were measured before and after 1 min irradiation with 420 nm light. Samples were kept in the dark for 1 h before being measured and irradiated for a maximum of three cycles. Maximum fluorescence was recorded after sonication of the samples with EtOH (1% final concentration) for 15 min. The percentage of calcein release was calculated following the equation (1):

$$\%\, Calcein\, release = 100\frac{(F_t - F_0)}{(F_{max} - F_0)} \tag{1}$$

where F_t is the fluorescence emission at the measured time, F_o is the fluorescence emission prior to any exposure to light and F_{max} is the maximum fluorescence measured after incubation with EtOH.

8.1.6 Cell cultures

A549 cells (lung carcinoma, human; ATCC® CCL-185™) were routinely cultured in DMEM supplemented with 10% FBS, 100 U mL^{-1} penicillin and 100 U mL^{-1} streptomycin. Cells were maintained at 37 °C in a humidified atmosphere containing 5% CO_2.

Cell viability assay: Cell viability was evaluated by CellTiter 96® AQueous One solution cell proliferation assay (MTS). In brief, cells were seeded at a concentration of 3,000 cells per well in a 96-well plate (100 µL). After 24 h, 100 µL of fresh medium containing polymersomes in PBS (0.35 mg mL^{-1}) or PBS was added. The next day, the supernatant was removed, cells were rinsed once with PBS before adding fresh medium (100 µL). For irradiation at 430 nm, 96-well plates were exposed to Lite-On LEDs (six LEDs, 3.5 cm from each other, device dimensions: (13 × 9 × 3.5) cm, Mouser Electronics, 3.4 V, 50 Hz, 0.5 Ampere (AMPS), 430 nm), irradiated for 1 min and were then cultured at 37 °C for another 24 h. The supernatant was removed, and fresh medium (100 µL) was added together with MTS reagent (10 µL) to each well. After 1 h incubation at 37 °C, absorbance was measured at 490 nm using a SpectraMax plate reader. The data were normalized to PBS-treated control cells, irradiated or nonirradiated as indicated, after background absorbance removal. Statistical analysis was performed using OriginPro 2020.

For cell viability studies that did not involve polymersomes, MTS was carried out correspondingly except that after 24 h, 100 µL of fresh medium containing PEM (5 µM), supernatant of irradiated (λ = 430 nm, 1 min) polymersomes containing PEM (5 µM) or PBS was added to each well before 1 min irradiation at 430 nm.

8.1.7 Statistical analysis

Pooled data is presented as mean ± SD unless otherwise indicated. Information regarding sample size, error bars and statistical analysis used is described in each figure legend. P values for statistical analysis of two experimental groups or for multiple comparisons were calculated using OriginLab version 2021. Statistical significance was assessed using unpaired two-tailed t tests. Significance is reported following American Psychological Association (APA) guidelines (*$P \leq 0.05$, **$P \leq 0.01$, ***$P \leq 0.001$, ****$P \leq 0.0001$).

8.2 Chapter 4

8.2.1 Materials

Β-glucuronidase (GUS, *E. coli* Type VII-A), melittin (from honey bee venom), 4-methylumbelliferyl-β-d-glucuronide (4-MUG), proteinase K (from *Tritirachium album*), fluorescent dye Atto647, penicillin, streptomycin, l-glutamine, Sepharose® (4B, 45–165 µm beads diameter), and Whatman® Nucleopore™ Track-Etched membranes (100 nm) were purchased from Sigma-Aldrich (USA). Atto488 *N*-hydroxysuccinimide ester (Atto488 NHS-Ester) was purchased from ATTO-TEC (Germany). Enhanced Pierce bicinchonic acid (BCA) assay, and wheat germ agglutinin – Alexa Fluor™ 555 conjugate were purchased from Thermo Fisher Scientific (USA). Phosphate buffered saline (PBS) and fetal bovine serum (FBS) were purchased from BioConcept (Switzerland). Minimum essential medium and non-essential amino acids (NEAA) were purchased from Gibco Life Sciences (USA). CellTiter 96® AQueous One Solution Cell Proliferation Assay (MTS) and Hoechst 33342 trihydrochloride trihydrate were purchased from Invitrogen (USA).

8.2.2 Nanocompartment preparation

Polymersomes containing enzymes, henceforth termed catalytic nanocompartments (CNCs) and 'empty' polymersomes were prepared using the film rehydration method. In brief, a thin film of $PDMS_{25}$-*b*-$PMOXA_{10}$[212] (5 mg mL^{-1} polymer in EtOH) was formed by rotary evaporation of the solvent (100 rpm at 40 °C, 160 mbar for 45 min). For the preparation of permeabilized CNCs containing GUS (GUS–melCNCs), the polymer film was rehydrated in the dark in PBS (pH 7.2) containing β-glucuronidase (0.4 mg mL^{-1}, 25 kU) and melittin (50 µM), by stirring overnight at room temperature (RT). Polymersomes without melittin pores and enzyme (PSs), melittin-permeabilized polymersomes (melPSs), and CNCs without melittin (GUS–CNCs) were obtained by rehydrating the polymer film with PBS, PBS and melittin, and PBS and β-glucuronidase, respectively. For Atto647-labeled polymersomes (Atto647-PSs), the film was rehydrated with PBS containing Atto647 (0.02 mg mL^{-1}). Following self-assembly, nanocompartments were incubated with proteinase K (0.05 mg mL^{-1}) for 2 h at 37 °C to remove non-encapsulated protein, followed by extrusion (10 times) through a 100 nm Whatman Nuclepore polycarbonate membrane. Size exclusion chromatography (SEC) on a Sepharose® 4B (45–165 µm beads diameter) column equilibrated in PBS was performed for further purification. Nanocompartment suspensions were stored at 4 °C until further use.

8.2.3 Characterization of nanocompartments

Light scattering: Dynamic light scattering (DLS) experiments were performed using a Zetasizer Nano ZSP (Malvern Instruments Ltd., U.K.) at RT. A laser wavelength of 633 nm and a scattering angle of 173° were used. Samples were diluted to a final concentration of 0.3 mg mL^{-1} polymer. Measurements were carried out in triplicate and each measurement consisted of 11 runs.

Static light scattering (SLS) experiments were performed on a light scattering spectrometer (LS instruments, Switzerland), equipped with a He–Ne 21 mW laser (λ = 632.8 nm) at scattering angles from 30° to 135° at 25 °C. The samples were diluted to 0.03 mg mL^{-1} final concentration of polymer in order to reduce multiple scattering. The radius of gyration (R_g) was obtained from the SLS data using Guinier plots, while the hydrodynamic radius (R_h) was obtained from DLS.[339]

Nanoparticle tracking analysis (NTA): Nanoparticle tracking analysis (NTA) was performed using a NanoSight NS 300 instrument (NanoSight Ltd, U.K.) equipped with a 532 nm laser. The samples were diluted to 0.0125 mg mL^{-1} of polymer and applied to the viewing chamber. Three videos of 60 s were captured at RT for each measurement. The NTA software (version 3.4, NanoSight) was used to analyze the movement of nanocompartments based on tracking each particle on a frame-by-frame basis (Brownian motion) in order to obtain their mean and median size, together with the estimated concentration of nanocompartments in solution.

Transmission electron microscopy (TEM): CNCs (5 µL, 0.2 mg mL^{-1}) were adsorbed on 400 mesh copper grids for 1 min, washed with water, and blotted to remove excess liquid. Specimens were negatively stained with uranyl acetate (2%) for 10 sec, washed and blotted. Transmission electron microscopy micrographs were recorded on a Philips CM100 with an accelerating voltage of 80 kV.

Fluorescence correlation spectroscopy (FCS): For labelling GUS with fluorescent dye, the enzyme was incubated in the dark with a 7-fold excess of Atto488 NHS-Ester in dimethylformamide (DMF) for 48 h at 4 °C under stirring conditions. Unconjugated dye was removed by SEC (Sepharose® 4B, 45–165 µm beads diameter) using PBS for equilibration and elution.

For fluorescence correlation spectroscopy, an inverted laser scanning confocal microscope (LSM 880, Carl Zeiss, Germany) with a water immersion objective (Zeiss C/Apochromat, M = 40, NA = 1.2) was used. An Argon laser (wavelength 488 nm) with appropriate filter (MBS 488) was used to excite Atto488. The pinhole size (34 µm, 1 AU) was adjusted before recording FCS curves of the free dye.

For FCS measurements, 20 µL of the free fluorophore, fluorophore labelled-enzyme or polymersomes in PBS (1 : 2 dilution), were placed on a 0.15 mm thick glass coverslip mounted on the microscope stage. Fluorescence signals from free fluorophore, Atto488-labeled enzyme and polymersomes loaded with Atto488-labeled enzyme were measured in a real time (5 s with 30 repetitions) and autocorrelation function was obtained by a QuickFit 3.0 software calculator. The experimental autocorrelation curves for the free fluorophore were fitted according to equation (2) with a one component diffusion model:

$$G(\tau) = 1 + \left(1 + \frac{T}{1-T} e^{-\left(\frac{\tau}{\tau_{trip}}\right)}\right) \frac{1}{N} \left[\frac{1}{1 + \frac{\tau}{\tau_D} \sqrt{1 + R^2 \frac{\tau}{\tau_D}}}\right] \tag{2}$$

where N represents the average number of particles in the observation volume, τ_D is the diffusional correlation time and R is the structural parameter, set to 5. T is the fraction of molecules in triple state, while τ_{trip} is the triplet time. The diffusion coefficient D was calculated using the relation between the x–y dimension of the confocal volume (ω_{xy}) and τ_D as in following equation (3):

$$\tau_D = \frac{\omega_{xy^2}}{4D} \tag{3}$$

Two component diffusion model, presented in equation (4) was used for fitting the experimental autocorrelation curves for the free labelled enzyme and the nanocompartment encapsulating labelled enzyme:

$$G(\tau) = 1 + \left(1 + \frac{T}{1-T} e^{-\left(\frac{\tau}{\tau_{trip}}\right)}\right) \frac{1}{N} \left[\frac{f1}{1 + \frac{\tau}{\tau_{D1}} \sqrt{1 + R^2 \frac{\tau}{\tau_{D1}}}}\right] + \frac{1}{N} \left[\frac{f2}{1 + \frac{\tau}{\tau_{D2}} \sqrt{1 + R^2 \frac{\tau}{\tau_{D2}}}}\right] \tag{4}$$

The number of dye molecules per enzyme (NPE) was calculated by equation (5):

$$NPE = \frac{Counts\ per\ molecule_{enzyme}}{Counts\ per\ molecule_{free\ dye}} \tag{5}$$

The number of enzymes per nanoreactor (NPN) was calculated by equation (6):

$$NPE = \frac{Counts\ per\ molecule_{nanocompartment}}{Counts\ per\ molecule_{free\ dye}} \tag{6}$$

Calculation of hydrodynamic radius (R_h) by Fluorescence Correlation Spectroscopy (FCS): The hydrodynamic radius (R_h) of polymersomes, was calculated using Einstein-Stokes equation (7), where D is the diffusion coefficient, k_B – Boltzmann's constant, T – absolute temperature, and η –viscosity of the surrounding medium.

$$\mathrm{D} = \frac{\mathrm{k_B T}}{6\pi\eta \mathrm{R_h}} \tag{7}$$

Estimation of number of melittin pores: The number of melittin pores per nanoreactor (NMP) was calculated by equation (8):

$$\mathrm{NMP} = \frac{\frac{\mathrm{c\ N_A}}{M_w\ \mathrm{c_{max}}}}{12} \tag{8}$$

where c is the concentration of melittin in the total volume of polymersomes, N_A – the Avogadro number, M_W – the molecular weight of melittin, and c_{max} – the total concentration of GUS-melCNCs. This value was divided by 12, which is the average number of melittin monomers forming a pore.[65]

To estimate the number of melittin pores per nanoreactor, we prepared polymersomes with inserted melittin pores (50 µM) (melPSs) by film rehydration method. After SEC purification, the fraction containing non-inserted melittin was collected and its concentration was measured using a NanoDrop 2000c spectrophotometer (Thermofischer, U.S.A.). This value was multiplied by the volume of SEC fraction and subtracted by the initial concentration, resulting in the concentration of melittin in the total volume of polymersomes. The total concentration of polymersomes was determined by single nanoparticle tracking analysis (NTA) using a NanoSight NS300 device (Malvern, U.K.).

8.2.4 BCA assay for determining enzyme encapsulation efficiency

In the case of unlabeled β-glucuronidase, the amount of enzyme inside nanocompartments was calculated by subtracting the amount of protein released after rupturing CNCs from the initial amount of protein added to the film rehydration solution. Protein was quantified using the enhanced Pierce bicinchonic acid (BCA) assay according to the supplier's protocol with the following modifications; a calibration curve was prepared with different concentrations of GUS rather than with bovine serum albumin. Non-permeabilized GUS–CNCs were first ruptured by sonication and then incubated with ethanol at a ratio of 3 : 1 (v/v) for 1 h at 37 °C. The solution was filtered through 0.2 µm nylon membrane, 4 mm filter (Whatman™, General Electric, U.K.) and added at a 1 : 2 ratio to the BCA reagent. Samples and GUS standards were incubated for 2 h at 37 °C, and the absorbance was measured at 562 nm using a SpectraMax id3 plate reader (Molecular Devices, USA). The amount of encapsulated protein was multiplied by the volume of the sample after SEC purification and subtracted from the total amount that was used for rehydration, yielding the final GUS concentration in the nanocompartments solution.

8.2.5 Enzyme activity assays

Fluorescence assays were performed using 96-well, flat bottom black plates (Thermo Fisher Scientific). The increase of fluorescence was measured at λ_{ex} (365 nm) and λ_{em} (445 nm) in a SpectraMax id3 microplate reader (Molecular Devices, USA). 4-Methylumbelliferyl-β-d-glucuronide (4-MUG, 5 µM) was added to CNCs (1.25 mg mL^{-1}, [GUS] 24 U mL^{-1}) or the respective amount of free enzyme in solution (24 U mL^{-1}) in a final volume of 200 µL PBS or minimum essential medium containing 10% FBS ('MEM') per well. 4-MUG (5 µM) without CNCs or free enzyme was added in PBS or MEM as control. All assay conditions were performed in triplicate. Fluorescence emission was monitored for 90 min at 37 °C.

For estimating drug production, the fluorescence intensity of 0, 5, 10, 20, 40 µM 4-MU either in PBS or MEM was measured and a calibration curve was prepared. Hymecromone production from 4-MUG by free and encapsulated GUS was calculated based on the calibration curve at time points when the reaction reached maximum fluorescence intensity (t = 10 min for free GUS in PBS, t = 90 min for GUS–melCNCs in PBS, t = 30 min for free GUS in MEM, t = 60 min for GUS–melCNCs in MEM).

For the evaluation of enzyme stability, free GUS, GUS–melCNCs and GUS–CNCs were stored in PBS for 2 months at 4 °C. After filtration through a 100 nm Whatman Nuclepore polycarbonate membrane, 5 µM 4-MUG were added and the increase in fluorescence was monitored for 90 min at 37 °C. The activity of aged samples was compared to that of freshly prepared samples at 18 min (time point of 4-MU maximum catalysed by free GUS) and at 60 min (time point of 4-MU maximum catalysed by GUS–CNCs).

Kinetic parameters for free enzyme and GUS–melCNCs were calculated using the Michaelis–Menten model as in equations (9) and (10):

$$\mathrm{v} = \frac{V_{\max[S]0}}{K_M + [S]_0} \tag{9}$$

$$k_{cat} = \frac{V_{\max}}{[E]_0} \tag{10}$$

where v is the velocity of the enzyme, V_{max} is the maximum velocity at saturating concentration, $[S]_0$ is initial the concentration of the substrate S, K_{M} is the Michaelis–Menten constant, k_{cat} is the turnover number, and $[E]_0$ is the concentration of catalytic sites, equivalent with the concentration of enzyme.

GUS–melCNCs or free GUS in solution ([GUS] 24 U mL^{-1}) were incubated with increasing concentrations of 4-MUG in PBS (30, 90, 150, 300, 600, 750 µM) or MEM (80, 120, 200, 400, 800 µM). The increase in fluorescence associated with the production of hymecromone was monitored over 1 h at 37 °C, and K_{M}, V_{max}, and k_{cat} values were calculated.

8.2.6 Cell cultures

HepG2 cells (hepatocellular carcinoma, human; ATCC® HB-8065™) were routinely cultured in minimum essential medium supplemented with 10% FBS, 100 U mL^{-1} penicillin, 100 U mL^{-1} streptomycin, 1% l-glutamine and 1% non-essential amino acids. Cells were maintained at 37 °C in a humidified atmosphere containing 5% CO_2.

Cell viability assay: Cell viability was evaluated by CellTiter 96® AQueous One solution cell proliferation assay (MTS) following the supplier's protocol. In brief, cells were seeded at a concentration of 2000 cells per well in a 96 well plate (100 µL). After 24 h, the medium was removed and replaced with 150 µL of fresh MEM mixed with 50 µL of nanocompartments in PBS (1.25 mg mL^{-1}), free enzyme ([GUS] 24 U mL^{-1}) or PBS. The cells were then cultured at 37 °C for another 24 h. The MTS reagent (20 µL) was added to each well and after 2 h at 37 °C absorbance was measured at 490 nm using a SpectraMax plate reader. The data was normalized to PBS treated control cells after background absorbance removal.

Cellular uptake and imaging: Cells were seeded at a concentration of 25 000 cells (in 200 µL MEM) in each well of an ibidi 8-well chambered glass bottom coverslip (Vitaris, Switzerland). After 24 h, the medium was replaced with fresh MEM containing either Atto647-labeled polymersomes (Atto647-PSs, 1.25 mg mL^{-1}) or the respective amount of PBS as a control. After

24 h incubation, cells were gently washed with PBS (3×). Nuclei were stained by incubating cells with a 20 000-fold dilution of Hoechst 33342 fluorescent dye (20 mins, 37 °C), followed by 3 washing steps with PBS. Cells were fixed with 4% paraformaldehyde (15 mins at RT), followed by rinsing with PBS (3×). Fixed cells were incubated with wheat germ agglutinin–Alexa Fluor™ 555 conjugate (200-fold dilution, 10 min at RT) for membrane staining. The cells were washed with PBS (3×) and imaged by confocal laser scanning microscopy (LSM 880, Carl Zeiss, Germany) using an oil immersion objective (Zeiss, 63× Plan-Apochromat, NA 1.4). Images were recorded using a 633 nm HeNe laser to visualize Atto647-PSs (detection range: 643–758 nm), a 561 nm DPSS 5561-10 laser for Alexa Fluor™ 555 (detection range: 570–615 nm), and a UV laser for Hoechst 33342 detection (detection range: 415–470 nm). The images were analyzed using the ZEN 3.2 software (blue edition) and Imaris software (Bitplane) for 3D reconstructions.

Activity of CNCs in HepG2 Cells: HepG2 cells were seeded in a black 96-well, flat bottom plate at a concentration of 2000 cells per well (100 µL) and incubated at 37 °C and 5% CO_2. The next day, the medium was replaced with 150 µL fresh MEM mixed with 50 µL nanocompartment solution (1.25 mg mL^{-1}), free enzyme or PBS (untreated control). All conditions were carried out in triplicate. After 24 h incubation at 37 °C and 5% CO_2, the supernatant was removed, cells were washed with PBS, and 180 µL fresh MEM was added. 4-MUG was added in a final concentration of 400 µM (20 µL) and the fluorescence was recorded at several timepoints over 24 h. Control cells were incubated with 20 µL of PBS as substrate. To estimate hymecromone production, reference values were obtained by directly incubating corresponding cultures with 400 µM 4-MU.

8.3 Chapter 5

8.3.1 Materials

β-glucuronidase (GUS, E. coli Type VII-A), Glucose Oxidase (GOx, A. niger Type VII), Peroxidase from horseradish (HRP, Type VI), melittin (from honey bee venom), Concanavalin A (FITC-ConA, C. ensiformis FITC conjugate, Type IV), 4-methylumbelliferyl-β-d-glucuronide (4-MUG), proteinase K (from Tritirachium album), fluorescent dye Atto647, penicillin, streptomycin, l-glutamine, Sepharose® (4B, 45–165 µm beads diameter), Whatman® Nucleopore™ Track-Etched membranes (100 nm), (+)-Sodium L-ascorbate, Copper(II) sulfate pentahydrate and the Copper Assay Kit were purchased from Sigma-Aldrich (USA). Atto488 N-hydroxysuccinimide ester (Atto488 NHS-Ester) and Atto633 N-hydroxysuccinimide ester (Atto633 NHS-Ester) were purchased from ATTO-TEC (Germany). CM5 sensor chips were purchased from Cytiva Life Sciences (USA). MBL, Dectin-1, DC-SIGN and Mannose Receptor 1 were purchased from Bio-Techne (USA). Enhanced Pierce bicinchonic acid (BCA) assay, calcein, AlexaFluor™647 Alkyne, Amplex™ Red Reagent and wheat germ agglutinin – Alexa Fluor™ 555 conjugate were purchased from Thermo Fisher Scientific (USA). Phosphate buffered saline (PBS) and fetal bovine serum (FBS) were purchased from BioConcept (Switzerland). Dulbecco's Modified Eagle's Medium (DMEM) and non-essential amino acids (NEAA) were purchased from Gibco Life Sciences (USA). CellTiter 96® AQueous One Solution Cell Proliferation Assay (MTS) and Hoechst 33342 trihydrochloride trihydrate were purchased from Invitrogen (USA). The Reactive Oxygen Species (ROS) Detection Assay Kit (ab287839) was purchased from Abcam (UK). HeLa-GFP (HeLa S3 cells stably expressing histone H2B-GFP) were obtained from the Nigg laboratory (Biozentrum, Basel).[340] All moisture-sensitive reactions were carried out under an inert atmosphere of nitrogen using standard syringe/septa techniques.

8.3.2 Nanocompartment preparation

All nanocompartments in this study were prepared with the film rehydration method. For the formation of the enzyme-containing catalytic nanocompartments equipped with melittin pores and functionalized with the glycooligomer (GUS-GOx-CNCs-Gly), a thin film of $PDMS_{25}$-*b*-$PMOXA_{10}$ and $PDMS_{22}$-*b*-$PMOXA_8$-OEG_3-N_3[89,212] (1:1 mol%, 5 or 10 mg mL^{-1} polymer in EtOH) was formed by rotary evaporation of the solvent (100 rpm at 40 °C, 160 mbar for 45 min). The film was rehydrated by stirring overnight at room temperature (RT) using a solution of PBS containing β-glucuronidase (0.5 mg mL^{-1}, 25 kU), glucose oxidase (0.5 mg mL^{-1}, 10 kU) and melittin (50 μM). Control nanocompartments lacking any of the components were prepared according to the same procedure, but missing the corresponding molecules. For Cy5-melittin polymersomes, the film was rehydrated with PBS containing Cy5-melittin (25, 50 or 75 μM). For Atto647-encapsulating polymersomes, the film was rehydrated with PBS containing Atto647 (0.02 mg mL^{-1}). To remove non-encapsulated proteins, nanocompartments were incubated with proteinase K (0.05 mg mL^{-1}) for 2 h at 37 °C, following extrusion (21x) through a 100 nm Whatman Nuclepore polycarbonate membrane. For further purification, size exclusion chromatography (SEC, Sepharose® 4B, PBS) was performed. CuAAC was performed for the functionalization of the outer polymer membrane with glycooligomer. Nanocompartments were incubated with glycooligomer (1:1 mol ratio of azide-terminated polymer and glycooligomer, PBS, (+)-Sodium L-ascorbate 10 mol%, Copper(II) sulfate pentahydrate 1 mol%) overnight and stirring at RT. Size exclusion chromatography (Sepharose® 4B, PBS) was performed for further purification. Nanocompartment suspensions were stored at 4 °C until further use.

8.3.3 Characterization of nanocompartments

Light scattering (DLS/SLS), nanoparticle tracking analysis (NTA), transmission electron microscopy (TEM) and fluorescence correlation spectroscopy (FCS) were performed according to sections 8.2.3. Atto488 was excited with an Argon (λ = 488 nm, MBS 488 filter) and Atto633 was excited using a HeNe laser (λ = 633 nm, MBS 488/561/633 filter). Fluorescence cross-correlation spectroscopy (FCCS) was performed similarly to FCS on nanocompartments containing both of the labeled enzymes, in FCCS mode.

8.3.4 Estimation of number of melittin pores

FCS experiments were conducted for determining the number of melittin pores. Cy5 was excited using a HeNe laser (λ = 633 nm, MBS 488/561/633 filter). The number of melittin pores per nanocompartment (NMP) was calculated by equation (11):

$$NMP = \frac{\dfrac{Counts\ per\ molecule_{nanocompartments}}{Counts\ per\ molecule_{melittin-Cy5}}}{\dfrac{4}{3}} \tag{11}$$

8.3.5 Concanavalin A (ConA) clustering assay

Glycooligomer-functionalized Atto647-encapsulating polymersomes or non-functionalized polymerosmes (PBS, 0.85 mg mL^{-1}) were incubated (1 h, RT) with FITC-ConA (PBS, 0.65 mg mL^{-1}). Samples (20 µL) were placed on a 0.15 mm thick glass coverslip and imaged on an inverted laser scanning confocal microscope (LSM 880, Carl Zeiss, Germany) with a water immersion objective (Zeiss C/Apochromat, M = 40, NA = 1.2). FITC was excited using an Argon (λ = 488 nm, MBS 488 filter) and Atto647 using a HeNe laser (λ = 633 nm, MBS488/561/633 filter). The ImageJ software was used to analyze the images and calculate the Pearson's colocalization coefficient.

8.3.6 Surface plasmon resonance (SPR)

Surface Plasmon Resonance (SPR) was used to determine the extent of interaction between the glycooligomer-functionalized polymersomes and lectins. Samples were analyzed on a BIAcore T200 system (Cytiva Life Sciences). The lectins (25 µg mL^{-1}) were immobilized via a standard amino coupling protocol onto a CM5 sensor chip that was activated by flowing a 1:1 mixture of 0.1 M N-hydroxysuccinimide (NHS) and 0.4 M N-ethyl-N' (dimethylaminopropyl)-carbodiimide (EDC) over the chip for 5 min at 20 °C at a flow rate of 5 µL min^{-1} after system equilibration with HEPES-Buffered Saline (HBS) buffer (10 mM HEPES pH 7.4, 150 mM NaCl, 5 mM $CaCl_2$). Subsequently, channels 1 (blank), 2, 3 and 4 were blocked by flowing a solution of ethanolamine (1 M pH 8.5) for 10 min at 5 µL min^{-1} to block remaining reactive groups on the channels. Sample solutions were prepared at varying concentrations (100 µM - 3.125 µM) in the same HBS buffer to calculate the binding kinetics. Sensorgrams for each sample concentration were recorded at 20 °C with a flow rate of 25 µL min^{-1}. Injection of polymer solution 350 s (on period) was followed by 200 s of buffer alone (off period). Regeneration of the sensor chip surfaces was performed using a solution of 10 mM HEPES pH 7.4, 150 mM NaCl, 10 mM EDTA, 0.01% Tween20. All binding curves were subjected to double referencing by subtracting the signal of a reference channel without protein on the chip and the signal of a blank buffer injection. Kinetic data was evaluated using a 1:1 Langmuir binding model in the BIA evaluation 3.1 software.

8.3.7 Estimation of glycooligomer per nanocompartment

The number of glycooligomers per nanocompartment (GPN) was calculated by equation (12):

$$GNP = \frac{cN_A}{M_w c_{max}} \tag{12}$$

Where c is the concentration of glycooligomer in the total volume of polymersomes, N_A is the Avogadro number, M_w is the molecular weight of the glycooligomer and c_{max} is the maximum concentration of polymersomes. For the estimation, the absorbance of glycooligomer (0.05 mg mL^{-1}), empty polymersomes (0.1 mg mL^{-1} polymer) and glycooligomer-functionalized polymersomes (0.1 mg mL^{-1} polymer) was measured at $\lambda = 250$ nm on a Nanodrop 2000c UV-Vis spectrophotometer (ThermoFisher, USA). The absorbance value of empty polymersomes was subtracted from the glycooligomer-functionalized polymersomes' value and used for the calculation of glycooligomer concentration in the sample. The concentration of polymersomes was determined by NTA using a NanoSight NS300 device (Malvern, U.K.).

8.3.8 BCA assay for determining enzyme encapsulation efficiency

In the case of unlabeled enzymes, the amount of encapsulated proteins was calculated by subtracting the amount of protein in CNCs from the initial, total amount of protein used in the film rehydration solution. The quantification of protein was conducted by the enhanced Pierce bicinchonic acid (BCA) assay according to the supplier's protocol with the following modifications; a calibration curve was prepared with different concentrations of GUS, GOx. Non-permeabilized, non-functionalized GUS-GOx–CNCs were first ruptured by sonication and then incubated with ethanol at a ratio of 3 : 1 (v/v) for 1 h at 37 °C. The solution was added at a 1 : 2 ratio to the BCA reagent. Samples and standards were incubated for 1 h at 37 °C, and the absorbance was measured at 562 nm using a SpectraMax id3 plate reader (Molecular Devices, USA).

8.3.9 Detection of Copper

The Copper Detection Kit was used according to the manufacturer's protocol with the following modifications. Cu^{2+} standards (0, 15, 30, 45 µM) and samples were prepared by adding Reagent A (3:1 v/v), mixing well and transferred to a 96-well plate. Master Reaction Mix was prepared by adding Reagent B and Reagent C in a 1:30 (v/v) ratio, added to the wells in a 1.5:1 ratio (v/v) to the samples and standards and mixed well. Plate was incubated at RT for 5 min, in dark and absorbance was measured at 359 nm using a SpectraMax id3 plate reader (Molecular Devices, USA). A calibration curve was constructed for estimating the amount of Cu^{2+} in the samples.

8.3.10 Enzyme activity assays

Fluorescence assays were performed using 96-well, flat bottom black plates (Thermo Fisher Scientific). The increase of fluorescence for 4-MU (λ_{ex} = 365 nm, λ_{em} = 445 nm) and resorufin (λ_{ex} = 550 nm, λ_{em} = 590 nm) was measured in a SpectraMax id3 microplate reader (Molecular Devices, USA). 4-Methylumbelliferyl-β-d-glucuronide (4-MUG, 10 µM) was added to CNCs ([GUS] 13 µg mL^{-1}, [GOx] 97 µg mL^{-1}) or the respective amount of free enzymes in solution in PBS or PBS containing 50% Dulbecco's Modified Eagle Medium (DMEM) Phenol Red free with 10% Fetal Bovine Serum ([glucose] 12.5 mM) per well (100 µL). 4-MUG (10 µM) without CNCs or free enzymes was added in the mixture as control. Fluorescence emission (λ_{em} = 445 nm) was monitored for 60 min at 37 °C. For evaluating the production of H_2O_2, reactions were then diluted 1:1250 and HRP ([HRP] 100 µg mL^{-1}) and Amplex™ Red ([Amplex™ Red] 10 µM) were added. Fluorescence emission (λ_{em} = 590 nm) was monitored for total of 2 h at 37 °C.

For estimating 4-MU and resorufin production, the fluorescence intensity of 0, 2, 4, 6, 8, 10 µM 4-MU and 0, 1.5, 3, 4.5, 6, 7.5 µM resorufin in PBS containing 50% Dulbecco's Modified Eagle Medium (DMEM) Phenol Red free with 10% Fetal Bovine Serum were measured and calibration curves were constructed. 4-MU and resorufin produced by free and encapsulated enzymes was calculated based on their calibration curves when the reaction reached maximum fluorescence intensity.

8.3.11Cell cultures

HepG2 (hepatocellular carcinoma, human; ATCC® HB-8065™) and HeLa S3 H2B-GFP (cervical adenocarcinoma, human) cells were routinely cultured in DMEM supplemented with 10% FBS, 100 U mL^{-1} penicillin, 100 U mL^{-1} streptomycin, 1% l-glutamine and 1% non-essential amino acids. Cells were maintained at 37 °C in a humidified atmosphere containing 5% CO_2.

Cellular uptake and imaging: Cells (HepG2 or HepG2 & HeLa S3 H2B-GFP) were seeded at a concentration of 30000 cells (300 µL) in each well of an ibidi 8-well chambered glass bottom coverslip (Vitaris, Switzerland). After 24 h, the medium was replaced with fresh DMEM containing either glycooligomer-functionalized Atto647-encapsulating polymersomes (0.3 mg mL^{-1}) or non-functionalized polymersomes (0.3 mg mL^{-1}). Following a 24 h incubation, cells were washed with PBS (3×), fixed with 4% paraformaldehyde (15 min, RT) and rinsed with PBS (3×). Nuclei were stained by incubating cells with a 20000-fold dilution of Hoechst 33342 fluorescent dye (20 min, 37 °C), followed by washing (PBS, 3×). To stain their membrane of co-cultured cells, cells were incubated with wheat germ agglutinin–Alexa Fluor™555 conjugate (200-fold dilution, 5 min, RT). The cells were washed with PBS (3×) and imaged by confocal laser scanning microscopy (LSM 880, Carl Zeiss, Germany) using an oil immersion objective (Zeiss, 63× Plan-Apochromat, NA 1.4). Micrographs were recorded using a 633 nm HeNe laser to visualize Atto647-encapsulating polymersomes (detection range: 638–759 nm), a 561 nm DPSS 5561-10 laser for Alexa Fluor™ 555 (detection range: 519–644 nm), and a UV laser for Hoechst 33342 detection (detection range: 426–520 nm). The micrographs were analyzed using the ZEN 3.2 software (blue edition), the ImageJ software for uptake calculations and superimpose reconstructions, and Imaris software (Bitplane) for 3D reconstructions.

Endosomal escape assay: For the endosomal escape of our CNCs, we performed calcein assays. HepG2 cells (30.000 cells/well) were plated in the wells of an ibidi 8-well chambered glass bottom coverslip (Vitaris, Switzerland) and cultured for 24 h. The next day, they were placed on ice for 10 min, followed by removal of the medium and addition of fresh, cold medium containing calcein (250 µM) and polymersomes (0.3 mg mL^{-1}). Cells were incubated on ice for further 30 min and returned to incubator (5% CO_2, 37 °C) for 4 h. Followed the incubation, cells were washed with PBS (3x) and phenol-free DMEM (200 µL) was added to each well. Cells were imaged under CLSM (λ_{ex} = 488 nm, Argon laser, λ_{em} = 498 – 543 nm) and micrographs were processed using the ZEN Blue software (v.3.2, Carl Zeiss Microscopy GmbH) and ImageJ.

Hymecromone production: HepG2 and HeLa S3 H2B-GFP cells were seeded separately at a concentration of 5000 cells per well in a 96 well plate (100 µL). After 24 h, the medium was removed and replaced fresh DMEM mixed with nanocompartments in PBS (0.3 mg mL^{-1}), free enzymes ([GUS] 13 µg mL^{-1}, [GOx] 97 µg mL^{-1}) or PBS. The cells were cultured at 37 °C for another 24 h. The next day, cells were washed with PBS and fresh DMEM was added containing 4-MUG (500 µM) or the equivalent amount of PBS. The fluorescence (λ_{ex}: 365 nm, λ_{em}: 445 nm) was monitored at several timepoints for 24 h on a SpectraMax id3 microplate reader (Molecular Devices, USA). For the estimation of hymecromone production, the GUS-GOx-CNCs-Gly incubated HepG2 cells were diluted (50x) at 24 h and their fluorescence intensity was measured. Based on constructed calibration curves of 0, 2, 4, 6, 8, 10 µM 4-MU in DMEM, the produced hymecromone was calculated.

Detection of H_2O_2: HepG2 and HeLa S3 H2B-GFP cells were seeded at a concentration of 30000 and 20000 cells (200 µL), respectively in each well of an ibidi 8-well chambered glass bottom coverslip (Vitaris, Switzerland). After 24 h, the medium was replaced with fresh DMEM containing either GUS-GOx-CNCs (0.3 mg mL^{-1}), GUS-GOx-CNCs (0.3 mg mL^{-1}), cGUS-GOx-CNCs (0.3 mg mL^{-1}), empty polymersomes (0.3 mg mL^{-1}), free enzymes ([GUS] 13 µg mL^{-1}, [GOx] 97 µg mL^{-1}) or the equivalent amount of PBS. Following a 24 h incubation, cells were washed and the intracellularly produced H_2O_2 was detected using a ROS detection assay kit according to manufacturer's instructions. As positive control, untreated cells were incubated with tert-butyl hydroperoxide (inducer, provided by manufacturer) in ROS assay buffer for 1 h, 37 °C. Next, all samples were incubated with 2',7'-dichlorodihydrofluorescein diacetate in ROS assay buffer (ROS label, provided by manufacturer, 150 µL/well) for 45 min, 37 °C, following a washing step with ROS assay buffer. Cells were imaged in ROS assay buffer (200 µL/well) under a CLSM (Argon laser, λ_{ex} = 488 nm, detection range 499 – 573 nm). Micrographs were analyzed using ZEN Blue software (v3.2, Carl Zeiss Microscopy GmbH) and ImageJ.

Cell viability assay: HepG2 and HeLa S3 H2B-GFP cell viability was evaluated by CellTiter 96® AQueous One solution cell proliferation assay (MTS) following the supplier's protocol. Briefly, cells were seeded at a concentration of 5000 cells per well in a 96 well plate (100 µL). After 24 h, the medium was removed and replaced fresh DMEM mixed with nanocompartments in PBS (0.3 mg mL^{-1}), free glycooligomer (0.06 mg mL^{-1}), free enzymes ([GUS] 13 µg mL^{-1}, [GOx] 97 µg mL^{-1}) or PBS. The cells were cultured at 37 °C for another 24 h. The MTS reagent (10 µL) was added to each well. Following a 2 h incubation at 37 °C, absorbance was measured at 490 nm using a SpectraMax plate reader. The data was normalized to PBS treated control cells after background absorbance removal.

For evaluating the cell viability after the addition of 4-MUG, cells were seeded and incubated with nanocompartments, free enzymes and PBS as described above. After 24 h of incubation, cells were washed and fresh DMEM was added containing 4-MUG (500 µM) or the equivalent amount of PBS and returned to incubator. The next day, the MTS cell proliferation assay was conducted as described above.

8.3.12 Statistical Analysis

For comparative analysis, independent two-tailed t-tests were used. $P < 0.05$ was considered statistically significant. The significance level was indicated by asterisks: $P < 0.05$ (*), $P < 0.01$ (**), $P < 0.001$ (***), $P < 0.0001$ (****).

8.4 Chapter 6

8.4.1 Materials

Polyethylene glycol (PEG, Mn = 35,000), polyvinyl alcohol (PVA, MW 13,000-23,000, 87-89 % hydrolyzed), chloroform (99 %), anhydrous hexane (95 %), fluorescein di-(β-D-galactopyranoside) (FGD), sucrose, sodium chloride, melittin (from honey bee venom, ≥ 85 % by HPLC), $CaCl_2$, β-Galactosidase from E. coli (Grade VIII, ≥500 units mg-1 protein), proteinase K (from Tritirachium album), ionomycin calcium salt (Streptomyces conglobatus, ≥98% (HPLC)), Sepharose® (4B, 45-165 µm beads diameter), and Whatman® Nucleopore™ Track-Etched membranes were obtained from Sigma-Aldrich. Calcium Green™-5N (hexapotassium salt, cell impermeant) was purchased from Invitrogen. Rhod-5N (tripotassium salt) was obtained from AAT Bioquest. Pluronic F-68 Non-ionic Surfactant (100X) was obtained from Gibco. BODIPY 630/650 was obtained from Thermo Scientific Inc. Cy5-labelled melittin was purchased from Biosynth Ltd. ATTO488-carboxyl was obtained from ATTO-TEC. Aquapel was obtained from PGW Auto Glass. DNA nanopores were obtained from Tilibit Nanosystems. All chemicals were used as received unless stated otherwise.

8.4.2 Preparation of artificial organelles

AOs were prepared using the film rehydration method. Briefly, a thin film of $PDMS_{25}$-*b*-$PMOXA_{10}$[212] (5 or 10 mg mL^{-1} polymer in EtOH) was formed by rotary evaporation. For AOs containing the molecular motor (AO_MM_A488, AO_MM_FDG), the motor was dissolved in EtOH and mixed with the polymer solution (25 mol % relative to polymer). For ATTO488-containing AOs, the film was rehydrated (overnight, stirring, RT) with PBS containing ATTO488-carboxyl (100 µM). For Cy5-melittin AOs, the film was rehydrated with Cy5-melittin (10 or 50 µM) in PBS. For FDG-containing AOs, the rehydration was performed with FDG (50 µM) in PBS. For AO_CaGreen, the rehydration was performed with CalciumGreen™

(CaGreen) in MilliQ water (100 µM) and melittin (10 µM), for the case of AO_mel_CaGreen. For AOs containing β-Galactosidase (βGal), the film was rehydrated with a solution of βGal in PBS (100 U mL^{-1}) and melittin (50 µM), for AO_mel_βGal. The enzyme-containing AOs were incubated with proteinase K (0.05 mg mL^{-1}) for 1 h at 37 °C. AOs were extruded through a 200 nm Whatman Nuclepore polycarbonate membrane, followed by purification by size exclusion chromatography (SEC, Sepharose®). All samples were kept at 4 °C until further use.

8.4.3 Characterization of artificial organelles

Light scattering (DLS/SLS), nanoparticle tracking analysis (NTA), transmission electron microscopy (TEM) and fluorescence correlation spectroscopy (FCS) were performed according to sections 8.3.3.

8.4.4 Estimation of melittin pores

The estimation of melittin pores was conducted according to 8.3.4.

8.4.5 Enzyme encapsulation efficiency by BCA assay

The enzyme encapsulation efficiency experiments by BCA assay were performed according to 8.2.4.

8.4.6 Ca^{2+}-sensing in artificial organelles

FCS experiments were performed on free CaGreen (10 nM), AO_CaGreen and AO_mel_CaGreen for measuring the fluorescence intensity (kHz) upon administration of increasing concentration of $CaCl_2$ (0-1000 µM). Similarly, samples (20 µL) were placed on a 0.15 mm thick glass coverslip and CaGreen was excited using the Argon laser. The fluorescent fluctuations were recorded for 60s, 6 repetitions and the raw data were analyzed using the ZEN software.

8.4.7 Molecular Motor Activation

AOs containing molecular motors in their membranes were irradiated using a self-made illumination device equipped with 6 Lite-On LEDs (Mouser Electronics, 3.7 V, 50 Hz, 0.5 A, 430 nm) with distances of 3.5 cm between them.[259] Device dimension were 13 x 9 x 3.5 cm. The light intensity was estimated to be ~ 31.8 W m^{-2} in the sample.

8.4.8 Enzyme activity assays in bulk

Samples (30 µL) were placed on a 0.15 mm thick glass coverslip and images were taken over the course of 1 h at RT. For detecting the production of fluorescein from FDG (25 nM) by free or encapsulated βGal (10 U mL^{-1}), samples were imaged after excitation at 488 nm. For measurements with irradiated samples, FDG, AO_FDG or AO_MM_FDG were irradiated for 10 min before the addition of the catalyst. The fluorescence intensity of the images was analyzed using ImageJ.

8.4.9 Double Emulsion Fabrication and Dewetting – Formation of artificial cells

PBS supplemented with 200 mM sucrose was used as an inner aqueous phase (IA). The $PDMS_{25}$-*b*-$PMOXA_{10}$ was dissolved at 4 mg mL^{-1} in a 3:2 v/v mixture of hexane and chloroform. For the outer aqueous phase (OA), PBS was supplemented with 5 % $PEG_{35,000,}$ 0.1 % Pluronic F-68 and 100 mM NaCl to decrease the osmolarity difference to the IA. A freezing point osmometer (Gonotec Osmomat) was used to measure the osmolarity. Flow rates of 1, 3, and 5 µL min^{-1} were used to flow the PO, IA, and OA phases into the microfluidic chip. After double emulsion formation in the chip, the formed emulsions were collected for 10 min in a 1.5 mL Eppendorf tube containing 300 µL OA phase. Evaporation of the organic phase yielded ~ 10^6 GUVs at a concentration of 10^6 mL.[32,318]

For preparation of AO-loaded artificial cells, AOs were directly added to the IA prior to double emulsion production. An overview over the employed AO concentrations can be found in **Table 10.9** in *Appendix*. Artificial cells were produced under the same flow conditions as non-AO-encapsulating cells.

For artificial cell membrane permeabilization, DNA nanopores were used as purchased.[312] DNA nanopore concentration was optimized using free β-galactosidase in artificial cells and free FDG added from the outside. The pores were typically added to the protocell suspension 1 h prior to imaging at a final concentration of 1 nM in OA.

8.4.10 Artificial cell communication

For artificial cells communication assays, the sender cells were diluted in OA in a 1:3 ratio and subsequently illuminated for 10 min at 430 nm in an Ibidi µ-slide. After illumination, receiver cells were added to a final dilution of 1:20 (final ratio sender cell:receiver cell 1:6) and DNA nanopores were added to a final concentration of 1 nM. Protocell populations were imaged after 1 h incubation at room temperature. For imaging, 2 frames were integrated to achieve an increased signal to noise ratio.

8.4.11 Statistical analysis

For comparative analysis, two-way Analysis of Variance (ANOVA) were used, followed by post-hoc Tukey's honestly significant difference (HSD) testing. $p < 0.05$ was considered statistically significant. The significance level of the calculated p values was indicated using asterisks: $p > 0.05$ (n.s.), $p < 0.05$ (*), $p < 0.005$ (**), and $p < 0.0005$ (***). Data was normalized to the control dataset and unless otherwise stated, the mean ± standard deviation is presented. In boxplots, boxes span the interquartile range (25–75%).

9. Bibliography

1. Alberts, B. *et al.* The Compartmentalization of Cells. in *Molecular Biology of the Cell* (Garland Science, 2002).

2. Meyer, C. E., Abram, S. L., Craciun, I. & Palivan, C. G. Biomolecule–polymer hybrid compartments: combining the best of both worlds. *Phys. Chem. Chem. Phys.* **22**, 11197–11218 (2020).

3. Riaz, M. K. *et al.* Surface Functionalization and Targeting Strategies of Liposomes in Solid Tumor Therapy: A Review. *Int. J. Mol. Sci.* **19**, 195 (2018).

4. Monnard, P. A. & Deamer, D. W. Nutrient uptake by protocells: a liposome model system. *Orig. Life Evol. Biosph.* **31**, 147–155 (2001).

5. Anajafi, T. & Mallik, S. Polymersome-based drug-delivery strategies for cancer therapeutics. *Ther. Deliv.* **6**, 521 (2015).

6. Rideau, E., Dimova, R., Schwille, P., Wurm, F. R. & Landfester, K. Liposomes and polymersomes: a comparative review towards cell mimicking. *Chem. Soc. Rev.* **47**, 8572–8610 (2018).

7. Discher, B. M. *et al.* Polymersomes: Tough vesicles made from diblock copolymers. *Science (80-.).* **284**, 1143–1146 (1999).

8. Itel, F., Najer, A., Palivan, C. G. & Meier, W. Dynamics of Membrane Proteins within Synthetic Polymer Membranes with Large Hydrophobic Mismatch. *Nano Lett.* **15**, 3871–3878 (2015).

9. Chang, H. Y., Sheng, Y. J. & Tsao, H. K. Structural and mechanical characteristics of polymersomes. *Soft Matter* **10**, 6373–6381 (2014).

10. Mohammadi, M., Ramezani, M., Abnous, K. & Alibolandi, M. Biocompatible polymersomes-based cancer theranostics: Towards multifunctional nanomedicine. *Int. J. Pharm.* **519**, 287–303 (2017).

11. Feng, H., Lu, X., Wang, W., Kang, N. G. & Mays, J. W. Block Copolymers: Synthesis, Self-Assembly, and Applications. *Polymers (Basel).* **9**, 494 (2017).

12. Guo, X. *et al.* Polymer Synthesis with More Than One Form of Living Polymerization Method. *Macromol. Rapid Commun.* **39**, 1800479 (2018).

13. LoPresti, C., Lomas, H., Massignani, M., Smart, T. & Battaglia, G. Polymersomes:

nature inspired nanometer sized compartments. *J. Mater. Chem.* **19**, 3576–3590 (2009).

14. Lopresti, C. *et al.* Controlling polymersome surface topology at the nanoscale by membrane confined polymer/polymer phase separation. *ACS Nano* **5**, 1775–1784 (2011).

15. Konishcheva, E. V., Zhumaev, U. E. & Meier, W. P. PEO-b-PCL-b-PMOXA Triblock Copolymers: From Synthesis to Microscale Polymersomes with Asymmetric Membrane. *Macromolecules* **50**, 1512–1520 (2017).

16. Daimon, H., Okitsu, H. & Kumanotani, J. Glass Transition Behaviors of Random and Block Copolymers and Polymer Blends of Styrene and Cyclododecyl Acrylate. I. Glass Transition Temperatures. *Polym. J.* **7**, 460–466 (1975).

17. Itel, F. *et al.* Molecular organization and dynamics in polymersome membranes: A lateral diffusion study. *Macromolecules* **47**, 7588–7596 (2014).

18. Miller, A. J., Pearce, A. K., Foster, J. C. & O'Reilly, R. K. Probing and Tuning the Permeability of Polymersomes. *ACS Cent. Sci.* **7**, 30–38 (2021).

19. Doncom, K. E. B., Blackman, L. D., Wright, D. B., Gibson, M. I. & O'Reilly, R. K. Dispersity effects in polymer self-assemblies: a matter of hierarchical control. *Chem. Soc. Rev.* **46**, 4119–4134 (2017).

20. Garni, M. *et al.* Polymer membranes as templates for bio-applications ranging from artificial cells to active surfaces. *Eur. Polym. J.* **112**, 346–364 (2019).

21. Blanazs, A., Armes, S. P. & Ryan, A. J. Self-Assembled Block Copolymer Aggregates: From Micelles to Vesicles and their Biological Applications. *Macromol. Rapid Commun.* **30**, 267–277 (2009).

22. Smart, T. *et al.* Block copolymer nanostructures. *Nano Today* **3**, 38–46 (2008).

23. Wu, D. *et al.* Effect of molecular parameters on the architecture and membrane properties of 3D assemblies of amphiphilic copolymers. *Macromolecules* **47**, 5060–5069 (2014).

24. Li, F., Danquah, M. & Mahato, R. I. Synthesis and characterization of amphiphilic lipopolymers for micellar drug delivery. *Biomacromolecules* **11**, 2610–2620 (2010).

25. Mai, Y. & Eisenberg, A. Self-assembly of block copolymers. *Chem. Soc. Rev.* **41**, 5969–5985 (2012).

26. Heuberger, L., Korpidou, M., Eggenberger, O. M., Kyropoulou, M. & Palivan, C. G.

Current Perspectives on Synthetic Compartments for Biomedical Applications. *Int. J. Mol. Sci.* **23**, 5718 (2022).

27. Dionzou, M. *et al.* Comparison of methods for the fabrication and the characterization of polymer self-assemblies: what are the important parameters? *Soft Matter* **12**, 2166–2176 (2016).

28. Kita-Tokarczyk, K., Grumelard, J., Haefele, T. & Meier, W. Block copolymer vesicles—using concepts from polymer chemistry to mimic biomembranes. *Polymer (Guildf).* **46**, 3540–3563 (2005).

29. Ibarboure, E., Fauquignon, M. & Le Meins, J. F. Obtention of Giant Unilamellar Hybrid Vesicles by Electroformation and Measurement of their Mechanical Properties by Micropipette Aspiration. *J. Vis. Exp.* **2020**, e60199 (2020).

30. Peyret, A., Ibarboure, E., Le Meins, J.-F. & Lecommandoux, S. Asymmetric Hybrid Polymer-Lipid Giant Vesicles as Cell Membrane Mimics. *Adv. Sci.* **5**, 1700453 (2018).

31. dos Santos, E. C., Angelini, A., Hürlimann, D., Meier, W. & Palivan, C. G. Giant Polymer Compartments for Confined Reactions. *Chemistry (Easton).* **2**, 470–489 (2020).

32. dos Santos, E. C. *et al.* Combinatorial Strategy for Studying Biochemical Pathways in Double Emulsion Templated Cell-Sized Compartments. *Adv. Mater.* **32**, 2004804 (2020).

33. Yao, P., Zhang, Y., Meng, H., Sun, H. & Zhong, Z. Smart Polymersomes Dually Functionalized with cRGD and Fusogenic GALA Peptides Enable Specific and High-Efficiency Cytosolic Delivery of Apoptotic Proteins. *Biomacromolecules* **20**, 184–191 (2019).

34. Pourtau, L. *et al.* Antibody-Functionalized Magnetic Polymersomes: In vivo Targeting and Imaging of Bone Metastases using High Resolution MRI. *Adv. Healthc. Mater.* **2**, 1420–1424 (2013).

35. Anajafi, T. *et al.* Nuclear Localizing Peptide-Conjugated, Redox-Sensitive Polymersomes for Delivering Curcumin and Doxorubicin to Pancreatic Cancer Microtumors. *Mol. Pharm.* **14**, 1916–1928 (2017).

36. Scheerstra, J. F., Wauters, A. C., Tel, J., Abdelmohsen, L. K. E. A. & van Hest, J. C. M. Polymersomes as a potential platform for cancer immunotherapy. *Mater. Today Adv.* **13**, 100203 (2022).

37. Leong, J. *et al.* Engineering Polymersomes for Diagnostics and Therapy. *Adv. Healthc. Mater.* **7**, 1701276 (2018).

38. Rigo, S., Gunkel-Grabole, G., Meier, W. & Palivan, C. G. Surfaces with Dual Functionality through Specific Coimmobilization of Self-Assembled Polymeric Nanostructures. *Langmuir* **35**, 4557–4565 (2019).

39. Egli, S. *et al.* Biocompatible functionalization of polymersome surfaces: A new approach to surface immobilization and cell targeting using polymersomes. *J. Am. Chem. Soc.* **133**, 4476–4483 (2011).

40. Moulahoum, H., Ghorbanizamani, F., Zihnioglu, F. & Timur, S. Surface Biomodification of Liposomes and Polymersomes for Efficient Targeted Drug Delivery. *Bioconjug. Chem.* **32**, 1491–1502 (2021).

41. Van Dongen, S. F. M., Nallani, M., Cornelissen, J. J. L. M., Nolte, R. J. M. & Van Hest, J. C. M. A Three-Enzyme Cascade Reaction through Positional Assembly of Enzymes in a Polymersome Nanoreactor. *Chem. – A Eur. J.* **15**, 1107–1114 (2009).

42. Wei, Y. *et al.* Transferrin-binding peptide functionalized polymersomes mediate targeted doxorubicin delivery to colorectal cancer in vivo. *J. Control. Release* **319**, 407–415 (2020).

43. Jia, T. T. *et al.* A dual brain-targeting curcumin-loaded polymersomes ameliorated cognitive dysfunction in intrahippocampal amyloid-β1-42-injected mice. *Int. J. Nanomedicine* **11**, 3765–3775 (2016).

44. Simón-Gracia, L. *et al.* Application of polymersomes engineered to target p32 protein for detection of small breast tumors in mice. *Oncotarget* **9**, 18682–18697 (2018).

45. Fang, Y. *et al.* EGFR-targeted multifunctional polymersomal doxorubicin induces selective and potent suppression of orthotopic human liver cancer in vivo. *Acta Biomater.* **64**, 323–333 (2017).

46. Jiang, Y., Zhang, J., Meng, F. & Zhong, Z. Apolipoprotein e Peptide-Directed Chimeric Polymersomes Mediate an Ultrahigh-Efficiency Targeted Protein Therapy for Glioblastoma. *ACS Nano* **12**, 11070–11079 (2018).

47. Alibolandi, M., Ramezani, M., Abnous, K. & Hadizadeh, F. AS1411 Aptamer-Decorated Biodegradable Polyethylene Glycol–Poly(lactic-co-glycolic acid) Nanopolymersomes for the Targeted Delivery of Gemcitabine to Non–Small Cell Lung Cancer In Vitro. *J. Pharm. Sci.* **105**, 1741–1750 (2016).

48. Li, X., Zhu, X. & Qiu, L. Constructing aptamer anchored nanovesicles for enhanced tumor penetration and cellular uptake of water soluble chemotherapeutics. *Acta Biomater.* **35**, 269–279 (2016).

49. Wang, X. *et al.* Galactose-decorated reduction-sensitive degradable chimaeric polymersomes as a multifunctional nanocarrier to efficiently chaperone apoptotic proteins into hepatoma cells. *Biomacromolecules* **14**, 2873–2882 (2013).

50. Belluati, A. *et al.* How Do the Properties of Amphiphilic Polymer Membranes Influence the Functional Insertion of Peptide Pores? *Biomacromolecules* **21**, 701–715 (2019).

51. Einfalt, T. *et al.* Biomimetic artificial organelles with in vitro and in vivo activity triggered by reduction in microenvironment. *Nat. Commun.* **9**, 1127 (2018).

52. Hammer, D. A. *et al.* Leuko-polymersomes. *Faraday Discuss.* **139**, 129–141 (2008).

53. Luo, R. *et al.* DNA-Based Assembly of Multi-Compartment Polymersome Networks. *Adv. Funct. Mater.* **30**, 2003480 (2020).

54. Liu, J. *et al.* DNA-Mediated Self-Organization of Polymeric Nanocompartments Leads to Interconnected Artificial Organelles. *Nano Lett.* **16**, 7128–7136 (2016).

55. Lomora, M. *et al.* Polymersomes with engineered ion selective permeability as stimuli-responsive nanocompartments with preserved architecture. *Biomaterials* **53**, 406–414 (2015).

56. Klermund, L., Poschenrieder, S. T. & Castiglione, K. Simple surface functionalization of polymersomes using non-antibacterial peptide anchors. *J. Nanobiotechnology* **14**, 1–12 (2016).

57. Baumann, P., Spulber, M., Fischer, O., Car, A. & Meier, W. Investigation of Horseradish Peroxidase Kinetics in an “Organelle-Like” Environment. *Small* **13**, 1603943 (2017).

58. Liu, X. & Gao, W. In situ growth of self-assembled protein-polymer nanovesicles for enhanced intracellular protein delivery. *ACS Appl. Mater. Interfaces* **9**, 2023–2028 (2017).

59. Stoenescu, R., Graff, A. & Meier, W. Asymmetric ABC-Triblock Copolymer Membranes Induce a Directed Insertion of Membrane Proteins. *Macromol. Biosci.* **4**, 930–935 (2004).

60. Lomora, M., Gunkel-Grabole, G., Mantri, S. & Palivan, C. G. Bio-catalytic

nanocompartments for in situ production of glucose-6-phosphate. *Chem. Commun.* **53**, 10148–10151 (2017).

61. Bippes, C. A., Muller, D. J., Choi, H.-J., Germain, J. & Montemagno, C. D. Effects of different reconstitution procedures on membrane protein activities inproteopolymersomes. *Nanotechnology* **17**, 1825 (2006).

62. Goers, R. *et al.* Optimized reconstitution of membrane proteins into synthetic membranes. *Commun. Chem.* **1**, 1–10 (2018).

63. Haldar, S., Raghuraman, H. & Chattopadhyay, A. Monitoring orientation and dynamics of membrane-bound melittin utilizing dansyl fluorescence. *J. Phys. Chem. B* **112**, 14075–14082 (2008).

64. Terwilliger, T. C. & Eisenberg, D. The structure of melittin. II. Interpretation of the structure. *J. Biol. Chem.* **257**, 6016–6022 (1982).

65. Lin, J. H. & Baumgaertner, A. Stability of a melittin pore in a lipid bilayer: A molecular dynamics study. *Biophys. J.* **78**, 1714–1724 (2000).

66. Malmsten, M. Antimicrobial peptides. *Ups. J. Med. Sci.* **119**, 199–204 (2014).

67. Popplewell, J. F., Swann, M. J., Freeman, N. J., McDonnell, C. & Ford, R. C. Quantifying the effects of melittin on liposomes. *Biochim. Biophys. Acta - Biomembr.* **1768**, 13–20 (2007).

68. Allende, D., Simon, S. A. & McIntosh, T. J. Melittin-Induced Bilayer Leakage Depends on Lipid Material Properties: Evidence for Toroidal Pores. *Biophys. J.* **88**, 1828–1837 (2005).

69. Maffeis, V. *et al.* Clustering of catalytic nanocompartments for enhancing an extracellular non-native cascade reaction. *Chem. Sci.* **12**, 12274–12285 (2021).

70. Camblin, M. *et al.* Polymersomes containing quantum dots for cellular imaging. *Int. J. Nanomedicine* **9**, 2287–2298 (2014).

71. Askes, S. H. C. *et al.* Imaging Upconverting Polymersomes in Cancer Cells: Biocompatible Antioxidants Brighten Triplet-Triplet Annihilation Upconversion. *Small* **12**, 5579–5590 (2016).

72. Askes, S. H. C. *et al.* Dynamics of dual-fluorescent polymersomes with durable integrity in living cancer cells and zebrafish embryos. *Biomaterials* **168**, 54–63 (2018).

73. Ferrero, C., Casas, M. & Caraballo, I. Redox-Responsive Polymersomes as Smart

Doxorubicin Delivery Systems. *Pharmaceutics* **14**, 1724 (2022).

74. Yang, W. *et al.* Lung cancer specific and reduction-responsive chimaeric polymersomes for highly efficient loading of pemetrexed and targeted suppression of lung tumor in vivo. *Acta Biomater.* **70**, 177–185 (2018).

75. Zhou, D. *et al.* Dual-responsive polymersomes as anticancer drug carriers for the co-delivery of doxorubicin and paclitaxel. *J. Mater. Chem. B* **9**, 801–808 (2021).

76. Chen, J., Liu, Q., Xiao, J. & Du, J. EpCAM-Antibody-Labeled Noncytotoxic Polymer Vesicles for Cancer Stem Cells-Targeted Delivery of Anticancer Drug and siRNA. *Biomacromolecules* **16**, 1695–1705 (2015).

77. Lomas, H. *et al.* Efficient Encapsulation of Plasmid DNA in pH-Sensitive PMPC–PDPA Polymersomes: Study of the Effect of PDPA Block Length on Copolymer–DNA Binding Affinity. *Macromol. Biosci.* **10**, 513–530 (2010).

78. de la Fuente, M. *et al.* Enzyme Therapy: Current Challenges and Future Perspectives. *Int. J. Mol. Sci.* **22**, 9181 (2021).

79. Tripathi, S., Siddiqui, M. H., Kumar, A. & Vimal, A. Nanoparticles: a promising vehicle for the delivery of therapeutic enzymes. *Int. Nano Lett.* **13**, 209–221 (2022).

80. Concolino, D., Deodato, F. & Parini, R. Enzyme replacement therapy: Efficacy and limitations. *Ital. J. Pediatr.* **44**, 117–126 (2018).

81. Belluati, A., Craciun, I., Meyer, C. E., Rigo, S. & Palivan, C. G. Enzymatic reactions in polymeric compartments: nanotechnology meets nature. *Curr. Opin. Biotechnol.* **60**, 53–62 (2019).

82. Nishimura, T., Sasaki, Y. & Akiyoshi, K. Biotransporting Self-Assembled Nanofactories Using Polymer Vesicles with Molecular Permeability for Enzyme Prodrug Cancer Therapy. *Adv. Mater.* **29**, 1702406 (2017).

83. Belluati, A., Craciun, I., Liu, J. & Palivan, C. G. Nanoscale Enzymatic Compartments in Tandem Support Cascade Reactions in Vitro. *Biomacromolecules* **19**, 4023–4033 (2018).

84. Tanner, P., Onaca, O., Balasubramanian, V., Meier, W. & Palivan, C. G. Enzymatic Cascade Reactions inside Polymeric Nanocontainers: A Means to Combat Oxidative Stress. *Chem. – A Eur. J.* **17**, 4552–4560 (2011).

85. Belluati, A., Craciun, I. & Palivan, C. G. Bioactive Catalytic Nanocompartments Integrated into Cell Physiology and Their Amplification of a Native Signaling Cascade.

ACS Nano **14**, 12101–12112 (2020).

86. Oliveira, C. A. *et al.* Catalase-loaded polymersomes as a promising safe ingredient to active photoprotection. *J. Photochem. Photobiol.* 7, 100056 (2021).

87. Khan, S., Li, M., Muench, S. P., Jeuken, L. J. C. & Beales, P. A. Durable proteo-hybrid vesicles for the extended functional lifetime of membrane proteins in bionanotechnology. *Chem. Commun.* **52**, 11020–11023 (2016).

88. Kleineberg, C. *et al.* Light-Driven ATP Regeneration in Diblock/Grafted Hybrid Vesicles. *ChemBioChem* **21**, 2149–2160 (2020).

89. Meyer, C. E. *et al.* Segregated Nanocompartments Containing Therapeutic Enzymes and Imaging Compounds within DNA-Zipped Polymersome Clusters for Advanced Nanotheranostic Platform. *Small* **16**, 1906492 (2020).

90. Ke, W. *et al.* Therapeutic Polymersome Nanoreactors with Tumor-Specific Activable Cascade Reactions for Cooperative Cancer Therapy. *ACS Nano* **13**, 2357–2369 (2019).

91. Liu, J. *et al.* DNA-directed arrangement of soft synthetic compartments and their behavior in vitro and in vivo. *Nanoscale* **12**, 9786–9799 (2020).

92. Bueno, C. Z. *et al.* L-Asparaginase Encapsulation into Asymmetric Permeable Polymersomes. *ACS Macro Lett.* **9**, 1471–1477 (2020).

93. Blackman, L. D. *et al.* Confinement of Therapeutic Enzymes in Selectively Permeable Polymer Vesicles by Polymerization-Induced Self-Assembly (PISA) Reduces Antibody Binding and Proteolytic Susceptibility. *ACS Cent. Sci.* **4**, 718–723 (2018).

94. Belluati, A. *et al.* Multicompartment Polymer Vesicles with Artificial Organelles for Signal-Triggered Cascade Reactions Including Cytoskeleton Formation. *Adv. Funct. Mater.* **30**, 2002949 (2020).

95. Meyer, C. E., Craciun, I., Schoenenberger, C.-A., Wehr, R. & Palivan, C. G. Catalytic polymersomes to produce strong and long-lasting bioluminescence. *Nanoscale* **13**, 66–70 (2021).

96. Langowska, K., Palivan, C. G. & Meier, W. Polymer nanoreactors shown to produce and release antibiotics locally. *Chem. Commun.* **49**, 128–130 (2013).

97. Messager, L. *et al.* Biomimetic Hybrid Nanocontainers with Selective Permeability. *Angew. Chemie Int. Ed.* **55**, 11106–11109 (2016).

98. Meyer, C. E., Schoenenberger, C. A., Wehr, R. P., Wu, D. & Palivan, C. G. Artificial

Melanogenesis by Confining Melanin/Polydopamine Production inside Polymersomes. *Macromol. Biosci.* **21**, 2100249 (2021).

99. Lu, L. *et al.* MRI-Visible siRNA Nanomedicine Directing Neuronal Differentiation of Neural Stem Cells in Stroke. *Adv. Funct. Mater.* **28**, 1706769 (2018).

100. Najer, A., Wu, D., Vasquez, D., Palivan, C. G. & Meier, W. Polymer nanocompartments in broad-spectrum medical applications. *Nanomedicine* **8**, 425–447 (2013).

101. Ahmed, F. *et al.* Shrinkage of a rapidly growing tumor by drug-loaded polymersomes: pH-triggered release through copolymer degradation. *Mol. Pharm.* **3**, 340–350 (2006).

102. García, M. C. Stimuli-responsive polymersomes for drug delivery applications. in *Stimuli Responsive Polymeric Nanocarriers for Drug Delivery Applications* 345–392 (Woodhead Publishing, 2019).

103. Ratemi, E. pH-responsive polymers for drug delivery applications. in *Stimuli Responsive Polymeric Nanocarriers for Drug Delivery Applications* 121–141 (Woodhead Publishing, 2018).

104. Hsu, P.-H. & Almutairi, A. Recent progress of redox-responsive polymeric nanomaterials for controlled release. *J. Mater. Chem. B* **9**, 2179–2188 (2021).

105. Paruchuri, B. C., Gopal, V., Sarupria, S. & Larsen, J. Toward enzyme-responsive polymersome drug delivery. *Nanomedicine* **16**, 2679–2693 (2021).

106. Wang, J. *et al.* Glucose-Responsive Insulin and Delivery Systems: Innovation and Translation. *Adv. Mater.* **32**, 1902004 (2020).

107. Darabi, A., Jessop, P. G. & Cunningham, M. F. CO 2 -responsive polymeric materials: synthesis, self-assembly, and functional applications. *Chem. Soc. Rev.* **45**, 4391–4436 (2016).

108. Ward, M. A. & Georgiou, T. K. Thermoresponsive Polymers for Biomedical Applications. *Polymers (Basel).* **3**, 1215–1242 (2011).

109. Becerra, H. *et al.* Light-Triggered Polymersome-Based Anticancer Therapeutics Delivery. *Nanomaterials* **12**, 836 (2022).

110. Wei, P., Cornel, E. J. & Du, J. Ultrasound-responsive polymer-based drug delivery systems. *Drug Deliv. Transl. Res.* **11**, 1323–1339 (2021).

111. Manouras, T. & Vamvakaki, M. Field responsive materials: photo-, electro-, magnetic- and ultrasound-sensitive polymers. *Polym. Chem.* **8**, 74–96 (2016).

112. Mukerabigwi, J. F., Ge, Z. & Kataoka, K. Therapeutic Nanoreactors as In Vivo Nanoplatforms for Cancer Therapy. *Chem. - A Eur. J.* **24**, 15706–15724 (2018).

113. Oerlemans, R. A. J. F., Timmermans, S. B. P. E. & van Hest, J. C. M. Artificial Organelles: Towards Adding or Restoring Intracellular Activity. *ChemBioChem* **22**, 2051–2078 (2021).

114. Japir, A. A. W. M. M. *et al.* Tumor-dilated polymersome nanofactories for enhanced enzyme prodrug chemo-immunotherapy. *J. Control. Release* **339**, 418–429 (2021).

115. Lee, K. Y. *et al.* Photosynthetic artificial organelles sustain and control ATP-dependent reactions in a protocellular system. *Nat. Biotechnol.* **36**, 530–535 (2018).

116. Xu, Y., Fei, J., Li, G., Yuan, T. & Li, J. Compartmentalized Assembly of Motor Protein Reconstituted on Protocell Membrane toward Highly Efficient Photophosphorylation. *ACS Nano* **11**, 10175–10183 (2017).

117. Simons, K. & Sampaio, J. L. Membrane Organization and Lipid Rafts. *Cold Spring Harb. Perspect. Biol.* **3**, a004697 (2011).

118. Go, Y. K., Kambar, N. & Leal, C. Hybrid Unilamellar Vesicles of Phospholipids and Block Copolymers with Crystalline Domains. *Polymers (Basel).* **12**, 1232 (2020).

119. Vega-Cabrera, L. A. & Pardo-López, L. Membrane remodeling and organization: Elements common to prokaryotes and eukaryotes. *IUBMB Life* **69**, 55–62 (2017).

120. Thamboo, S. *et al.* Mimicking Cellular Signaling Pathways within Synthetic Multicompartment Vesicles with Triggered Enzyme Activity and Induced Ion Channel Recruitment. *Adv. Funct. Mater.* **29**, 1904267 (2019).

121. Chen, A. H. & Silver, P. A. Designing biological compartmentalization. *Trends Cell Biol.* **22**, 662–670 (2012).

122. Peters, R. J. R. W. *et al.* Cascade reactions in multicompartmentalized polymersomes. *Angew. Chemie - Int. Ed.* **53**, 146–150 (2014).

123. Kostarelos, K. The emergence of nanomedicine: A field in the making. *Nanomedicine* **1**, 1–3 (2006).

124. Jia, R. *et al.* Advances in Multiple Stimuli-Responsive Drug-Delivery Systems for Cancer Therapy. *Int. J. Nanomedicine* **16**, 1525–1551 (2021).

125. Bhatia, S. N., Chen, X., Dobrovolskaia, M. A. & Lammers, T. Cancer nanomedicine. *Nat. Rev. Cancer* **22**, 550–556 (2022).

126. Sudheesh, M. S., Pavithran, K. & Sabitha, M. Revisiting the outstanding questions in cancer nanomedicine with a future outlook. *Nanoscale Adv.* **4**, 634–653 (2022).

127. Jahangirian, H., Lemraski, E. G., Webster, T. J., Rafiee-Moghaddam, R. & Abdollahi, Y. A review of drug delivery systems based on nanotechnology and green chemistry: green nanomedicine. *Int. J. Nanomedicine* **12**, 2957–2978 (2017).

128. Mitchell, M. J. *et al.* Engineering precision nanoparticles for drug delivery. *Nat. Rev. Drug Discov.* **20**, 101–124 (2021).

129. Patra, J. K. *et al.* Nano based drug delivery systems: recent developments and future prospects. *J. Nanobiotechnology* **16**, 1–33 (2018).

130. Suri, S. S., Fenniri, H. & Singh, B. Nanotechnology-based drug delivery systems. *J. Occup. Med. Toxicol.* **2**, 1–6 (2007).

131. Wilczewska, A. Z., Niemirowicz, K., Markiewicz, K. H. & Car, H. Nanoparticles as drug delivery systems. *Pharmacol. Rep.* **64**, 1020–1037 (2012).

132. Barenholz, Y. Doxil® — The first FDA-approved nano-drug: Lessons learned. *J. Control. Release* **160**, 117–134 (2012).

133. Lasic, D. D., Frederik, P. M., Stuart, M. C. A., Barenholz, Y. & McIntosh, T. J. Gelation of liposome interior A novel method for drug encapsulation. *FEBS Lett.* **312**, 255–258 (1992).

134. Shah, M. R., Imran, M. & Ullah, S. Liposomes. in *Lipid-Based Nanocarriers for Drug Delivery and Diagnosis* 63–110 (William Andrew Publishing, 2017).

135. Date, T. *et al.* Lipid-polymer hybrid nanocarriers for delivering cancer therapeutics. *J. Control. Release* **271**, 60–73 (2018).

136. Kiaie, S. H. *et al.* Axial pharmaceutical properties of liposome in cancer therapy: Recent advances and perspectives. *Int. J. Pharm.* **581**, 119269 (2020).

137. Sercombe, L. *et al.* Advances and challenges of liposome assisted drug delivery. *Front. Pharmacol.* **6**, 163819 (2015).

138. Moosavian, S. A., Bianconi, V., Pirro, M. & Sahebkar, A. Challenges and pitfalls in the development of liposomal delivery systems for cancer therapy. *Semin. Cancer Biol.* **69**, 337–348 (2021).

139. Pentak, D., Ploch-Jankowska, A., Zięba, A. & Kozik, V. The Advances and Challenges of Liposome-Assisted Drug Release in the Presence of Serum Albumin Molecules: The Influence of Surrounding pH. *Materials (Basel).* **15**, 1586 (2022).

140. Sung, Y. K. & Kim, S. W. Recent advances in polymeric drug delivery systems. *Biomater. Res.* **24**, 1–12 (2020).

141. Hafner, A., Lovrić, J., Lakŏ, G. P. & Pepić, I. Nanotherapeutics in the EU: An overview on current state and future directions. *Int. J. Nanomedicine* **9**, 1005–1023 (2014).

142. Zartner, L., Maffeis, V., Schoenenberger, C. A., Dinu, I. A. & Palivan, C. G. Membrane protein channels equipped with a cleavable linker for inducing catalysis inside nanocompartments. *J. Mater. Chem. B* **9**, 9012–9022 (2021).

143. Hossen, S. *et al.* Smart nanocarrier-based drug delivery systems for cancer therapy and toxicity studies: A review. *J. Adv. Res.* **15**, 1–18 (2019).

144. Askari, E. *et al.* Stimuli-Responsive Hydrogels for Local Post-Surgical Drug Delivery. *Gels* **6**, 14 (2020).

145. Tang, Q. *et al.* Stimuli Responsive Nanoparticles for Controlled Anti-cancer Drug Release. *Curr. Med. Chem.* **25**, 1837–1866 (2018).

146. Mu, Y., Gong, L., Peng, T., Yao, J. & Lin, Z. Advances in pH-responsive drug delivery systems. *OpenNano* **5**, 100031 (2021).

147. Debabrata, G. D. & Chakrabarti, G. Thermoresponsive Drug Delivery Systems, Characterization and Application. in *Applications of Targeted Nano Drugs and Delivery Systems: Nanoscience and Nanotechnology in Drug Delivery* 133–155 (Elsevier, 2019).

148. Yang, H. Y., Li, Y. & Lee, D. S. Multifunctional and Stimuli-Responsive Magnetic Nanoparticle-Based Delivery Systems for Biomedical Applications. *Adv. Ther.* **1**, 1800011 (2018).

149. Liu, Y. *et al.* An Electric-Field Responsive Microsystem for Controllable Miniaturised Drug Delivery Applications. *Procedia Eng.* **25**, 984–987 (2011).

150. Qian, B., Zhao, Q. & Ye, X. Ultrasound and Magnetic Responsive Drug Delivery Systems for Cardiovascular Application. *J. Cardiovasc. Pharmacol.* **76**, 414–426 (2020).

151. Lopes, J. R., Santos, G., Barata, P., Oliveira, R. & Lopes, C. M. Physical and Chemical Stimuli-Responsive Drug Delivery Systems: Targeted Delivery and Main Routes of Administration. *Curr. Pharm. Des.* **19**, 7169–7184 (2013).

152. Yun, S. H. & Kwok, S. J. J. Light in diagnosis, therapy and surgery. *Nat. Biomed. Eng.* **1**, 1–16 (2017).

153. Pianowski, Z. L. Molecular Photoswitches: Chemistry, Properties, and Applications. in *Molecular Photoswitches* 1–1112 (Wiley-VCH Verlag, 2022).

154. Vickerman, B. M., Zywot, E. M., Tarrant, T. K. & Lawrence, D. S. Taking phototherapeutics from concept to clinical launch. *Nat. Rev. Chem.* **5**, 816–834 (2021).

155. Mulatihan, D., Guo, T. & Zhao, Y. Azobenzene Photoswitch for Isomerization-Dependent Cancer Therapy via Azo-Combretastatin A4 and Phototrexate. *Photochem. Photobiol.* **96**, 1163–1168 (2020).

156. Wang, G. & Zhang, J. Photoresponsive molecular switches for biotechnology. *J. Photochem. Photobiol. C Photochem. Rev.* **13**, 299–309 (2012).

157. Twieg, R. J. *et al.* Photodegradation of azobenzene nonlinear optical chromophores: the influence of structure and environment. *JOSA B* **17**, 1992–2000 (2000).

158. Joseph, J. M., Destaillats, H., Hung, H. M. & Hoffmann, M. R. The Sonochemical Degradation of Azobenzene and Related Azo Dyes: Rate Enhancements via Fenton's Reactions. *J. Phys. Chem. A* **104**, 301–307 (2000).

159. Matsumura, Y. & Ananthaswamy, H. N. Toxic effects of ultraviolet radiation on the skin. *Toxicol. Appl. Pharmacol.* **195**, 298–308 (2004).

160. Welleman, I. M., Hoorens, M. W. H., Feringa, B. L., Boersma, H. H. & Szymański, W. Photoresponsive molecular tools for emerging applications of light in medicine. *Chem. Sci.* **11**, 11672–11691 (2020).

161. Kistemaker, J. C. M., Lubbe, A. S. & Feringa, B. L. Exploring molecular motors. *Mater. Chem. Front.* **5**, 2900–2906 (2021).

162. Pooler, D. R. S., Lubbe, A. S., Crespi, S. & Feringa, B. L. Designing light-driven rotary molecular motors. *Chem. Sci.* **12**, 14964–14986 (2021).

163. Koumura, N., Zijistra, R. W. J., Van Delden, R. A., Harada, N. & Feringa, B. L. Light-driven monodirectional molecular rotor. *Nature* **401**, 152–155 (1999).

164. Stähler, C. *et al.* Light-driven molecular motors embedded in covalent organic frameworks. *Chem. Sci.* **13**, 8253–8264 (2022).

165. Freese, T. *et al.* A molecular motor from lignocellulose. *Green Chem.* **24**, 3689–3696 (2022).

166. Xu, F. *et al.* Dynamic Control of a Multistate Chiral Supramolecular Polymer in Water. *J. Am. Chem. Soc.* **144**, 6019–6027 (2022).

167. Chen, S. *et al.* Photoactuating Artificial Muscles of Motor Amphiphiles as an Extracellular Matrix Mimetic Scaffold for Mesenchymal Stem Cells. *J. Am. Chem. Soc.* **144**, 3543–3553 (2022).

168. Palivan, C. G. *et al.* Bioinspired polymer vesicles and membranes for biological and medical applications. *Chem. Soc. Rev.* **45**, 377–411 (2016).

169. Korpidou, M. *et al.* Inverting glucuronidation of hymecromone in situ by catalytic nanocompartments. *J. Mater. Chem. B* **10**, 3916–3926 (2022).

170. Abdelmohsen, L. K. E. A., Rikken, R. S. M., Christianen, P. C. M., van Hest, J. C. M. & Wilson, D. A. Shape characterization of polymersome morphologies via light scattering techniques. *Polymer (Guildf).* **107**, 445–449 (2016).

171. Doane, T. L., Chuang, C. H., Hill, R. J. & Burda, C. Nanoparticle ζ -potentials. *Acc. Chem. Res.* **45**, 317–326 (2012).

172. Swineharf, D. F., The, E. & Law, B.-L. The Beer-Lambert Law. *J. Chem. Educ.* **39**, 333–335 (1962).

173. Pabst, G., Rappolt, M., Amenitsch, H. & Laggner, P. Structural information from multilamellar liposomes at full hydration: Full *q*-range fitting with high quality x-ray data. *Phys. Rev. E* **62**, 4000 (2000).

174. Clark, G. N. I., Hura, G. L., Teixeira, J., Soper, A. K. & Head-Gordon, T. Small-angle scattering and the structure of ambient liquid water. *Proc. Natl. Acad. Sci. U. S. A.* **107**, 14003–14007 (2010).

175. Hamann, S. *et al.* Measurement of Cell Volume Changes by Fluorescence Self-Quenching. *J. Fluoresc.* **12**, 139–145 (2002).

176. Chattopadhyay, S., Moran, R. G. & Goldman, I. D. Pemetrexed: biochemical and cellular pharmacology, mechanisms, and clinical applications. *Mol. Cancer Ther.* **6**, 404–417 (2007).

177. Soni, K., Mujtaba, A. & Kohli, K. Lipid drug conjugate nanoparticle as a potential nanocarrier for the oral delivery of pemetrexed diacid: Formulation design, characterization, ex vivo, and in vivo assessment. *Int. J. Biol. Macromol.* **103**, 139–151 (2017).

178. Pangeni, R., Choi, J. U., Panth, V. K., Byun, Y. & Park, J. W. Enhanced oral absorption of pemetrexed by ion-pairing complex formation with deoxycholic acid derivative and multiple nanoemulsion formulations: preparation, characterization, and in vivo oral

bioavailability and anticancer effect. *Int. J. Nanomedicine* **13**, 3329–3351 (2018).

179. Maharjan, R. *et al.* Metronomic delivery of orally available pemetrexed-incorporated colloidal dispersions for boosting tumor-specific immunity. *Drug Deliv.* **28**, 2313–2328 (2021).

180. Balasubramanian, V. *et al.* A surprising system: polymeric nanoreactors containing a mimic with dual-enzyme activity. *Soft Matter* **7**, 5595–5603 (2011).

181. Adjei, A. A. Pharmacology and mechanism of action of pemetrexed. *Clin. Lung Cancer* **5**, S51–S55 (2004).

182. Stanley, L. A. Drug Metabolism. in *Pharmacognosy* 597–624 (Academic Press, 2024).

183. Longo, L. P. & Johnson, B. Addiction: Part I. Benzodiazepines-Side Effects, Abuse Risk and Alternatives. *Am. Fam. Physician* **61**, 2121–2128 (2000).

184. Sproule, B., Brands, B., Li, S. & Catz-Biro, L. Changing patterns in opioid addiction: Characterizing users of oxycodone and other opioids. *Can. Fam. Physician* **55**, 68–69 (2009).

185. Cao, S., Lv, Z., Guo, S., Jiang, G. & Liu, H. An update - Prolonging the action of protein and peptide drugs. *J. Drug Deliv. Sci. Technol.* **61**, 102124 (2021).

186. Tan, C., Wang, J. & Sun, B. Biopolymer-liposome hybrid systems for controlled delivery of bioactive compounds: Recent advances. *Biotechnol. Adv.* **48**, 107727 (2021).

187. Gu, W. *et al.* CD44-Specific A6 Short Peptide Boosts Targetability and Anticancer Efficacy of Polymersomal Epirubicin to Orthotopic Human Multiple Myeloma. *Adv. Mater.* **31**, 1904742 (2019).

188. Upadhyay, K. K. *et al.* The in vivo behavior and antitumor activity of doxorubicin-loaded poly(γ-benzyl l-glutamate)-block-hyaluronan polymersomes in Ehrlich ascites tumor-bearing BalB/c mice. *Nanomedicine Nanotechnology, Biol. Med.* **8**, 71–80 (2012).

189. Dhapte, V. & Pokharkar, V. Nanosystems for drug delivery: Design, engineering, and applications. in *Green Synthesis, Characterization and Applications of Nanoparticles* 321–345 (Elsevier, 2019).

190. Li, X. *et al.* Polymeric Nanoreactors as Emerging Nanoplatforms for Cancer Precise Nanomedicine. *Macromol. Biosci.* **21**, 2000424 (2021).

191. Kumar Upadhyay, K. *et al.* Biomimetic doxorubicin loaded polymersomes from

hyaluronan-block- poly(γ-benzyl glutamate) copolymers. *Biomacromolecules* **10**, 2802–2808 (2009).

192. Bermudez, H., Brannan, A. K., Hammer, D. A., Bates, F. S. & Discher, D. E. Molecular weight dependence of polymersome membrane structure, elasticity, and stability. *Macromolecules* **35**, 8203–8208 (2002).

193. Du, J. & O'Reilly, R. K. Advances and challenges in smart and functional polymer vesicles. *Soft Matter* **5**, 3544–3561 (2009).

194. Oliveira, H. *et al.* Magnetic field triggered drug release from polymersomes for cancer therapeutics. *J. Control. Release* **169**, 165–170 (2013).

195. Bialas, F., Reichinger, D. & Becker, C. F. W. Biomimetic and biopolymer-based enzyme encapsulation. *Enzyme Microb. Technol.* **150**, 109864 (2021).

196. Sueyoshi, D., Anraku, Y., Komatsu, T., Urano, Y. & Kataoka, K. Enzyme-Loaded Polyion Complex Vesicles as in Vivo Nanoreactors Working Sustainably under the Blood Circulation: Characterization and Functional Evaluation. *Biomacromolecules* **18**, 1189–1196 (2017).

197. Anraku, Y. *et al.* Systemically Injectable Enzyme-Loaded Polyion Complex Vesicles as In Vivo Nanoreactors Functioning in Tumors. *Angew. Chemie Int. Ed.* **55**, 560–565 (2016).

198. Spulber, M. *et al.* Poly(N-vinylpyrrolidone)-poly(dimethylsiloxane)-based polymersome nanoreactors for laccase-catalyzed biotransformations. *Biomacromolecules* **15**, 1469–1475 (2014).

199. Kim, B. S. *et al.* Noncovalent Stabilization of Vesicular Polyion Complexes with Chemically Modified/Single-Stranded Oligonucleotides and PEG-b-guanidinylated Polypeptides for Intracavity Encapsulation of Effector Enzymes Aimed at Cooperative Gene Knockdown. *Biomacromolecules* **21**, 4365–4376 (2020).

200. Takeda, S. & Aburada, M. The choleretic mechanism of coumarin compounds and phenolic compounds. *J. Pharmacobiodyn.* **4**, 724–734 (1981).

201. Nagy, N. *et al.* 4-Methylumbelliferyl glucuronide contributes to hyaluronan synthesis inhibition. *J. Biol. Chem.* **294**, 7864–7877 (2019).

202. Nagy, N. *et al.* Inhibition of hyaluronan synthesis restores immune tolerance during autoimmune insulitis. *J. Clin. Invest.* **125**, 3928–3940 (2015).

203. Li, W. *et al.* SARS-CoV-2 RNA elements share human sequence identity and

upregulate hyaluronan via NamiRNA-enhancer network. *eBioMedicine* **76**, (2022).

204. Turgeon, D., Carrier, J. S., Lévesque, E., Hum, D. W. & Bélanger, A. Relative enzymatic activity, protein stability, and tissue distribution of human steroid-metabolizing UGT2B subfamily members. *Endocrinology* **142**, 778–787 (2001).

205. Kuipers, H. F. *et al.* The pharmacokinetics and dosing of oral 4-methylumbelliferone for inhibition of hyaluronan synthesis in mice. *Clin. Exp. Immunol.* **185**, 372–381 (2016).

206. Garrett, E. R., Venitz, J., Eberst, K. & Cerda, J. J. Pharmacokinetics and bioavailabilities of hymecromone in human volunteers. *Biopharm. Drug Dispos.* **14**, 13–39 (1993).

207. Song, X., Jiang, Z., Li, L. & Wu, H. Immobilization of β-glucuronidase in lysozyme-induced biosilica particles to improve its stability. *Front. Chem. Sci. Eng.* **8**, 353–361 (2014).

208. Yeom, S.-J. *et al.* Controlled Aggregation and Increased Stability of β-Glucuronidase by Cellulose Binding Domain Fusion. *PLoS One* **12**, e0170398 (2017).

209. Kemp, P. M. & Cliburn, K. D. *Federal Aviation Administration Comparison of Species-Specific β-Glucuronidase Hydrolysis of Cannabinoid Metabolites in Human Urine. FAA Civil Aerospace Medical Institute* www.faa.gov/go/oamtechreports (2015).

210. Garrett, E. R. & Venitz, J. Comparisons of Detections, Stabilities, and Kinetics of Degradation of Hymecromone and Its Glucuronide and Sulfate Metabolites. *J. Pharm. Sci.* **83**, 115–116 (1994).

211. Kiene, K. *et al.* PDMS-b-PMOXA polymersomes for hepatocyte targeting and assessment of toxicity. *Eur. J. Pharm. Biopharm.* **119**, 322–332 (2017).

212. Wehr, R. *et al.* Fully amorphous atactic and isotactic block copolymers and their self-assembly into nano- and microscopic vesicles. *Polym. Chem.* **37**, 5377–5389 (2021).

213. Liu, K., Wang, X., Li-Blatter, X., Wolf, M. & Hunziker, P. Systematic and Quantitative Structure-Property Relationships of Polymeric Medical Nanomaterials: From Systematic Synthesis and Characterization to Computer Modeling and Nano-Bio Interaction and Toxicity. *ACS Appl. Bio Mater.* **3**, 6919–6931 (2020).

214. Daubian, D., Gaitzsch, J. & Meier, W. Synthesis and complex self-assembly of amphiphilic block copolymers with a branched hydrophobic poly(2-oxazoline) into

multicompartment micelles, pseudo-vesicles and yolk/shell nanoparticles. *Polym. Chem.* **11**, 1237–1248 (2020).

215. Chen, Q., Schönherr, H. & Vancso, G. J. Block-copolymer vesicles as nanoreactors for enzymatic reactions. *Small* **5**, 1436–1445 (2009).

216. Moquin, A., Ji, J., Neibert, K., Winnik, F. M. & Maysinger, D. Encapsulation and Delivery of Neutrophic Proteins and Hydrophobic Agents Using PMOXA-PDMS-PMOXA Triblock Polymersomes. *ACS Omega* **3**, 13882–13893 (2018).

217. Mertz, M. & Castiglione, K. Increased protein encapsulation in polymersomes with hydrophobic membrane anchoring peptides in a scalable process. *Int. J. Mol. Sci.* **22**, 7134 (2021).

218. Martin, T., Wöhner, R.-V., Hummel, S., Willmitzer, L. & Frommer, W. B. The GUS Reporter System as a Tool to Study Plant Gene Expression. in *Gus Protocols: Using the GUS Gene as a Reporter of Gene Expression* (ed. Gallagher, S. R.) 23–43 (Academic press, 1992).

219. Dashnyam, P. *et al.* β-Glucuronidases of opportunistic bacteria are the major contributors to xenobiotic-induced toxicity in the gut. *Sci. Rep.* **8**, 1–12 (2018).

220. Zotter, A., Bäuerle, F., Dey, D., Kiss, V. & Schreiber, G. Quantifying enzyme activity in living cells. *J. Biol. Chem.* **292**, 15838–15848 (2017).

221. Segel, L. A. & Slemrod, M. The Quasi-Steady-State Assumption: A Case Study in Perturbation. *SIAM Rev.* **31**, 446–477 (1989).

222. Varlas, S. *et al.* Tuning the membrane permeability of polymersome nanoreactors developed by aqueous emulsion polymerization-induced self-assembly. *Nanoscale* **11**, 12643–12654 (2019).

223. Chen, Q., Kristin, G. R., Schönherr, H. & Vancso, G. J. α-Chymotrypsin-Catalyzed Reaction Confined in Block-Copolymer Vesicles. *ChemPhysChem* **11**, 3534–3540 (2010).

224. van Eunen, K. & Bakker, B. M. The importance and challenges of in vivo-like enzyme kinetics. *Perspect. Sci.* **1**, 126–130 (2014).

225. Eisenthal, R., Danson, M. J. & Hough, D. W. Catalytic efficiency and kcat/KM: a useful comparator? *Trends Biotechnol.* **25**, 247–249 (2007).

226. Hoffmann, R. M., Schwarz, G., Pohl, C., Ziegenhagen, D. J. & Kruis, W. Gallensäure-unabhängige wirkung von hymecromon auf die gallesekretion und die motilität der

gallenwege. *Dtsch. Medizinische Wochenschrift* **130**, 1938–1943 (2005).

227. Kundu, B., Saha, P., Datta, K. & Kundu, S. C. A silk fibroin based hepatocarcinoma model and the assessment of the drug response in hyaluronan-binding protein 1 overexpressed HepG2 cells. *Biomaterials* **34**, 9462–9474 (2013).

228. Piccioni, F. *et al.* Antitumor effects of hyaluronic acid inhibitor 4-methylumbelliferone in an orthotopic hepatocellular carcinoma model in mice. *Glycobiology* **22**, 400–410 (2012).

229. Buttke, T. M., McCubrey, J. A. & Owen, T. C. Use of an aqueous soluble tetrazolium/formazan assay to measure viability and proliferation of lymphokine-dependent cell lines. *J. Immunol. Methods* **157**, 233–240 (1993).

230. Nakamura, T. *et al.* Effect of 4-methylumbelliferone on cell-free-synthesis of hyaluronic acid. *Biochem. Mol. Biol. Int.* **43**, 263–268 (1997).

231. Lokeshwar, V. B. *et al.* Antitumor activity of hyaluronic acid synthesis inhibitor 4-methylumbelliferone in prostate cancer cells. *Cancer Res.* **70**, 2613–2623 (2010).

232. Kakizaki, I. *et al.* A novel mechanism for the inhibition of hyaluronan biosynthesis by 4-methylumbelliferone. *J. Biol. Chem.* **279**, 33281–33289 (2004).

233. Kakizaki, I. *et al.* Inhibition of hyaluronan synthesis in Streptococcus equi FM100 by 4-methylumbelliferone. *Eur. J. Biochem.* **269**, 5066–5075 (2002).

234. Kishnani, P. S. Challenges of Enzyme Replacement Therapy: Poor Tissue Distribution in Lysosomal Diseases Using Pompe Disease as a Model. *AAPS Adv. Pharm. Sci. Ser.* **19**, 9–21 (2015).

235. Biela, B. H., Khawli, L. A., Hu, P. & Epstein, A. L. Chimeric TNT-3/human β-glucuronidase fusion proteins for antibody-directed enzyme prodrug therapy (ADEPT). *Cancer Biother. Radiopharm.* **18**, 339–353 (2003).

236. De Vocht, C. *et al.* Assessment of stability, toxicity and immunogenicity of new polymeric nanoreactors for use in enzyme replacement therapy of MNGIE. *J. Control. Release* **137**, 246–254 (2009).

237. Nagy, N. *et al.* 4-Methylumbelliferone treatment and hyaluronan inhibition as a therapeutic strategy in inflammation, autoimmunity, and cancer. *Front. Immunol.* **6**, 134238 (2015).

238. Zelmer, C. *et al.* Organelle-specific targeting of polymersomes into the cell nucleus. *PNAS* **117**, 2770–2778 (2020).

239. Suk, J. S., Xu, Q., Kim, N., Hanes, J. & Ensign, L. M. PEGylation as a strategy for improving nanoparticle-based drug and gene delivery. *Adv. Drug Deliv. Rev.* **99**, 28 (2016).

240. Maffeis, V. *et al.* A DNA-Micropatterned Surface for Propagating Biomolecular Signals by Positional on-off Assembly of Catalytic Nanocompartments. *Small* **19**, 2202818 (2023).

241. Nishimura, T., Akiyoshi, K., Nishimura, T. & Akiyoshi, K. Biotransporting Biocatalytic Reactors toward Therapeutic Nanofactories. *Adv. Sci.* **5**, 1800801 (2018).

242. Kudo, M. A Paradigm Change in the Treatment Strategy for Hepatocellular Carcinoma. *Liver cancer* **9**, 367–377 (2020).

243. Sonbol, M. B. *et al.* Systemic Therapy and Sequencing Options in Advanced Hepatocellular Carcinoma: A Systematic Review and Network Meta-analysis. *JAMA Oncol.* **6**, e204930 (2020).

244. Li, J. *et al.* Polymer Prodrug-Based Nanoreactors Activated by Tumor Acidity for Orchestrated Oxidation/Chemotherapy. *Nano Lett.* **17**, 6983–6990 (2017).

245. Wang, Y. *et al.* Ferrocene-containing polymersome nanoreactors for synergistically amplified tumor-specific chemodynamic therapy. *J. Control. Release* **333**, 500–510 (2021).

246. Che, H., Cao, S. & Van Hest, J. C. M. Feedback-Induced Temporal Control of 'Breathing' Polymersomes To Create Self-Adaptive Nanoreactors. *J. Am. Chem. Soc* **140**, 52 (2018).

247. Rasool, M. *et al.* New challenges in the use of nanomedicine in cancer therapy. *Bioengineered* **13**, 759 (2022).

248. Onzi, G., Guterres, S. S., Pohlmann, A. R. & Frank, L. A. Active Targeting of Nanocarriers. in *The ADME Encyclopedia* 1–13 (Springer, Cham, 2021).

249. Deng, H. *et al.* Targeted-detection and sequential-treatment of small hepatocellular carcinoma in the complex liver environment by GPC-3-targeted nanoparticles. *J. Nanobiotechnology* **20**, 1–20 (2022).

250. Maffeis, V. *et al.* Advancing the design of artificial nano-organelles for targeted cellular detoxification of reactive oxygen species. *NanoLetters* **24**, 2698–2704 (2024).

251. Awolade, P. *et al.* Therapeutic significance of β-glucuronidase activity and its inhibitors: A review. *Eur. J. Med. Chem.* **187**, 111921 (2020).

252. Compain, G. *et al.* A β-glucuronidase-responsive albumin-binding prodrug for potential selective kinase inhibitor-based cancer chemotherapy. *Eur. J. Med. Chem.* **158**, 1–6 (2018).

253. Wang, C., Yang, J., Dong, C. & Shi, S. Glucose Oxidase-Related Cancer Therapies. *Adv. Ther.* **3**, 2000110 (2020).

254. Wang, M. *et al.* Recent Advances in Glucose-Oxidase-Based Nanocomposites for Tumor Therapy. *Small* **15**, 1903895 (2019).

255. Imlay, J. A., Chin, S. M. & Linn, S. Toxic DNA Damage by Hydrogen Peroxide Through the Fenton Reaction in Vivo and in Vitro. *Science (80-.).* **240**, 640–642 (1988).

256. Tochigi, M. *et al.* Hydrogen peroxide induces cell death in human TRAIL-resistant melanoma through intracellular superoxide generation. *Int. J. Oncol.* **42**, 863–872 (2013).

257. Perillo, B. *et al.* ROS in cancer therapy: the bright side of the moon. *Exp. Mol. Med.* **52**, 192–203 (2020).

258. Zhang, X. & Zhang, P. Polymersomes in Nanomedicine - A Review. *Curr. Med. Chem.* **13**, 124 (2017).

259. Guinart, A. *et al.* Synthetic Molecular Motor Activates Drug Delivery from Polymersomes. *PNAS* **120**, e2301279120 (2023).

260. van der Zande, H. J. P., Nitsche, D., Schlautmann, L., Guigas, B. & Burgdorf, S. The Mannose Receptor: From Endocytic Receptor and Biomarker to Regulator of (Meta)Inflammation. *Front. Immunol.* **12**, 765034 (2021).

261. Jiang, Q. L. *et al.* Plant lectins, from ancient sugar-binding proteins to emerging anti-cancer drugs in apoptosis and autophagy. *Cell Prolif.* **48**, 17–28 (2015).

262. Nangia-Makker, P., Conklin, J., Hogan, V. & Raz, A. Carbohydrate-binding proteins in cancer, and their ligands as therapeutic agents. *Trends Mol. Med.* **8**, 187–192 (2002).

263. Bouffard, E. *et al.* Why Anticancer Nanomedicine Needs Sugars? *Curr. Med. Chem.* **22**, 3014–3024 (2015).

264. S. Eroglu, M., Toksoy Oner, E., Cansever Mutlu, E. & Sennaroglu Bostan, M. Sugar Based Biopolymers in Nanomedicine; New Emerging Era for Cancer Imaging and Therapy. *Curr. Top. Med. Chem.* **17**, 1507–1520 (2017).

265. Wu, J. *et al.* Dual-responsive core crosslinking glycopolymer-drug conjugates

nanoparticles for precise hepatocarcinoma therapy. *Front. Pharmacol.* **9**, 392470 (2018).

266. Li, J. *et al.* Collaborative assembly of doxorubicin and galactosyl diblock glycopolymers for targeted drug delivery of hepatocellular carcinoma. *Biomater. Sci.* **8**, 189–200 (2019).

267. Demir Duman, F., Monaco, A., Foulkes, R., Becer, C. R. & Forgan, R. S. Glycopolymer-Functionalized MOF-808 Nanoparticles as a Cancer-Targeted Dual Drug Delivery System for Carboplatin and Floxuridine. *ACS Appl. Nano Mater.* **5**, 13862–13873 (2022).

268. Guan, C. *et al.* Glycosylated liposomes loading carbon dots for targeted recognition to HepG2 cells. *Talanta* **182**, 314–323 (2018).

269. Gou, Y. *et al.* A Detailed Study on Understanding Glycopolymer Library and Con A Interactions. *J. Polym. Sci. A. Polym. Chem.* **51**, 2588 (2013).

270. Yilmaz, G. & Becer, C. R. Glycopolymer code based on well-defined glycopolymers or glyconanomaterials and their biomolecular recognition. *Front. Bioeng. Biotechnol.* **2**, 104561 (2014).

271. Gadekar, A. *et al.* A Glycotherapeutic Approach to Functionalize Biomaterials-Based Systems. *Adv. Funct. Mater.* **30**, 1910031 (2020).

272. Gupta, A. & Gupta, G. S. Applications of mannose-binding lectins and mannan glycoconjugates in nanomedicine. *J. Nanoparticle Res.* **24**, 1–31 (2022).

273. Philips, C. A. *et al.* Hepatocellular Carcinoma in 2021: An Exhaustive Update. *Cureus* **13**, e19274 (2021).

274. Lin, S. *et al.* Ultrasound-responsive glycopolymer micelles for targeted dual drug delivery in cancer therapy. *Biomater. Sci.* **11**, 6149–6159 (2023).

275. Jiang, M. *et al.* Preparation of CdSe QDs-carbohydrate Conjugation and its Application for HepG2 Cells Labeling. *Bull. KOREAN Chem. Soc.* **33**, 571–574 (2012).

276. Das, R. K. & Mohapatra, S. Highly luminescent, heteroatom-doped carbon quantum dots for ultrasensitive sensing of glucosamine and targeted imaging of liver cancer cells. *J. Mater. Chem. B* **5**, 2190–2197 (2017).

277. Fan, W. *et al.* Identification of CD206 as a potential biomarker of cancer stem-like cells and therapeutic agent in liver cancer. *Oncol. Lett.* **18**, 3218–3226 (2019).

278. Frison, N. *et al.* Oligolysine-based Oligosaccharide Clusters. *J. Biol. Chem.* **278**,

23922–23929 (2003).

279. Hartweg, M. *et al.* Synthetic Glycomacromolecules of Defined Valency, Absolute Configuration, and Topology Distinguish between Human Lectins. *JACS Au* **1**, 1621–1630 (2021).

280. Tapia, L. *et al.* Metallothionein is crucial for safe intracellular copper storage and cell survival at normal and supra-physiological exposure levels. *Biochem. J.* **378**, 617–624 (2004).

281. Zhao, T. *et al.* Hierarchy of Complex Glycomacromolecules: From Controlled Topologies to Biomedical Applications. *Biomacromolecules* **23**, 543–575 (2022).

282. Becker, J., Terracciano, R., Yilmaz, G., Napier, R. & Becer, C. R. Step-Growth Glycopolymers with a Defined Tacticity for Selective Carbohydrate-Lectin Recognition. *Biomacromolecules* **24**, 1924–1933 (2023).

283. Turner, M. W. The role of mannose-binding lectin in health and disease. *Mol. Immunol.* **40**, 423–429 (2003).

284. Osorio, F. & Reis e Sousa, C. Myeloid C-type lectin receptors in pathogen recognition and host defense. *Immunity* **34**, 651–664 (2011).

285. Geijtenbeek, T. B. H. *et al.* DC-SIGN, a Dendritic Cell–Specific HIV-1-Binding Protein that Enhances trans-Infection of T Cells. *Cell* **100**, 587–597 (2000).

286. Herre, J., Gordon, S. & Brown, G. D. Dectin-1 and its role in the recognition of β-glucans by macrophages. *Mol. Immunol.* **40**, 869–876 (2004).

287. Yu, L. *et al.* A Comprehensive Review of Fluorescence Correlation Spectroscopy. *Front. Phys.* **9**, 644450 (2021).

288. Opanasopit, P. *et al.* In vivo recognition of mannosylated proteins by hepatic mannose receptors and mannan-binding protein. *Am. J. Physiol. - Gastrointest. Liver Physiol.* **280**, G879–G889 (2001).

289. Segat, L. *et al.* MBL2 and MASP2 gene polymorphisms in patients with hepatocellular carcinoma. *J. Viral Hepat.* **15**, 387–391 (2008).

290. Eurich, D. *et al.* Association of mannose-binding lectin-2 gene polymorphism with the development of hepatitis C-induced hepatocellular carcinoma. *Liver Int.* **31**, 1006–1012 (2011).

291. Neglia, L. *et al.* Mannose-binding lectin has a direct deleterious effect on ischemic brain microvascular endothelial cells. *J. Cereb. Blood Flow Metab.* **40**, 1608–1620

(2020).

292. Li, J. *et al.* Mannan-binding lectin suppresses growth of hepatocellular carcinoma by regulating hepatic stellate cell activation via the ERK/COX-2/PGE2 pathway. *Oncoimmunology* **8**, e1527650 (2018).

293. Thompson, D. B., Villaseñor, R., Dorr, B. M., Zerial, M. & Liu, D. R. Cellular Uptake Mechanisms and Endosomal Trafficking of Supercharged Proteins. *Chem. Biol.* **19**, 831 (2012).

294. Wang, F. *et al.* Recent progress of cell-penetrating peptides as new carriers for intracellular cargo delivery. *J. Control. Release* **174**, 126–136 (2014).

295. Park, K. C., Dharmasivam, M. & Richardson, D. R. The Role of Extracellular Proteases in Tumor Progression and the Development of Innovative Metal Ion Chelators That Inhibit Their Activity. *Int. J. Mol. Sci.* **21**, 1–22 (2020).

296. Yan, F., Chen, Y., Azat, R. & Zheng, X. Mulberry Anthocyanin Extract Ameliorates Oxidative Damage in HepG2 Cells and Prolongs the Lifespan of Caenorhabditis elegans through MAPK and Nrf2 Pathways. *Oxid. Med. Cell. Longev.* **2017**, (2017).

297. Benitez, A., Yates, T. J., Shamaldevi, N., Bowen, T. & Lokeshwar, V. B. Dietary Supplement Hymecromone and Sorafenib: A Novel Combination for the Control of Renal Cell Carcinoma. *J. Urol.* **190**, 285–290 (2013).

298. Kang, M. *et al.* Glucose Deprivation Induces Cancer Cell Death through Failure of ROS Regulation. *Int. J. Mol. Sci.* **24**, 11969 (2023).

299. Nagase, H. *et al.* 4-Methylumbelliferone Suppresses Hyaluronan Synthesis and Tumor Progression in SCID Mice Intra-abdominally Inoculated With Pancreatic Cancer Cells. *Pancreas* **46**, 190 (2017).

300. Bradshaw, R. A. & Dennis, E. A. *Handbook of Cell Signaling*. vols 1–3 (Elsevier, 2003).

301. Antebi, Y. E., Nandagopal, N. & Elowitz, M. B. An operational view of intercellular signaling pathways. *Curr. Opin. Syst. Biol.* **1**, 16–24 (2017).

302. Robinson, A. O., Venero, O. M. & Adamala, K. P. Toward synthetic life: Biomimetic synthetic cell communication. *Curr. Opin. Chem. Biol.* **64**, 165–173 (2021).

303. Smith, J. M., Chowdhry, R. & Booth, M. J. Controlling Synthetic Cell-Cell Communication. *Front. Mol. Biosci.* **8**, 809945 (2022).

304. Noireaux, V. & Libchaber, A. A vesicle bioreactor as a step toward an artificial cell

assembly. *Proc. Natl. Acad. Sci. U. S. A.* **101**, 17669–17674 (2004).

305. Kurihara, K. *et al.* Self-reproduction of supramolecular giant vesicles combined with the amplification of encapsulated DNA. *Nat. Chem.* **3**, 775–781 (2011).

306. Chakraborty, T. & Wegner, S. V. Cell to Cell Signaling through Light in Artificial Cell Communities: Glowing Predator Lures Prey. *ACS Nano* **15**, 9434–9444 (2021).

307. Altenburg, W. J. *et al.* Programmed spatial organization of biomacromolecules into discrete, coacervate-based protocells. *Nat. Commun.* **11**, 1–10 (2020).

308. Buddingh', B. C., Elzinga, J. & van Hest, J. C. M. Intercellular communication between artificial cells by allosteric amplification of a molecular signal. *Nat. Commun.* **11**, 1–10 (2020).

309. Jiang, W. *et al.* Artificial Cells: Past, Present and Future. *ACS Nano* **16**, 15705–15733 (2022).

310. Ghosh, B. Artificial cell design: reconstructing biology for life science applications. *Emerg. Top. life Sci.* **6**, 619–627 (2022).

311. Elani, Y., Law, R. V. & Ces, O. Vesicle-based artificial cells as chemical microreactors with spatially segregated reaction pathways. *Nat. Commun.* **5**, 1–5 (2014).

312. Cochereau, R., Maffeis, V., dos Santos, E. C., Lörtscher, E. & Palivan, C. G. Polymeric Giant Unilamellar Vesicles with Integrated DNA-Origami Nanopores: An Efficient Platform for Tuning Bioreaction Dynamics Through Controlled Molecular Diffusion. *Adv. Funct. Mater.* **33**, 2304782 (2023).

313. Tang, T. Y. D. *et al.* Gene-Mediated Chemical Communication in Synthetic Protocell Communities. *ACS Synth. Biol.* **7**, 339–346 (2018).

314. Marušič, N. *et al.* Constructing artificial respiratory chain in polymer compartments: Insights into the interplay between bo3 oxidase and the membrane. *Proc. Natl. Acad. Sci. U. S. A.* **117**, 15006–15017 (2020).

315. Biner, O., Fedor, J. G., Yin, Z. & Hirst, J. Bottom-Up Construction of a Minimal System for Cellular Respiration and Energy Regeneration. *ACS Synth. Biol.* **9**, 1450–1459 (2020).

316. Dolder, N., Müller, P. & von Ballmoos, C. Experimental platform for the functional investigation of membrane proteins in giant unilamellar vesicles. *Soft Matter* **18**, 5877–5893 (2022).

317. Deng, N. N., Yelleswarapu, M., Zheng, L. & Huck, W. T. S. Microfluidic Assembly of

Monodisperse Vesosomes as Artificial Cell Models. *J. Am. Chem. Soc.* **139**, 587–590 (2017).

318. Heuberger, L. *et al.* Microfluidic Giant Polymer Vesicles Equipped with Biopores for High-Throughput Screening of Bacteria. *Adv. Sci.* 2307103 (2023) doi:10.1002/ADVS.202307103.

319. Krizaj, D. & Copenhagen, D. R. CALCIUM REGULATION IN PHOTORECEPTORS. *Front. Biosci.* 7, d2023 (2002).

320. Thoreson, W. B. Transmission at rod and cone ribbon synapses in the retina. *Pflugers Arch.* **473**, 1469–1491 (2021).

321. Park, B. *et al.* Artificial Rod and Cone Photoreceptors with Human-Like Spectral Sensitivities. *Adv. Mater.* **30**, 1706764 (2018).

322. Coats, J. P. *et al.* Trends in the Synthesis of Polymer Nano- and Microscale Materials for Bio-Related Applications. *Macromol. Biosci.* **23**, (2023).

323. Deshpande, S., Caspi, Y., Meijering, A. E. C. & Dekker, C. Octanol-assisted liposome assembly on chip. *Nat. Commun.* 7, 1–9 (2016).

324. Schvartzman, C. *et al.* Control of Enzyme Reactivity in Response to Osmotic Pressure Modulation Mimicking Dynamic Assembly of Intracellular Organelles. *Adv. Mater.* **35**, 2301856 (2023).

325. Seo, H. & Lee, H. Spatiotemporal control of signal-driven enzymatic reaction in artificial cell-like polymersomes. *Nat. Commun.* **13**, 1–12 (2022).

326. Martino, C. *et al.* Protein expression, aggregation, and triggered release from polymersomes as artificial cell-like structures. *Angew. Chem. Int. Ed. Engl.* **51**, 6416–6420 (2012).

327. Regus-Leidig, H. & Brandstätter, J. H. Structure and function of a complex sensory synapse. *Acta Physiol.* **204**, 479–486 (2012).

328. Raffaello, A., Mammucari, C., Gherardi, G. & Rizzuto, R. Calcium at the Center of Cell Signaling: Interplay between Endoplasmic Reticulum, Mitochondria, and Lysosomes. *Trends Biochem. Sci.* **41**, 1035–1049 (2016).

329. Christensen, K. A., Myers, J. T. & Swanson, J. A. pH-dependent regulation of lysosomal calcium in macrophages. *J. Cell Sci.* **115**, 599–607 (2002).

330. Medina, D. L. *et al.* Lysosomal calcium signalling regulates autophagy through

calcineurin and TFEB. *Nat. Cell Biol.* **17**, 288–299 (2015).

331. Feng, X. & Yang, J. Lysosomal Calcium in Neurodegeneration. *Messenger (Los Angeles, Calif. Print)* **5**, 56 (2016).

332. Rajdev, S. & Reynolds, I. J. Calcium green-5N, a novel fluorescent probe for monitoring high intracellular free Ca2+ concentrations associated with glutamate excitotoxicity in cultured rat brain neurons. *Neurosci. Lett.* **162**, 149–152 (1993).

333. Qutbuddin, Y. *et al.* Light-Activated Synthetic Rotary Motors in Lipid Membranes Induce Shape Changes Through Membrane Expansion. *Adv. Mater.* (2024) doi:10.1002/ADMA.202311176.

334. Ferreira, C. R. & Gahl, W. A. Lysosomal Storage Disease. in *Metabolic Diseases: Foundations of Clinical Management, Genetics, and Pathology* 367–440 (StatPearls Publishing, 2023).

335. Barnes, S. & Kelly, M. E. M. Calcium Channels at the Photoreceptor Synapse. in *Photoreceptors and Calcium* 465–476 (Landes Bioscience, 2002).

336. Saqib, S., Akram, A., Halim, S. A. & Tassaduq, R. Sources of β-galactosidase and its applications in food industry. *3 Biotech* 7, (2017).

337. Wutor, V. C., Togo, C. A. & Pletschke, B. I. The effect of physico-chemical parameters and chemical compounds on the activity of beta-d-galactosidase (B-GAL), a marker enzyme for indicator microorganisms in water. *Chemosphere* **68**, 622–627 (2007).

338. Huber, R. E., Parfett, C., Woulfe-Flanagan, H. & Thompson, D. J. Interaction of divalent cations with beta-galactosidase (Escherichia coli). *Biochemistry* **18**, 4090–4095 (1979).

339. Guinier, A. & Walker, C. B. *SMALL-ANGLE SCATTERING OF X-RAYS.* (John Wiley & Sons, Inc., 1955).

340. Silljé, H. H. W., Nagel, S., Körner, R. & Nigg, E. A. HURP Is a Ran-Importin β-Regulated Protein that Stabilizes Kinetochore Microtubules in the Vicinity of Chromosomes. *Curr. Biol.* **16**, 731–742 (2006).

10. Appendix

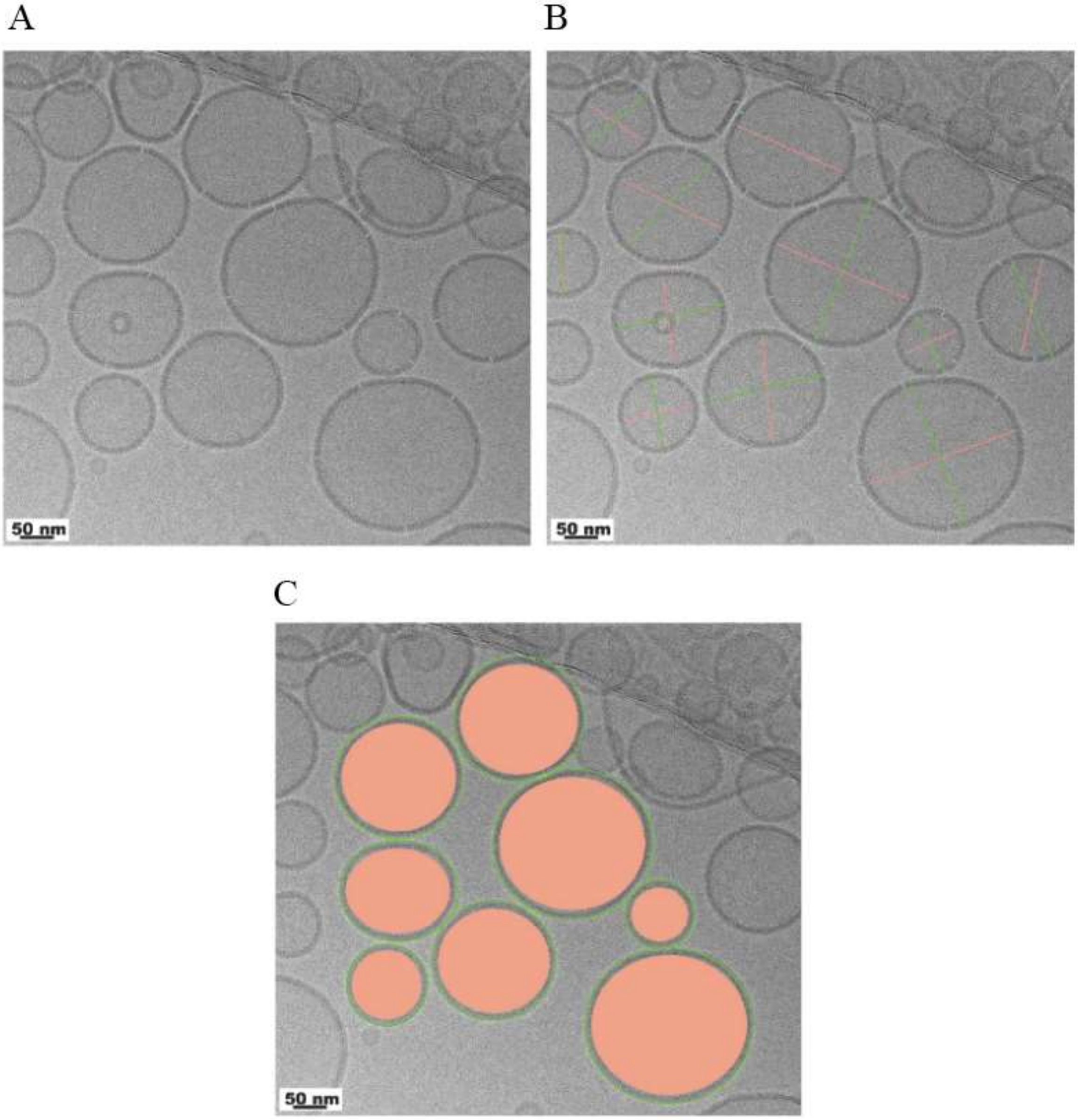

Figure 10.1. *Representative geometrical analysis of empty polymersomes using cryoTEM. (A) blue bars represent membrane thickness. (B) orange/green bars represent inner and outer diameter respectively. (C) orange/green circles represent inner/outer circular space of polymersome vesicles, respectively.*

Table 10.1. *Geometrical analysis and their data of empty polymersomes evaluated from cryoTEM images. Analysis performed with imaging software Image J.*

	Mean ± **SD**
Membrane thickness (nm)	9 ± 0.1
Inner diameter (nm)	145 ± 4.6

Outer diameter (nm)	160 ± 4.5
Inner area (nm²)	20552 ± 105.2
Otter area (nm²)	26140 ± 122.3
Circularity	1 ± 0.0
Roundness	1 ± 0.1
Solidity	1 ± 0.0

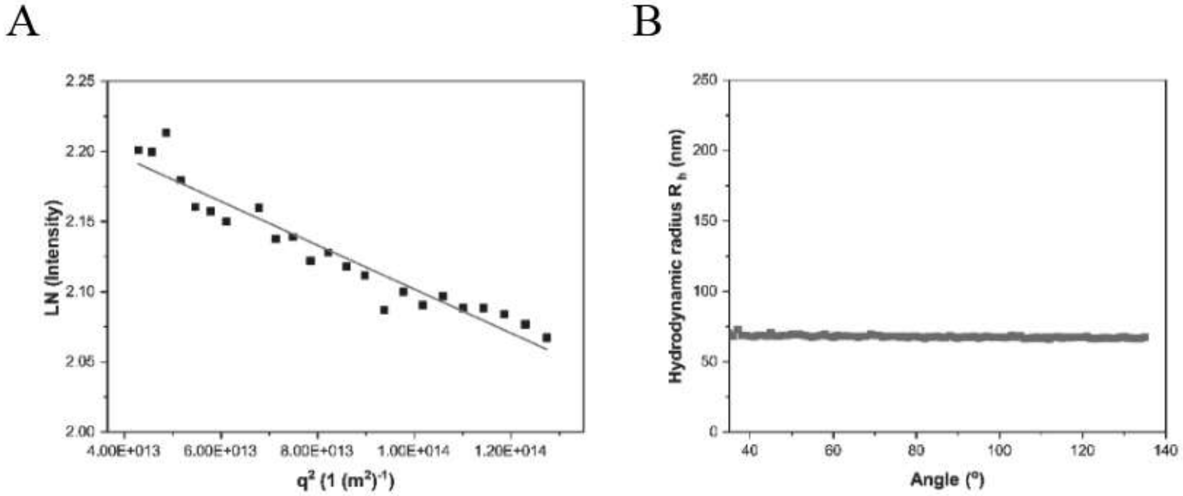

Figure 10.2. *SLS measurements of MM2 polymersomes. (A) SLS data of polymersomes containing 25 mol% MM2 in MilliQ water and linear fit to the Guinier equation. (B) SLS profile of polymersomes containing 25 mol% MM2.*

Table 10.2. *Z- potential values obtained for empty polymersomes and polymersomes containing MM2.*

	Mean ± SD
Empty Polymersomes	-9.72 ± 0.91
Polymersomes + 10 mol% MM2	-3.13 ± 0.29
Polymersomes + 25 mol% MM2	1.26 ± 0.40

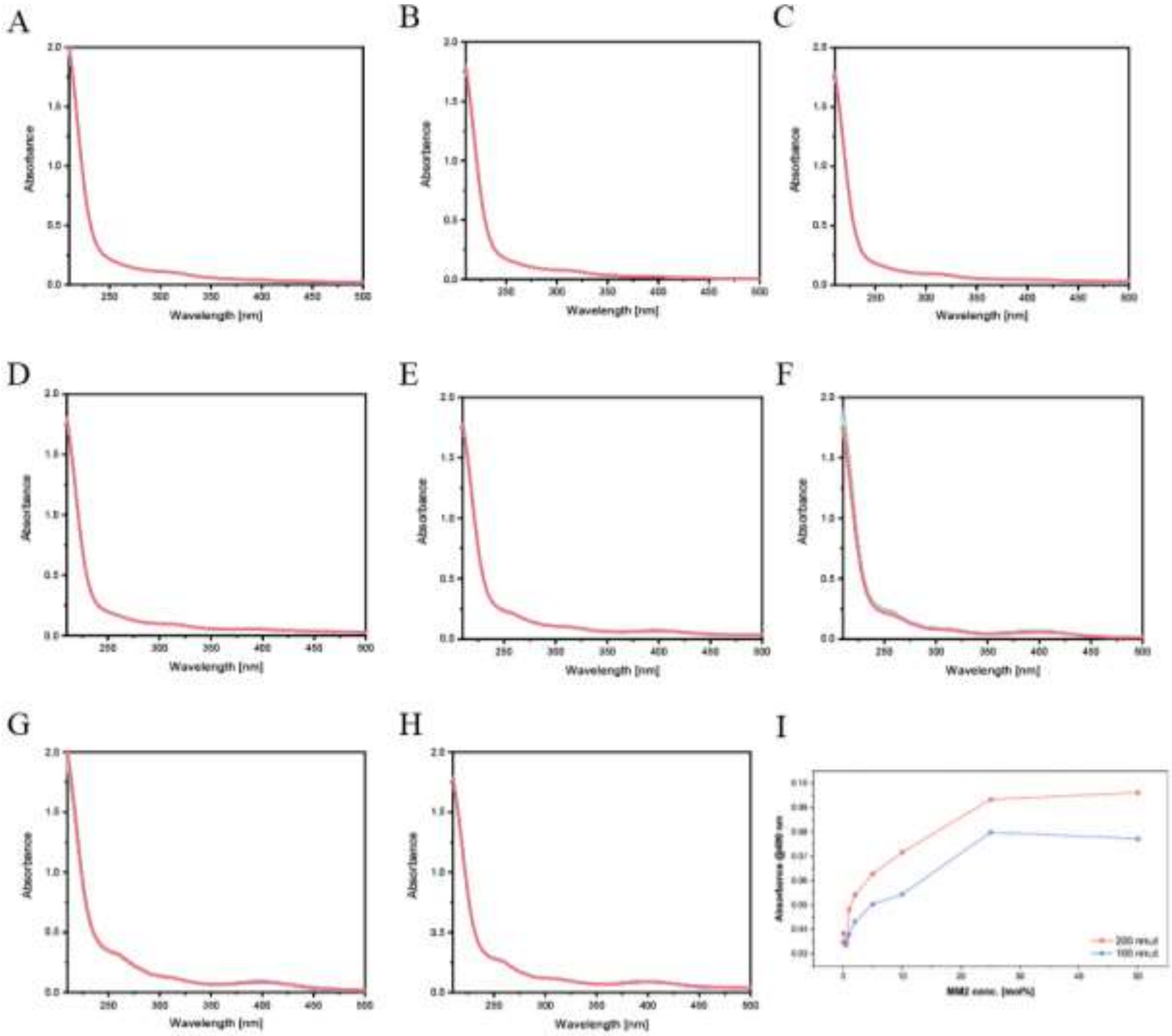

Figure 10.3. *UV-Vis spectra and absorbance value at 400 nm of MM2. (A) 0 mol%, (B) 0.5 mol%, (C) 1 mol%, (D) 2 mol%, (E) 5 mol%, (F) 10 mol%, (G) 25 mol%, (H) 50 mol% MM2 polymersome solution in PBS (C $_T$ = 0.1 g mL^{-1}) under light exposure. Irradiation was done with λ = 420 nm, 6.9 mW, 1 min at 25 °C. (I) Absorbance value at 400 nm of corresponding MM2 loaded polymersomes until saturation.*

Table 10.3. *Changes in the hydrodynamic radius (Z-average), polydispersity index (PDI) and mean count rate of polymersomes inoculated with 0 to 50 mol% of MM2, with and without irradiation using 420 nm light.*

	Ø (nm)	***hv* 420 nm**	**Z-average ± SD (nm)**	**PDI ± SD**	**Mean count rate (kcps)**	**Intercept**
Control	200	No	204 ± *7*	0.041 ± *0.007*	115.0 ± *9.9*	1.002 ± *0.005*
	200	Yes	203 ±*4*	0.046 ± *0.035*	173.3 ± *0.7*	0.983 ± *0.001*
0.5 mol% MM2	200	No	186 ± *3*	0.043 ± *0.010*	166.0 ± *2.0*	0.998 ± *0.010*
	200	Yes	178 ± *4*	0.043 ± *0.016*	144.3 ± *1.7*	0.986 ± *0.001*
1 mol% MM2	200	No	177 ± *4*	0.053 ± *0.024*	428.3 ± *1.8*	0.975 ± *0.003*
	200	Yes	170 ± *3*	0.020 ± *0.015*	458.0 ± *0.4*	0.966 ± *0.002*

2 mol% MM2	200	No	172 ± *4*	0.045 ± *0.021*	460.9 ± *0.6*	0.974 ± *0.004*
	200	Yes	171 ± *4*	0.048 ± *0.038*	432.0 ± *0.9*	0.971 ± *0.001*
5 mol% MM2	200	No	176 ± *4*	0.050 ± *0.007*	423.3 ± *1.1*	0.971 ± *0.003*
	200	Yes	174 ± *3*	0.051 ± *0.009*	418.1 ± *2.207*	0.964 ± *0.001*
10 mol% MM2	200	No	163 ± *4*	0.058 ± *0.019*	414.8 ± *0.5*	0.971 ± *0.002*
	200	Yes	164 ± *4*	0.051 ± *0.015*	404.7 ± *1.3*	0.966 ± *0.001*
25 mol% MM2	200	No	183.7 ± *5*	0.032 ± *0.012*	192.2 ± *0.7*	0.983 ± *0.001*
	200	Yes	185 ± *4*	0.081 ± *0.007*	185.9 ± *1.0*	0.977 ± *0.003*
50 mol% MM2	200	No	167 ± *4*	0.044 ± *0.010*	457.1 ± *0.4*	0.972 ± *0.004*
	200	Yes	163 ± *4*	0.056 ± *0.020*	454.7 ± *1.3*	0.967 ± *0.002*
Ctrl	100	No	135 ± *3*	0.227 ± *0.058*	478.1 ± *0.9*	0.985 ± *0.008*
	100	Yes	133 ± *3*	0.021 ± *0.015*	419.2 ± *3.4*	0.974 ± *0.001*
0.5 mol% MM2	100	No	134 ± *4*	0.045 ± *0.015*	445.4 ± *1.8*	0.971 ± *0.001*
	100	Yes	133 ± *4*	0.006 ± *0.002*	401.6 ± *1.1*	0.975 ± *0.004*
1 mol% MM2	100	No	135 ± *4*	0.022 ± *0.020*	468.6 ± *0.7*	0.973 ± *0.001*
	100	Yes	136 ± *3*	0.035 ± *0.027*	452.1 ± *2.1*	0.965 ± *0.001*
2 mol% MM2	100	No	135 ± *3*	0.022 ± *0.013*	476.4 ± *2.0*	0.974 ± *0.002*
	100	Yes	136 ± *3*	0.201 ± *0.009*	197.8 ± *1.0*	0.932 ± *0.000*
5 mol% MM2	100	No	130 ± *5*	0.010 ± *0.007*	150.5 ± *1.2*	0.985 ± *0.003*
	100	Yes	130 ± *2*	0.177 ± *0.012*	252.3 ± *0.5*	0.883 ± *0.003*
10 mol% MM2	100	No	114 ± *3*	0.040 ± *0.010*	325.4 ± *0.8*	0.976 ± *0.002*
	100	Yes	115 ± *4*	0.025 ± *0.010*	314.4 ± *1.0*	0.971 ± *0.000*
25 mol% MM2	100	No	123 ± *6*	0.067 ± *0.018*	443.3 ± *2.3*	0.974 ± *0.002*
	100	Yes	120 ± *4*	0.048 ± *0.006*	447.2 ± *1.0*	0.970 ± *0.001*
50 mol% MM2	100	No	135 ± *1*	0.040 ± *0.005*	246.3 ± *0.0*	0.977 ± *0.000*
	100	Yes	135 ± *5*	0.017 ± *0.006*	464.5 ± *0.9*	0.961 ± *0.002*

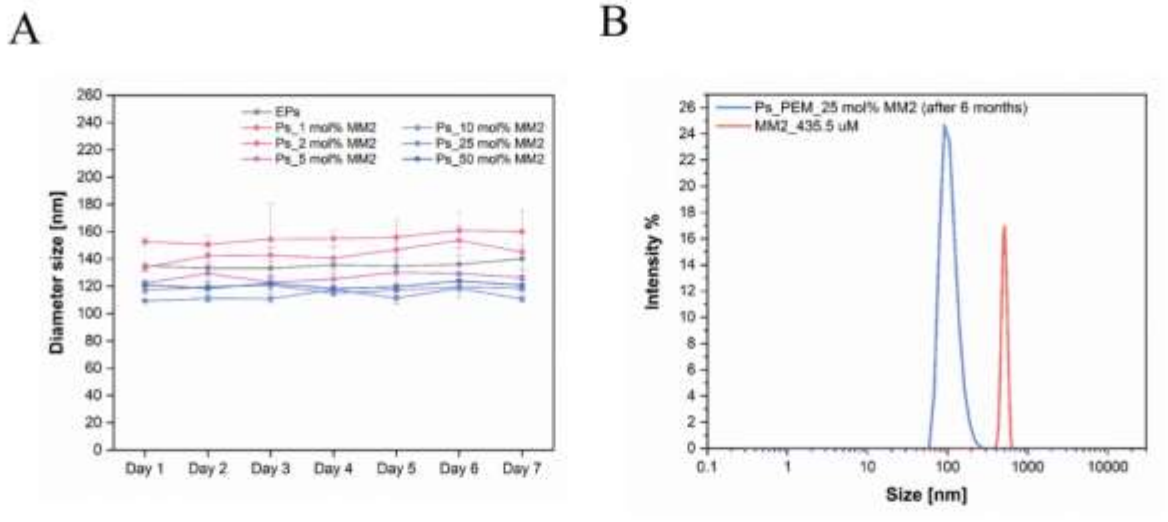

Figure 10.4. *Stability of polymersomes. (A) Physical stability of empty and MM2 loaded polymersomes over 7 days. (B) Structural stability of a Ps_PEM_25mol% MM2 sample after 6 months storage at 4 °C (blue). Representative aggregate sample of the corresponding MM2 concentration to illustrate how an unstable sample would show (red).*

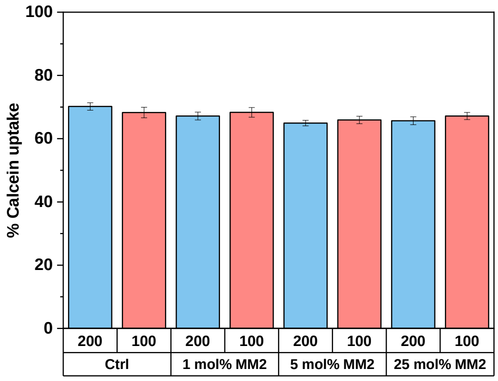

Figure 10.5. *% Calcein uptake in polymersomes (100 nm & 200 nm diameter).*

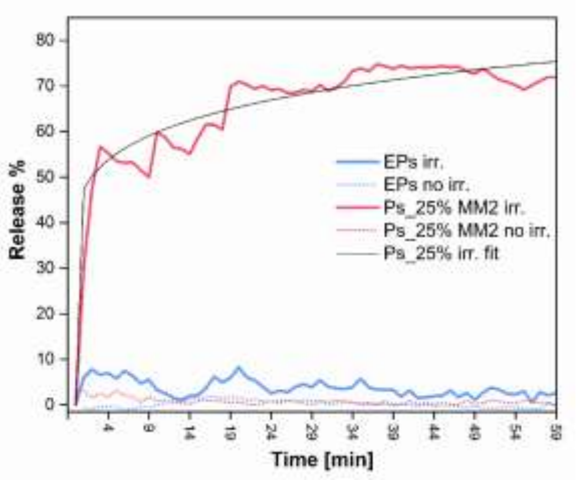

Figure 10.6. *Calcein release under continuous irradiation followed over 1 h. Data points obtained every min. Dashed lines corresponding to samples without irradiation. Black line corresponds to exponential fit.*

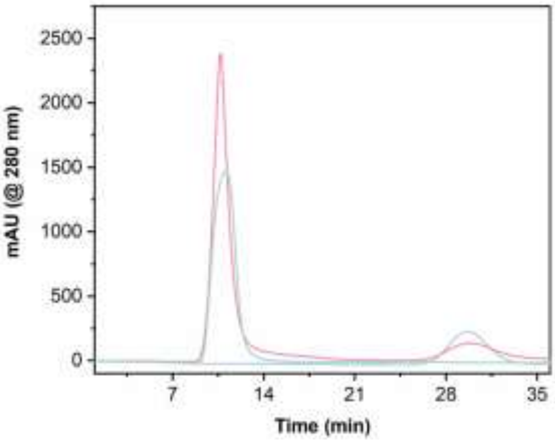

Figure 10.7. *Representative size exclusion chromatography (SEC) chromatogram of Pemetrexed drug (5 μM, blue), empty polymersomes (5 mg mL^{-1}, green) and polymersomes containing Pemetrexed (5 μM, 5 mg mL^{-1}, pink). (Eluent PBS).*

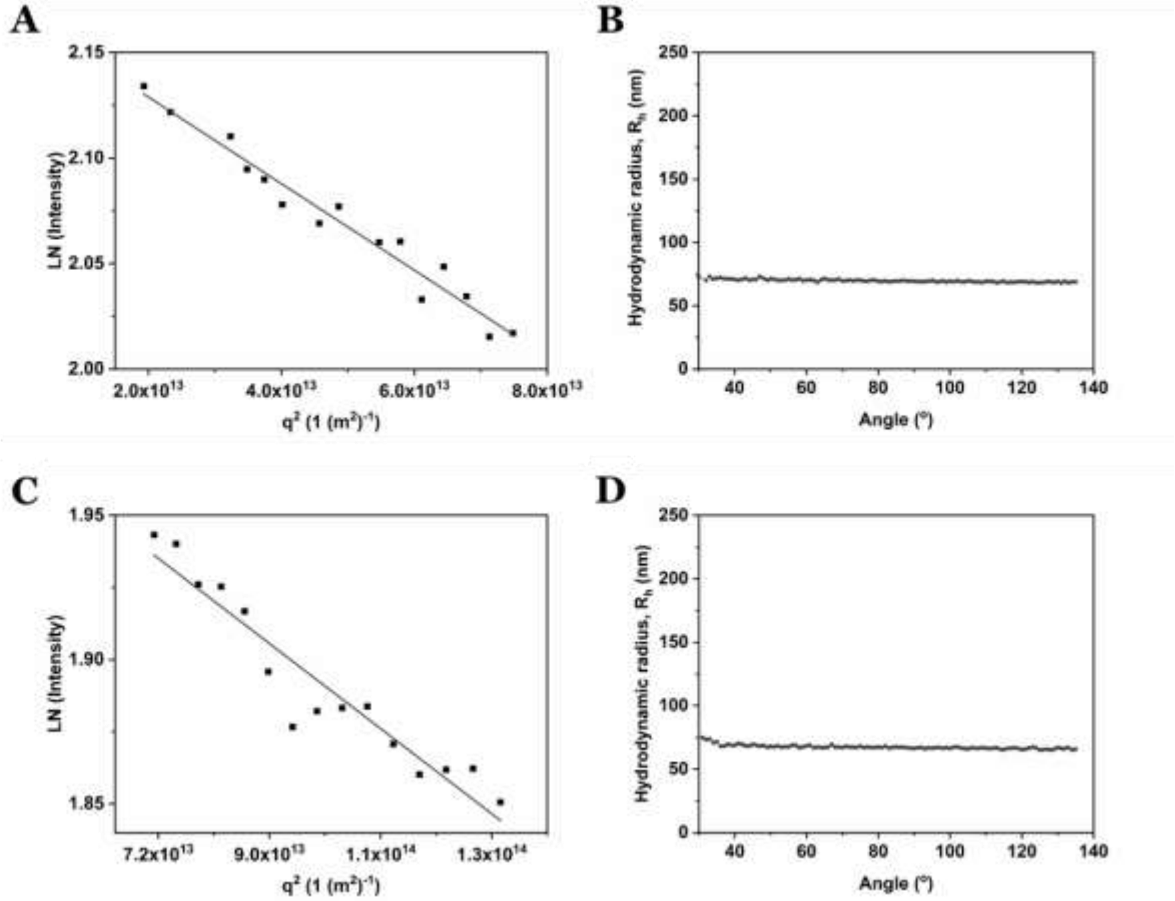

Figure 10.8. *SLS measurements of CNCs. SLS data of (A) GUS-melCNCs and (C) GUS-CNCs and linear fit to the Guinier equation. DLS profile of (B) GUS-melCNCs and (D) GUS-CNCs showing the mean hydrodynamic radius,* R_h.

Table 10.4. *Enzyme- and nanocompartment-related parameters quantified by FCS.*

	Free dye	**Dye-labeled GUS**	**GUS-melCNCs**	**GUS-CNCs**
Diffusion time (τ_D) (μs)	35 ± 1.6	427 ± 40	3364 ± 705	3505 ± 1186
Hydrodynamic diameter (nm)	na	na	120 ± 19	120 ± 33

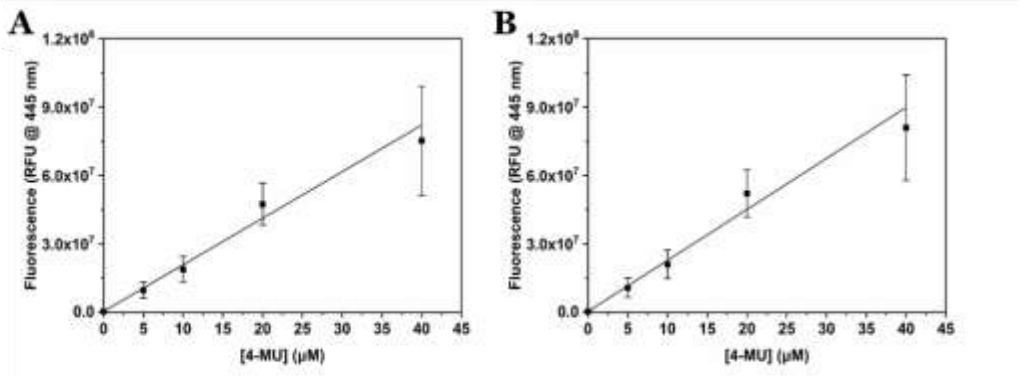

Figure 10.9. Calibration curve using 4-MU standards in (A) PBS and (B) MEM (R^2=0.98).

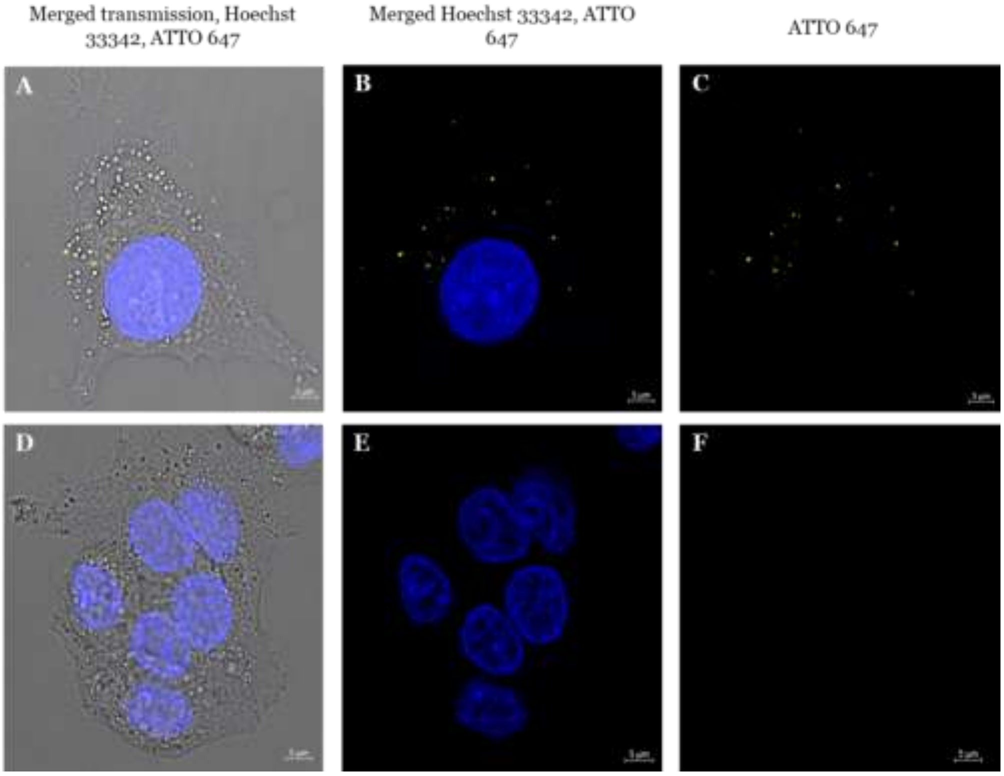

Figure 10.10. *Uptake of Atto647-PSs by HepG2 cells. (A - C) HepG2 cells incubated with Atto647-PSs (1.25 mg mL^{-1}) for 24 h. (D - F) HepG2 control cells imaged under identical conditions. Scale bar: 5 µm.*

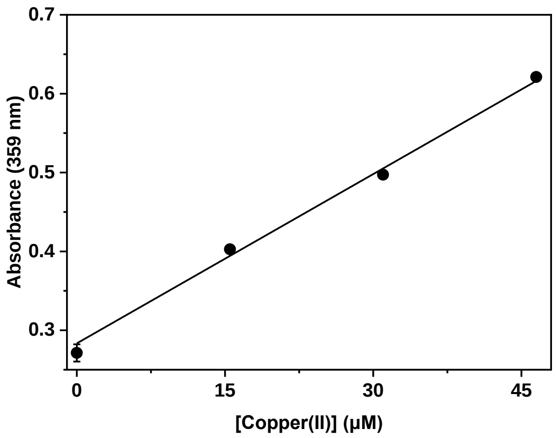

Figure 10.11. *Copper(II) calibration curve (R^2 = 0.99).*

Table 10.5. *Characterization of polymersomes.*

	Diameter (nm) by DLS	**PDI**	**Diameter (nm) by NTA**	**ρ (R_g/ R_h)**	**Concentration (polymersomes mL^{-1})**
Glycooligomer-functionalized polymersomes	135 ± 54	0.1	138 ± 38	0.81 ± 0.16	(5.6 ± 0.5) x 10^{11}
Non-functionalized polymersomes	122 ± 40	0.07	108 ± 22	0.97 ± 0.05	(7.9 ± 0.5) x 10^{11}
Glycooligomer-functionalized Atto647-encapsulating polymersomes	137 ± 39	0.05	140 ± 26	1.05 ± 0.23	(6.7 ± 0.1) x 10^{11}
Non-functionalized Atto647-encapsulating polymersomes	128 ± 40	0.1	112 ± 23	1.03 ± 0.1	(6.5 ± 0.18) x 10^{11}

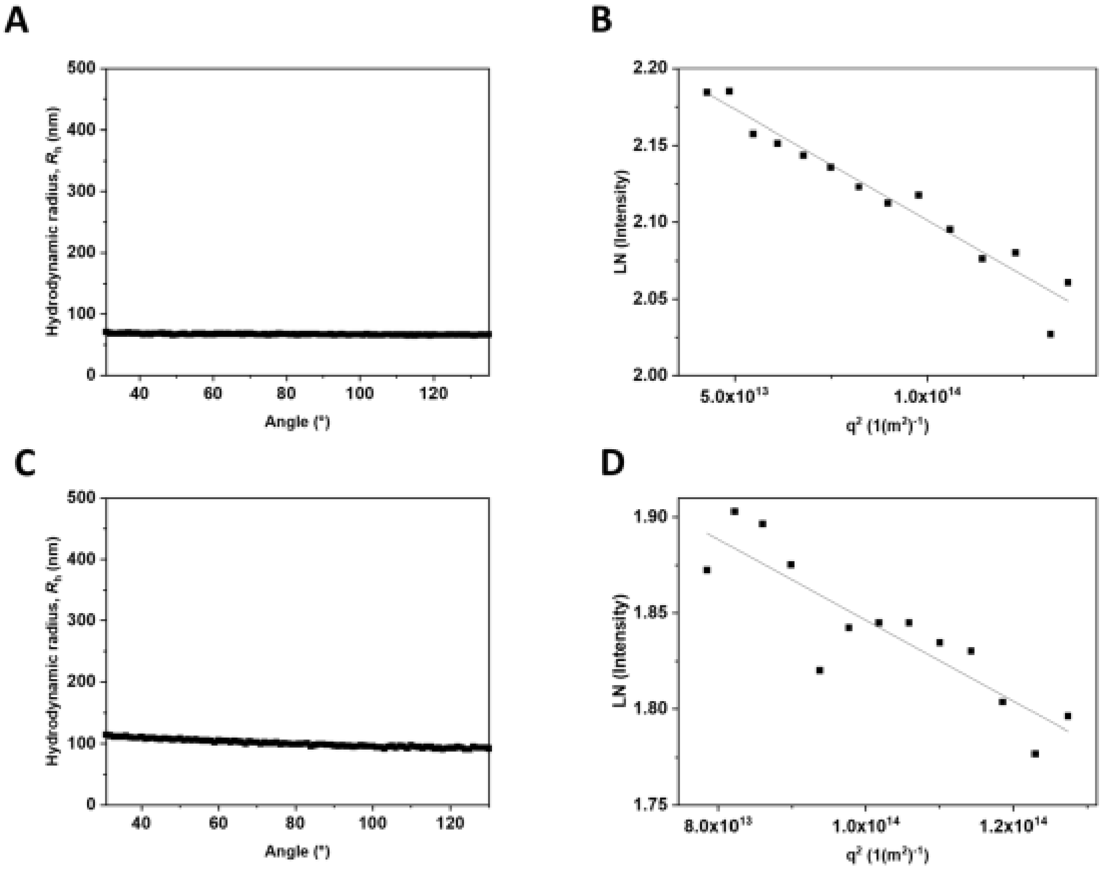

Figure 10.12. *SLS measurements of polymersomes with and without glycooligomer functionalization. DLS profile of (A) non-functionalized and (C) glycooligomer-functionalized polymersomes showing the mean hydrodynamic radius, R_h. SLS data of (B) non-functionalized and (D) glycooligomer-functionalized polymersomes and linear fit to the Guinier equation.*

Table 10.6. *Number of melittin pores per polymersome.*

Sample	**Diffusion time (µs)**	**No. of melittin pores/ polymersome**
PSs-Cy5-mel (25 µM)	4754 ± 1712	133 ± 12
PSs-Cy5-mel (50 µM)	4289 ± 1501	242 ± 28
PSs-Cy5-mel (75 µM)	5533 ± 2170	225 ± 28
PSs-Cy5-mel-Gly (50 µM)	4959 ± 1975	220 ± 16

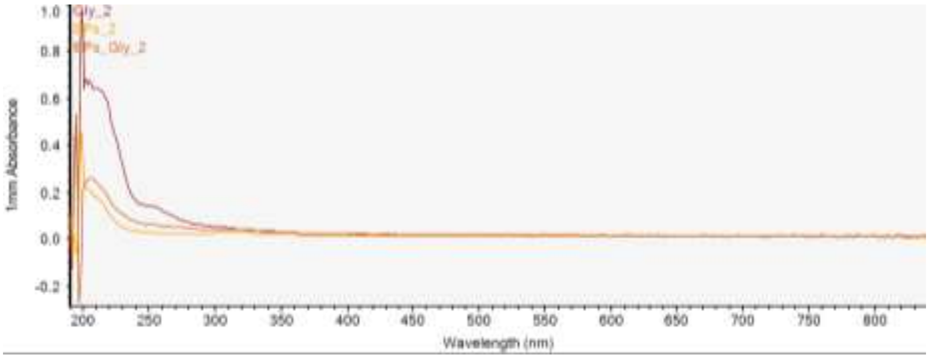

Figure 10.13. *Representative UV-Vis spectra of glycooligomer 3 (Gly), empty, non-functionalized polymersomes (EPs) and glycooligomer-functionalized polymersomes (EPs_Gly).*

Table 10.7. *Kinetic binding data for glycooligomer 3 and PDMS-b-PMOXA-Gly obtained from fitting the SPR binding curves with the 1:1 Langmuir binding model.*

Sample	**Lectin**	**k_A [M^{-1} s^{-1}]**	**k_D [s^{-1}]**	**R_{max} [RU]**	**K_A [M^{-1}]**	**K_D [M]**
Glycooligomer (**3**)	MBL	961	1.38 x 10^{-3}	117	6.98 x 10^{5}	1.43 x 10^{-6}
Glycooligomer (**3**)	DC-SIGN	355	3.25 x 10^{-4}	193	1.09 x 10^{6}	9.15 x10^{-7}
Glycooligomer (**3**)	MR	101	5.15 x 10^{-4}	105	1.96 x 10^{5}	5.10 x10^{-6}
Glycooligomer-functionalized polymersomes	MBL	200	1.29 x 10^{-3}	130	1.55 x 10^{5}	6.43 x 10^{-6}
Glycooligomer-functionalized polymersomes	DC-SIGN	121	5.42 x 10^{-4}	188	2.24 x 10^{5}	4.47 x10^{-6}
Glycooligomer-functionalized polymersomes	MR	1770	2.75 x 10^{-3}	118	6.45 x 10^{5}	1.55 x10^{-6}

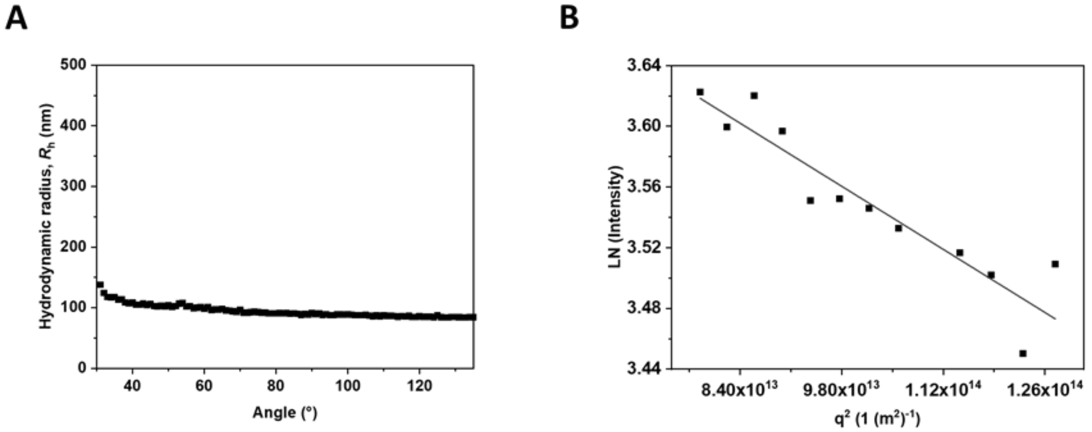

Figure 10.14. *SLS measurements of GUS-GOx-CNCs-Gly. (A) DLS profile of GUS-GOx-CNCs-Gly showing the mean hydrodynamic radius, R_h. (B) SLS data of GUS-GOx-CNCs-Gly and linear fit to the Guinier equation.*

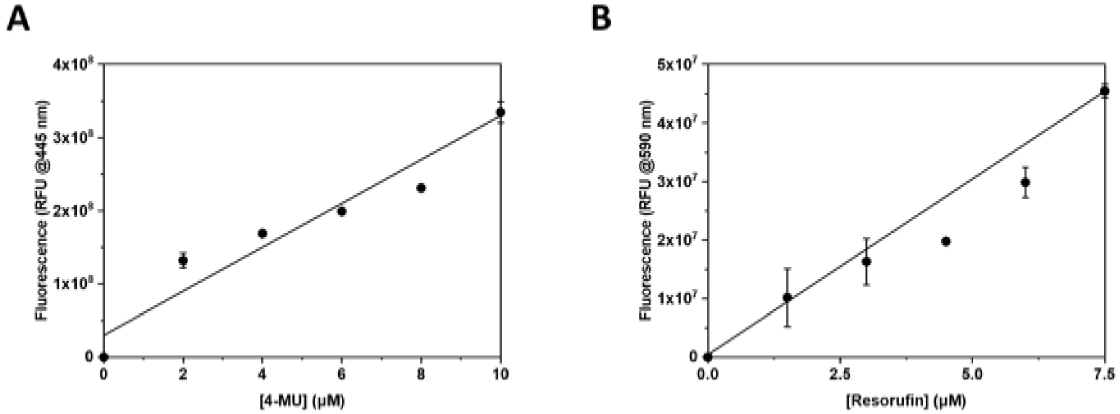

Figure 10.15. *Calibration curves using (A) 4-MU ($R^2 = 0.93$) and (B) resorufin standards ($R^2 = 0.96$) in PBS containing 50% Dulbecco's Modified Eagle Medium (DMEM) Phenol Red free with 10% Fetal Bovine Serum.*

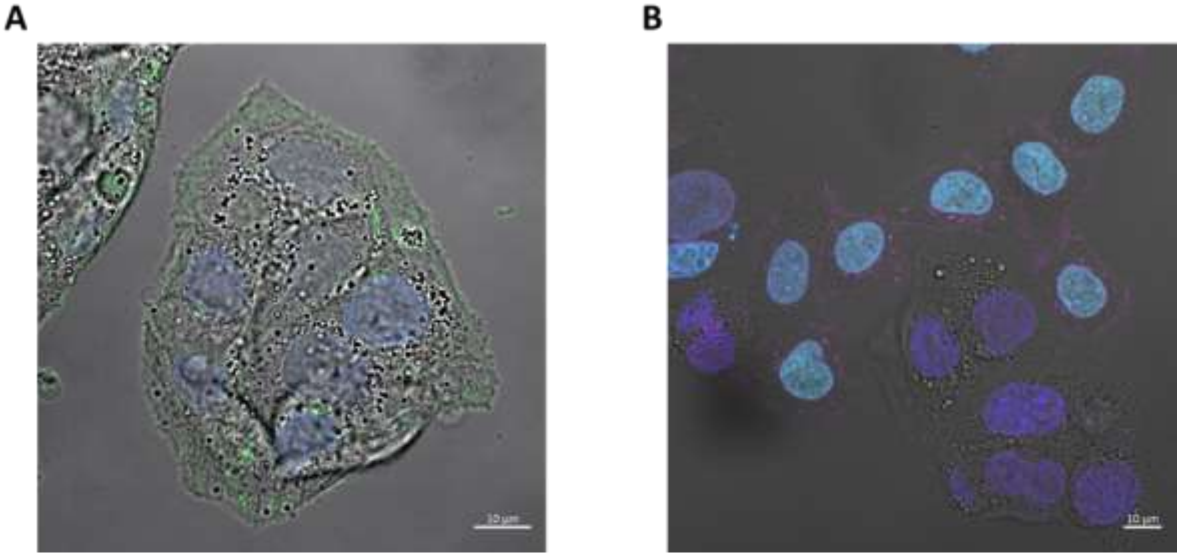

Figure 10.16. *HepG2 and HeLa S3 H2B-GFP cells incubated with PBS. (A) HepG2 cells incubated with the equivalent amount of PBS, Yellow: polymersomes, Atto647, Green: Cell membranes, Atto488-WGA, Blue: nuclei, Hoechst 33342. (B) HepG2 and HeLa S3 H2B-GFP co-cultured cells incubated with the equivalent amount of PBS, Yellow: polymersomes, Atto647, Pink: Cell membranes, Atto555-WGA, Blue: nuclei, Hoechst 33342, Green: nuclei, GFP. Scale bar: 10 µm.*

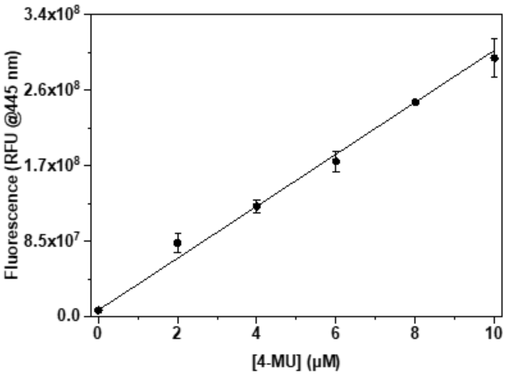

Figure 10.17. *Calibration curves using 4-MU in full Dulbecco's Modified Eagle Medium (R^2 = 0.99).*

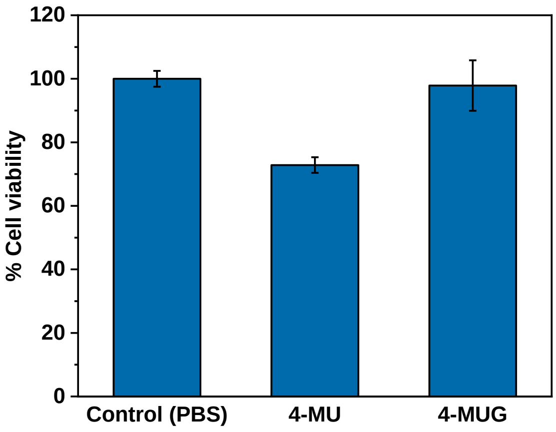

Figure 10.18. *Cell viability of HepG2 cells. Cell viability as percentage of HepG2 cells incubated with only PBS (control), 4-MU (190 µM) or 4-MUG (190 µM). Graph shows mean ± s.d. of six repetitions.*

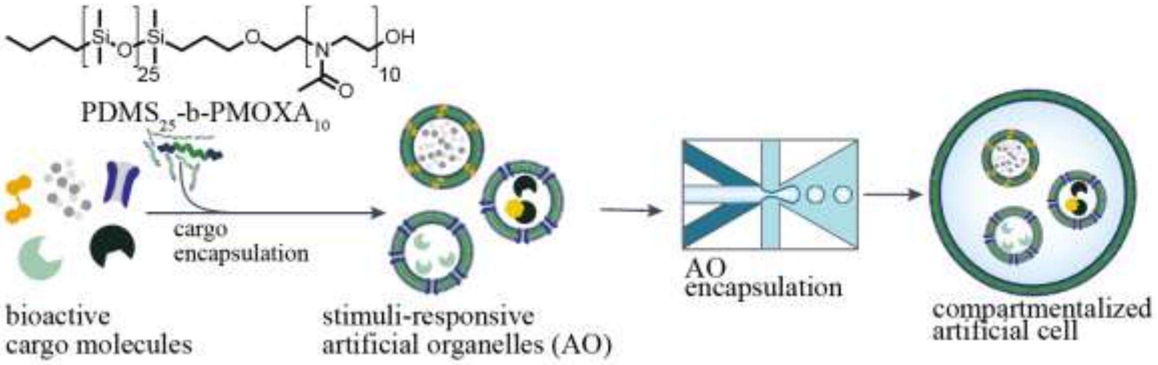

Figure 10.19. *Formation of compartmentalized artificial cells. Bioactive cargo molecules are encapsulated in self-assembled artificial organelles by film rehydration, forming functional artificial organelles. Subsequently, stimuli-responsive artificial organelles are encapsulated into GUVs using double emulsion microfluidics.*

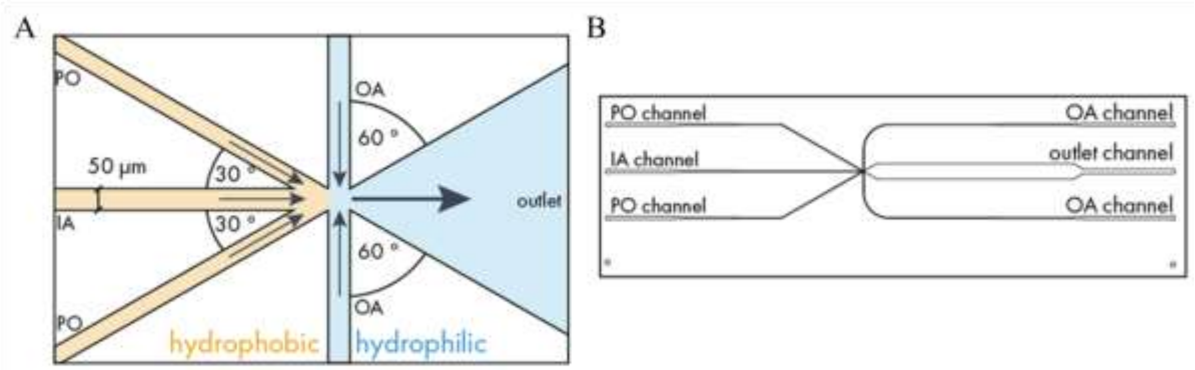

Figure 10.20. *Microfluidic chip design. (A) Design of six-way junction used for double emulsion generation aided by hydrophobic and hydrophilic channel coating. Inner aqueous (IA) and polymer organic (PO) channels are rendered hydrophobic through coating with Aquapel and outer aqueous*

(OA) and outlet channels are rendered hydrophilic through plasma activation followed by coating using polyvinyl alcohol.[318] *(B) Complete design of microfluidic six-way junction on a silicon glass chip.*

Table 10.8. *Concentration of AOs in IA.*

	Dilution Factor	**Concentration in IA [AO mL^{-1}]**
AO_A488	1000 - 10	$3.4 \times 10^{9} – 3.4 \times 10^{11}$
AO_MM_A488	25	$6.7 \pm 1.2 \times 10^{9}$
AO_CaGreen	5	$3.8 \pm 0.4 \times 10^{11}$
AO_mel_CaGreen	5	$3.4 \pm 5 \times 10^{11}$
AO_βGal	50	$2.8 \pm 0.1 \times 10^{10}$
AO_mel_βGal (Fig 4d)	50	$1.5 \pm 0.2 \times 10^{10}$
AO_mel_βGal (Fig 5)	6.25	$1.2 \pm 0.2 \times 10^{11}$
AO_MM_FDG	25	$6.0 \pm 0.4 \times 10^{10}$
AO_mel_CaRed	5	$2.6 \pm 0.01 \times 10^{11}$

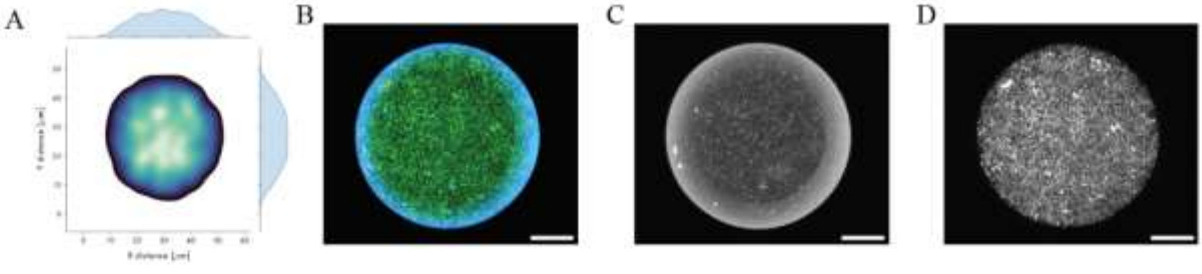

Figure 10.21. *Encapsulation and distribution of AO_Atto488 in protocells. (A) Three-dimensional AO distribution within a protocell at a concentration of 3.4×10^{10} mL^{-1} visualized through a two-dimensional Kernel Density Estimation plot with 20 levels along the x and y axes. Histograms represent the AO density distribution along the x and y axes. The centralized peak and symmetric density contours suggest a uniform particle distribution in the sphere's volume, with a higher concentration at the core (n=3). (B – D) Maximal projection of an exemplary GUV containing ATTO488-encapsulating AOs (green) formed with an input AO concentration of 3.4×10^{11} AO mL^{-1}. The GUV membrane was stained with 2.5 µM BODIPY 630/650 (cyan). Merged fluorescence (B) and single channel images of the stained membrane (C) and AOs (D) show no aggregation of AOs at the membrane. Scale bar: 10 µm.*

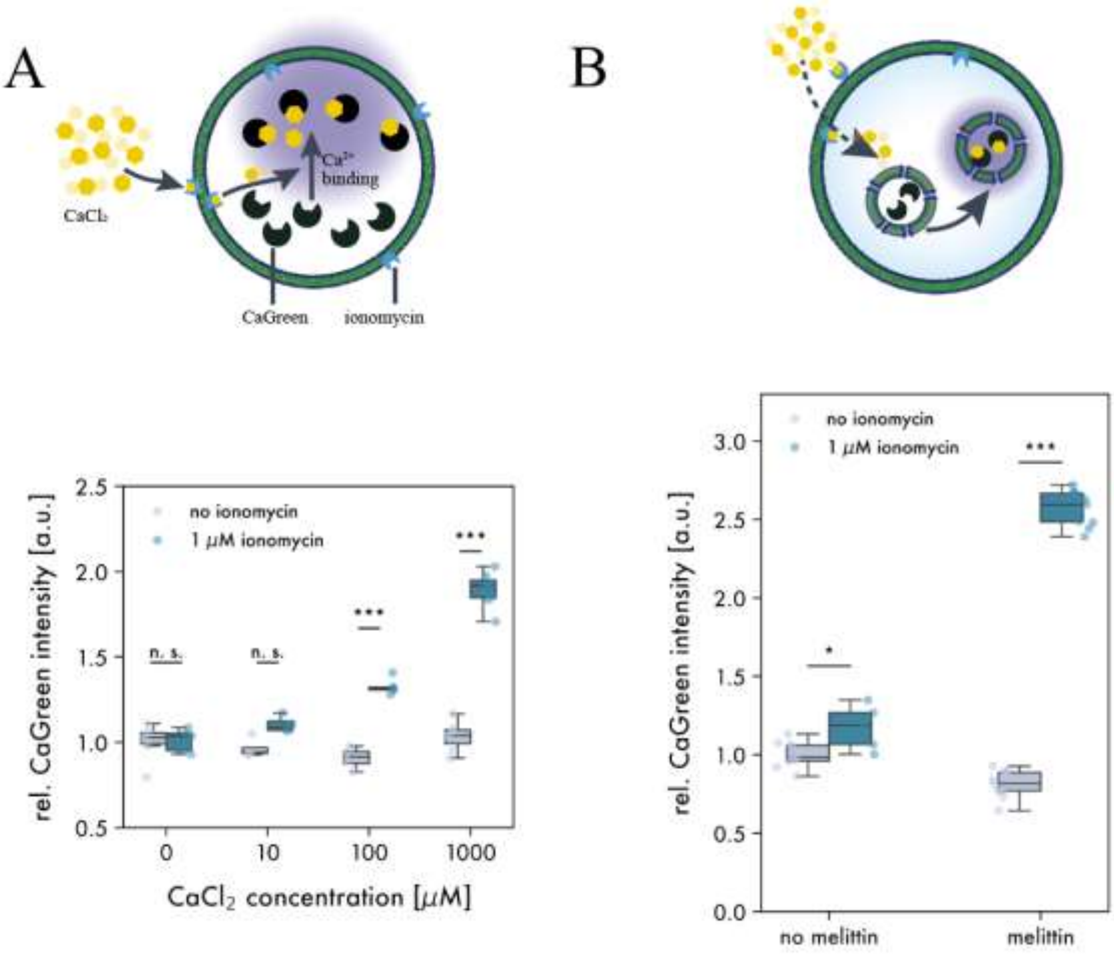

Figure 10.22. *Schematic representation of calcium detection in an artificial cell with ionomycin in the polymer membrane. Calcium enters the artificial cells via ionomycin-facilitated transport and binds to the Ca^{2+}-sensitive dye CaGreen, thereby increasing its fluorescence. (A) Normalized CaGreen fluorescence inside artificial cells upon extravesicular administration of 0-1000 μM $CaCl_2$. (B) Normalized CaGreen fluorescence inside artificial cell encapsulating CaGreen-loaded AOs upon extravesicular administration of 1 mM $CaCl_2$. (n>5 per condition) Significance levels: $p > 0.05$ (n.s.), $p < 0.05$ (*), $p < 0.005$ (**), and $p < 0.0005$ (***).*

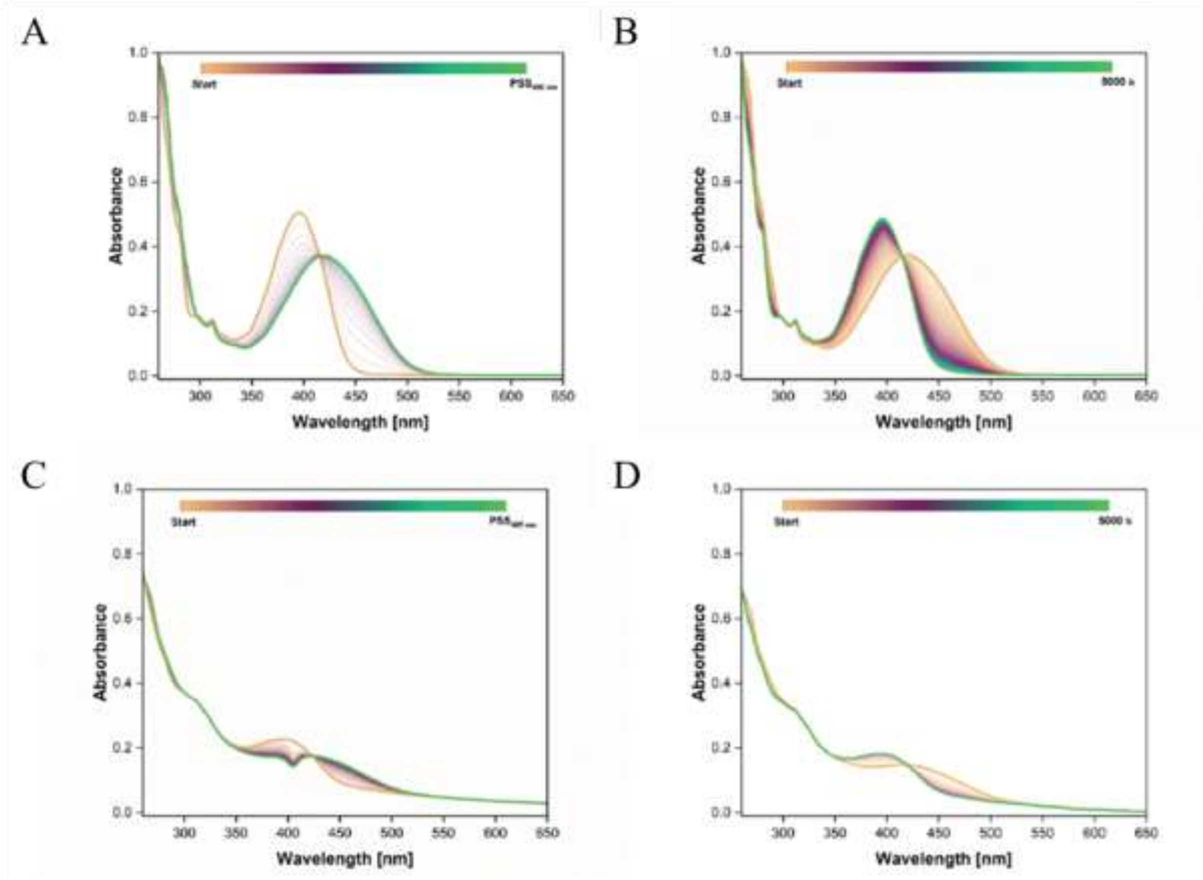

Figure 10.23. *Photoisomerization of MM.(A) Photoisomerization of Molecular Motor (MM). (B) MM Thermal helix inversion (405 nm, $CH_{12}H_{26}$, 25 °C, 50uM). (C) Photoisomerization of AOs with 25mol% MM. (D) AOs with 25%mol MM Thermal helix inversion (405 nm, PBS, 25 °C, 50 μM).*

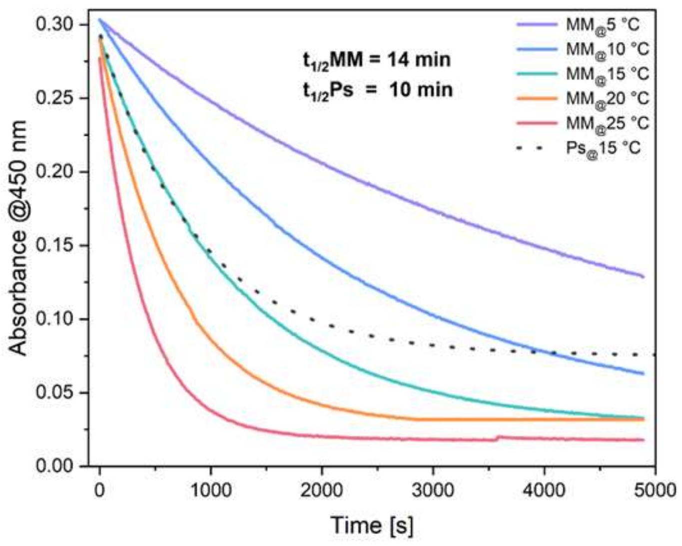

Figure 10.24. *E-Z isomerization in AO_MM. Speed determination – Thermodynamic activation parameters - Eyring Plot decays. Half speed of rotation of the MM in solution or in the AO membrane.*

Table 10.9. *Quantum yield of molecular motors inside and outside of AO membranes*

	Quantum yield ± sd
MM	*15.09 ± 0.51*
AO + 25 mol%	*8.34 ± 2.51*

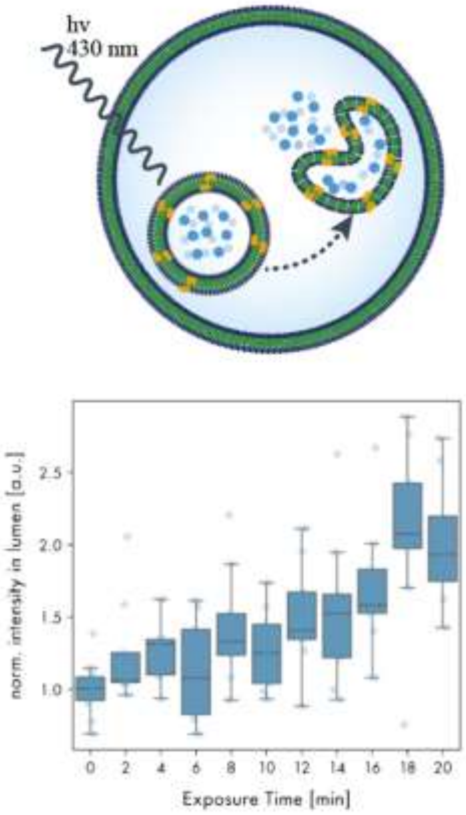

Figure 10.25. *Response to light triggers and cargo release by AOs in ACs.* Release of ATTO488 dye from the intracellular AO upon exposure at 430 nm for up to 20 min with 2 min intervals. Fluorescence measured in the lumen of artificial cells from fluorescence micrographs (n=3 per condition).

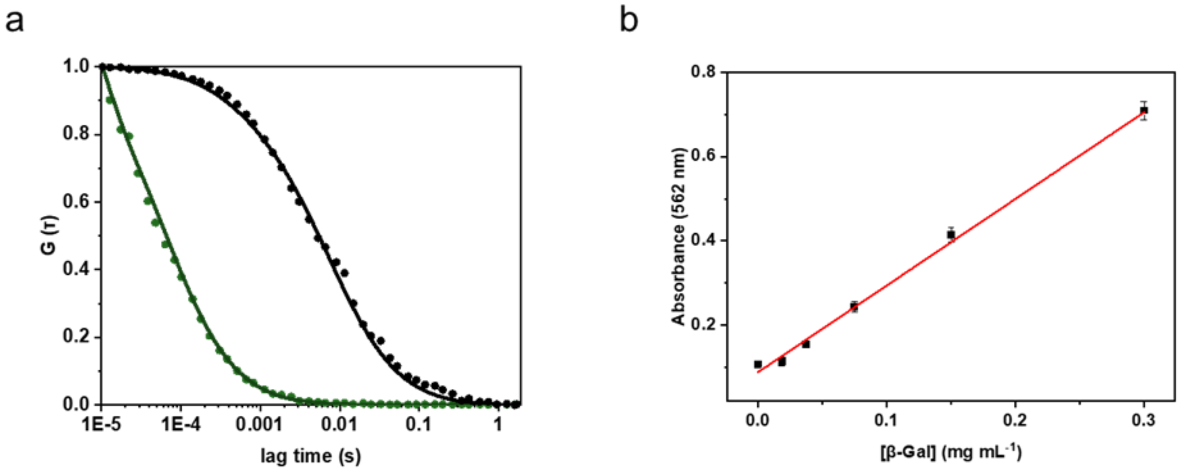

Figure 10.26. *FCS measurements of Cy5-melittin polymersomes and βGal calibration curve.Normalized FCS autocorrelation curves of free Cy5-melittin (green, τ_D = 500 µs) and AO_Cy5-melittin (50 µM initial melittin concentration, black, τ_D = 4400 µs). Symbols: raw data, Lines: fitted curves. (B) Calibration curve for the BCA protein assay for βGal (R^2 = 0.99).*

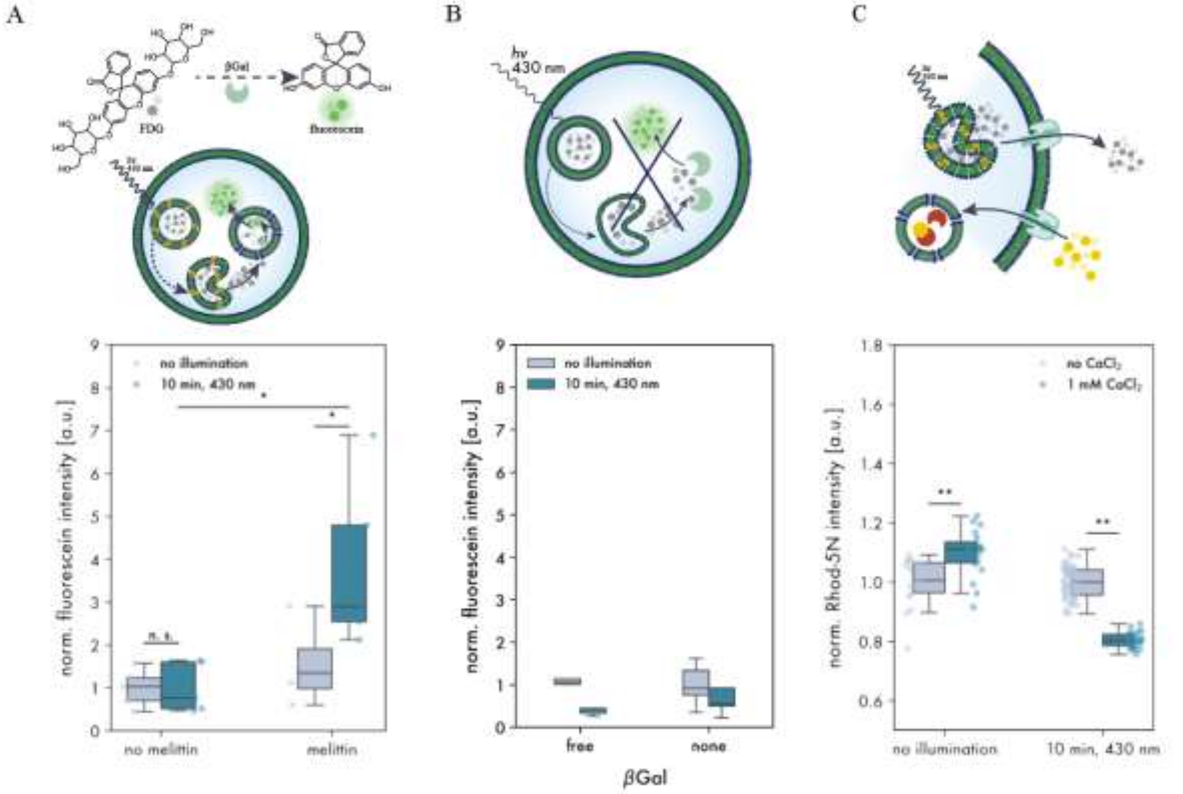

Figure 10.27. *Intracellular communication mimic and calcium response upon light input. Schematic representation of stimuli-responsive intracellular signaling cascade between AOs in a protocell. Upon irradiation, MM-AO release FDG which can diffuse through melittin pores into a second, βGal-encapsulating AO. The βGal hydrolyzes the non-fluorescent substrate FDG to the fluorescent fluorescein product. Normalized fluorescence inside artificial cells encapsulating AOs_MM_FDG and AOs_βGal with and without melittin pores after 1 h of incubation (n=5 per condition). (B) Controls for compartmentalized intracellular signaling without molecular motors in the FDG-containing AOs (C) Artificial cells are harnessed with calcium sensing capability by co-encapsulating AOs loaded with Ca^{2+}-sensitive dye and FDG-releasing AOs. Normalized Rhod-5N fluorescence inside not-illuminated*

(left) and illuminated (right) sender cells upon incubation with 0 or 1 mM $CaCl_2$. Significance levels: $p > 0.05$ (n.s.), $p < 0.05$ (*), $p < 0.005$ (**), and $p < 0.0005$ (***).

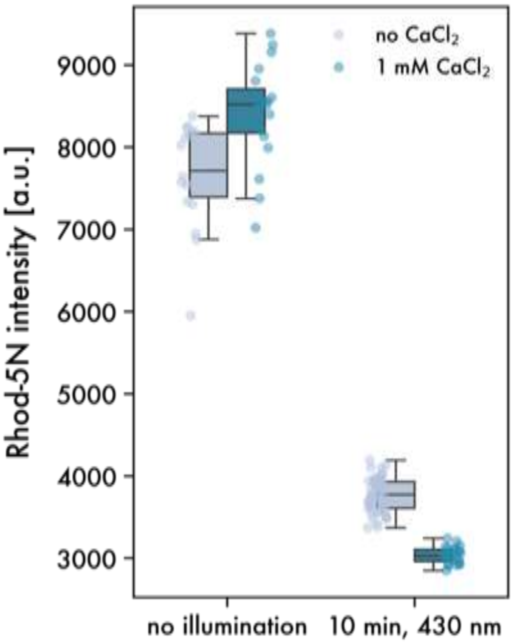

Figure 10.28. *Non-normalized Rhod-5N fluorescence intensity in GUVs permeabilized with DNA-nanopores containing AO_mel_R5N and AO_MM_AO with and without illumination and with different externally added CaCl2.*

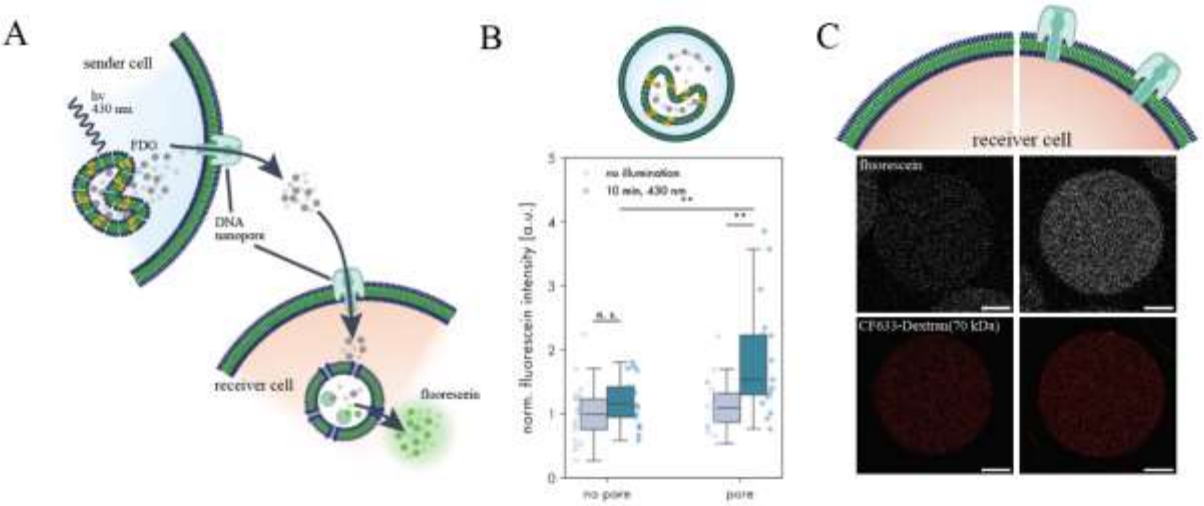

Figure 10.29. *Intercellular signaling involving organelles spatially confined in separate protocells.Schematic overview of light-triggered signaling cascade from sender to receiver cell in a 6:1 ratio. Irradiation at 430 nm causes of FDG-encapsulating AOs to rupture, releasing non-fluorescent FDG. FDG diffuses via DNA nanopores from the sender cell to the receiver cell containing AOs encapsulating the enzyme βGal. Inside the receiver cells, FDG enters AOs_mel_βGal via melittin pores, and finally gets hydrolyzed to its fluorescent product fluorescein by the confined enzyme. (B) Normalized fluorescence inside receiver cell encapsulating AO_mel_βGal with and without DNA*

nanopores after 1 h of co-incubation with sender cells encapsulating FDG in photolabile AOs (AO_MM_FDG) (n≥5 per condition). (C) Fluorescence micrographs of representative single receiver cell from (B) equipped with CF633-dextran(70 kDa) (red, bottom) showing fluorescein fluorescence (green, top) without (left) and with (right) DNA nanopores after 1 h co-incubation with FDG_MM_AO-encapsulating sender cells. Scale bar: 10 µm.

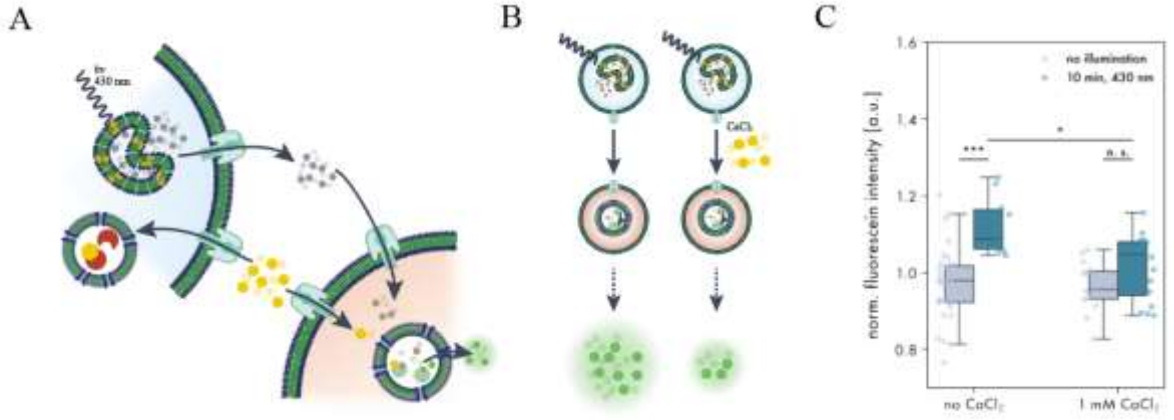

Figure 10.30. *Sensitivity modulation of artificial cell-cell communication. The external addition of $CaCl_2$ decreases the signal transmission in the receiver cell, thereby decreasing the gain of the system. (B) Calcium has an inhibitory effect on βGal encapsulated in the receiver cell, thereby modulating the overall photosensitivity of the receiver cell. (C) Normalized fluorescein intensity in receiver cells encapsulating AO_mel_βGal in the presence or absence of $CaCl_2$ after 1 hour of incubation (n≥5). Significance levels: $p > 0.05$ (n.s.), $p < 0.05$ (*), $p < 0.005$ (**), and $p < 0.0005$ (***).*

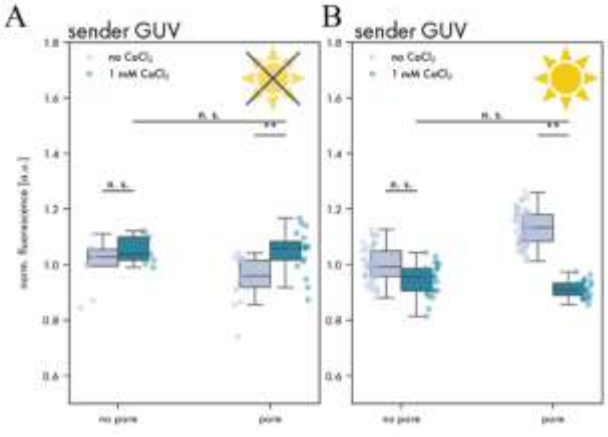

Figure 10.31. *Changes in Rhod-5N sender protocells. (A & B) Rhod-5N fluorescence change upon administration of 1 mM $CaCl_2$ in sender protocell without (A) and with (B) 10 min illumination at 430 nm. (C & D).*